

**TNO report****TNO 2020 R12004****Techno-Economic Modelling of Large-Scale  
Energy Storage Systems**Princetonlaan 6  
3584 CB Utrecht  
P.O. Box 80015  
3508 TA Utrecht  
The Netherlands[www.tno.nl](http://www.tno.nl)T +31 88 866 42 56  
F +31 88 866 44 75

|                      |  |
|----------------------|--|
| Date                 | 30 August 2020   |
| Author(s)            | Remco Groenenberg, Joaquim Juez-Larré, Cintia Goncalvez, Laura Wasch, Hester Dijkstra, Brecht Wassing, Bogdan Orlic, Logan Brunner, Kaj van der Valk, Thomas Hajonides van der Meulen, Karin Kranenburg-Bruinsma |
| Number of pages      | 154 (incl. appendices)   |
| Number of appendices | 3  |
| Sponsor              | NAM, Gasunie, Gasterra, Nouryon, EBN, Rijksdienst voor Ondernemend Nederland (RVO)   |
| Project name         | Large-Scale Energy Storage in Salt Caverns and Depleted Gas Fields (Acronym: LSES)   |
| Project number       | 060.36821, subsidy reference: TGEO118002   |

All rights reserved.

No part of this publication may be reproduced and/or published by print, photoprint, microfilm or any other means without the previous written consent of TNO.

In case this report was drafted on instructions, the rights and obligations of contracting parties are subject to either the General Terms and Conditions for commissions to TNO, or the relevant agreement concluded between the contracting parties. Submitting the report for inspection to parties who have a direct interest is permitted.

© 2020 TNO

## Preface

This report details the results of the activities performed in work package 2 of the research project “Large-Scale Energy Storage in Salt Caverns and Depleted Gas Fields”, abbreviated as LSES. The project, which was given subsidy by RVO, had two main goals:

1. Improve insights into the role that large-scale subsurface energy storage options can play in providing flexibility to the current and future transitioning energy system;
2. Address techno-economic challenges, identify societal and regulatory barriers to deployment, and assess risks associated with selected large-scale subsurface energy storage technologies, in particular Compressed Air Energy Storage (CAES) and Underground Hydrogen Storage (UHS).

The research was carried out by TNO in close collaboration with project partners EBN, Gasunie, Gasterra, NAM and Nouryon. Activities were divided over 4 work packages that ran in parallel:

1. Analysis of the role of large-scale storage in the future energy system: what will be the demand for large-scale storage, when in time will it arise, and where geographically in our energy system will it be needed?
2. Techno-economic modelling (performance, cost, economics) of large-scale energy storage systems, focusing in CAES and UHS in salt caverns, and UHS in depleted gasfields - analogous to UGS (Underground natural Gas Storage).
3. Assessment of the current policy and regulatory frameworks and how they limit or support the deployment of large-scale energy storage, and stakeholder perception regarding energy storage.
4. Risk identification and screening for the selected large-scale subsurface energy storage technologies.

In this report, the results of the activities performed in work package 2 on techno-economic modelling of large-scale energy storage systems are detailed. The results of the other work packages are detailed in three other reports.

### Project details

|                       |   |
|-----------------------|---|
| Subsidy reference:    | TGEO118002  |
| Project name:         | Large-Scale Energy Storage in Salt Caverns and Depleted Gas Fields    |
| Project period:       | April 16, 2019 until August 30, 2020                                  |
| Project participants: | TNO (executive organization), EBN, Gasunie, Gasterra, NAM and Nouryon |

### Acknowledgements

The authors would like to thank Shell for their contribution to the geo- and biochemical modelling methodology for UHS (section 3.4), Uniper for information on the technical specifications and performance of the Huntorf CAES plant, and Corre Energy Storage for information on the value of storage, and CAES in particular. All project partners (EBN, NAM, Gasunie, GasTerra, and Nouryon) are thanked for their reviews of the final draft of this report.

*Het project is uitgevoerd met subsidie van het Ministerie van Economische Zaken en Klimaat, Nationale regelingen EZ-subsidies, Topsector Energie uitgevoerd door Rijksdienst voor Ondernemend Nederland.*

## Summary

Our future energy system will be characterised by a larger share of intermittent renewables (wind, solar), complemented by other flexible forms of power/heat production. Energy storage will play a pivotal role in providing the needed flexibility to balance energy supply and demand in the integrated system. In particular for the longer-term balancing needs, large-scale, centralized storage of energy underground is an attractive and potentially cost-effective solution. It can provide flexible bulk power management services for electricity, gas and heat commodities, and offers essential services to society in the form of strategic energy reserves, energy system adequacy and balancing solutions for unavoidable seasonal variations and other energy security challenges.

Today, many of these services are provided by the storage of natural gas, which is already safely stored in large quantities (about 13 billion m<sup>3</sup>, or 130TWh) in salt caverns and depleted gas fields in the Dutch subsurface, and that of many other countries in Europe, to balance supply and demand on a daily basis and secure supply during cold winters. However, as the role of natural gas will decrease in the Dutch energy system the need grows for the large-scale storage of energy in a different form. In this report, we focus on two such alternative forms of energy storage underground: Compressed Air energy Storage (CAES) in salt caverns and Underground Hydrogen Storage (UHS) in salt caverns and depleted gas fields.

Recently published estimates (Van Gessel et al., 2018; Gasunie and TenneT, 2018; Berenschot and Kalavasta, 2020) of required hydrogen storage capacities in the Netherlands in 2050 range from single-digit bcm (billion cubic meters) on the low end (for a normal weather year) to tens of bcm on the high end (for an extreme weather year), and that surpluses of electricity that might need to be stored and/or converted could be in the range of 20-140TWh. Although they make clear that large-scale energy storage technologies such as CAES and UHS need to be ready for deployment, their techno-economic feasibility is yet to be confirmed. In this report, we therefore reviewed the concepts and deployment status of these technologies, assessed their technical performance, and addressed several open questions regarding the techno-economic feasibility of these technologies.

### **Compressed Air Energy Storage**

CAES is an electricity storage technology. At charge, electrical energy is stored in mechanical form by compressing air, and stored in (commonly) salt caverns. At discharge, electricity is regenerated by using the compressed air to drive a turbo-expander/turbine. There are two main technology concepts, which mainly differ in how they deal with the temperature change of the air during compression and expansion: diabatic CAES (D-CAES) and advanced adiabatic CAES (AA-CAES).

In a D-CAES system, the heat that is generated on compression of the air is not stored. Hence an external fuel must be combusted at time of generation to heat up the air prior to driving the turbine. Natural gas is conventionally used, but its combustion causes CO<sub>2</sub> emissions. Hydrogen is emerging as an alternative, in particular because combustion of hydrogen does not emit CO<sub>2</sub>, and it can be produced from renewable electricity (also without emitting CO<sub>2</sub>). Worldwide, two CAES plants have been commercially operational for many years, one in Germany

(Huntorf, 321MW/2.5GWh) and one in the US (McIntosh, 110MW/2.6GWh), both of which are based on the relatively mature D-CAES concept (TRL 7-8). Round-trip efficiencies of up to 60% are deemed feasible with efficient utilization of waste heat (produced while combusting the fuel) during the generation process. In an AA-CAES system, the heat of compression is stored in a TES (Thermal Energy Storage device) and re-used during the discharging process, which eliminates the need to combust a fuel. With this method higher round-trip (power-to-power) efficiencies of up to 70% can be reached. However, efficient thermal storage of heat at the very high temperatures involved (up to 580°C) is challenging and costly, and the TRL of this technology (TRL 5) is currently not high enough to be commercially applied.

Storage of air in the subsurface, in salt caverns (or potentially also in aquifers or abandoned mines), forms an integral part of the design of a CAES facility. In general, salt caverns designed for CAES range in volume from 100,000 m<sup>3</sup> to 1,000,000 m<sup>3</sup>. They are created (“leached”) by a process called “solution mining”. Solution mining has been practiced for many decades, and the techniques and procedures to ensure that a cavern develops according to the design specifications in terms of location, depth, dimensions, and volume have seen continuous improvement. To ensure the geomechanical stability and integrity of caverns, design and operational criteria must be adhered to, and this must be accounted for in spatial planning.

Cyclic injection and withdrawal of air causes variations in the internal cavern pressure and temperature, which in turn could have adverse effects on the mechanical integrity and stability of the salt cavern. Geomechanical numerical simulations that were done in this project show that effects of cyclic injection and withdrawal of air do not jeopardize cavern stability and integrity. Although temperature fluctuations are observed that may lead to the creation of fractures in a thin skin at the cavern wall (<1m thick damage zone), they do not pose a real threat to cavern integrity due the limited depth of penetration in the cavern wall. Even during maintenance periods, or in extreme cases, when the cavern would experience atmospheric conditions for a prolonged period (months), although the width of the damage zone would be larger, the results suggest that it would not jeopardize cavern stability and integrity.

CAES systems are classified by two performance parameters: their generation capacity at full load (power output in MW), and the duration (in hours) over which this power can be delivered. By multiplying one with the other, the electricity production capacity (in MWh) is obtained. Typically, the power range of CAES systems is between 100-500MW, and the duration over which this power can be delivered ranges from hours to a day. Start-up times of CAES plants in normal situations are below 15 minutes and this enables them to provide secondary (and tertiary) reserve power to grid operators for frequency restoration. Also, in an emergency situation, they can provide black-start services to grid operators to contribute to the process of recovering a power station to operation, because they can start main blocks of generation onsite without having to rely on an external power source.

CAES systems are designed to be competitive in delivering a suite of flexibility services that are valued by utility companies, owners of generation assets, and grid operators. They can generate revenue from two main groups of services: arbitrage, i.e., providing electricity traders a means to earn money by leveraging the hourly price differences on electricity markets; and ancillary services, such as frequency regulation, reserve power, black start, load following, and synchronous inertia, that are procured by grid operators and asset owners of generation assets to manage grid

stability. An exploratory economic analysis that was done in this project indicates that a price arbitrage-only business case for D-CAES may not be viable. Due to a significant price spread requirement to break-even operationally, D-CAES only charges at a very low electricity price in the analysis, which results in a very limited number of operational hours, and thus limited revenues. Although the business case for AA-CAES shows more operational hours than for D-CAES, due to a less severe price spread requirement, revenues are not sufficient to realise a positive NPV. An important limitation in the analysis is the assumption of full-load only operation mode, which leads to economically suboptimal simulated asset operation. CAES is however well-suited to operate at lower power, and can do so with minimal efficiency loss at power outputs down to 15% of rated power. Furthermore, the exploratory analysis does not include additional (complementary) revenue streams (e.g. from ancillary services such as grid balancing, redispatch, black start, etc.), and excludes a multi-year stochastic analysis of the variability of renewables feed-in and its influence on electricity prices. Hence the total revenue is probably underestimated significantly. Several recent studies (Heuberger et al., 2017; Guerra et al., 2020; van Hout et al., 2014) show the basis of a positive business case and the importance of co-optimising energy revenues with ancillary services. Hence, to be able to conclude on the economic viability and business case of the D-CAES and AA-CAES technology, additional key business models should be assessed in addition to the day-ahead wholesale market business model of this study.

In recent years, several demonstration and (commercial) development projects have been conducted and/or are ongoing, which indicates a strong renewed interest in CAES, probably sparked by the increasing need for flexibility services to integrate the growing share of variable renewables (wind, solar). Most recently, project developer Corre Energy Storage announced its intention to develop a 320-MW D-CAES plant in The Netherlands with a storage capacity of 3-4GWh. The project obtained the status of European Project of Common Interest (PCI) in 2017 and receives financial support from the Connected Europe Facility (CEF) fund, which can be considered a recognition of the potential value of this technology in providing flexibility to the increasingly renewables-based European energy system.

### **Underground Hydrogen Storage**

Hydrogen can be stored in compressed gaseous form (at pressures up to 750 bar), in liquid form and in solid form (in chemical compounds that reversibly release hydrogen upon heating). In this project we focused on large-scale storage of hydrogen underground, in compressed gaseous form, in salt caverns and depleted gas fields, in which tens of millions to (potentially) billions of m<sup>3</sup> (bcm) of hydrogen can be stored.

Hydrogen is currently stored in pure form in large quantities (10-100 million m<sup>3</sup>) in salt caverns in the US and in the UK. Practical experience with these sites has shown that hydrogen can be safely stored in this way for long periods of time. No issues (biological and/or chemical degradation, etc.) are reported in literature with respect to storage in salt caverns. On account of the fact that four storage facilities are currently operational in the world, hydrogen storage in salt caverns could be considered mature. However, these storages are designed to provide security of supply of feedstock to the chemical industry, where demand profiles are typically very static, reflecting the continuous mode operation of chemical production processes. In contrast, to cancel out supply-demand imbalance caused not only by variations on the demand side but also by large weather-controlled variations in supply, injection

and withdrawal are expected to occur much more frequently and cyclically, and at higher volumetric rates. This kind of fast-cycle operation brings with it specific challenges that must be addressed, in particular in relation to the integrity and durability of wellbore materials and interfaces. Hence the TRL must be considered to be lower. Several pilot- and demonstration projects are being prepared in Europe to raise the TRL to 7, one of which in the Netherlands by Energystock (a subsidiary of Gasunie).

Hydrogen can also potentially be stored in depleted gas reservoirs, similar to natural gas. Natural gas is already safely stored in large quantities in depleted gas fields in the Dutch subsurface ( $\approx 14$  bcm), and that of many other countries in Europe. No sites exist however where pure hydrogen is stored, and there are open questions regarding the influence of geo- and biochemical reactions of hydrogen with rocks, fluids and micro-organisms in depleted gas reservoirs and the potential (technical, environmental, economic) risks associated with these reactions, in particular the formation of hazardous and/or corrosive fluids, and the degradation of injection and/or withdrawal performance.

Recent demonstration projects in Argentina and Austria with injection of up to 10% of hydrogen in a mix with natural gas into a depleted gas field have shown that hydrogen can be safely stored without adverse effects to installations and the environment. However, not all hydrogen was recoverable due to diffusion, dissolution (into formation water), and conversion to methane. Furthermore, in the past, town gas, containing 50-60% of hydrogen, was stored underground in salt caverns, depleted fields and aquifers. Although no major HSE (health, safety, environment) issues with these storages are reported in literature, little research was done regarding conversion to methane or other processes (e.g. trapping of hydrogen in the reservoir) that adversely affect the amount and quality of the hydrogen that can be recovered. In any case, it is expected that significant gas treatment (purification, drying) will be required to deliver a highly pure hydrogen stream back to the grid after withdrawing it from a depleted gasfield, and this will impact the economics.

A technical performance analysis of the Grijpskerk, Norg and Alkmaar UGS facilities as if they would be used for storing hydrogen, and a comparison to their current performance for natural gas, reveals that the lower density (8-10 times) and viscosity of hydrogen relative to methane results in 2.4 to 2.7 times higher withdrawal rates. These high rates partly compensate for the lower energy content (3-4 times lower), resulting in an energy throughput of 0.7 to 0.8 times that of methane.

Although maximum withdrawal rates for hydrogen up to  $\approx 33$  million  $\text{Sm}^3/\text{day}$  ( $99\text{GWh}_{\text{LHV}}/\text{day}$ , or  $\approx 4.1\text{GW}$  energy throughput) for a well with a 7-inch tubing (internal diameter) are theoretically possible, there are several factors (erosional velocity limit, bottomhole drawdown, 3-month plateau rate period) that limit the practical withdrawal rate. For example, for the Grijpskerk UGS, the withdrawal rate would drop to just below 20 million  $\text{Sm}^3/\text{day}$  ( $57\text{GWh}_{\text{LHV}}/\text{day}$ , or  $\approx 2.3\text{GW}$  energy throughput) for a well with a 7-inch tubing. Use of a 9-inch tubing would increase the withdrawal rate by 57% for the Grijpskerk UGS, yet also the bottom-hole drawdowns by 42%, which increases the risk of mechanical damage to the wellbore, and a significant reduction of the flow performances.

Furthermore, we observe higher injection rates for hydrogen than for methane at higher wellhead pressures. Despite the higher density (weight) of methane, this gas has also a higher viscosity, which at high flow rate apparently hampers injection into the reservoir. Injection rates will also be limited by the erosional velocity and bottom-

hole build-up as previously discussed for withdrawal. Further research is needed to obtain a good estimate of injection rates.

For a well in typical gas storage salt caverns, such as are operational in Zuidwending, we estimate very high theoretical withdrawal rates of hydrogen up to 35 million Sm<sup>3</sup>/day. This is 3-4 times faster than that of a well in a salt cavern filled with natural gas, and 1.5 to 2.5 times faster than a well in a porous reservoir filled with hydrogen. Differently from porous reservoirs though, we observe that the very high theoretical withdrawal rates and the working volumes in salt caverns are primarily limited by daily allowable pressure depletion (10 bar/day) in order to preserve the structural integrity of the cavern and reduce the loss of (geometric) volume due to salt creep. In Zuidwending it limits the withdrawal rate for natural gas per well to 7.3 million Sm<sup>3</sup>/day (67 GWh/day), which is 1.6 times lower than the 12 mln Sm<sup>3</sup>/day we estimated as the theoretical maximum rate per well. In fact, the 7.3 million Sm<sup>3</sup>/day is the limit rate per cavern in Zuidwending, and since every cavern is equipped with two wells, the limit rate per well would be half of that if both wells are used simultaneously. In the case of hydrogen the maximum withdrawal rate per well would be 5.2 million Sm<sup>3</sup>/day (15GWh/day). Furthermore, it must be noted here that these are the limit rates per day, i.e., higher withdrawal rates per hour are possible as long as the daily allowable pressure drop is not exceeded.

If Zuidwending would be operated at the same pressure range of today, yet storing hydrogen instead of natural gas, the energy content of the hydrogen working volume would be only 22% of the 3.6 TWh available today as natural gas. This is due to the faster pressure drop in the salt cavern during the withdrawal of hydrogen.

Geochemical processes that could be of concern for hydrogen storage in the Netherlands include a) reduction of iron minerals (pyrite) forming H<sub>2</sub>S; b) reduction of hematite to magnetite, sequestering H<sub>2</sub> and producing H<sub>2</sub>O; and c) reduction reactions and H<sub>2</sub>S formation changing the fluid composition and pH, possibly resulting in precipitation and dissolution of secondary minerals (changing the pore space).

Geochemical simulations with PHREEQC that were done in this project show that pyrite reduction as a result of H<sub>2</sub> storage may occur, leading to H<sub>2</sub>S formation in the gas phase, which may affect safety, materials selection, facility design and economics. H<sub>2</sub>S release increases with depth (as the partial pressure increases), and with the amount of initial pyrite in the reservoir. However, because kinetic effects were not taken into account, these results reflect a worst case scenario. To accurately assess the risk of H<sub>2</sub>S formation in hydrogen storage reservoirs it is of the utmost importance to improve the predictive power of the geochemical models by incorporating kinetic rates at high temperatures and high H<sub>2</sub> partial pressures, which can be obtained with laboratory experiments.

Furthermore, on the use of nitrogen as cushion gas, geochemical modelling indicates that nitrogen has negligible impact on rock-gas-water reactions, which conforms with results reported in literature. The only effect is the change in hydrogen partial pressure when nitrogen is present as cushion gas which causes lower reactivity of hydrogen in the reservoir. Therefore, nitrogen would be suitable to use as a cushion gas for hydrogen storage at least from a geochemical perspective.

Biochemical simulations with PHREEQC indicate that bacterial sulphate reduction and methanogenesis, may both pose a risk for underground hydrogen storage, which is also reported in literature. In the simulations however, maximum growth rates are assumed that occur at temperatures of 37 °C for methanogenesis and 30°C for

bacterial sulphate reduction. Because the temperature in potential reservoirs for hydrogen storage in the Dutch subsurface is considerably higher, the results must be considered a worst-case scenario.

Geomechanical numerical simulations that were done in this project show that effects of cyclic injection and withdrawal of hydrogen do not jeopardize cavern stability and integrity. Temperature fluctuations of up to 40 C° are simulated within a distance of 1 m into the cavern wall, in particular when injection cycles are short (weekly) or wellhead injection temperatures are high. Although such temperature fluctuations may lead to the creation of fractures in a thin skin at the cavern wall (<1m thick damage zone), they do not pose a real threat to cavern integrity due the limited depth of penetration in the cavern wall. Furthermore, cavern wall displacement of 35 cm is simulated in a monthly cycling scenario with 23 days injection (3 weeks) and 7 days production (1 week). However, the geological tightness of the cavern and cavern integrity are not jeopardized during UHS normal cycling operations.

An exploratory analysis of the economics of a flexible hydrogen production asset with storage in a salt cavern vs. continuous hydrogen production that was done in this project indicates that the lower electricity costs in the business case for the flexible production asset, due to reaped benefits from being able to “overproduce” (and store) hydrogen at low electricity prices, appears insufficient to compensate for the extra investments in a larger electrolyser, the storage and the related equipment, and the higher operational costs. Especially an increase in the number of hours with low electricity prices (due to a larger installed capacity of solar and offshore wind) and further developments in PEM technology favour the business case of flexible hydrogen production and storage, and provide perspective on a positive NPV. Additional revenue streams (to selling hydrogen) can be generated by including alternative benefits of storage in the business model that were outside the scope of this study, such as earnings from offering flexibility services to the electricity system with the up- and down- regulating capacities of the electrolysers, and remunerations for offering security of supply of hydrogen to market players.

# Contents

|          |   |            |
|----------|---|------------|
|          | <b>Preface</b>  | <b>2</b>   |
|          | Project details   | 2          |
|          | Acknowledgements  | 2          |
|          | <b>Summary</b>  | <b>3</b>   |
|          | <b>Contents</b>   | <b>9</b>   |
| <b>1</b> | <b>Introduction</b>   | <b>10</b>  |
| <b>2</b> | <b>Compressed Air Energy Storage (CAES)</b>                               | <b>12</b>  |
| 2.1      | Technology concept(s)   | 12         |
| 2.2      | Deployment status   | 15         |
| 2.3      | Technical performance characteristics                                     | 18         |
| 2.4      | Cavern design and spatial planning  | 21         |
| 2.5      | Geomechanical effects of CAES in salt caverns                             | 24         |
| 2.6      | Economic assessment of CAES and AA-CAES in salt caverns                   | 37         |
| <b>3</b> | <b>Underground Hydrogen Storage (UHS)</b>                                 | <b>54</b>  |
| 3.1      | Technology concept(s)   | 54         |
| 3.2      | Deployment status   | 60         |
| 3.3      | Technical performance analysis of underground H <sub>2</sub> storage      | 62         |
| 3.4      | Geo- and biochemistry of H <sub>2</sub> storage in depleted gasfields     | 94         |
| 3.5      | Geomechanical effects of H <sub>2</sub> storage in salt caverns           | 114        |
| 3.6      | Economic assessment of underground H <sub>2</sub> storage in salt caverns | 124        |
| <b>4</b> | <b>Conclusions</b>  | <b>136</b> |
| 4.1      | Conclusions on CAES   | 136        |
| 4.2      | Conclusions on UHS  | 138        |
|          | <b>References</b>   | <b>144</b> |
|          | <b>Appendix A: Techno-economic parameters</b>                             | <b>149</b> |
|          | <b>Appendix B: Detailed sensitivity analysis description</b>              | <b>152</b> |
|          | <b>Appendix C: Business case details 2025, 2030, 2050</b>                 | <b>153</b> |

# 1 Introduction

Our future energy system will be characterised by a larger share of intermittent renewables (wind, solar), complemented by other flexible forms of power/heat production. Energy storage will play a pivotal role in providing the needed flexibility to balance energy supply and demand in the integrated system, from low power and fast response solutions for short-duration (< 1kW; <1s) to longer-term balancing needs for the grid (>1GW; hours to days and beyond). In particular for the longer-term balancing needs, large-scale, centralized storage of energy underground is an attractive and potentially cost-effective solution, because it can provide flexible bulk power management services for electricity, gas and heat commodities.

It is also a key enabler for the Power-to-Gas value chain, i.e., the large-scale conversion of renewable electricity into molecules, by offering a (temporary) sink for versatile molecular energy carriers such as hydrogen that can be efficiently transported and stored for longer periods of time. In this way, it can play a key role in the integration of (in particular) the planned and potential offshore wind capacity into the electricity grid. At times of oversupply, it can shift the use of excess electricity generated forward in time to periods of deficit, thereby turning an intermittent non-dispatchable renewable electricity source into a dispatchable one, and maximizing the utilization of renewable electricity generated. As such, it offers essential services to society in the form of strategic energy reserves, energy system adequacy<sup>1</sup> and balancing solutions for unavoidable seasonal variations and other energy security challenges.

Today, many of these services are provided by the storage of natural gas, which is already safely stored in large quantities (about 14 billion m<sup>3</sup>, or 140TWh) in salt caverns and depleted gas fields in the Dutch subsurface, and that of many other countries in Europe, to balance supply and demand on a daily basis and secure supply during cold winters. However, as the role of natural gas will decrease in the Dutch energy system the need grows for the large-scale storage of energy in a different form. In this project, we focus on two such alternative forms of energy storage underground: Compressed Air energy Storage (CAES) in salt caverns and Underground Hydrogen Storage (UHS) in salt caverns and depleted gas fields.

Recent studies by TNO/EBN (Van Gessel et al., 2018), and Gasunie/TenneT (2018) estimate that required hydrogen storage capacities in the Netherlands may range between 1.3-4.3 bcm and 3.3-6.7 bcm respectively, for a year with normal weather conditions. Furthermore, the analysis of Berenschot/Kalavasta (2020) shows that 4-8 bcm of hydrogen storage capacity may be required in a year with normal weather conditions, and as much as 20-38 bcm in an extreme weather year, depending on scenario. Their analysis also shows that the surpluses of electricity that might need to be stored and/or converted could be in the range of 20-140TWh, again depending on scenario and weather year (Berenschot and Kalavasta, 2020). These studies make clear that large-scale energy storage technologies such as CAES and UHS need to be ready for deployment to enable a meaningful and substantial role in

---

<sup>1</sup> METIS studies, Generation and system adequacy analysis, 2016, European Commission, Contract no. ENER/C2/2014-639.

<https://op.europa.eu/en/publication-detail/-/publication/59a1b96c-713f-11e9-9f05-01aa75ed71a1/language-en/format-PDF/source-96287997>

optimizing the productive use of renewable energy sources and substantially reducing curtailment as part of a cost-effective energy transition. However, the techno-economic feasibility of CAES and UHS is yet to be confirmed. In this work package, we therefore addressed several open questions regarding the techno-economic feasibility of these technologies.

In Chapter 2 we focus completely on CAES. In Section 2.1 we explain the technology concepts, and in Section 2.2 its deployment status. In Section 2.3, we review the technical performance characteristics, and in Section 2.4. we explain how salt caverns, the most-used storage medium for CAES, are constructed, and review the design considerations that must ensure safe operation with minimal impact to the environment. In Section 2.5 we detail the results of an in-depth geomechanical assessment of the effects of cyclic injection and withdrawal of air during CAES operation, and in Section 2.6 we present the results of an exploratory economic analysis that focused on potential revenues from arbitrage.

In Chapter 3 we focus completely on UHS. In Section 3.1 we describe the technology options for storage of hydrogen at large scale, and in Section 3.2 we review their deployment status. In Section 3.3 we detail the results of a technical performance assessment aimed at quantifying and comparing the differences in performance between hydrogen and methane (as a proxy for natural gas) storage in porous reservoirs and salt caverns. In Section 3.4, we detail the results of a geo- and biochemical modeling study to assess the effects of geochemical processes and biochemical interactions of hydrogen with rocks, fluids and micro-organisms in depleted gas reservoirs in the Dutch subsurface. In Section 3.5, we present the results and conclusions of an in-depth geomechanical assessment of the effects of cyclic injection and withdrawal of air during UHS operation. Finally, in Section 3.6 we present the results of an exploratory economic analysis that was done to compare the business case of a continuous hydrogen production asset without storage vs. that of a flexible hydrogen production asset with storage in a salt cavern.

## 2 Compressed Air Energy Storage (CAES)

In this chapter, we start with a description of the two main technology concepts (diabatic vs. diabatic) in Section 2.1, and deployment status of this technology in Section 2.2. Next, in Section 2.3, we review the technical performance characteristics of CAES, i.e., what are the typical ranges of power capacity (MW), energy storage capacity (MWh), how long can they absorb and produce, and how fast can they respond, etc., and explain which services it can deliver to market players and to grid operators. In Section 2.4, we describe how the salt caverns are constructed in which the energy is stored (in the form of compressed air), review the relevant design parameters of salt caverns (depth, volume, dimensions), and explain what criteria are used to optimally position salt caverns spatially while ensuring geomechanical stability and integrity (leak tightness), and minimizing interference. In Section 2.5, we present the results and conclusions of an in-depth geomechanical assessment of the effects of cyclic injection and withdrawal of air during CAES operation, and the extent to which they affect cavern stability and integrity. Finally, in Section 2.6, we detail the results of an exploratory economic analysis that focused on potential revenues from arbitrage, a business model that exploits the volatility in electricity prices (EPEX).

### 2.1 Technology concept(s)

CAES is a mechanical storage technology. It stores electrical energy in the form of compressed air. The technology concept is displayed in Figure 2.1.

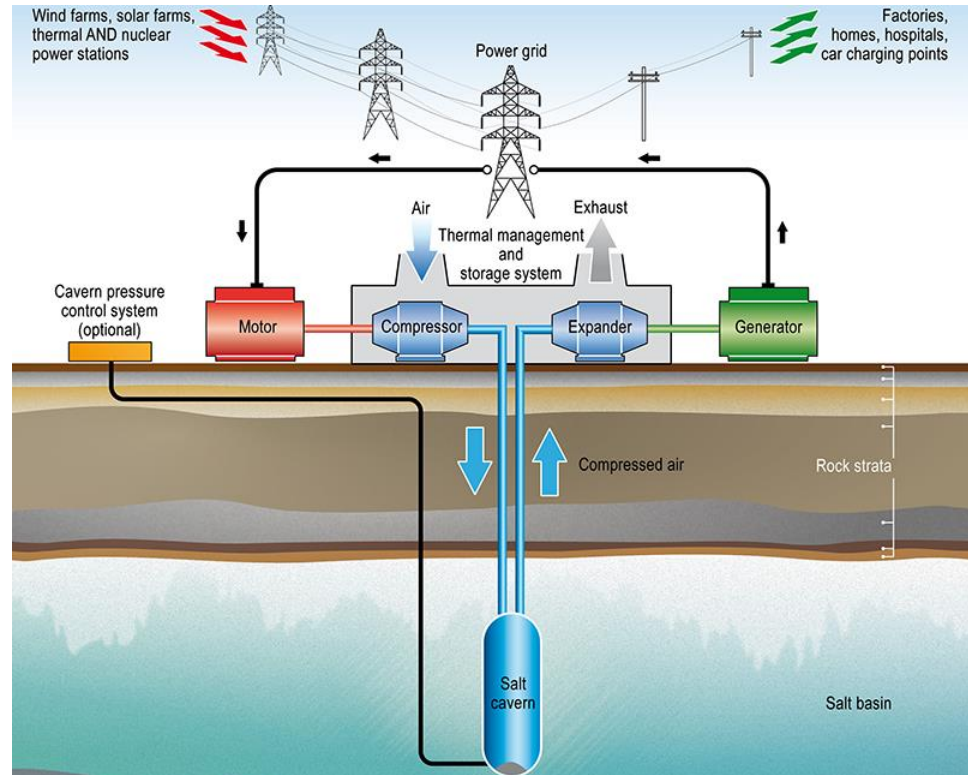


Figure 2.1: Illustration of a CAES system, obtained from website<sup>2</sup>

<sup>2</sup> <https://www.storelectric.com/technology/>

In a CAES system, an electric motor drives a compressor that consumes electricity to compress air. It does this during off-peak hours when low-cost generating capacity is available (e.g. from nuclear or thermal power stations) or non-dispatchable electricity is produced from variable RES (wind, solar). The compressed air is stored in underground reservoirs (commonly salt caverns) at high pressure. The electricity is re-generated by retrieving the compressed air from the storage reservoir to run an air (turbo-) expander or a gas turbine that drives an electricity generator to deliver electricity back to the grid. Because compressed air has a relatively low energy density (2-6 kWh per m<sup>3</sup> of storage space at pressures of 50-200 bar, Lunz et al., 2014), large volumes of air (in the order of 50-100 million Sm<sup>3</sup>) are required to conduct CAES at large scale (power outputs in the order of several 100s of MW and discharge durations of 6-12 hours). High-pressure vessels on the ground cannot practically meet this requirement because of space limitations and manufacturing costs. Storage of compressed air in salt caverns (at depths of 300—1500m below surface) therefore proves to be the most economical option (Eckroad & Gyuk, 2003).

CAES is a gas turbine based technology, hence the experience on gas turbine technology gained during decades of industrial use can be applied to CAES systems, which decreases operational uncertainties and reduces risks. The compressor and turbine are the core of the system, and the performance of this machinery is essential for the efficiency and lifetime (usually 30-40 years) of the CAES system (Chen et al., 2016; Li et al., 2018). CAES systems operate in a similar way as conventional gas turbines except that compression and expansion operations occur independently and at different times (Succar & Williams, 2011). In conventional gas turbines, typically around 2/3 of the output power after the expansion stage is required to run the compressor to pressurize combustion air (Energy Storage Association, 2020; Succar & Williams, 2011). In contrast, a CAES turbine does not need compression during turbine operation as the compression energy is supplied separately. This has the advantage that the output from the CAES turbine is capable of generating 3 times more electricity during expansion for the same amount of fuel used (in case of diabatic CAES, see below), which reduces CO<sub>2</sub> emissions by 40-60% compared to a conventional combined-cycle gas turbine (CCGT; Energy Storage Association, 2020). Furthermore, when running below baseload capacity (down to 15% minimum) a CAES turbine burns proportionally less fuel and emits proportionally less CO<sub>2</sub> (if the fuel is natural gas) whereas a CCGT needs to be kept warm and running at 40-50% of baseload capacity. Therefore, a CAES turbine can deliver regulation and reserve power in a much cleaner way compared to a CCGT.

There are two main CAES concepts, which mainly differ in how they deal with the temperature change of the air during compression and expansion: diabatic CAES (D-CAES) and adiabatic CAES (A-CAES). These two concepts will be further explained below.

### 2.1.1 *Diabatic CAES*

In a D-CAES system, the heat of compression is lost during the compression phase. This lost energy will be compensated for during the expansion phase when the air must be heated up to prevent it from freezing. Heating of the high-pressure air is done by combustion of a fuel in a combustor prior to its entry into the turbine. Apart from burning fuel, waste heat of the combustion process can be used in a recuperator to pre-heat the incoming air before the expansion phase. Round-trip efficiencies of D-CAES are approximately 42% without and 55% with waste heat utilization.

In principle, D-CAES gas turbine plants can operate on any fuel by slightly modifying the combustor and gas turbine designs (Khaitan & Raju, 2012). Natural gas is conventionally used, but its combustion causes CO<sub>2</sub> emissions. Therefore, hydrogen is emerging as an alternative, in particular because combustion of hydrogen does not emit CO<sub>2</sub>, and it can be produced from renewable electricity (also without emitting CO<sub>2</sub>). As such, a hydrogen-fired D-CAES system can greatly contribute to the emission reduction targets and help to establish a green hydrogen economy. Indeed, several turbine manufacturers (Siemens, Mitsubishi, Kawasaki) are in the process of developing turbines, aiming to go from a 50-50% natural gas-hydrogen system by 2025 to a 100% hydrogen system in 2030 (Bartela, 2020; Klumpp, 2016; Noordelijke Innovation Board, 2018). The feasibility of using hydrogen as a fuel is demonstrated for the existing Huntorf CAES plant, where actual data is being used and has been reported in literature (Crotagino et al., 2001). Supply of hydrogen can either take place by generating hydrogen with electrolyzers on-site as part of the CAES plant, and/or by electrolyzers that are located off-site, which requires the hydrogen to be transported by high-pressure pipelines towards the plant (Khaitan & Raju, 2012).

Two D-CAES plants have been commercialized and are still operational (McIntosh, USA and Huntorf, Germany; see Section 2.2), which puts the Technological Readiness Level (TRL) of D-CAES at 7-8.

### 2.1.2 *Adiabatic CAES*

In an A-CAES system, the heat of compression is stored and re-used during the discharging process, which eliminates the need to combust a fuel (Barbour et al., 2015). There are two types of A-CAES: without and with a Thermal Energy Storage (TES) device. In A-CAES without TES, the heat of compression is stored in the hot air itself inside a combined thermal energy and compressed air storage volume. However, due to the high temperatures already reached at rather low-pressure ratios *these concepts require highly temperature-resistant storage volumes. For example, adiabatically compressed ambient air heats up to about 277°C when reversibly compressed just to a moderate pressure of 10 bar, which would likely cause integrity issues in the underground storage system (salt caverns and wells). Therefore, A-CAES without TES are restricted to rather low storage pressures and consequently to low energy densities as well (Budt et al., 2016).*

In A-CAES with TES, which is often termed Advanced Adiabatic CAES (AA-CAES), the heat of compression is thermally stored (separately) e.g. by flowing the air through a packed bed TES to which the heat is transferred. By removing the heat from the air stream, the cooled pressurized air can be stored at much higher final pressures in the underground storage system (at least 60 bar, and up to 200 bar) and therefore higher energy densities can be reached. With this method higher round-trip (power-to-power) efficiencies of up to 70% can be reached relative to D-CAES (Energy Storage Association, 2020). However, efficient thermal storage of heat at the very high temperatures involved (up to 580°C) is challenging and costly, and the TRL of this technology (TRL 5) is currently not high enough to be commercially applied. Therefore, in contrast to D-CAES, no AA-CAES systems are commercially operational, and their development is limited to pilot projects (e.g. ADELE project, see next section).

## 2.2 Deployment status

Only the Huntorf and McIntosh CAES plants have been commercially operational for many years, both of which are based on the D-CAES concept. However, there have been and/or are demonstration and (commercial) development projects in recent years (see Table 2-1), which indicates a strong renewed interest in CAES, probably sparked by the increasing need for flexibility services to integrate the growing share of variable renewables (wind, solar). In the next subsections, the operational characteristics of the Huntorf and McIntosh plants will be reviewed in more detail, and a brief overview will be given of the recent demonstration and (commercial) development projects that are listed in Table 2-1.

Table 2-1: Operational CAES facilities and recent demonstration and (commercial) development projects (Wang et al., 2017).

| Name             | Country | Power Capacity (MW) | Geological Formation | Depth (m) | Cavern Volume (m <sup>3</sup> ) | Operation Pressure (MPa) | Status       |
|------------------|---------|---------------------|----------------------|-----------|---------------------------------|--------------------------|--------------|
| Huntorf          | Germany | 290                 | Salt Rock            | 650       | 310,000                         | 4.3-7.0                  | Operation    |
| McIntosh         | USA     | 110                 | Salt Rock            | 442       | 580,000                         | 4.5-7.4                  | Operation    |
| Norton           | USA     | 2700                | Hard Rock            | 670       | 9,600,000                       | 5.5-11.0                 | Construction |
| Iowa Energy Park | USA     | 270                 | Porous Formation     | 914       | -                               | -                        | Construction |
| ADELE            | Germany | 300                 | Salt Rock            | -         | -                               | -                        | Planning     |
| Matagorga        | USA     | 540                 | Salt Rock            | -         | -                               | -                        | Planning     |
| Seneca           | USA     | 150-270             | Salt Rock            | 760       | 150,000                         | 8.0-11.0                 | Planning     |
| PG&E             | USA     | 300                 | Porous Formation     | -         | -                               | -                        | Planning     |
| Datang CAES      | China   | 300                 | Porous Formation     | 500       | 900,000                         | 5.0-8.0                  | Planning     |

### 2.2.1 Operational plants: Huntorf and McIntosh

#### 2.2.1.1 Huntorf, Germany

The 321-MW Huntorf CAES plant in Germany, currently owned by Uniper, is the first CAES power station in the world. It started with commercial operation in December 1978. Alstom was the main contractor supplying the turbo-machinery.

In the Huntorf plant ambient air is compressed in an intercooled process by two separate turbo-compressor units to a maximum pressure of 72 bar. The compressed air is stored in two solution-mined salt caverns between 640 and 790 meters below the surface with a total volume of 0.31 million cubic meters. The caverns have a maximum diameter of about 61 m and a height of 152 m. Air pressure in the caverns is cycled between 46 and 72 bar, i.e., they never reach ambient pressure. At the compressor airflow rate of 108 kg/s, the plant requires 12 hours for full recharge. At full power, the turbine draws 417 kg/s of airflow from the caverns for up to 4 hours. After that, the cavern pressure is too low to allow generation at 321 MW and the airflow supplied by the caverns decreases (although the plant will produce power at an exponentially declining power level for over 10 more hours) (Knoke, 2002). The round-trip efficiency of the plant is 42%.

Originally, the plant was built to provide flexibility for the baseload-producing inflexible nuclear plants in the German power system. In recent years, the Huntorf plant has been operated as a reserve plant providing tertiary control reserve and for internal portfolio optimization. Moreover, the plant also has black start capability and is able to provide reactive power. The provision of reactive power and frequency regulation

can be performed even when the plant is neither charging nor discharging by opening both clutches. In this way, the synchronous machine can be operated idling in parallel to the grid (Radgen, 2008; Budt et al., 2016).

#### 2.2.1.2 McIntosh, USA

The 110-MW McIntosh plant, currently owned by PowerSouth, is the second CAES power plant in the world, and the first one in the United States. Dresser-Rand (now part of Siemens) designed and constructed the entire turbo-machinery train. The overall plant (turbo-machinery, building, and underground cavern) was constructed in 30 months for a cost of 51 million dollars and became operational in June 1991. Air is compressed in three stages, each followed by an intercooler. The compressed air is stored in a single salt cavern between 460 and 760 m below the surface with a total volume of 0.54 million cubic meters, yielding a power-generating duration of 26 hours at full power and at 154 kg/s airflow. The cavern air pressure ranges from 46 to 75 bar during normal operation. The reheat turboexpander train has high- and low-pressure expanders with high- and low-pressure combustors and drives the electric motor/generator to produce peak electric power. Dual-fuel combustors are capable of burning natural gas or fuel oil. An advanced regenerator is used to extract thermal energy from the low-pressure expander exhaust to preheat inlet air from the storage cavern before it goes to the inlet of the high-pressure combustor. The regenerator reduces fuel consumption by approximately 25% (Knoke, 2002). The round-trip efficiency of the plant is 54%.

#### 2.2.2 *R&D, demonstrations and planned projects*

Apart from the 2 operational D-CAES plants, there are and/or have been demonstration and (commercial) development projects in recent years (see Table 2-1):

- 1) The Norton energy Storage project by FirstEnergy Generation Corp (3<sup>rd</sup> line item in Table 2-1) was announced in 2009. It had the intention to build CAES plants in several phases from about 270 MW to a total capacity of up to 2700 MW. In 2013 the project was delayed due to market conditions, lower power prices and insufficient demand (Succar & Williams, 2011).
- 2) The Iowa Stored Energy Park project (4<sup>th</sup> line item in Table 2-1) was planned by the Iowa Association of Municipal Utilities. The intention was to build a 270 MW CAES plant coupled with 75 MW to 100 MW of wind capacity. However, this project was terminated as the porous sandstone aquifers were not suitable for CAES and due to economic reasons (John, 2013).
- 3) RWE Power, General Electric, Zublin and DLR launched the world's first large-scale AA-CAES demonstration project called ADELE in 2010 (5<sup>th</sup> line item in Table 2-1). Apart from the considerable R&D effort, the plan was to design and build a demo plant with a storage capacity of 360 MWh and a power output (turbine) of 90 MW, and with a 70% cycle efficiency (Finkenrath et al., 2009). From an R&D perspective, significant advances were made in the design of all system components, in particular the TES, which confirmed that round-trip efficiencies towards 70% are indeed feasible. However, the demo plant itself has not yet been built due to challenging economics (Chen et al., 2016).
- 4) Ridge Energy Storage & Grid Services L.P. (6<sup>th</sup> line item in Table 2-1) developed plans for several CAES projects in Texas. This included four CAES systems of 135 MW each in Matagorda County that would re-use previously developed brine

- caverns and was based on the McIntosh Dresser Rand design (Succar & Williams, 2011).
- 5) NYSEG developed plans for the Seneca CAES project (150-270 MW, 7<sup>th</sup> line item in Table 2-1) at the east coast of the USA, but cancelled it in 2012 due to economic aspects.
  - 6) In California PG&E is planning to construct a D-CAES system with a reserve for 10 hours of generation at 300 MW rated power, and with the compressed air stored in porous rock formations. The plant is intended to be operational in 2020–2021 (DOE, 2014).

Other noteworthy D-CAES development projects are the Apex CAES project at the Bethel Energy Centre near Dallas (Texas) and the Larne project, a 330-MW plant consisting of two 165-MW trains that was to be built in Larne, Northern Ireland using an underground salt formation for storage. The Larne project was well on its way to being realized, having obtained the status of European Project of Common Interest (PCI) and receiving considerable financial support from the Connected Europe Facility fund, which is a recognition of the value of large-scale energy storage in providing flexibility to the increasingly renewables-based European energy system. Its development ceased due a bankruptcy of the project developer Gaelectric<sup>3</sup>. A sale of the project to a third party did not materialize, which may in part be due to the large uncertainties around the status of Northern-Ireland caused by the Brexit.

Most recently, project developer Corre Energy Storage announced its intention to develop a 320-MW D-CAES plant in The Netherlands<sup>4</sup> with a storage capacity of 3-4GWh. Like the Larne project, it too obtained the PCI status. A unique aspect of this project is that its two 160MW turbines will be designed to ultimately run on 100% (renewable) hydrogen.

---

<sup>3</sup> <https://www.modernpowersystems.com/news/news-larne-caes-plans-withdrawn-7376728>

<sup>4</sup> <https://correenergystorage.nl/caes-the-project/>

## 2.3 Technical performance characteristics

CAES systems are designed to be competitive in delivering a suite of flexibility services that are valued by utility companies, owners of generation assets, and grid operators. Typically, a CAES facility is designed to generate revenue from two main groups of services:

1. Arbitrage, i.e., providing electricity traders a means to earn money by leveraging the hourly price differences on electricity markets. In this business model, traders would procure storage space (MWh) and charge/discharge capacity (MW) to buy electricity at low prices, store it, and sell it again at high prices on the intra-day and day-ahead electricity markets. Here, there is a trend towards also storing electricity for trading purposes over longer periods than days to provide e.g. owners of intermittent assets (wind in particular) to procure some form of back-up supply to compensate for when their assets are not producing.
2. Ancillary services, such as frequency regulation, reserve power, black start, load following, and synchronous inertia, that are procured by grid operators and asset owners of generation assets to manage grid stability. As the share of variable renewable energy sources in the electricity mix grows, the need for these services will increase to be able to cope with the variability in output at timescales ranging from seconds to days and capacities in the order of 100s of MW to GW.

In designing a CAES facility, a key aspect is to maximize the revenue expected from delivering these services by stacking them. As an example, owners of a CAES facility can offer certain ancillary services to a grid operator (TSO), for which it gets remunerated. In doing this, it delivers generation capacity with a certain response time to allow the grid operator to stabilize the grid. However, the asset is also generating electricity that can be traded, and if this electricity was stored at lower prices this constitutes additional revenue from arbitrage.

A CAES system typically consists of three groups of components (see Figure 2.1):

1. A multi-stage compressor train driven by a motor to charge the storage with compressed air;
2. A storage reservoir (typically salt caverns, but an aquifer or abandoned mine could potentially also be used to store the air), wells and transport pipelines to store the compressed air and transport it to the plant;
3. An expander/generator train to discharge the storage and re-generate electricity, consisting of an expander or gas turbine and generator.

The technical performance parameters of each of these components in the Huntorf and McIntosh plants are compared in Table 2-2. CAES systems are commonly classified by two performance parameters: 1) their generation capacity at full load (power output in MW), and 2) the duration (in hours) over which this power can be delivered. By multiplying one with the other, the electricity production capacity (in MWh) is obtained. Typically, the power range of CAES systems is between 100-500MW, and the duration over which this power can be delivered ranges from hours to a day (see also Table 2-1).

Table 2-2: Comparison of performance parameters of operational plants at Huntorf and McIntosh. (modified from Budt et al., 2016 - data sources: Pollak, 1994; Tuschy et al., 2004; Radgen, 2008; Nakhamkin et al., 1992; pers. comm. Uniper).

|   | Huntorf   | McIntosh   |
|---|---|--|
| <i>Plant</i>                              |   |  |
| Operating utility                         | Uniper  | PowerSouth                                       |
| Cycle efficiency                          | 0.46  | 0.54   |
| Energy input for kWh <sub>el</sub> output | 0.8 kWh <sub>electricity</sub> / 1.7 kWh <sub>gas</sub> | 0.69 kWh <sub>el</sub> / 1.17 kWh <sub>gas</sub> |
| Energy produced                           | 2568MWh   | 2640MWh  |
| Start operation                           | 1978 (refurbished 2007)                                 | 1991   |
| <i>Compression</i>                        |   |  |
| Max. el. input power                      | 68MW  | 50MW   |
| Max. air mass flow rate                   | 108kg/s   | 90kg/s   |
| Compressor units                          | 2   | 4  |
| Charging time (at full load)              | 18  | 38   |
| <i>Storage</i>                            |   |  |
| Cavern depth                              | 640-790m  | 460-760m   |
| Cavern pressure range                     | 46-72 bar   | 46-75 bar  |
| Cavern volume                             | 310,000 m <sup>3</sup> (2 caverns)                      | 538,000 m <sup>3</sup> (1 cavern)                |
| Well diameter                             | 24 inch casing / 20.5 inch tubing                       | unknown  |
| <i>Expansion</i>                          |   |  |
| Max. el. output power                     | 321MW   | 110MW  |
| Control range (output)                    | 100-321MW   | 10-110MW   |
| Discharging time (at full load)           | 8   | 24   |
| Start-up t. (normal/emergency)            | 14/8 minutes  | 12/7 minutes                                     |
| Max. mass flow rate                       | 455 kg/s  | 154kg/s  |
| HP turbine inlet                          | 41 bar  | 42 bar   |

CAES is a scalable technology, i.e., it consists of surface equipment (compressor, turbo-expander, generator) and subsurface components (cavern, wells) that all have their own characteristic scales. Typical sizes of compressor trains (multiple compressor units) are in the order of 10s to 100MW, and typical sizes of turbo-expander/generator trains are in the order of 100-200MW. If larger capacities are required, and for reasons of redundancy, CAES plants often comprise of multiple compressor trains and multiple generation trains. For example, Huntorf consists of one compressor train with 2 compressor units (low-pressure and high-pressure) and 2 generation trains of 160MW each (Table 2-2). While the compressor power determines the down-regulating capacity, i.e., the capacity to consume electricity (thus reducing grid load), the expander/generator train determines the up-regulating capacity, i.e., the capacity to produce electricity (and stabilize the grid). In CAES systems, compressor power is commonly lower than generation power, which to some extent reflects its principle of operation, i.e., charge at low prices and over a longer period of time (e.g. during the night), and generate at high prices at high capacity during a short period to maximize revenue.

Because CAES turbo-expander/generator trains are driven by the compressed air that comes out of the caverns, their size and design inlet pressure determine the pressure and rate at which the compressed air must be withdrawn. Inlet pressures of

high-pressure CAES turbo-expanders in Huntorf and McIntosh are comparable (around 40 bar, see Table 2-2) but mass flow rates on withdrawal in Huntorf (455kg/s) are 3 times larger than in McIntosh (154kg/s), and this also determines the requirements for the diameters of the wells through which the air flows into and out of the caverns. While in natural gas storage, well diameters of 9 $\frac{5}{8}$  to 13 $\frac{3}{8}$  inch (casing) are the standard, wells for CAES can have larger diameters to allow the high mass flow rates without a significant pressure drop and without damaging the well. In Huntorf for example, each cavern has a well with a 24.5 inch casing (Crotagino et al., 2001) to allow the mass flow rate stated in Table 2-2. Furthermore, multiple caverns are often developed, that typically range in size from a few hundreds of thousands of m<sup>3</sup> to one million m<sup>3</sup> geometric volume, depending on the number and size of the generation train and the discharge duration.

Another important performance parameter is response time, i.e., the start-up time needed to go from 0 power output to full capacity. Start-up times of CAES plants in normal situations are below 15 minutes (see Table 2-2), and this enables them to provide secondary (and tertiary) reserve power to grid operators for frequency restoration. Furthermore, in an emergency situation, they can provide black-start services to grid operators to contribute to the process of recovering a power station to operation, because they can start main blocks of generation onsite without having to rely on an external power source (Knight, 2001).

Finally, a key performance parameter in energy storage systems is the cycle efficiency (often referred to as the round-trip efficiency), which is calculated by dividing the amount of (primary) energy discharged by the amount of (primary) energy charged. However, because D-CAES is a hybrid electricity generation and storage technology, which requires firing of a secondary fuel at generation, round-trip efficiencies are commonly calculated by including the (thermal) energy value of the fuel in the charging step (Budt et al., 2016).

## 2.4 Cavern design and spatial planning

Storage of air in the subsurface, in salt caverns, forms an integral part of the design of a CAES facility. Salt caverns are created (“leached”) by a process called “solution mining”, whereby fresh water is injected through a well into a layer of rock salt the subsurface (see Figure 2.2, phases 1 and 2). At depth, the water dissolves the salt, and (saturated) brine is pumped back up to be processed in a salt production facility, where it is purified, and the water is evaporated to obtain pure salt. Alternatively, the brine is purged into the sea, but this is not allowed under the Dutch Mining Law. Due to the dissolution of salt (called “leaching”), a cavity forms and this cavity is called a “salt cavern”. During solution mining, the cavity is at all times filled with brine. A unique property of rock salt is that it is so tight that it effectively does not allow any fluid or gas to pass through it, i.e., it is impervious. Because of this, a salt cavern is a perfect storage container for fluids or gases. In general, geometric volumes of caverns that are created for the purpose of salt mining range from 100,000 m<sup>3</sup> to several millions of m<sup>3</sup>. However, in practice, when caverns are solution-mined for the purpose of gas storage, they rarely exceed 1,000,000 m<sup>3</sup>.

After the leaching stage the brine in the cavern must be displaced to make room to store the gas. During this process, which is called “debrining”, gas is injected into the cavern through the production string that ends at the top of the cavern (see Figure 2.2, phases 3 and 4). While gas accumulates in the top part of the cavern, the pressure increases, and when it exceeds the halmostatic pressure (the pressure due to the weight of the column of saturated brine), the saturated brine is pushed down and out of the cavern through the debrining string that ends at the base of the cavern.

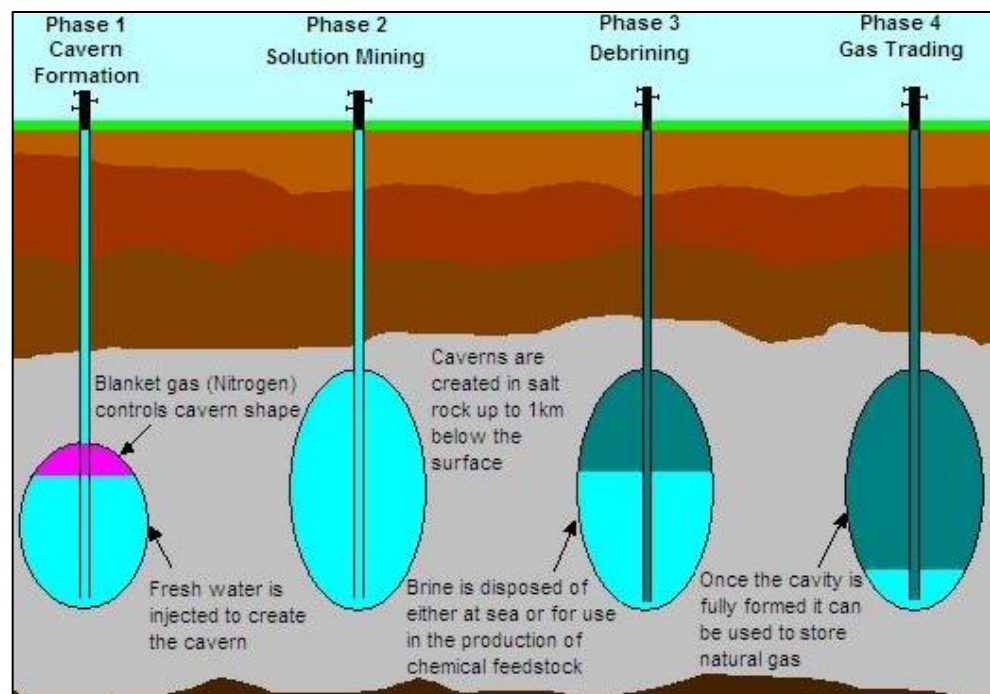


Figure 2.2: Schematic representation of the 4 stages in the creation process of salt cavern for storage of gas. Source and copyright: CNG services<sup>5</sup>. Here, Nitrogen gas is the blanket fluid that is used to control the cavern shape, but compressed air could also serve as blanket fluid.

<sup>5</sup> <http://www.cngservices.co.uk/index.php/services/onshore-gas/gas-storage>

Eventually, the bulk of the cavern volume will be filled with compressed gas, with only a few meters of brine column remaining at its base.

Solution mining has been practiced for many decades, and the techniques and procedures to ensure that a cavern develops according to the design specifications in terms of location, depth, dimensions, and volume have seen continuous improvement. A schematic diagram of a salt cavern illustrating the most important design parameters is display in Figure 2.3. The geometric volume of the cavern is determined by its diameter  $D_{cav}$  and height  $H_{cav}$ . Furthermore, the depth of the last cemented casing shoe ( $Z_{LCCS}$ ), which is usually slightly above the roof of the cavern, determines the (absolute) maximum working pressure at which the air can be stored. The maximum working pressure is found by multiplying the depth by 0.80-0.85 times the lithostatic pressure gradient in bar/m. Likewise, (absolute) minimum working pressures are determined by multiplying  $Z_{LCCS}$  with 0.25-0.30 times the lithostatic pressure gradient in bar/m. This ensures geotechnical safety during storage operations (Energystock, 2017; Caglayan et al., 2020).

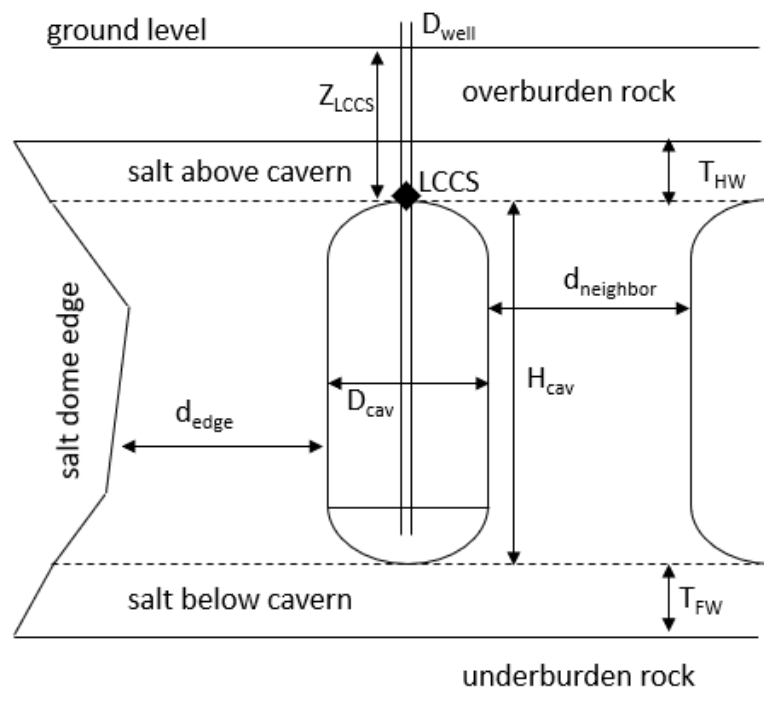


Figure 2.3: Schematic diagram of a salt cavern illustrating the most important design parameters.  $D_{well}$  – well diameter;  $D_{cav}$  – cavern diameter;  $H_{cav}$  – cavern height; LCCS: Last Cemented Casing Shoe;  $T_{HW}$  – thickness of salt layer above cavern;  $T_{FW}$  – thickness of salt layer below cavern;  $d_{edge}$  – distance of cavern to edge of salt dome;  $d_{neighbor}$  – distance of cavern to its nearest neighbour.

Furthermore, in order to ensure the geomechanical safety of caverns, minimum thicknesses of the salt roof above the cavern ( $T_{HW}$ ) and floor below the cavern ( $T_{FW}$ ) must be ensured. Here, Wang et al. (2015) suggest a value of 75% of the cavern diameter for the roof, and 25% of the cavern diameter for the floor. Finally, safe distances must be maintained between caverns ( $d_{neighbor}$ ), to avoid interaction, and between a cavern and the edge of the salt dome ( $d_{edge}$ ), and this puts spatial constraints on the placement of caverns. TNO (Remmelts, 2011) used a calculation method of German consultant IfG (IfG, 2008) to calculate  $d_{neighbor}$  for caverns at depths between 1000-1500m and with a diameter of 90m, which resulted in values between 1.77 and 2.33 times  $D_{cav}$  for  $d_{neighbor}$ . Following German salt mining

regulations<sup>6</sup>, for  $d_{\text{edge}}$  TNO used 150m. Above criteria were also used in the permit application process of the Zuidwending gas storage facility. Caglayan et al. (2020), in their paper on technical potential for using salt caverns for hydrogen storage in Europe, use much more conservative criteria: 4 times the cavern diameter  $D_{\text{cav}}$  for calculating  $d_{\text{neighbor}}$ , and 500m for  $d_{\text{edge}}$ , but this choice must be considered in the context of the purpose of their paper, i.e., to (conservatively) explore the technical potential for creating caverns for storing hydrogen.

In the next section, the validity of these safety distances will be further explored in the context of an assessment of the geomechanical effects of cyclic injection and withdrawal of air and the extent to which they affect cavern integrity.

---

<sup>6</sup> „Allgemeine Bergverordnung“ (ABVO) of Lower Saxony

## 2.5 Geomechanical effects of CAES in salt caverns

Cyclic injection and withdrawal of gas (air or hydrogen in this study) causes variations in the internal cavern pressure and temperature, which in turn could have adverse effects on the mechanical integrity and stability of the salt cavern. To assess these effects, and the extent to which they affect cavern integrity, geomechanical numerical simulations were conducted of a salt cavern subjected to cycles of injection and withdrawal that are typical for Compressed Air Energy Storage (CAES) and Underground Hydrogen Storage (UHS). In this section, the input, model set-up, and results of the geomechanical simulations for CAES are detailed. In Section 3.5, the same is provided for the geomechanical simulations for UHS.

Our focus in this geomechanical modeling study was on analyzing the cavern wall convergence and the thermo-mechanical effects of cycling loading on the rock salt surrounding the salt cavern. For this purpose, two single-cavern geomechanical models were developed: (i) a model of a salt cavern used for storage of air for CAES and (ii) a model of a salt cavern used for storing hydrogen for UHS. The input parameters and assumptions of the two models are largely based on the Dutch subsurface conditions and the data available from the underground gas storage site at the Zuidwending salt dome (Nederlandse Gasunie, 2012). The model stratigraphy and the cavern geometry are chosen to be representative for the Dutch cases. The characteristics of multiple injection and withdrawal cycles were assumed to vary in a wide range, based on the literature, current considerations and possible future upscaling of energy storage operations.

In subsection 2.5.1 the data and the models developed for both CAES and UHS are first described. Next, in subsection 2.5.2 the results of the model simulations are presented and discussed for CAES only. Conclusions and recommendations for further research on geomechanical effects of cyclic injection and withdrawal on caverns (and well systems) used for CAES are given in subsection 2.5.3.

### 2.5.1 *Numerical model*

Numerical simulations were conducted to evaluate the geomechanical effects of compressed air energy storage (CAES) and hydrogen energy storage (UHS) in salt caverns. A general purpose finite-element package DIANA (DIANA FEA, 2019) was used to develop numerical models of the storage cavern and perform calculations. This section describes model setup, simulation scenarios and results.

#### 2.5.1.1 Model geometry

The stratigraphy of the overburden and the Zuidwending salt dome comprises the formations found at the following average depths (Nederlandse Gasunie, 2012):

- Quaternary clay and sand. from 0 to 65 m;
- Tertiary clay, from 65 to 115 m;
- Gypsum, anhydrite and clay, from 115 to 200 m;
- Zechstein rock salt, from 200 to about 2,700 m;
- Rotliegend sandstone below 2,700 m.

The Quaternary and Tertiary are lithologically similar and therefore lumped into one geomechanical unit, the North Sea Group. The other geomechanical units (Caprock, Zechstein halite and Rotliegend) are kept equivalent to the geological formations.

Two axial symmetric geomechanical models of a single storage cavern were constructed, one for CAES and one for UHS (see Figure 2.4; Table 2-3). The same stratigraphical subdivision was used in both finite-element models. A single cylindrical cavern was introduced in both models. However, the cavern for CAES simulations is smaller ( $\sim 0.5$  million  $\text{m}^3$ , Figure 2.4a) than the cavern for UHS simulations ( $\sim 1$  million  $\text{m}^3$ , Figure 2.4b). It must be noted here that the diameters used are average diameters. In practice, the maximum diameter of caverns for gas storage can reach up to 90-100m, which allows the creation of caverns that are less high to achieve the same geometric volume. This reduction in height results in caverns that reach less deep, and are therefore less susceptible to creep in their lower parts, which reduces subsidence.

Table 2-3: Cavern dimensions used for CAES and UHS simulations.

| Cavern use | Cavern shape | Cavern height [m] | Depth cavern roof [m] | Depth cavern base [m] | Avg. radius [m] | Volume [mln $\text{m}^3$ ] |
|------------|--------------|-------------------|-----------------------|-----------------------|-----------------|----------------------------|
| CAES       | cylindrical  | 350               | 1100                  | 1450                  | 22              | 0.53                       |
| UHS        | cylindrical  | 450               | 1150                  | 1600                  | 27              | 1.0                        |

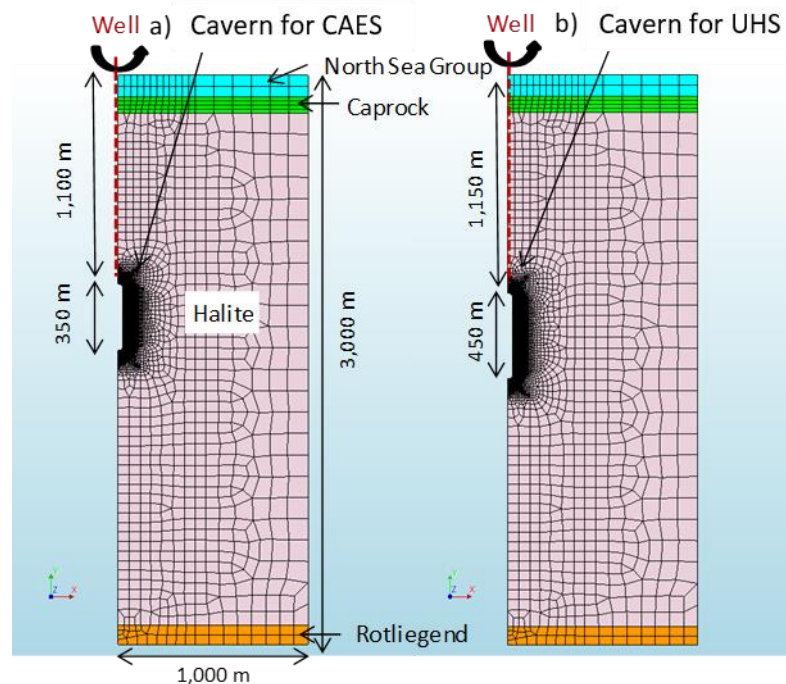


Figure 2.4: Vertical cross-section of the axial symmetric finite element model of a storage cavern used for (a) compressed air energy storage (CAES) and (b) hydrogen energy storage (UHS).

The well through which the gas is injected into and withdrawn from the cavern is vertical and aligned with the cavern axis and the axis of the finite-element model. The horizontal model layers were meshed using quadratic second-order eight-node quadrilateral elements for better solution accuracy. The outer model boundary was set at a radial distance of 1 km from the cavern axis and the model base at a depth of 3 km, below the halite layer, to minimize the effects of boundaries on simulation results. The structural boundary conditions were prescribed to constrain displacements in the direction normal to the outer side and the base of the model.

### 2.5.1.2 Constitutive models and material properties

Physical, elastic and thermal properties of model layers were adopted from the literature and previous geomechanical modelling studies (Table 2-4). The elastic properties of halite were measured on the core taken from the Zuidwending salt dome (IfG report 11/2007, 2007). All the layers except the Zechstein halite were assumed to exhibit pure elastic behavior.

Table 2-4: Physical, elastic and thermal properties of layers used in simulations.

| Layer        | Density [kg/m <sup>3</sup> ] | Young's modulus [GPa] | Poisson's coef. | Thermal expansion coef. [1/K] | Heat conductivity [J/(day m K)] | Heat capacity [J/(m <sup>3</sup> K)] |
|--------------|------------------------------|-----------------------|-----------------|-------------------------------|---------------------------------|--------------------------------------|
| North Sea Gr | 2050                         | 10                    | 0.25            | 3e-5                          | 1.71e5                          | 1.84e6                               |
| Caprock      | 2050                         | 15                    | 0.25            | 3e-5                          | 1.71e5                          | 1.84e6                               |
| Zechstein    | 2179                         | 32                    | 0.26            | 5e-5                          | 4.28e5*                         | 1.84e6**                             |
| Rotliegend   | 2200                         | 15                    | 0.2             | 3e-5                          | 1.71e5                          | 1.84e6                               |

\* Equal to 4.95 W/(m K); \*\*Equal to 0.92 J/(g K)

Salt deformation was modelled taking into account the steady-state creep deformation mechanism driven by the differential stress. The constitutive model for the steady-state salt creep used in simulations combines the two different terms: (i) a branch for the non-linear creep (i.e. a power-law branch) and (ii) a linear creep branch. The material model for salt creep is described in Fokker (1995) and implemented in the numerical simulator DIANA used in this study (DIANA FEA, 2019). The constitutive model can be written as follows:

$$\dot{\epsilon}_{axial} = A_1 \exp\left(-\frac{Q_1}{RT}\right) \left(\frac{\Delta\sigma}{\alpha}\right)^{n_1} + A_2 \exp\left(-\frac{Q_2}{RT}\right) \left(\frac{\Delta\sigma}{\alpha}\right)^{n_2}$$

where  $\dot{\epsilon}_{axial}$  is the vertical strain rate [1/s],  $\Delta\sigma = \sigma_{axial} - \sigma_{radial}$  is the differential stress of a triaxial loading test [Pa]; A1 and A2 are the creep strain rate coefficients [1/s], Q1 and Q2 are the activation energies in [J/mol], R is the gas constant (8.314 J/°K/mol), T is the ambient temperature [°K],  $\alpha$  is the reference stress [Pa];  $n_1$  and  $n_2$  are the stress exponents for the non-linear creep ( $n_1 > 1$ ) and the linear creep ( $n_2=1$ ), respectively. The material properties' values for steady-state creep were obtained by plotting the Zuidwending experimental data (available from the IfG report 11/2007, 2007) and fitting the different constitutive laws to the data (Figure 2.5, Table 2-5).

Simulations described in the subsequent sections were conducted assuming the ZwdNLC creep law (a power-law model) and the ZwdNLCLLC law (a combined power-law and low-linear-creep model). The third model fitted to the data (ZwdNLCHLC) was omitted from further considerations as it may be more representative for salt leaching from the very deep solution-mined caverns (~2.5-3 km) in the Barradeel concession compared to the energy storage caverns (at depth range of ~1 to 1.5 km) considered in the present study.

The salt dilation criterium used to evaluate the integrity of the salt cavern is based on the following expression (DeVries, 2006):

$$\sqrt{J_2} = C I_1$$

Where  $J_2$  is the second invariant of the deviatoric stress tensor,  $I_1$  is the first invariant of the stress tensor and C is a material constant with a value typically near -0.27.

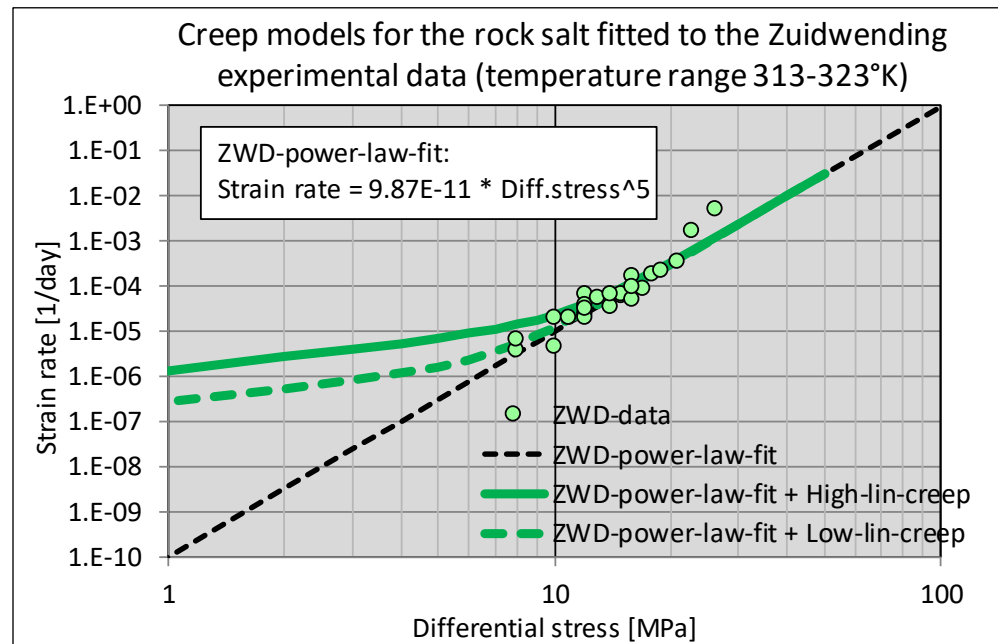


Figure 2.5: Various constitutive models for the steady-state creep of rock salt fitted to the Zuidwending experimental data (ZWD-data, *IFG report 11/2007, 2007*).

ZWD-power-law-fit: corresponds to ZwdNLC (NLC=Non-linear creep) in Table 2-5.

ZWD-power-law-fit + High-lin-creep: corresponds to ZwdNLCHLC.

ZWD-power-law-fit + Low-lin-creep: corresponds to ZwdLCLLC

Table 2-5 :Salt creep properties' values for the various constitutive models fitted to the Zuidwending experimental data, plotted in Figure 2.5.

| Constitutive model                            | A <sub>1</sub><br>[1/day] | n <sub>1</sub> | Q <sub>1</sub> /R<br>[°K] | A <sub>2</sub><br>[1/day] | n <sub>2</sub> | Q <sub>2</sub> /R<br>[°K] | α<br>[MPa] |
|---|---------------------------|----------------|---------------------------|---------------------------|----------------|---------------------------|------------|
| ZwdNLC<br>(ZWD-power-law-fit)                 | 0.053                     | 5              | 6495                      | -                         | -              | -                         | 1          |
| ZwdNLCLLC<br>(power-law-fit + Low-lin-creep)  | 0.053                     | 5              | 6495                      | 0.0029                    | 1              | 3007                      | 1          |
| ZwdNLCHLC<br>(power-law-fit + High-lin-creep) | 0.053                     | 5              | 6495                      | 0.0148                    | 1              | 3007                      | 1          |

### 2.5.1.3 Model initialization and cavern leaching phase

The in-situ stresses and temperatures were initialized in the numerical models by applying the following procedures:

- Stress initialization is achieved by applying the gravity load and assuming the total horizontal-to-vertical stress ratio  $K_0=1$  within the Zechstein halite layer and  $K_0=0.7$  within other layers. In this way, the initial stress state in halite was isotropic.
- The initial field temperature was introduced by applying a depth-dependent temperature profile based on a thermal gradient of 0.025 °C/m. The average value of geothermal gradient for the subsurface onshore Netherlands is somewhat higher (0.031 °C/m; Bonté et al., 2012). The lower value (0.025 °C/m) used in this study is generally more representative for salt deposits.

The time needed to leach out a storage cavern was assumed to be 2 years for the smaller cavern used for CAES and 3.5 years for the larger cavern used for UHS. The leaching phase was modelled by assuming that the storage cavern was present in the numerical model from the start of simulations. Initially, the pressure inside the cavern (acting on the cavern roof, wall and floor) was equal to the isotropic lithostatic

stress in the salt surrounding the cavern. In this way, the initial stresses introduced in the model with a void (cavern) were equal to the in-situ isotropic stresses in the rock salt prior to cavern leaching. Cavern leaching was modelled simply by gradually reducing the initial lithostatic pressure inside the cavern to the hydrostatic pressure of brine, i.e. halmostatic pressure (defined with a pressure gradient of 11.8 kPa/m), over the leaching period of 2 years (cavern for CAES) and 3.5 years (cavern for UHS).

Thermal effects of leaching are caused by injection of brine at temperatures lower than the in-situ salt temperature. The brine temperature is 15°C, while the in-situ temperature in salt for the cavern depth range considered in this study is between 40-50°C. A thermal boundary condition was applied on the cavern roof, walls and floor. This boundary introduces cooling down of salt in the surrounding of the cavern due to injection of cold brine. Cooling down was applied as a linear function of time needed to leach out the storage cavern (2 years for CAES and 3.5 years for UHS).

#### 2.5.1.4 Load cases for CAES

Cavern debrining is assumed to take place immediately after cavern leaching. During debrining, the air is injected in the cavern while simultaneously removing the brine. Debrining lasted 30 days and the brine was assumed to be fully replaced with the air. At the end of debrining, the pressure of air in the cavern was 14 MPa (Figure 2.6a).

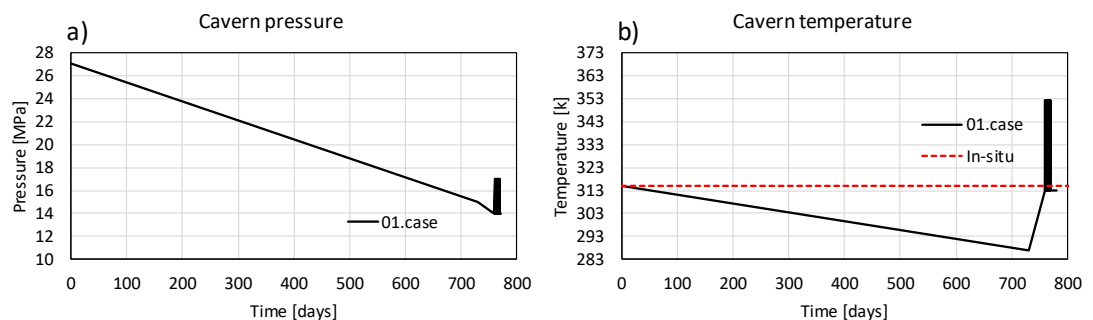


Figure 2.6: (a) Cavern pressure and (b) cavern temperature as a function of time during the leaching phase (0-730 days), debrining (730-760 days) and the CAES cycling (on a daily basis from 730 days onwards).

During the leaching phase, the cavern was gradually cooled down by the brine from the in-situ temperature of 40-50°C to 15°C (287°K). During the subsequent debrining, the cavern is warmed up by injection of hot compressed air. At the end of debrining, the temperature of air in the cavern was 40°C (313°K; Figure 2.6b).

Model initialization, the cavern leaching phase and the phase of debrining were simulated in the same way in all calculated scenarios of CAES. Estimates of cavern temperature changes during injection and withdrawal of the air were based on the literature data (Nieland, 2008; Düsterloh and Lux, 2010). It should be noted that there are several proprietary tools for simulating the thermodynamics and heat transfer related to storage of different gases in salt caverns (Nieland, 2008; Zander-Schiebenhöfer, 2010).

Generally, gas temperature fluctuations in the cavern depend on the rate of pressure rise or decline, which is determined by the duration of injection/withdrawal cycles, and the temperature of air at the well head. We adopted an air temperature change in the cavern of 1.3°C/bar; that is, the air temperature increases during injection (due to gas compression) by 1.3°C for 1 bar pressure increase. During air withdrawal, the

temperature decreases by the same amount due to gas expansion. The adopted value of 1.3°C/bar is relatively high and representative for short periods of injection and withdrawal that may last from several hours to a day, depending on cavern volume and the operating pressure range (Düsterloh and Lux, 2010).

For CAES, 10 scenarios for injection and withdrawal cycles were assumed. The cases of CAES cycling considered five different pressure-and-temperature loading scenarios, two different salt creep models and two different temperatures of the air at the wellhead (Table 2-6 and Figure 2.7). The input parameters and conditions that were kept the same in all the scenarios are as follows:

- 10 injection and withdrawal cycles were simulated. 3 additional cycles were simulated in scenarios with a maintenance period after the initial 10 cycles (cases 03, 04, 05, 13, 14 and 15).
- Pressure in the cavern during cycling varies linearly between 14 MPa (minimum pressure) and 18 MPa (maximum pressure) and vice versa.
- During maintenance, pressure in the cavern amounts to 0.1 MPa (1 bar) and air temperature is 15°C.
- Temperature of the air in the cavern during cycling varies linearly between 313°K and 352°K (40°C to 79°C) and vice versa. This corresponds to a temperature change of 1.3°C/bar. Exceptions are cases 01a and 11a, which consider injection of air at higher temperatures (60°C at the wellhead, Table 2-6).

Table 2-6: Overview of CAES simulation scenarios.

| Case | Injection time [hr] | Idle time between inj. & ext. [hr] | Extraction time [hr] | Maintenance duration [day] | Salt creep model | Air temp. at wellhead [°C] |
|------|---------------------|------------------------------------|----------------------|----------------------------|------------------|----------------------------|
| 01   | 12                  | -                                  | 12                   | -                          | ZwdNLC           | 40                         |
| 01a  | 12                  | -                                  | 12                   | -                          | -/-              | 60                         |
| 02   | 12                  | 24                                 | 12                   | -                          | -/-              | 40                         |
| 03   | 12                  | 24                                 | 12                   | 1                          | -/-              | 40                         |
| 04   | 12                  | 24                                 | 12                   | 7                          | -/-              | 40                         |
| 05   | 12                  | 24                                 | 12                   | 30                         | ZwdNLC           | 40                         |
| 11   | 12                  | -                                  | 12                   | -                          | ZwdNLCLLC        | 40                         |
| 11a  | 12                  | -                                  | 12                   | -                          | -/-              | 60                         |
| 12   | 12                  | 24                                 | 12                   | -                          | -/-              | 40                         |
| 13   | 12                  | 24                                 | 12                   | 1                          | -/-              | 40                         |
| 14   | 12                  | 24                                 | 12                   | 7                          | -/-              | 40                         |
| 15   | 12                  | 24                                 | 12                   | 30                         | ZwdNLCLLC        | 40                         |

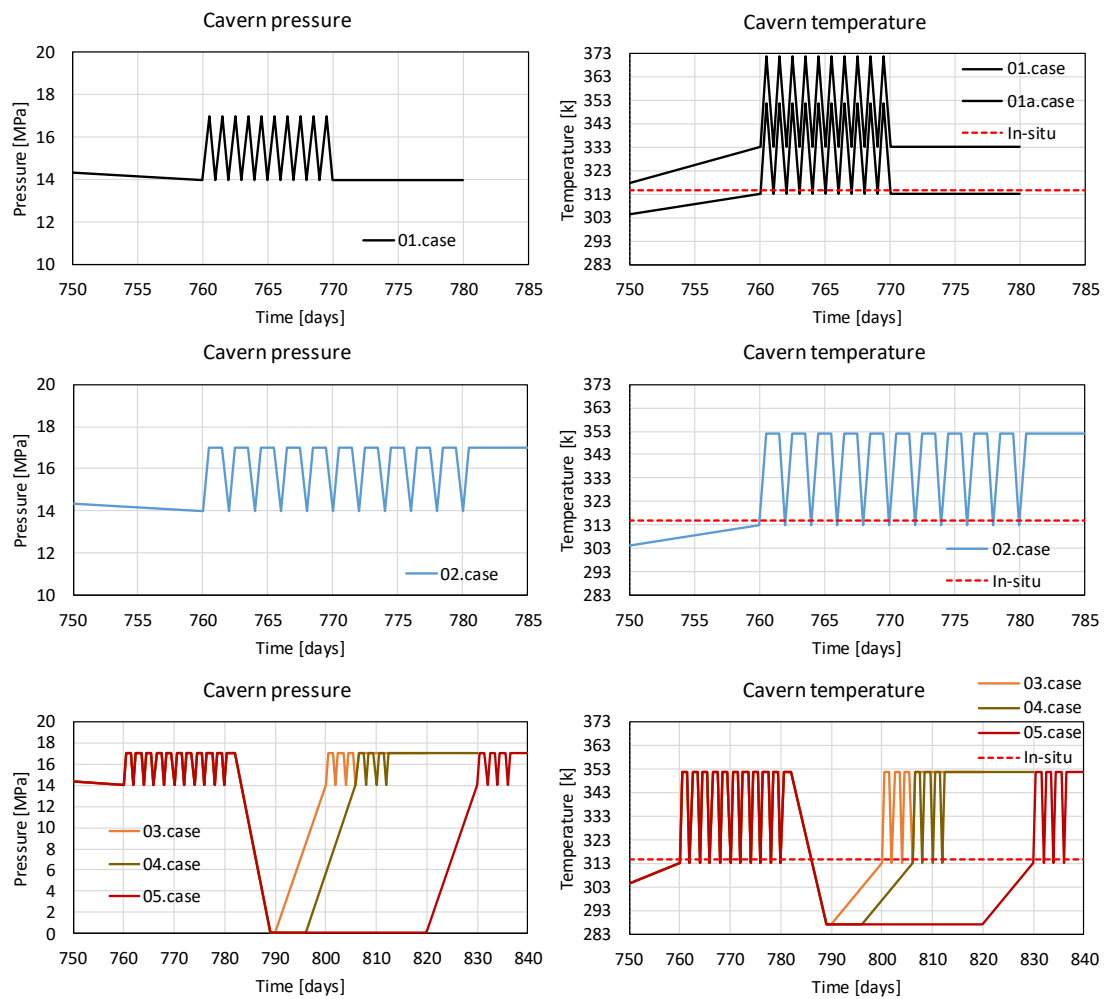


Figure 2.7: Scenarios for modelling CAES. Pressure and temperature evolution during CAES cycling. For description of cyclic characteristics, see Table 2-6.

### 2.5.2 Results CAES simulations

For every scenario, the response of the rocks in terms of displacements (wall convergence), temperature and stress evolution was analyzed. Displacements and stresses, and the potential of tensile failure and dilatant behavior in the rock salt were monitored close to the cavern wall, at a depth of 1275m (mid-height of the cavern for CAES). In addition, temperature changes into the cavern wall were monitored along a profile at a depth of 1275m (cavern mid-height), at different stages of the injection/withdrawal cycles: at the end of cavern leaching, at the end of the 1<sup>st</sup> injection- and withdrawal period, at the end of maintenance period (if applicable) and at the end of the last injection- and withdrawal cycle. Results for the different scenarios are presented in Figure 2.8 to Figure 2.15.

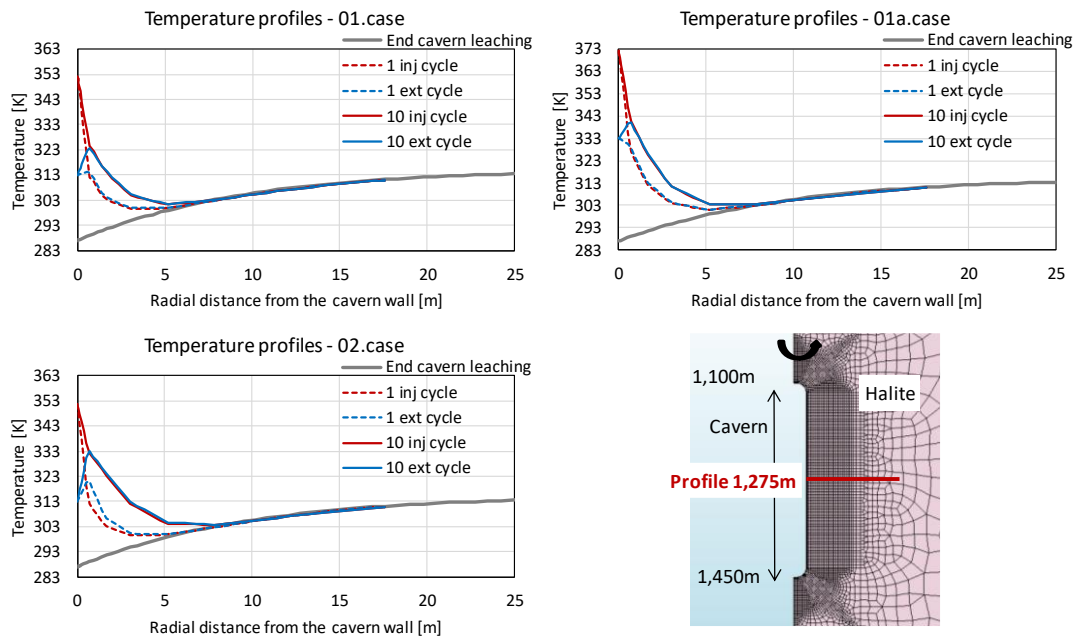


Figure 2.8: Temperature changes at the end of cavern leaching and during injection and withdrawal cycles, for the CAES scenarios without a maintenance period (01, 01a and 02).

Based on the evolution of temperatures, stresses and displacements in the cavern wall from the simulated scenarios, the following conclusions can be drawn for CAES:

Effect of air injection and withdrawal on temperature changes in the cavern wall:

- A significant cooling of the rock salt some tens of meters into the cavern wall occurs during cavern leaching.
- Cooling effect due to cavern leaching is gradually annihilated during CAES cycling. Warming up of the rock increases with the number of CAES cycles.
- Cavern wall temperatures increase above in-situ rock salt temperatures in all simulated scenarios of CAES cycling.
- Temperature fluctuations during CAES cycling are observed within a distance of 1 m into the cavern wall.
- Maintenance causes cooling of the rock. Penetration depth of cooling front into the cavern wall increases with the duration of maintenance period.
- CAES cycling after maintenance gradually warms up the rock salt.

Effect of the length of the injection and withdrawal cycles for CAES (case 01 versus case 02):

- Short cyclic loading promotes the potential for tensile failure and dilation of the rock salt close to the cavern wall. A potential for dilation and tensile stressing in the cavern wall is observed, which seems to be gradually increasing with the number of loading cycles.

Effect of idle time between injection and withdrawal period (case 01 versus case 02):

- Idle time results in an increase in tensile stressing and dilation in the cavern wall.

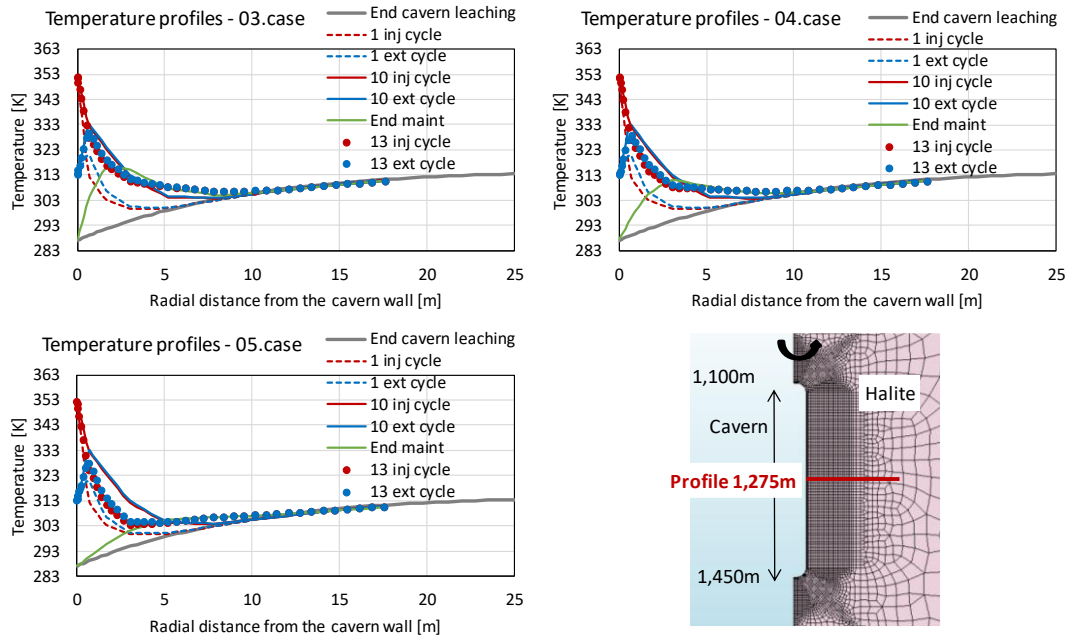


Figure 2.9: Temperature changes at the end of cavern leaching, during injection and withdrawal cycles, and at end of maintenance for the CAES scenarios with a maintenance period (03, 04 and 05).

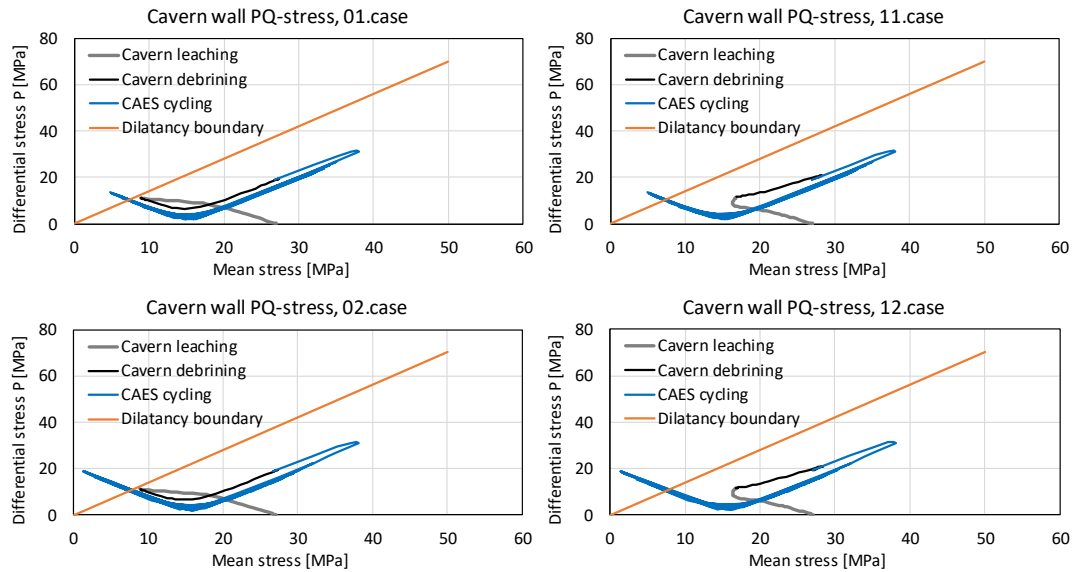


Figure 2.10: P-Q stress path versus dilation boundary based on Ratigan dilation criterium, for the CAES scenarios without a maintenance period. Left column: for ZwdNLC law creep law, right column for ZwdNLCLCC creep law. P,Q evolution plotted at location of cavern wall at a depth of -1275m (cavern mid-height).

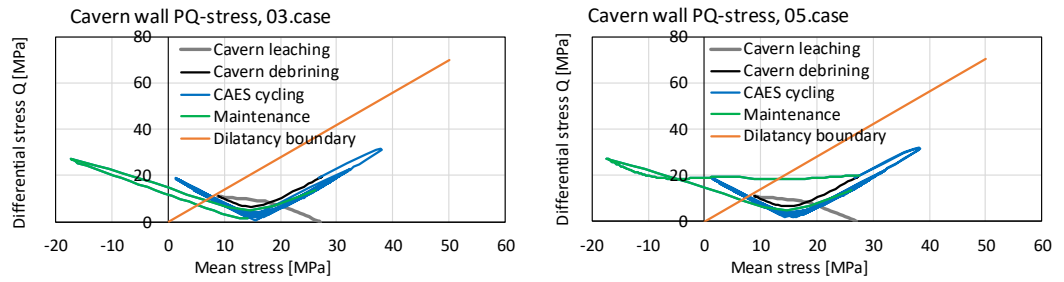


Figure 2.11: P-Q stress path versus dilation boundary based on Ratigan dilation criterium, for the CAES scenarios with a maintenance period, for ZwdNLC law creep law. P,Q evolution plotted at location of cavern wall at a depth of -1275m (cavern mid-height).

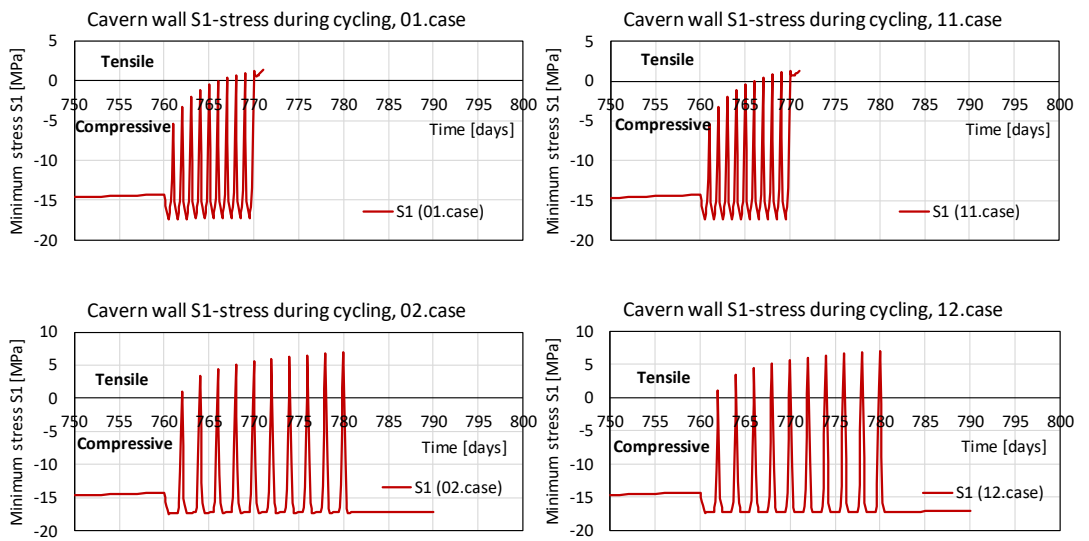


Figure 2.12: Minimum principal total stress near the cavern wall, at a depth of -1275m (cavern mid-height), for the CAES scenarios without a maintenance period. Left column: for ZwdNLC law creep law, right column for ZwdNLCCLCC creep law. S1 evolution plotted at location of cavern wall at a depth of -1275m (cavern mid-height).

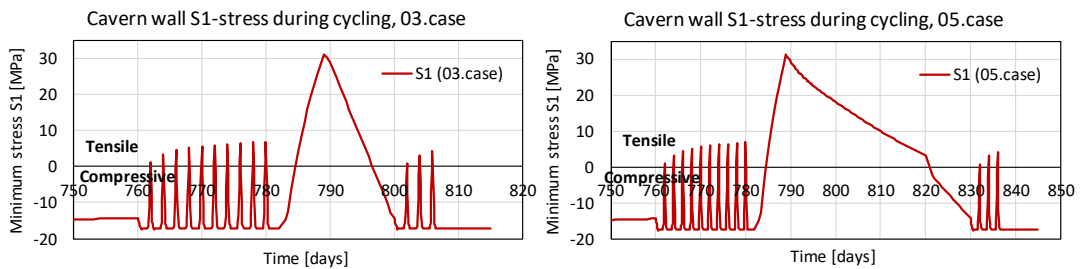


Figure 2.13: Minimum principal total stress near the cavern wall, at a depth of -1275m (cavern mid-height), for the CAES scenarios with a maintenance period, for ZwdNLC creep law. S1 evolution plotted at location of cavern wall at a depth of -1275m (cavern mid-height).

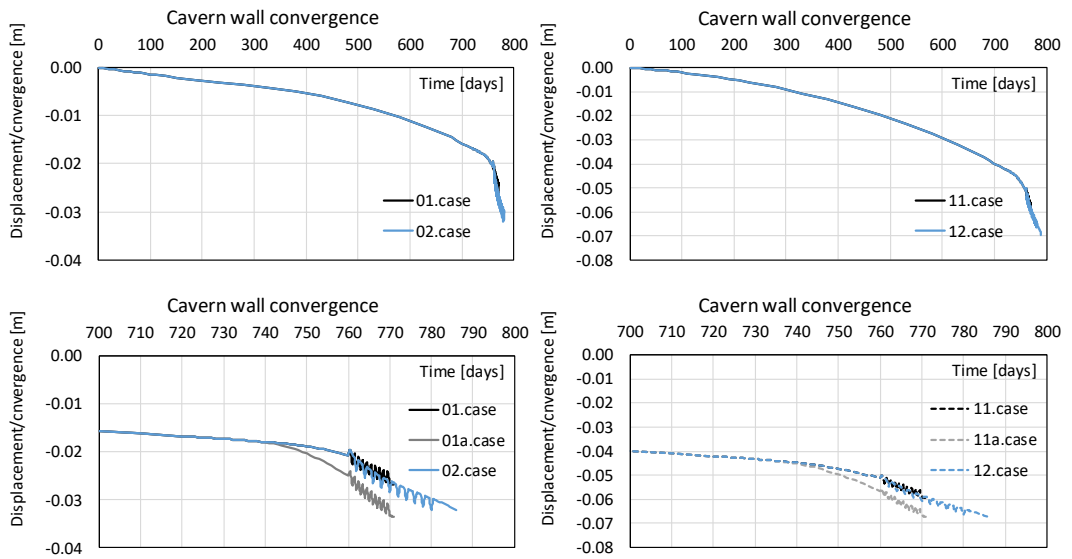


Figure 2.14: Radial displacements (cavern wall convergence) of the cavern wall at a depth of -1275m (cavern mid-height) for the CAES scenarios without a maintenance period. The lower graphs are zoom-ins of the upper graphs.

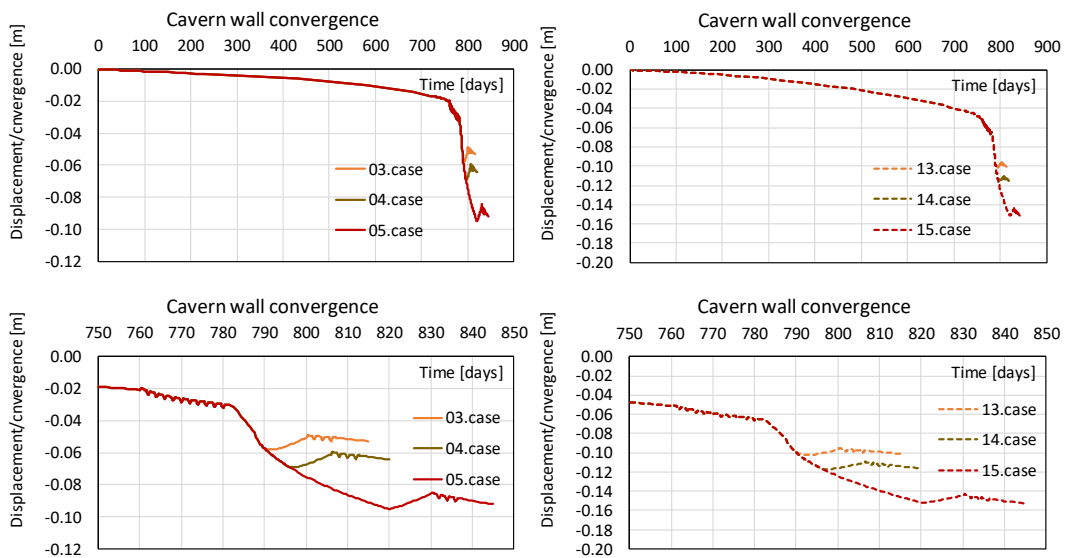


Figure 2.15: Radial displacements (cavern wall convergence) of the cavern wall at a depth of -1275m (cavern mid-height) for the CAES scenarios with a maintenance period. The lower graphs are zoom-ins of the upper graphs.

Effect of maintenance duration (case 03 versus case 04 versus case 05):

- A longer duration of maintenance period (30 days versus 7 days versus 1 day) promotes tensile stressing and dilation in the cavern wall.

Effect of the wellhead air temperature (case 01 versus case 01a, and case 11 versus case 11a):

- Higher wellhead temperatures of injected air imply higher temperatures of compressed air in the cavern. As the creep strain rates are temperature-dependent, convergence of the cavern wall is larger.

Effect of salt creep rates:

- Higher creep rates (resulting from a combination of linear and nonlinear creep in the ZwdNLCLLC creep model) result in 1.5 to 2 times larger convergence of the cavern wall (cases 01-05 versus cases 11-15).
- The salt with higher creep rates appears to have the same effect on the potential for tensile failure and dilation in the cavern wall during CAES cycling compared to the salt with lower creep rates. This is likely due to short duration of thermo-mechanical cyclic loading (several hours to a day). During short loading, the process of steady-state creep is likely not initiated to a significant degree to observe a difference between the different creep models used in simulations.

### 2.5.3 *Conclusions and future research*

#### 2.5.3.1 Conclusions

Based on the results of the geomechanical assessment, the following can be concluded regarding the effects of cyclic injection and withdrawal of air during CAES operation, and the extent to which they affect cavern stability and integrity:

- During cavern leaching, a gradual temperature decrease (up to 25°C lower than the initial temperature) is observed in the rock salt around the salt cavern, which extends up to a distance of 30m from the cavern wall.
- During CAES injection and withdrawal cycles, temperatures in the near-wall area are raised above original in-situ temperatures.
- Temperature fluctuations during CAES cycling are observed within a distance of 1 m into the cavern wall.
- Dilation of rock salt and tensile failure is observed at short distances from the cavern wall (<1m).
- Maintenance causes cooling of the rock, and promotes tensile stressing and dilation in the cavern wall. Penetration depth of cooling, tensile stressing and extent of dilation zone in the cavern wall increase with the duration of maintenance period.
- Tensile stressing can cause tensile failure and creation of fractures in a thin skin at the cavern wall (<1m thick). Fractures could lead to spalling, but they do not pose a real threat to cavern integrity due the limited depth of penetration in the cavern wall.
- Differences between convergence for different salt constitutive behavior (ZwdNLC and ZwdNLCLLC creep laws) are significant for the cavern leaching phase. However, differences between convergence and stress paths are less pronounced for the CAES cycling phase. This is likely due to short duration of cyclic loading that causes dominantly elastic deformation.

#### 2.5.3.2 Future research

In the presented study, the focus was on assessing the effects of cyclic injection and withdrawal of air during CAES operation on cavern stability and integrity. Although this is an important aspect of salt cavern storage, experience from previous incidents at underground storage facilities suggests that the biggest risks arise from well problems (Evans, 2008), i.e., the integrity of the well is compromised, which leads to leakage of stored product. A logical follow-up would therefore be to extend the geomechanical assessment to the well system through which the compressed air is injected and withdrawn from the cavern. For this purpose, a geomechanical model of the wellbore and near well area could be developed to simulate the effects cyclic air

injection and withdrawal on durability and integrity of wells. In particular, the formation of micro-annuli (i.e. circumferential fractures) at interfaces between the salt and well (at the last cemented casing shoe and along the wellbore) could then be examined, as well as the potential for leakage of air along those micro-annuli and through annular cement.

## 2.6 Economic assessment of CAES and AA-CAES in salt caverns

In this section, the results are detailed of the economic analysis that was done to analyse the business case of one business model for Compressed Air Energy Storage (CAES). The business case for Underground Hydrogen Storage (UHS), which was explored as part of the same effort, is further detailed in Section 0.

### 2.6.1 Goals and scope

In CAES, electrical energy is stored by compressing air to high pressure, and storing it in salt caverns in the subsurface. When the electrical energy must be regenerated, the compressed air is retrieved from storage to drive a turbine (turbo-expander) attached to a generator that generates electricity (see Section 0 for details on technology concepts). The ability of CAES to store energy puts CAES in a position to participate in price arbitrage and hedging activities on a variety of electricity trading markets.

In this study, the business cases of both D-CAES (diabatic, without reuse of heat generated during compression of the air) and AA-CAES (advanced adiabatic, with reuse of generated heat) are elaborated. Both the D-CAES and AA-CAES business cases are based on an arbitrage business model that makes use of volatile electricity prices (EPEX) on the day-ahead market only. Other potential revenues, as listed in Table 2-10, are left out of scope.

Goal of the business case analysis is to get insight into:

- The economic value and feasibility of D-CAES and AA-CAES when participating in price arbitrage on (only) the day-ahead market;
- The potential role and behaviour of CAES assets in the electricity system by day-ahead market simulations based on given 2030 and 2050 energy system scenarios;
- The main cost and revenue drivers of these assets;
- Sensitivities in the day-ahead business cases of D-CAES and AA-CAES.

In subsections 2.6.2 and 2.6.3, the methodologies and tools used for the analysis are first introduced, followed by the assumptions on energy system scenarios and costs for the years 2030 and 2050. Next, in subsection 2.6.4, the results of the business case analysis and its sensitivities are presented and discussed, and finally conclusions are drawn in subsection 2.6.5.

### 2.6.2 Methodology of business case analysis

The economic analysis is executed by following the steps presented in Figure 2.16. First the **scope** of the economic analysis is determined. The cases to elaborate are selected (D-CAES and AA-CAES, and hydrogen storage) (step 1) and a choice is made for technologies to use in the cases (step 2). Storage of compressed air or hydrogen is assumed to take place in salt caverns in both cases. For hydrogen production a PEM electrolyser is applied. Capacities are determined. Also choices for the underlying business model are made (step 3). Details on these choices and assumptions, and on the case specific parameters are discussed in subsection 2.6.4.1 for CAES and AA-CAES, and their the business model is elaborated in subsection 2.6.4.2. For hydrogen they are discussed in subsections 3.6.2.1 and 3.6.2.2.

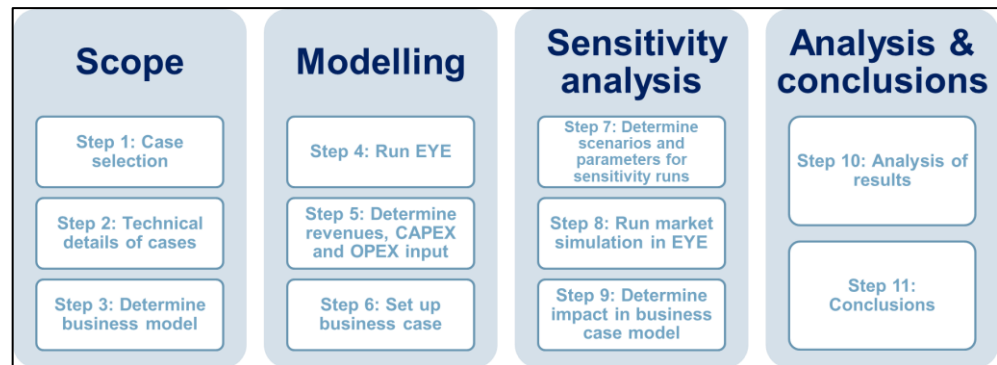


Figure 2.16 Steps followed in the economic analysis

The **modelling** of the business cases contains three steps:

- Energy market simulation in TNO's EYE model (step 3);
- Determine input for revenues, CAPEX and OPEX (step 4);
- Business cases modelling to determine the Net Present Value (step 5).

The energy market simulation with EYE is explained in subsection 2.6.3. The relating bid strategies of the assets for the cases D-CAES and AA-CAES are discussed in subsection 2.6.4.2, and for in subsection 3.6.2.2 for the case of flexible hydrogen production).

Input parameters regarding revenues, CAPEX and OPEX are determined. The business model is translated into revenue streams. These inputs, as well as the results of the energy market modelling and bidding behaviour from the EYE model are used to set up the business cases for the cases. The results of the business cases give insight into the value and cost of large-scale subsurface energy storage for the two cases. The business cases are elaborated to calculate the Net Present Value (NPV). The results of the business cases are presented in subsection 2.6.4.2 for D-CAES and AA-CAES and in subsection 3.6.2.2 for hydrogen storage.

The assumptions of the future energy scenario and the techno-economic asset parameters are stretched by means of a **sensitivity analysis** to assess the robustness of the results of the business case analysis.

First scenarios and parameters for the sensitivity runs are determined (step 7). The outcome of the sensitivity runs is determined in two steps: first the market simulation in EYE is executed (step 8); subsequently the outcome of this simulation is imported into the business case model (step 9), which will show the impact on the business case. The results of the sensitivity analysis are described in subsection 2.6.4.2 for D-CAES and AA-CAES and in subsection 3.6.2.2 for hydrogen storage.

Finally, the results of the modelling and sensitivity runs are **analysed** (step 10) and **conclusions** per case and overall are drawn (step 11). Case specific conclusions are presented in subsection 2.6.4.2 for D-CAES and AA-CAES, and in subsection 3.6.2.2 for hydrogen storage.

### 2.6.3 Energy market simulation with the EYE model

#### 2.6.3.1 Introduction to the Eye model

The EYE model is a deterministic (rules-based) energy dispatch simulation model. EYE comprises of an electricity system model which is capable of simulating marginal electricity price dispatch on the day-ahead market given a certain scenario (asset base, commodity prices, expected demand, etc.) and with perfect foresight knowledge of the electricity demand and renewable production. With this model, insight can be gained on the operational costs and benefits of assets that generate or consume electricity. Furthermore, asset-specific bid behaviour based on intra-market electricity price arbitrage as well as the impact of other flexible energy system assets on those market prices can be taken into account. This allows for analysis of earning potential of flexible assets and saturation levels of electricity generating and consuming assets. The EYE model does not optimise the operational performance of individual assets through risk-driven decision logic but aims to clear the electricity market such that social welfare is increased given all bids. EYE does not perform intra-day bid strategies and bids on multiple electricity markets.

#### 2.6.3.2 EYE functionalities and boundaries and the break-even bid price mechanism

The EYE model is developed to model the future electricity grid and flexibility options with a first order estimation, in order to study complex system effects quickly. It can be deployed at a local, regional and national level. EYE simulates expected electricity prices on day-ahead wholesale markets of one single country, without interaction and dynamics with international energy markets. Interconnections to other markets are implemented in a rudimentary way to supply energy if shortages in the national system occur.

Simulations are based on a future scenario. To do so, EYE is internally using bid ladders (merit orders) of hourly supply and demand, coupled with a clearing mechanism (marginal pricing) that is comparable with the clearing mechanism of wholesale markets (see Figure 2.17 for an illustration).



Figure 2.17: Electricity clearing mechanism to set the hourly electricity price, based on required electricity volume per hour. Including inflexible supply (e.g. wind energy) and inflexible demand (e.g. CCGT with base load heat supply)

By means of this functionality, EYE can determine an expected price per hour. The lower price boundary is set to 0 EUR/MWh manually, while the upper price boundary is equal to the highest cross-border interconnection electricity price of 86 EUR/MWh. Each LSES asset within the energy system has a minimal demand bid price and supply bid price based on which the asset will decide, on an hourly basis, whether to participate on the energy market or not.

Table 2-7 depicts the composition of the price spread required for a break-even operation of a large-scale energy storage asset: Note that this is the spread to break-even operationally – excluding CAPEX investments and constant yearly O&M costs. Calculating the required price spread to start operating the storage asset:

$$\text{Required price spread} = E_{\text{revenue discharge}} - E_{\text{cost discharge}} - E_{\text{cost charge}}$$

The revenue is built up from the electricity discharged (electrical power over time), multiplied with the existing electricity price:

$$E_{\text{revenue discharge}} = [E_{\text{discharge}} * E_{\text{price discharge}}]$$

$$E_{\text{charge}} = P_{\text{charge}} * t_{\text{charge}}$$

Discharge cost is the sum of the required added cost of fuel consumption per unit of energy discharged, the additional emission costs and the variable operation and maintenance cost:

$$E_{\text{cost discharge}} = E_{\text{discharge}} * \text{Fuelconsumption} * \text{Fuelprice}] \\ + [E_{\text{discharge}} * CO_2 \text{ emission} * CO_2 \text{ price}] + [E_{\text{discharge}} * \text{variable O\&M cost}]$$

The charge cost (electrical power over time), is given by multiplying the charged energy and the hour-specific price:

$$E_{\text{cost charge}} = [E_{\text{scharge}} * E_{\text{price scharge}}]$$

$$E_{\text{discharge}} = P_{\text{discharge}} * t_{\text{discharge}}$$

Table 2-7: Price spread example calculation

| Charge                                | Storage  | Discharge                |
|---------------------------------------|--|--------------------------|
| 1,14 MWh<br>€0                        | Cycle efficiency: 87%<br>Variable O&M cost: €2 / MWh <sub>charge</sub><br>Fuel cost: €0 / MWh <sub>discharge</sub> | 1 MWh<br>€100            |
| Charge cost<br>€0                     | Storage cost<br>€2   | Discharge revenue<br>€87 |
| Required price spread: €87 - €2 = €85 |  |                          |

It is possible to run simulations based on future energy system scenarios and, as a result, analyse the behaviour of future energy prices. An overview of the EYE simulator and its inputs and outputs is shown in Figure 2.18.

2.6.3.3 EYE input: Energy system assumptions

The energy system scenario is an input based on which the energy market clearing is performed. The energy system scenarios of 2030 and 2050 are based on the KEV2019<sup>7</sup> and the national governance scenario in the ES2050<sup>8</sup> studies respectively. Both these scenarios are elaborated on in detail in the report of work package 1 of the LSES project, in which the role of CAES and UHS in the future energy system is analysed based on results of energy system modelling. Therefore, this paragraph will only discuss the differences in scenario assumptions between this study and that of work package 1.



Figure 2.18: Overview of EYE simulator with inputs: models of demand and supply bid behaviour, and outputs such price and production/consumption profiles of individual assets.

There are four types of input categories:

**1. National energy demand**

Scenario assumptions on Dutch hourly electricity and hydrogen demand are discussed in the report of work package 1, to which the reader is referred.

**2. Energy generation technology mix**

The asset capacity from Table 2-8 is shown in power generation capacity of assets in the energy system. The total hourly yield of renewable assets is calculated using the yearly profile with resulting operational hours.

Table 2-8: Energy generation technology mix (selection of assets, complementing the scenario description in the report of work package 1)

| Energy generation technology mix | 2030 [GW] | 2050 [GW] |
|----------------------------------|-----------|-----------|
| Wind Onshore                     | 6         | 20        |
| Wind Offshore                    | 13.4      | 51.5      |
| Solar                            | 25.1      | 106       |
| Natural Gas                      | 11.9      | 0         |
| Hydrogen CCGT                    | 2.7       | 45.9      |

<sup>7</sup> Source: PBL (2019) Klimaat en Energie Verkenning 2030

<sup>8</sup> Source: Berenschot, Kalavasta (2020) Klimaatneutrale energiescenario's 2050

The installed capacity of hydrogen-fired combined cycle gas turbines (CCGT) in 2050 is estimated<sup>9</sup> to be 46 GW. In the EYE scenario, only CCGTs with a capacity of 437 MW each and varying efficiencies (46-56%) are assumed. The interconnection over the counter (OTC) contracts are accessible to close the demand-supply gap on the Dutch grid if required. The base case electricity price is country-dependent and varies between 60 and 86 EUR/MWh.

### 3. Flexibility and storage technology mix

A total installed capacity of 3 D-CAES, 2 AA-CAES and 1 flexible hydrogen production asset is assumed while modelling the electricity market in EYE. The LSES assets central in this business case analysis are included within this installed capacity. The techno-economic parameters of the large-scale energy storage assets D-CAES, AA-CAES and flexible hydrogen production are described in more detail in subsection 2.6.4.2 and subsection 3.6.2.2 respectively.

Table 2-9: Flexibility and storage technology mix (selection of assets, complementing the scenario description in the report of work package 1)

| Flexibility and storage technology mix   | 2030         |                       | 2050         |                       |
|--|--------------|-----------------------|--------------|-----------------------|
|  | Charge; [GW] | discharge rate [GW/h] | Charge; [GW] | discharge rate [GW/h] |
| Power-2-Hydrogen   | 1.14         |                       | 10.99        |                       |
| Storage (Electric vehicles)  | 19.52        | 0.47; 0.47            | 49.76        | 12.1; 12.1            |
| D-CAES ( <i>320MW<sub>e</sub> asset</i> )  | 0.96         | 0.75; 0.96            | 0.96         | 0.75; 0.96            |
| AA-CAES ( <i>140MW<sub>e</sub> asset</i> )                                       | 0.28         | 0.206; 0.28           | 0.28         | 0.206; 0.28           |
| Flexible H <sub>2</sub> prod. ( <i>600 MW<sub>H<sub>2</sub>LHV</sub> asset</i> ) | 0.6          | 1.5; 0.6              | 0.6          | 1.5; 0.6              |

### 4. Commodity Prices

Scenario assumptions on Dutch hourly electricity and hydrogen demand are discussed in the report of work package 1.

#### 2.6.3.4 EYE electricity market simulation software output

The output of per simulation run used in the subsequent business case analysis include:

- **Electricity clearing price profile:** price profile consisting of an expected electricity price per hour
- **Power, charge and discharge of assets:** the operational hours and the consumed/produced energy of every individual asset per hour
- **Fill level of assets:** fill level of storage buffers per hour
- **Market clearing insights:** e.g. consumer/producer surplus of electricity per hour.

#### 2.6.4 Economic cost comparison D-CAES and AA-CAES

In this subsection, the price arbitrage-only business cases for D-CAES and AA-CAES are elaborated. In subsection 2.6.4.1. the common basis of the business cases is described. The results of the business case for D-CAES and AA-CAES can be found in subsection 2.6.4.2.

<sup>9</sup> National governance scenario. Source: Berenschot, Kalavasta (2020) Klimaatneutrale energiescenario's 2050

### 2.6.4.1 Basic structure and assumptions

#### **Cost modelling methodology**

Costs consist of CAPEX (capital expenditure, investments) and OPEX (constant and variable operational expenditure). CAPEX consists of investment in the production asset. Planning, engineering and construction of the assets will in practice take several years, but for simplicity all CAPEX is assumed to be spent in 2025.

OPEX consists of the following cost items:

- Electricity consumption costs (determined by EYE simulation);
- Electricity grid connection costs (TSO costs);
- Operation & maintenance for the production and storage asset;
- Fuels consumption (only in case of D-CAES, to compensate cooling of expanding air) and related CO<sub>2</sub> emission costs.

#### **Business model of D-CAES and AA-CAES assets**

Business models of both assets are based on electricity market prices (EPEX market) and the volatility of those prices: when electricity prices are low, the storage is charged/filled. At moments of high prices, the storage is discharged/emptied. The differences in electricity prices are the revenue generator in this study. The times of charging and discharging are determined by an hour price scenario for electricity, that results from the EYE modelling.

Besides a business model based on volatility of electricity prices, also other business models are possible for D-CAES and AA-CAES. Benefits of storage are for example:

- Offering flexibility to the electricity system (TSO and DSO), e.g. by services like aFRR<sup>10</sup>, mFRR<sup>11</sup> and FCR<sup>12</sup> from TenneT, the Dutch TSO;
- Offering security of electricity supply by storage of electricity;
- Avoid or reduce investments in grid capacity extension by TSO and DSO;
- Utilisation of waste heat generated by the asset (CAES). Waste heat can be used for example in the industry or built environment.

These values offer possible additional revenue streams, but are not within the scope of the business case analysis in this study. Table 2-10 summarizes the business models in and out of scope in this study.

Table 2-10 Scope of business models analysed in economic assessment of D-CAES and AA-CAES

| Business model in scope  | Business model out of scope  |
|--|--|
| Electricity price arbitrage on the day-ahead wholesale market of the Netherlands | Electricity price arbitrage on international day-ahead wholesale market                              |
|  | Electricity supply and demand capacity bids on the aFRR and mFRR or the FCR in the Netherlands       |
|  | Electricity trades on the intra-day market, active up to 5 minutes before supply, of the Netherlands |
|  | Rental of storage capacity through private agreements  |
|  | Providing storage for congestion management  |

<sup>10</sup> aFRR: automatic Frequency Restoration Reserve

<sup>11</sup> mFRR: manual Frequency Restoration Reserve

<sup>12</sup> FCR: Frequency Containment Reserve

### **Business case analysis assumptions**

For the business case, the following financial parameters are assumed:

- A WACC (Weighted average cost of capital) of 5% is applied.
- The time period for the business case is from 2025-2060:
  - Investments and construction of assets from 2025-2029;
  - Asset is operational from 2030-2060
  - Decommissioning costs are left out of scope
- In the EYE simulation, an hour price scenario for 2030-2049 is determined, based on simulation of 2030; and a price scenario for 2050-2060 based on simulation of 2050.

### **Sensitivity analysis scenarios**

The assumptions of the future energy scenario and the techno-economic asset parameters are stretched by means of a sensitivity analysis to assess the robustness of the results of the business case analysis. Six sensitivity scenarios are defined. Table 2-11 describes the parameters that are varied and the values assumed to conduct this analysis. The scenarios are chosen such, that the main driver over this economic assessment, the electricity price, is subjected to potential changes to test the robustness of the market price in 2030 and 2050. Both the capacity or primary input variables of flexible power sources (S1, S3, S5, S6) and the inflexible power sources (S2) are aggressively stretched. The aggressive sensitivity analysis aims to yield insights on the energy system behaviour and the subsequent responses the storage assets. A rapid technological development is included to explore the benefits from lower electrolyser investment costs and better hourly performance (S4).

The values of varied parameters can be found in Appendix B: Detailed sensitivity analysis description.

Table 2-11: Definition of six sensitivity scenarios

| Sensitivity scenarios |   | Varied parameter(s)      |
|-----------------------|---|--------------------------|
| S1                    | Maximum natural gas-fired power plant [GW]  | +3.2 GW operational      |
| S2                    | Installed capacity solar (PV) [GW]          | 200% Solar <2050         |
|                       | Installed capacity offshore wind farms [GW] | 200% OWF >2050           |
| S3                    | Natural gas price [EUR/MWh]                 | 200% NG price            |
|                       | CO2 price [EUR/ton]                         | 200% CO2 price           |
| S4                    | Electrolyser power of P2G asset [MW/h]      | 200% production capacity |
|                       | Cavern charge rate of UGS asset [MW/h]      | 200% charge capacity     |
|                       | Electrolyser efficiency [%]                 | +10% efficiency          |
|                       | Electrolyser investment costs [EUR/MW]      | -20% investment cost     |
|                       | TSO costs flex [EUR/MW]                     | 50% TSO costs            |
| S5                    | Hydrogen price [EUR/kg (EUR/MWh)]           | 50% H2 price             |
| S6                    | Hydrogen price [EUR/kg (EUR/MWh)]           | 500% H2 price            |

#### 2.6.4.2 Business case D-CAES and AA-CAES

The business case analysis of the D-CAES and AA-CAES case study is presented in this paragraph. First the production strategy and techno-economic parameters are discussed. Subsequently, the results and sensitivity analysis of both the EYE market simulation and the economic cost modelling are presented. Finally, conclusions regarding the case study are drawn based on these results.

### **Production strategy CAES and AA-CAES**

An operation strategy is required to make recurring production-related decisions based on a predefined logic. The strategy explained below aims to generate revenues and could therefore be considered a *use case* of D-CAES and AA-CAES. Other electricity production strategies are possible, however for this project they are left out of scope.

Operating the D-CAES and AA-CAES assets is aimed at generating revenue through arbitrage. By applying the arbitrage practice, CAES aims to buy electricity (charge) when the wholesale electricity market price is below a certain value, and to sell electricity (discharge) when the price is above a certain value. The delta of sales price minus purchase price has to cover the operational costs to break-even (operationally). This delta, hereafter referred to as the price spread, is determined as follows:

1. A virtual electricity market is simulated excluding all non-must run assets (including competing storage assets such as batteries, flexible Power-2-gas assets and other D-CAES and AA-CAES assets). This virtual market can be considered a perfect forecast of future hourly prices.
2. The market prices are then sorted on ascending and descending. The ascending price list show the prices best fit for discharging first, the descending price list show the prices best fit for charging first. For each set of discharge and charge price, the cost in €/MWh is calculated (see 2.6.3.2).
3. The bid prices for charging and discharging are determined by looking at the lowest discharge price and highest charge price combination that still provides a positive benefit.
4. Based on the prices set by the virtual market run in step 1, the D-CAES and AA-CAES asset participates in the hourly electricity market bidding for both the consumption (charge) and production (discharge) of electricity, being constrained by the prices set in step 3, to achieve a break-even operation.

### **Techno-economic parameters D-CAES and AA-CAES**

The D-CAES and AA-CAES assets are defined by the parameters described in this paragraph. A selection of the most relevant parameters is found in Table 2-12 and Table 2-13. A detailed list of asset parameters can be found in Appendix A: Techno-economic parameters. The capacity of the AA-CAES is assumed lower than the D-CAES due to the more challenging application of this technology and current technology readiness level based on literature references<sup>13,14,15</sup>.

Table 2-12: Economic parameters of D-CAES and AA-CAES

| <b>Economic parameter</b> | <b>Unit</b> | <b>D-CAES</b>             | <b>AA-CAES</b> |
|---------------------------|-------------|---------------------------|----------------|
| Investment costs          | EUR/MW      | € 1,100,000 <sup>10</sup> | € 1,500,000    |
| Constant O&M costs        | % CAPEX     | 2.5%                      | 2.5%           |
| Variable O&M costs        | EUR/MWh     | € 2                       | € 2            |
| Variable TSO costs        | EUR/MW/year | € 37,000 <sup>16</sup>    | € 37,000       |

<sup>13</sup> Huang et al., (2017) Techno-economic modelling of large scale compressed air energy storage systems, Energy Procedia 105

<sup>14</sup> HyUnder D2.2 (2014) - Update of Benchmarking of large scale hydrogen underground storage with competing options

<sup>15</sup> EASE (2016) Technology factsheet AA-CAES

<sup>16</sup> Transmission system operator costs based on public VEMW and TenneT sources. Reference year: 2018

The initial investment costs (CAPEX) consider a greenfield site and therefore include the investment costs needed for geological survey, licensing, and infrastructure for brine extraction, transport and processing. In a brownfield situation, i.e., an existing cavern storage site connected to a brine processing facility, the initial investment costs can be 10-20% lower<sup>17</sup>.

Table 2-13: Technological parameters of D-CAES and AA-CAES

| Technological parameter            | Unit    | D-CAES | AA-CAES |
|------------------------------------|---------|--------|---------|
| Charge time                        | h       | 8      | 10.5    |
| Charge power                       | MW      | 250    | 103     |
| Charge efficiency                  | %       | 100    | 100     |
| Charge rate                        | MW/h    | 250    | 103     |
| Energy stored                      | MWh     | 2000   | 1081.5  |
| Discharge efficiency               | %       | 58     | 70      |
| Discharge Power                    | MW      | 320    | 140     |
| Discharge rate                     | MW/h    | 320    | 140     |
| Self-discharge                     | MWh/h   | 0      | 0       |
| Natural gas fuel consumption (LHV) | MWh/MWh | 1.13   |         |
| CO2 Emission                       | kg/MWh  | 210    |         |
| Heat storage                       | MWh/MWh |        | 0.78    |
| Heat supply                        | MWh/MWh |        | 1.09    |

Both the D-CAES and AA-CAES are modelled such that only full load operation (dispatching at maximal charge power and discharge power) is considered. CAES is however well-suited to operate at lower power, and can do so with minimal efficiency loss at power outputs down to 15% of rated power. Furthermore, at low power output the turbine can run largely on compressed air, i.e., much less external fuel (natural gas and/or hydrogen) is required, which significantly reduces both the cost of operation to keep it spinning (and generating electricity) at low output, and the emissions associated with burning the fuel. As such, CAES as better equipped to deliver flexibility than conventional gas turbines.

<sup>17</sup> Personal communication Corre Energy Storage, Nouryon

**Modelling results D-CAES and AA-CAES**

Simulating the energy market in 2030 and 2050, assuming the energy system characteristics discussed in subsection 2.6.3.3, yields the systemic and asset-specific results discussed below.

**Price duration curve:** The hourly electricity price throughout the year is rearranged to the *price duration curve* below in Figure 2.19. The electricity price ranges from **0 to 84.8 €/MWh in the 2030 simulation**, and ranges from **0 to 84.2 €/MWh in 2050**.

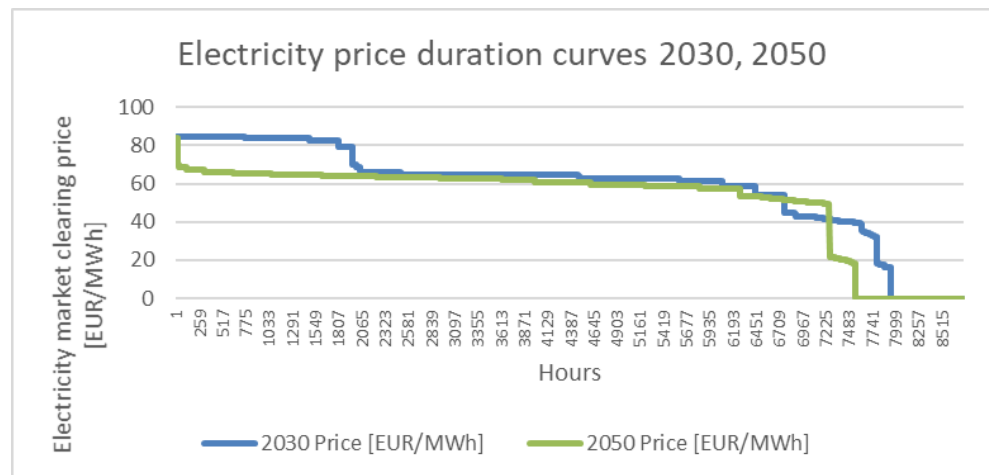


Figure 2.19: Price duration curve results 2030, 2050

**Annual fill level profile D-CAES:** The charge and discharge behaviour of the D-CAES asset, rooted in its production strategy logic, leads to the fill level profile depicted in Figure 2.20 and Figure 2.21.

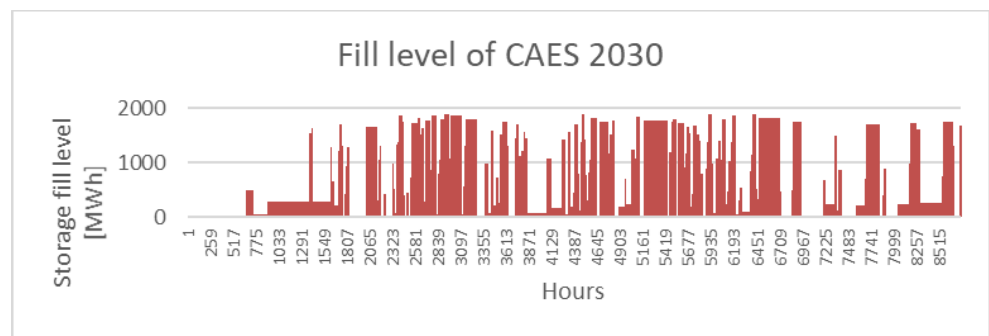


Figure 2.20: Hourly fill level of D-CAES 2030 (max. fill level is 2000MWh).

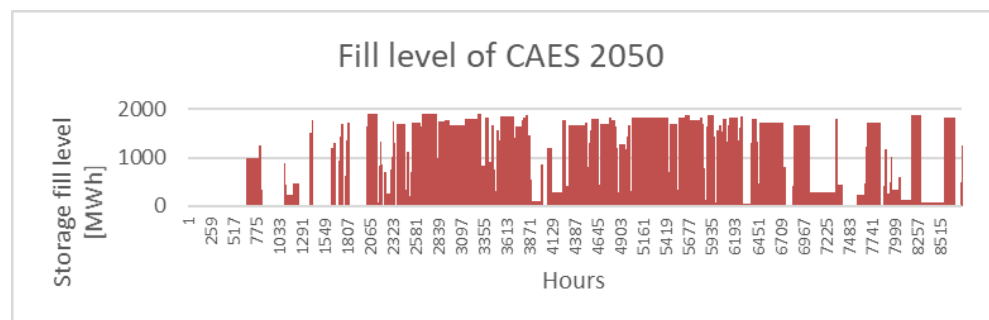


Figure 2.21: Hourly fill level of D-CAES 2050 (max. fill level is 2000MWh).

Annual fill level profile AA-CAES: The fill level profile of the AA-CAES is depicted in Figure 2.22 and Figure 2.23.

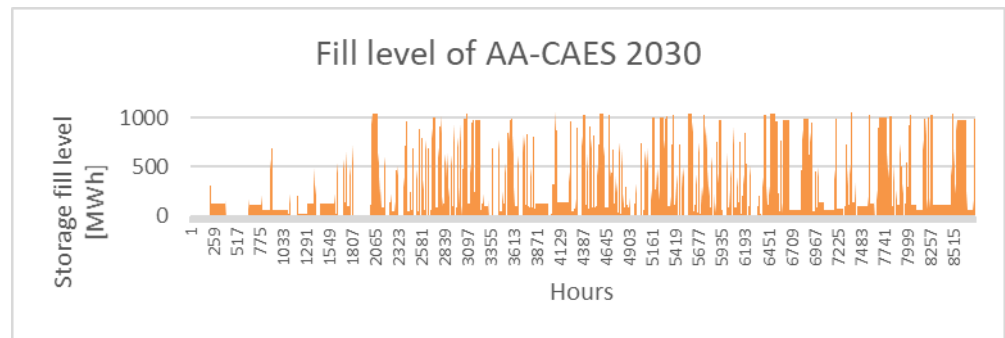


Figure 2.22: Hourly fill level of AA-CAES 2030 (max. fill level is 1081MWh)

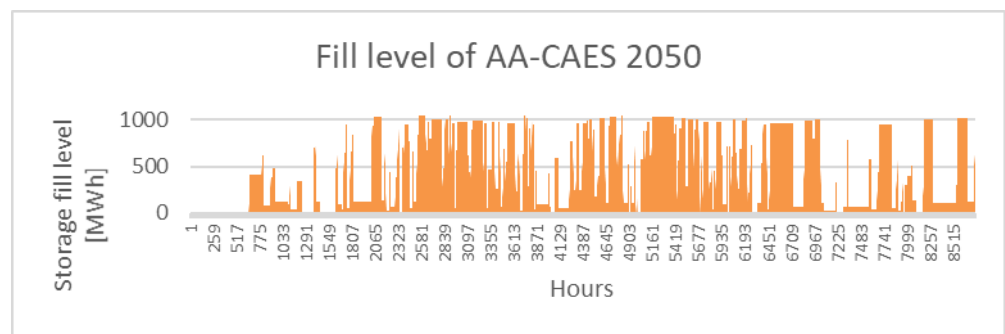


Figure 2.23: Hourly fill level of AA-CAES 2050 (max. fill level is 1081MWh)

Load duration curve D-CAES and AA-CAES: The load duration curve of the D-CAES and AA-CAES gives insight in the relation between the capacity requirements and capacity utilization throughout one year (Figure 2.24). Due to the presence of full load charge and discharge hours only there are no ramps in the load duration curve.

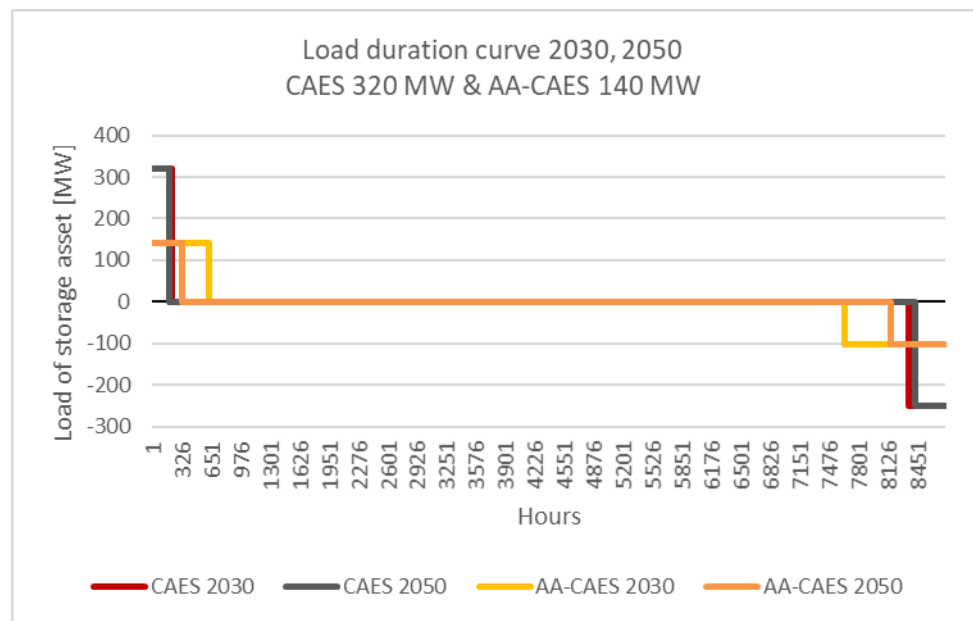


Figure 2.24: Load duration curves D-CAES and AA-CAES for 2030, 2050

The operational profiles of the D-CAES and AA-CAES, together with the hourly electricity price, are integrated in the economic cost model to calculate the cost breakdown and net present value per asset.

**Cost breakdown D-CAES and AA-CAES:** The total cost breakdown adds up the yearly revenue, constant and variable operational costs and investment costs (Figure 2.25). The revenue, OPEX and CAPEX of 2030 are assumed to be representative for the years 2030 up to 2050. The revenue, OPEX and CAPEX of 2050 is representative for 2050-2060. Detail on the cash flows can be found in Appendix C.

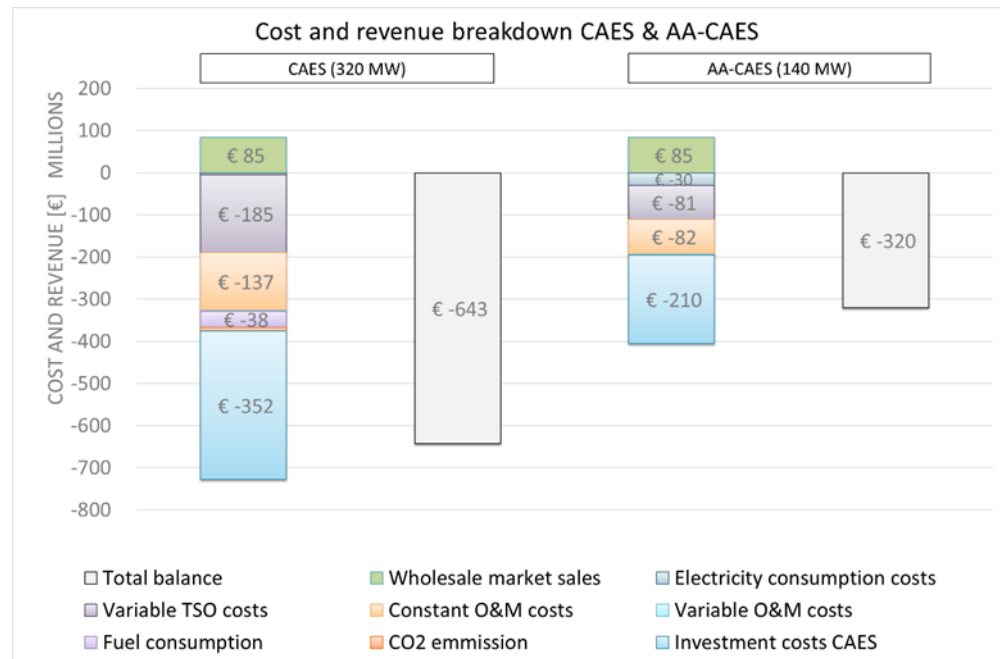


Figure 2.25: Breakdown of total cost and revenue over the lifetime of the business case (2025-2060) for D-CAES and AA-CAES

**NPV D-CAES and AA-CAES:** The cumulative cash flow and cumulative discounted cash flow of the D-CAES and AA-CAES assets are depicted in Figure 2.26.

### Sensitivity analysis of results

The robustness of the base case modelling results are challenged through a variety of extreme scenarios. These scenarios are discussed in 2.6.4.1. In Figure 2.27 the cumulative discounted cashflow per scenario is visualized.

### Discussion cost modelling D-CAES and AA-CAES

The price spread required between the electricity price for charge and discharge for a break-even operation for the D-CAES in 2030 is **€65/MWh**. For the AA-CAES, the required spread is **€22/MWh**. In 2050, the resulting price spread is **€66/MWh** and **€44/MWh for D-CAES and AA-CAES respectively**. The lowest price at which the D-CAES and AA-CAES will still discharge (the minimal supply bid), and highest price at which the D-CAES and AA-CAES will keep on charging (the maximum demand bid), are shown in Table 2-14. For both the max. demand bid, and min. supply bid, the objective is to respect the required minimal price spread between the charged, and discharged unit of energy, as is discussed in 2.6.3.2. Hereby, the asset guarantees the financial break-even objective of marginal cost and revenue.

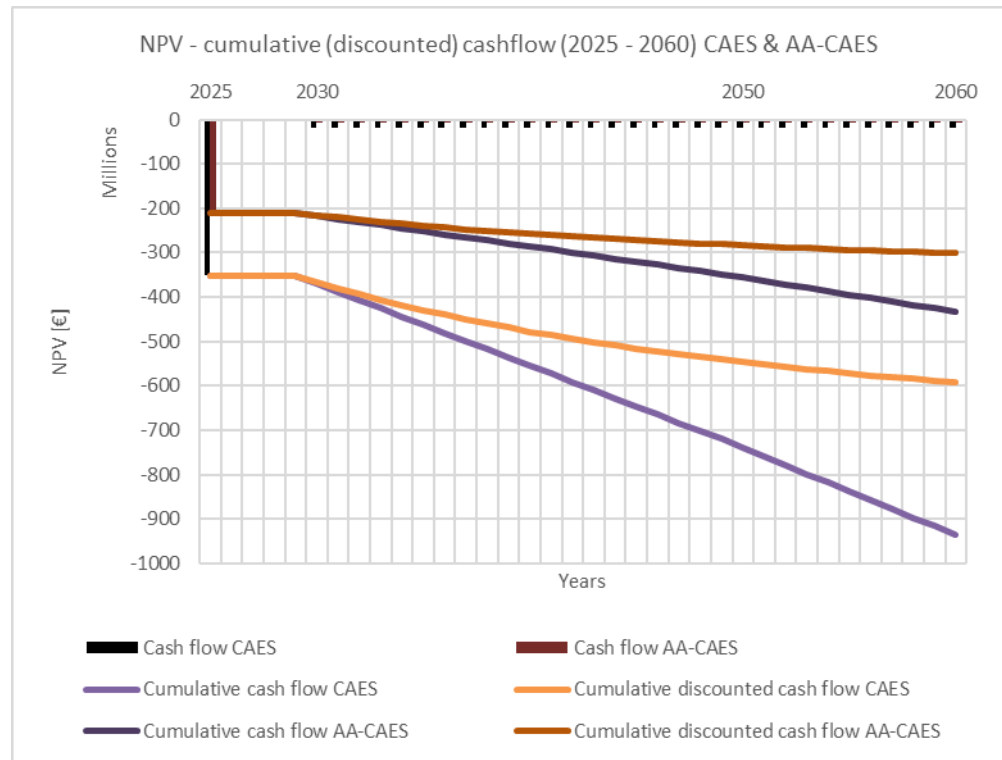


Figure 2.26: NPV and cash flow D-CAES and AA-CAES

Table 2-14 D-CAES and AA-CAES price spreads

|                         | 2030<br>€/MWh | 2030 spread<br>€/MWh | 2050<br>€/MWh | 2050 spread<br>€/MWh |
|-------------------------|---------------|----------------------|---------------|----------------------|
| CAES max. demand bid    | 18            | 65                   | 0             | 66                   |
| CAES min. supply bid    | 83            |                      | 66            |                      |
| AA-CAES max. demand bid | 43            | 22                   | 20            | 44                   |
| AA-CAES min. supply bid | 65            |                      | 64            |                      |

Considering the above mentioned required price spreads, the D-CAES and AA-CAES can operate a limited amount of hours in 2030 and 2050. The load duration curves indicate that the D-CAES is discharging 403 hours per year in the 2030 scenario, and 334 hours per year in the 2050 scenario. The AA-CAES has a higher amount of operational discharge hours, due to the smaller required price spread: 1114 hours in 2030 and 594 hours in 2050.

The initial investment costs of D-CAES (€352 million) and AA-CAES (€210 million) would require a substantial annual profit to become an attractive investment. Based on the operational profiles of both the D-CAES and AA-CAES, the total revenue generated by the arbitrage-only production strategy over the lifetime of the business case (D-CAES €85 million, AA-CAES €85 million) shows to be insufficient to result in positive cash flows. Over the lifetime of the business case from 2025-2060 the largest operational costs are the TSO grid connection costs (D-CAES €185 million, AA-CAES €81 million) and fixed operation and maintenance costs (D-CAES €137 million, AA-CAES €82 million). Consequently, the NPV of both assets is negative which leads to the conclusion that this arbitrage-only business case is negative for both types of assets given the assumptions in this case study. Furthermore, results they appear to be rather insensitive to the deviations in the sensitivity scenarios. In all scenarios, NPV for CAES and AA-CAES remain negative.

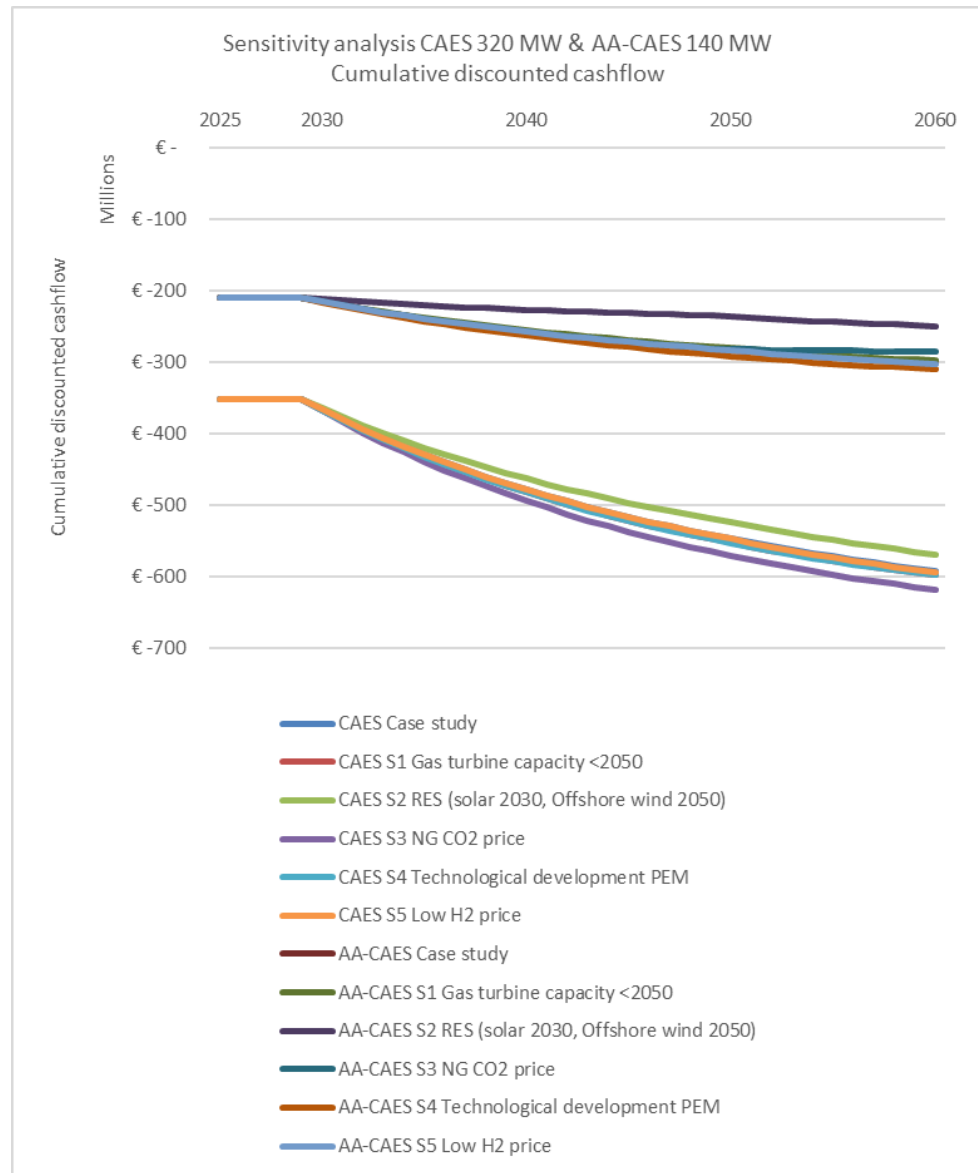


Figure 2.27: Sensitivity scenario analysis of NPV (AA-)CAES

## 2.6.5 Conclusions and future research

### 2.6.5.1 Conclusions

Based on the results of the economic analysis as presented, the following conclusions can be drawn for the D-CAES and AA-CAES business cases that have day-ahead electricity market arbitrage as their single source of revenue:

- The price arbitrage-only business case for D-CAES is negative and not sensitive to the parameter variations applied in the sensitivity scenarios. Due to a significant price spread requirement to break-even operationally (€65/MWh in 2030 and €66/MWh in 2050), D-CAES only charges at an electricity price of 0 EUR/MWh. This results in a very limited number of operational hours, and thus limited revenues. However, the initial investment costs of D-CAES (€352 million) would require a substantial annual profit to realise a positive NPV. Clearly, additional revenue streams are required (e.g. from ancillary services such as grid balancing, redispatch, black start, etc.) and/or investment and operational costs

must decrease. In relation to the latter, the TSO costs (€185 million) for the grid connection are significant and hard to overcome in the business case.

- The price arbitrage-only business case for AA-CAES shows more operational hours than for D-CAES, due to a less severe price spread requirement (€22/MWh in 2030 and €44/MWh in 2050). Revenues are however still not sufficient to realise a positive NPV.
- Both the D-CAES and AA-CAES cases appear to be rather insensitive to the deviations in the sensitivity scenarios. In all scenarios, NPV for D-CAES and AA-CAES remain negative. This means that revenues, or reduced costs, based on a business model that makes use of only volatile electricity prices (arbitrage business model) are not enough to compensate for (extra) CAPEX and OPEX.
- Due to the full load only operation mode, the hourly decision-logic and minimal risk acceptance level, the fill level of both the D-CAES and AA-CAES shows economically suboptimal asset operation. Power discharge occurs as soon as the required marginal price spread is met. Subsequently, the stored energy is sold for the electricity price that generates minimum revenue.
- A CAES system can be utilized by traders on the electricity market and by producers and consumers of electrical power to hedge risks of energy prices. The variety of business models that CAES systems may be able to support are expected to yield different operational revenues and costs. A perspective on a robust positive business case is offered by the following considerations and developments:
  - Additional revenue streams can be generated by considering additional business models that were outside the scope of this study, for example:
    - Offering flexibility to the electricity system (TSO and DSO), e.g. by services like aFRR, mFRR and FCR from TenneT, the Dutch TSO;
    - Offering security of supply by storage of electricity;
    - Combining trades on multiple electricity markets simultaneously
    - Discount the avoided or reduced investments in (public) grid infrastructure by the TSO and DSOs to the CAES system
    - Sales of waste heat generated by the asset (CAES or electrolyser). Waste heat can be used for example in the industry or built environment.
    - Utilizing the CAES systems on lower power output modes may yield additional revenue streams by operating the CAES more flexibly.
  - On the cost side, further reductions may appear possible, for example on the following items:
    - Efficiencies of the assets may turn out to be better than assumed in the business cases, due to further technical development than currently foreseen.
    - CAPEX of the assets may turn out to decrease in the future, due to technical developments and economies of scale.
    - OPEX may decrease, especially for TSO costs. The relatively high connection costs for flexible assets, that are supportive to the energy system, are subject of debate already.

- An increase of renewable energy sources, on top of the scenarios currently foreseen, will favour the business case of flexible storage assets.
- Several recent studies (Heuberger et al., 2017; Guerra et al., 2020; van Hout et al., 2014) show the basis of a positive business case and the importance of co-optimising energy revenues with ancillary services. To be able to conclude on the economic viability and business case of the D-CAES and AA-CAES technology, additional key business models should therefore be assessed in addition to the day-ahead wholesale market business model of this study, based on multi-year stochastic analysis of the variability of renewables feed-in.

#### 2.6.5.2 Future research

Complementary revenue streams are needed to make investments in D-CAES and AA-CAES pay back. Further research should focus on the potential value and business models of the additional revenue stream mentioned above.

## 3 Underground Hydrogen Storage (UHS)

In this chapter, we start in Section 3.1 with a description of the technology options for storage of hydrogen at large scale, above-ground, in tanks and/or the pipeline system, and below-ground, in salt caverns and depleted gasfields. In Section 3.2, we review the deployment status of underground hydrogen storage (UHS) in salt caverns and depleted gasfields. Next, in Section 3.3, we detail the results of a technical performance assessment aimed at quantifying and comparing the differences in performance between hydrogen and methane (as a proxy for natural gas) storage in porous reservoirs and salt caverns. The technical performance parameters that were quantified are the storage capacity, the withdrawal (send-out) rate and the injection (send-in) rate, and we assess their sensitivities to reservoir properties, operational pressures, well diameters, and differences in gas properties. In Section 3.4, we detail the results of a geo- and biochemical modeling study to assess the influence of geo- and biochemical reactions of hydrogen with rocks, fluids and micro-organisms in depleted gas reservoirs in the Dutch subsurface, and the potential risks associated with these interactions, in particular the formation of hazardous and/or corrosive fluids, and the degradation of injection and/or withdrawal performance. Furthermore, the interactions of hydrogen with other gases were investigated, in particular CO<sub>2</sub> and N<sub>2</sub>, to understand if they could potentially be used as a cushion gas instead of hydrogen. In Section 3.5, we present the results and conclusions of an-depth geomechanical assessment of the effects of cyclic injection and withdrawal of air during UHS operation, and the extent to which they affect cavern stability and integrity. Finally, in Section 3.6, we detail the results of an exploratory economic analysis that was done to compare the business case of a continuous hydrogen production asset without storage with that of a flexible hydrogen production asset with storage in a salt cavern.

### 3.1 Technology concept(s)

#### 3.1.1 *Large-scale H<sub>2</sub> storage technologies*

Hydrogen can be stored in compressed gaseous form (at pressures up to 750 bar), in liquid form and in solid form (in chemical compounds that reversibly release hydrogen upon heating). In this project, we are focusing on technologies for large-scale storage of hydrogen, i.e., at volumes of millions to (potentially) billions of m<sup>3</sup> (bcm) to provide flexibility to balance the intermittency of renewables. Available technologies for storing such large volumes of hydrogen are currently limited to:

- **Storage in tanks, in liquid form (above-ground, at cryogenic temperatures)**  
Liquid hydrogen has an energy density of 8,519 MJ/m<sup>3</sup> (at 1 bar and -253 degrees Celsius) which is more than 600 times higher than the same volume of hydrogen at atmospheric (uncompressed) conditions. At the Kennedy Space Center, liquid hydrogen is stored in spherical tanks above-ground with a volume of 3,200 m<sup>3</sup> (850,000 gallons<sup>18</sup>), which equals about 2,5 million m<sup>3</sup> of hydrogen in gaseous form. As such, to store 100 million m<sup>3</sup> of hydrogen in liquid form, 40 tanks would already be required.

---

<sup>18</sup> <https://www.nasa.gov/feature/innovative-liquid-hydrogen-storage-to-support-space-launch-system>

- Line pack storage, in compressed gaseous form

Line pack is a term that refers to the volume of gas that is available within the gas pipeline system itself. By changing the pressure within the pipeline system, the volume of gas that is stored in it changes due to (de-)compression. It is typically used by transmission system operators to balance supply and demand on an hourly basis (intraday). As an example of quantifying the capacity of line pack storage, let us assume that the high-pressure pipeline transmission system of Gasunie (Dutch TSO for gas) is used to transport pure hydrogen. It has a length of about 5,500 km and has pipes with diameters ranging between 24-inch and 36-inch<sup>19</sup>. Although for natural gas the system is operated at pressures between 65 and 80 bar, Gasunie is investigating if a future hydrogen transmission system can be operated at a lower pressure range, i.e., between 30 and 50 bar<sup>20</sup>. If we assume an average diameter of 30" for the pipelines, and use standard<sup>21</sup> m<sup>3</sup> (Sm<sup>3</sup>) to report the volumes, then at 50 bar the volume of H<sub>2</sub> gas stored in that pipeline system would be 115 million Sm<sup>3</sup>, and at 30 bar it would be 70 million Sm<sup>3</sup>, resulting in a working gas volume (the difference between the volume in the system at 30 and 50 bar, respectively) of 45 million Sm<sup>3</sup> of hydrogen. This working gas volume is the storage capacity of the pipeline system. It can be added or removed within the operating boundaries of the system and therefore can be used as a buffer to store and withdraw.

- Underground storage, in compressed gaseous form, in:

- Salt caverns - large cavities in rock salt created by solution mining of salt;
- Depleted gas fields – gas reservoirs from which natural gas has been produced;
- Aquifers – water-bearing porous rock formations that provide a natural trapping mechanism for gases such as hydrogen and methane.

Underground storage is a widely used technology for storing a variety of gases, such as natural gas, hydrogen, helium, air and nitrogen. In particular, underground (natural) gas storage (UGS) is widespread, as it plays an important role in providing flexibility in matching demand and supply at daily to seasonal timescales. In total, about 300 bcm of natural gas is stored underground worldwide (IGU, 2016; see Figure 3.1), the majority of which in depleted fields, salt caverns and aquifers. Other underground storage media, such as abandoned mines and lined hard-rock caverns, are rarely used, especially in Europe, where it accounts for less than 1% of the total working volume (Wallbrecht, 2009).

In The Netherlands, 5 UGS facilities are operational, of which 4 in depleted gas reservoirs (Alkmaar, Bergermeer, Grijpskerk, and Norg), and 1 in salt caverns (Zuidwending). The total storage capacity of these storages amounts to about 14 bcm. Underground hydrogen storage (UHS) is in many ways similar to UGS. In the next subsections, the two most widely used technologies for storing natural gas - storage in salt caverns, and in depleted gas fields - will be described in more detail.

---

<sup>19</sup> <https://www.gasunietransportservices.nl/>

<sup>20</sup> Gasunie statement

<sup>21</sup> Sm<sup>3</sup> : 0°C, 1 atm.

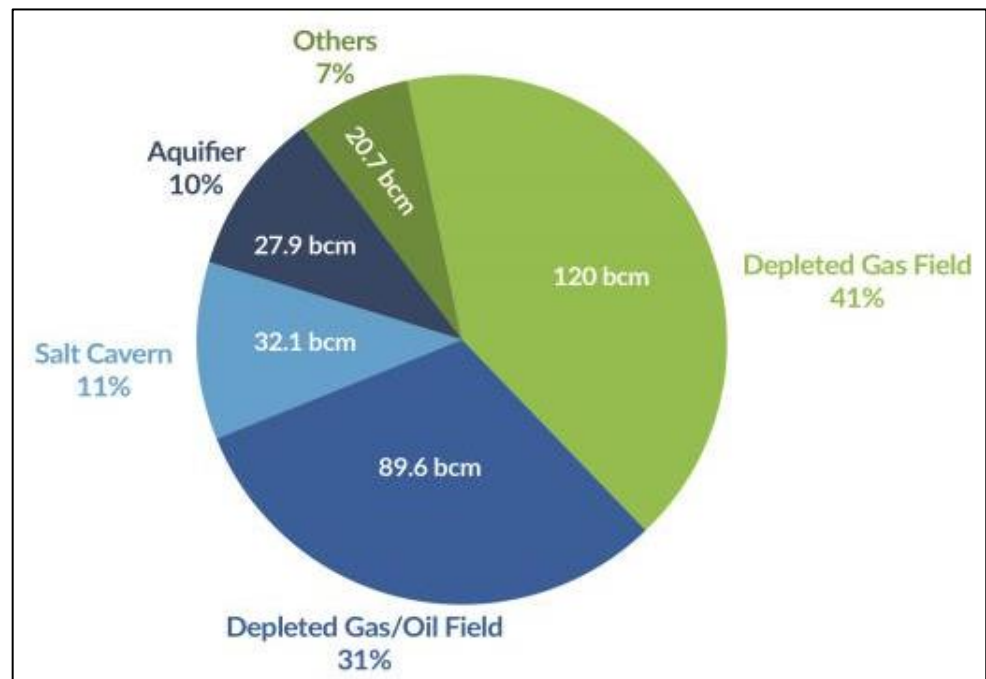


Figure 3.1: Global Gas Storage Capacity (bcm working volume; IGU, 2016).

### 3.1.2 $H_2$ storage in salt caverns

A cavern storage facility for hydrogen consists of one or more salt caverns (or a depleted gas reservoir, see next subsection), wells for injection into and withdrawal from the caverns, pipelines connecting the wells to gas processing facilities above-ground and electrical equipment (see Figure 3.2). Gas processing includes compression, expansion, drying and cleaning. Drying is required because the hydrogen picks up moisture while stored in caverns or porous reservoir, and for this glycol dryers are commonly used. Furthermore, cleaning of the hydrogen is an important step to ensure that the quality of the hydrogen meets the requirements. Quality requirements are very strict for use as chemical feedstock or in fuel cells (electricity generation, mobility), i.e., the hydrogen must be > 99% pure, but less so for use in gas turbines or burners. Pressure swing adsorption is the most widely used technology to purify hydrogen.

At injection, hydrogen flows from the pipelines of the  $H_2$  transportation network (backbone) to the storage facility. The backbone connects production facilities with facilities where hydrogen is consumed (see Figure 3.2). While the pressure level in the backbone will probably be in the range of 30-50 bar<sup>20</sup>, the storage pressures are higher, i.e., in the range of 80-200 bar for salt cavern storage. Additional compression and cooling of the hydrogen is therefore required (to temperatures between 15-40°C), after which it is led via the local pipeline network of the facility to wells through which it is injected into the caverns. At withdrawal, the hydrogen flows through the wells back to the surface, where it is first dried and then cleaned before expanding it. Once it reaches the required specifications (e.g. purity level, pressure, temperature, dew point), the hydrogen can be fed into the backbone again.

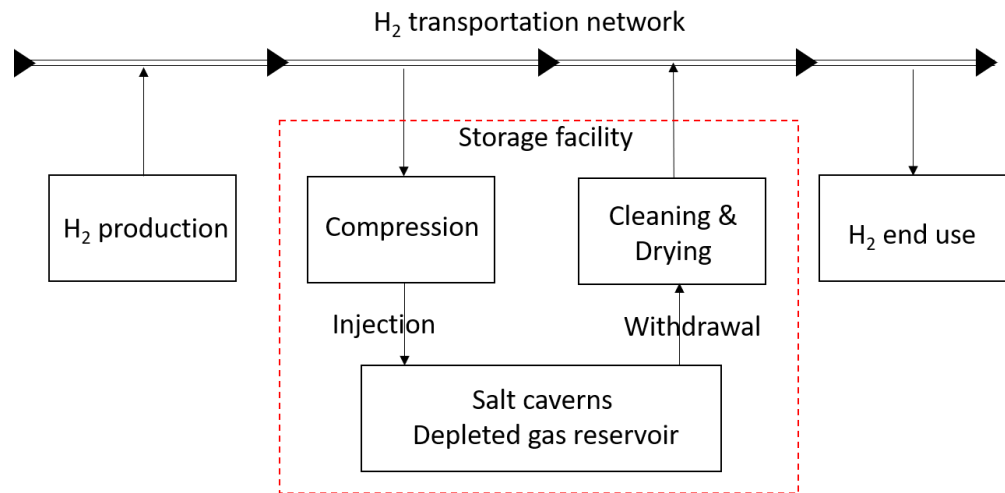


Figure 3.2: Schematic of the main components of an underground hydrogen storage facility.

Apart from the surface facilities, an underground hydrogen storage facility comprises two subsurface components: one or more salt caverns (or a porous reservoir), and wells. For a description of how salt caverns are created and converted for gas storage, and a generic explanation of the design criteria to ensure their geomechanical stability and integrity, the reader is referred to subsection 2.4 where this is explained in the context of another gas - compressed air. In the next paragraph, we focus on the well.

The well connects the above-ground gas processing facilities with the salt caverns (or depleted gas reservoir) in the subsurface (see Figure 3.3).

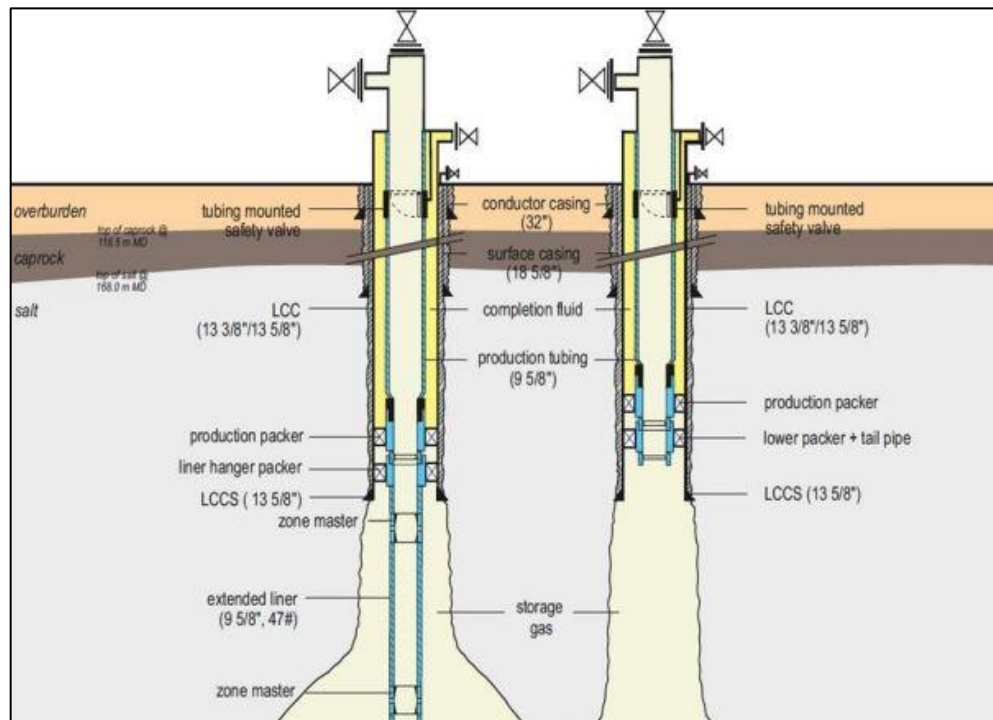


Figure 3.3: Schematic drawing of the design of wells of the gas storage facility in Zuidwending (NL) that can operate very flexible and at high withdrawal rates because it features 2 wells per cavern. LCC: last cemented casing; LCCS: last cemented casing shoe. Units of measure are in inches (EnergyStock, 2017).

Construction of a well starts with a drilling operation whereby a borehole is created from the surface into the salt and to the anticipated depth of the base of the cavern. At regular intervals during the drilling process, sections of thick metal pipe (the “casing”, diameter typically 13<sup>3</sup>/<sub>8</sub>- inch for modern-day salt cavern storage wells, but smaller diameters may be used) are inserted into the borehole from the surface to the anticipated depth of the top of the cavern, and between this casing and the borehole cement is poured. This creates a strong and stable borehole, whereby the cement prevents (upward) fluid flow through the space between the borehole wall and the casing. During the drilling process, the strength of the cement is always verified before moving to the next stage of the drilling process, because it largely determines the gas tightness of the cavern. After the cemented casing is fully in place, it is tested for gas tightness by performing a so-called mechanical integrity test (MIT; EnergyStock, 2017). After a successful gas-tightness test, the well is completed and the well head is placed on top of the well that contains the various valves required to operate it. Inside the casing a fully welded 9<sup>5</sup>/<sub>8</sub>-inch gas production riser, also called tubing, is mounted, through which the gas flows in and out of the cavern.

Typically, in modern-day salt cavern gas storage wells the diameter of the tubing is 9<sup>5</sup>/<sub>8</sub>-inch, but smaller diameters may be used. Optionally, in salt cavern storage wells, an extended liner can be used to have control over the depth at which the gas is withdrawn from the cavern (see Figure 3.3, left well). The tubing is fixed to the metal casing at the bottom of the well with one or multiple production packers. The packer closes the annulus (the space between the tubing and the casing) from the cavern, thereby effectively making the cavern a gas-tight pressure vessel. A nitrogen column (approximately 15 meters) is created on top of this liquid column with a pressure of 15 bar that is continuously monitored to ensure the integrity of the well. Finally, the subsurface safety valve (SSSV; denoted “tubing mounted safety valve in Figure 3.3) is installed and the well head is placed on top. The sole purpose of the SSSV, which can be controlled from the surface, is to close off the well automatically in the event of loss of hydraulic control pressure that would lead to uncontrolled release of the gas from the cavern (a so-called blow-out) (EnergyStock, 2017).

### 3.1.3 *H<sub>2</sub> storage in depleted gasfields*

A depleted gas field is a field from which gas was previously produced. It typically consists of a porous reservoir rock in which the gas was accumulated, and a “seal”, i.e., a layer of rock that is so tight that it prevents the gas from migrating further upward through the subsurface (see Figure 3.4). Because the gas was trapped in the pores of the reservoir rock for millions of years prior to being produced, the reservoir can be considered an effective storage medium for those substances. A third element is the aquifer underneath the reservoir, i.e., the part of the reservoir only filled with saline formation water, which in some cases provides pressure support for the reservoir (HyUnder, 2013).

The system design for hydrogen storage in a depleted field is similar to that of a cavern storage (see Figure 3.2), i.e., a storage container, which in this case is a depleted hydrocarbon reservoir, and wells connecting the reservoir to above-ground facilities for compression, cleaning and drying.

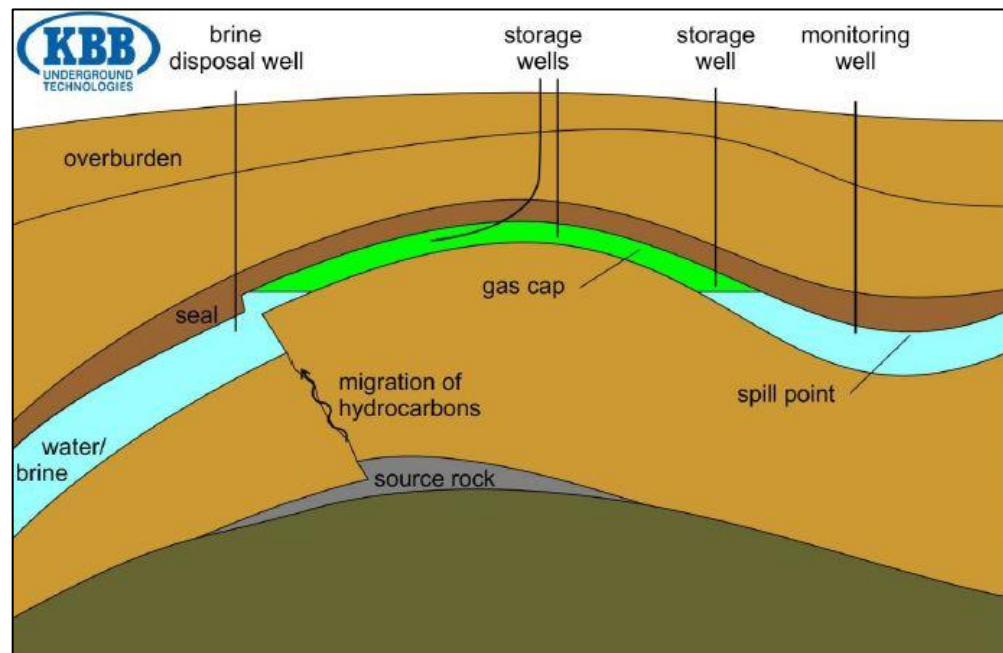


Figure 3.4: Schematic diagram showing the key elements of depleted gas field (HyUnder, 2013)

Storage wells for hydrogen storage in a depleted field will be largely similar in design to cavern storages, but the existing wells that were used for production of the gas may not allow the large diameters that are common for salt cavern storage wells, thus limiting their injection and withdrawal rates. Production wells typically have wellbore diameters of  $9\frac{5}{8}$ " or  $8\frac{3}{8}$ " (casing), in which a production tubing with a diameter of either  $8\frac{1}{2}$ " or  $7\frac{5}{8}$ " is installed (Juez-Larré, 2016). In most cases where depleted fields have been converted to storages, the existing wells are re-used for monitoring purposes, and for injection and withdrawal of the gas new wells are drilled with larger diameters.

## 3.2 Deployment status

### 3.2.1 $H_2$ storage in salt caverns

To date, pure hydrogen has been stored in caverns (3) in Teesside, UK, since 1972 and in caverns near the US Gulf Coast in Texas since 1983 (see Table 3-1 for details).

Table 3-1: Overview of operational hydrogen storage facilities in salt caverns (DBI-GUT, 2017)

| Parameter                                      | Clemens Dome    | Moss Bluff  | Spindletop  | Teesside             |
|--|-----------------|-------------|-------------|----------------------|
| Geology  | Salt diapir     | Salt diapir | Salt diapir | Bedded salt          |
| Operator                                       | Conoco Phillips | Praxair     | Air Liquide | Sabic Petrochemicals |
| Start  | 1983            | 2007        | 2016        | 1972                 |
| Geom. vol. [m <sup>3</sup> ]                   | 580,000         | 566,000     | 906,000     | 3 * 70,000           |
| Avg. depth [m]                                 | 1,000           | 1,200       | 1,340       | 365                  |
| Press. range [bar]                             | 70-137          | 55-152      | 68-202      | 45                   |
| Working vol. [10 <sup>6</sup> m <sup>3</sup> ] | 27.3            | 41.5        | 92.6        | 9.12                 |

Practical experience with these sites has shown that hydrogen can be safely stored in salt caverns for long periods of time. Furthermore, in the 1970s, town gas with hydrogen fractions larger than 50% were successfully stored in reservoirs (depleted fields, aquifers) and salt caverns. No issues (biological and/or chemical degradation, etc.) are reported in literature with respect to storage in salt caverns. Next to these examples, it is important to mention that natural gas has been successfully stored in salt caverns in Europe and USA since the 1970s. The technology of gas storage in salt caverns has been improved continuously over the years to achieve higher safety standards and lower maintenance and operational costs. The experience from the more than 300 salt caverns in Europe utilized for natural gas storages can be largely applied to hydrogen storage projects (HyUnder, 2013).

On account of the fact that four storage facilities are currently operational in the world, hydrogen storage in salt caverns can be considered to be at TRL 9<sup>22</sup> (“*actual system proven in operational environment*”). However, these storages are designed to provide security of supply of feedstock to the chemical industry, where demand profiles are typically very static, reflecting the continuous mode operation of chemical production processes. In contrast, to cancel out supply-demand imbalance caused not only by variations on the demand side but also by large weather-controlled variations in supply, injection and withdrawal are expected to occur much more frequently and cyclically, and at higher volumetric rates. This kind of fast-cycle operation brings with it specific challenges that must be addressed, in particular in relation to the integrity and durability of wellbore materials and interfaces. Hence the TRL must be considered to be lower. Several pilot- and demonstration projects are being prepared in Europe to raise the TRL to 7, one of which in the Netherlands by Energystock (a subsidiary of Gasunie).

<sup>22</sup> "Technology readiness levels (TRL); Extract from Part 19 - Commission Decision C(2014)4995" [https://ec.europa.eu/research/participants/data/ref/h2020/wp/2014\\_2015/annexes/h2020-wp1415-annex-g-trl\\_en.pdf](https://ec.europa.eu/research/participants/data/ref/h2020/wp/2014_2015/annexes/h2020-wp1415-annex-g-trl_en.pdf)

### 3.2.2 *H<sub>2</sub> storage in depleted gasfields*

Hydrogen storage in depleted gasfields is not proven technology, i.e., no sites exist where pure hydrogen is stored. In recent years, several demonstration projects have been executed though where hydrogen was mixed with natural gas and stored in depleted gasfields (see Table 3-2), one in Argentina (Hychico project) and one in Austria (Sun.Storage).

In 2010, Hychico<sup>23</sup> began geological studies to start an Underground Hydrogen Storage in a depleted gas reservoir (depth 850 m) located near its hydrogen production facilities (water electrolysis, 120 Nm<sup>3</sup>/hr hydrogen, 99.9% pure) close to an onshore wind park (6.3 MW). Once permits were obtained, multiple injection and withdrawal cycles were performed with different mixtures of hydrogen and natural gas. Injection flow rates reached 13,000 Nm<sup>3</sup>/day, whereas withdrawal flow rates reached 20,000 Nm<sup>3</sup>/day, at storage pressures in the reservoir of around 30 bar (Pérez, 2016).

A second project, called “Sun.Storage”<sup>24</sup>, ran in Austria between 2013-2017. It successfully demonstrated that hydrogen can be safely injected into, stored and withdrawn from a depleted natural gas reservoir in a mixture with natural gas at percentages of up to 10%. It was found that 82% of the injected hydrogen could be recovered. The rest was not recoverable due to diffusion, solution and conversion to methane. None of these processes were found to have any harmful effects on the reservoir or above ground installations (Sun.Storage, 2017).

Furthermore, in the past, town gas, a gas mixture that consists of methane, hydrogen, carbon-monoxide, carbon-dioxide, nitrogen and gas impurities, was stored in the subsurface in large quantities. Town gas is a refinery product of the coal gasification and was used for the local, urban gas-supply in Europe between the mid-19<sup>th</sup> and mid-20<sup>th</sup> century. Because it contains 50-60% hydrogen, it can be seen as a good equivalent for hydrogen storage (HyUnder, 2013). For decades, town gas storage was done in amongst others depleted gas reservoirs and also aquifers<sup>25</sup>. Examples of sites where town gas was previously stored in aquifers are Lobodice in the Czech Republic and Beynes in France (see Table 3-2, Van Gessel et al., 2018). In Lobodice, experience showed that after a few months of storage about half of the hydrogen was converted to methane, which was explained by biodegradation of hydrogen reacting with CO and CO<sub>2</sub> to methane (Panfilov, 2010).

Table 3-2: Overview of gas storage sites and demonstration projects with co-mixing of hydrogen with natural gas (Van Gessel et al., 2018)

| Location         | Geology   | Start | Status    | H <sub>2</sub> [%] | Depth [m] | Pressure [bar] |
|------------------|-----------|-------|-----------|--------------------|-----------|----------------|
| Ketzin (GE)      | Aquifer   | -     | Abandoned | 62                 | 200-250   | -              |
| Kiel (GE)        | Cavern    | -     | Storage   | 62                 | -         | 80-100         |
| Beynes (FR)      | Aquifer   | 1956  | Storage   | 50                 | 430       | -              |
| Lobodice (CZ)    | Aquifer   | 1965  | Active    | 50                 | 430       | 90             |
| Hychico (ARG)    | Gas field | 2010  | Finished  | 10                 | 800       | 30             |
| Sun.Storage (AT) | Gas field | 2015  | Finished  | 10                 | 1000      | 78             |

<sup>23</sup> <http://www.hychico.com.ar/eng/underground-hydrogen-storage.html>

<sup>24</sup> <https://www.underground-sun-storage.at/en.html>

<sup>25</sup> An underground layer of water-bearing permeable rock, rock fractures or unconsolidated materials (gravel, sand, or silt)

### 3.3 Technical performance analysis of underground H<sub>2</sub> storage

This section presents the results of an exploratory study to quantify the technical performance of underground hydrogen storage (UHS). While the technical performance of underground (natural) gas storage (UGS) is well-understood from decades of experience this is not the case for UHS. In this study we address this knowledge gap by investigating, quantifying and comparing the differences in performance between hydrogen and natural gas storage in porous reservoirs and salt caverns. To simplify the comparison, methane is used as a proxy for natural gas. The technical performance parameters analyzed are the storage capacity, the withdrawal (send-out) rate and the injection (send-in) rate. Variations in reservoir properties, operational pressures, well diameters, and differences in gas properties are assessed. For this purpose, we performed case studies of three currently operational UGS in porous reservoirs in the Netherlands (Grijpskerk, Norg, Alkmaar), and one UGS in salt caverns (Zuidwending). This allows us to validate our model predictions on natural gas, and investigate the factors determining the performance of these underground gas storages in case they would be (re)developed as UHS.

#### 3.3.1 Methodology and case studies

In this study we used the combination of the analytical Inflow Performance Relationship (IPR) (Vogel, 1968) and the Vertical Flow Performances (VFP) (outflow) methodologies to estimate the reservoir and well performances. The simplicity and reliability of these methodologies led to its widespread use throughout the oil and gas industry, becoming a standard practice in conventional reservoir engineering studies. IPR allows estimating the gas flow performances from an underground reservoir into the bottom-hole (inflow), and the VFP the flow from the bottom-hole to the surface (outflow). The inflow performance uses the Forchheimer equation (1901) to compute the Darcy and non-Darcy pseudo-steady state radial flow mass of a compressible dry gas in a porous medium. The flow equation uses pseudo-pressures to include the effects of changes in gas compressibility and viscosity due to pressure and temperature changes. The outflow performance calculations are based on a lift table equation including the effects of gravity, turbulent flow and friction of a gas along a production or injection well (Lingen, 1974). Along the well we assumed adiabatic conditions (no heat exchange). The intersection between the inflow and outflow curves gives the maximum initial withdrawal (send-out) or injection (send-in) rates. These rates are the maximum theoretical rates for a given gas and reservoir type, reservoir pressure, well (tubing) diameter and wellhead pressure, among others.

Figure 3.5 shows examples of two inflow and outflow curves for hydrogen (blue) and methane (green) for a reservoir pressure at 393 bar and a wellhead pressure of 1 bar. The solid and dashed lines of the same color show the relation between the inflow and outflow rates and the bottom-hole pressures. The intersection between the inflow and outflow curves gives the maximum theoretical initial withdrawal rate and corresponding bottom-hole pressure, which can be read on the X- and Y-axis. If the wellhead pressure is kept constant, the reservoir pressure (solid line) would decrease with time, and as a result the intersection point would move down along the outflow curve (dashed line) until reaching a given cut-off rate. At that rate (X-axis) the bottom-hole pressure can be read again in the Y-axis. This pressure together with the flow cut-off rate, are used to calculate the average reservoir pressure and working volume, using the Forchheimer and mass-balance equation.

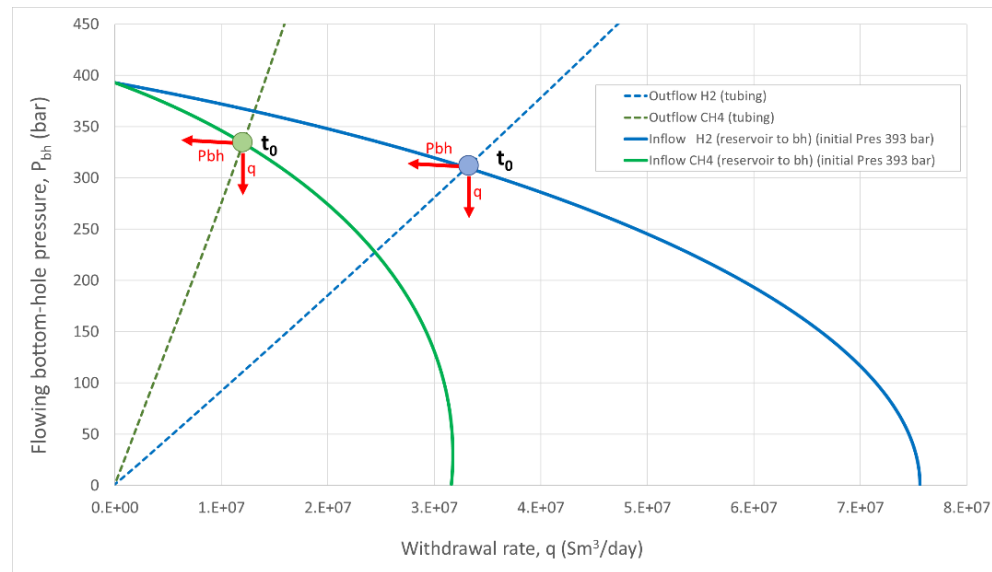


Figure 3.5 Hydrogen and methane inflow and outflow curves for the withdrawal scenarios with initial reservoir pressures at 393 bar for the case of the Grijpskerk UGS. For each gas type the outflow curves for a 7-inch tubing (ID), with a wellhead pressure of 1 bar, is also shown. The intersection between the inflow and outflow curves indicates the maximum theoretical withdrawal rate (X-axis) and corresponding bottom-hole pressure (Y-axis).

The minimum working pressure at which the gas must be stored in the reservoir is determined by the minimum withdrawal performance (send-out) expected for the wells -or well-clusters- designed for the storage facility. On the other hand, the maximum working pressure is limited by the rock geomechanics, technical and economic considerations, either because it would exceed the initial reservoir pressure of the natural depleted gas field, or because injecting gas into the reservoir at higher working pressures would require an much too expensive topside compression facility. The difference between the maximum and minimum pressures is the working pressure range, and effectively determines how much gas can be used from the total volume of gas in the reservoir. Hereafter we refer to this volume as the “working gas volume (wv)”. The gas that must remain in the reservoir at all times to maintain the minimum working pressure is known as “cushion gas volume (cv)”. This volume only provides pressure support. Further details on the basics of the inflow/outflow methodology can be found in Juez-Larré et al. (2016). In this article they described, used and tested the inflow/outflow methodology to estimate the performance of potential candidates for underground natural gas storages (UGS) in the Netherlands.

In this study we implemented the Inflow performance Relationship (IPR) (Vogel, 1968) and the vertical flow performances (VFP) (outflow) nodal analysis in a built-in-house Gas Storage Performance tool (GaSP) written in Python. The GaSP-tool allows to generate the inflow and outflow performance curves for a particular reservoir. In this GaSP-tool While the reservoir properties determine the reservoir input parameters, the user is free to define the well configuration (tubing diameter, length, roughness, etc.) and wellhead pressure. The tool incorporates a link to the CoolProp library (Bell et al., 2014), which is an open-source fluid/gas properties database used to calculate the PVT gas properties needed for the inflow/outflow curves. At present the GaSP-tool works with any single gas composition, yet in the

future a binary gas mixtures module will be added to allow simulating gas mixtures such as that of hydrogen and methane. For withdrawal operations the gas temperature is assumed to be equal to that of the reservoir, while for injection the gas temperature is a user-defined parameter. Besides the flow performances defined above, our GaSP-tool also allows the calculations of other parameters such as the maximum plateau rate ( $Q_p$ ), working volume (wv), erosional velocity ( $v_e$ ) and bottom-hole drawdown ( $BH_{dd}$ ), which we describe next. These are important parameters to characterize the performances of an UHS.

1. Plateau rate (withdrawal): A gas storage could only operate at the maximum theoretical withdrawal rate for a short period of time, after which it would decline due to the decrease in pressure in the reservoir. In practice gas storages operate at what is known as a “plateau rate”. The plateau rate is lower than the maximum theoretical rate therefore it can be kept constant for a given period of time from days up to a few months. Based on the maximum theoretical withdrawal rate, the Gas-Initially-In-Place and a given plateau duration, the maximum plateau rate can be calculated as follows (eq. 1):

$$Q_p = \frac{1}{\left(\frac{1}{Q_{ini}}\right) + \left(\frac{T_p}{GIIP}\right)}$$

This equation is the intersection between the mass balance equation (eq. 2):

$$Q_p = Q_{ini} \left(1 - \frac{G_p}{GIIP}\right)$$

and the given plateau rate (eq. 3):  $G_p = Q_p \cdot T_p$

where ( $Q_p$ ) is the plateau production rate ( $\text{Sm}^3/\text{day}$ ); ( $Q_{ini}$ ) is the maximum theoretical withdrawal rate ( $\text{Sm}^3/\text{day}$ ); ( $T_p$ ) is the number of days of plateau production (days); ( $GIIP$ ) the Gas-Initially-In-place ( $\text{Sm}^3$ ) is the gas contained in the reservoir at maximum working pressure; ( $G_p$ ) Plateau cumulative production ( $\text{Sm}^3$ ).

2. Storage capacity (working gas volume and cushion gas volume): The working gas volume is the fraction of gas that can be technically withdrawn from an underground reservoir while any well would be producing above a given cut-off rate. Based on the user-defined cut-off rate, the GaSP-tool calculates the corresponding final average reservoir pressure and volume withdrawn (working volume), using the mass balance equation (eq. 4).

$$G_p = \left(1 - \left(\frac{P_f * Z_i}{P_i * Z_f}\right)\right) * GIIP$$

where ( $G_p$ ) is cumulative production (working volume); ( $P_i$  and  $P_f$ ) average reservoir pressure at initial and cut-off withdrawal rate and corresponding Z-factors ( $Z_i$  and  $Z_f$ ); ( $GIIP$ ) Gas-Initially-In-Place at maximum working pressure. The  $GIIP$  minus the estimated working gas volume gives the cushion gas volume.

3. Erosional velocity and flow velocity profile along the production tubing: Based on the principle of mass conservation, the velocity of a gas flowing along a tubing increases as the density decreases as a result of the pressure drop. This is why the largest velocities in a tubing are reached at the wellhead during withdrawal, and at the bottom-hole during injection. In order to limit erosion-induced corrosion of the production/injection tubing and preserve its integrity, a certain threshold flow velocity, known as erosional velocity ( $v_e$ ), should not be exceeded (Madani Sani et al., 2019). This is an important issue we addressed in this study since it could limit the maximum theoretical flow rate we estimate for a single well. It is for that reason that for each run our GaSP-tool generates a gas velocity profile along the well (tubing). The  $V_e$  is calculated based on the average density ( $\rho_m$ ) of the gas/liquid flowing through the tubing and a constant variable (c-factor) (eq. 5):

$$V_e = \frac{c}{\sqrt{\rho_m}}$$

The use of this equation is a common practice amongst many oil and gas operators to limit erosion-corrosion of the mild steel lines and equipment used for production/injection operations. This is because of its simplicity and the little inputs required. However, this equation does not consider two important scenarios. First, the presence of solid particles in the gas/fluid, and second, the simultaneous occurrence of erosion and corrosion (Madani Sani et al., 2019). Sometimes test sites are used to adjust the empirical c-factor and based on that the erosional velocity for a field or a cluster of fields is determined. Despite all these uncertainties, many operators tend to use the most conservative value of 100 m/s to prevent the occurrence of erosion-corrosion (personal communication Stefan Belfroid, TNO-Delft). Based on this value we calculated the maximum flow velocities for 7- and 9-inch (inner diameter, ID) tubings used in conventional underground natural gas storages, and for comparison, also for 3- and 5-inch (ID) tubings in conventional natural gas fields. Figure 3.6 shows the  $V_e$  thresholds during withdrawal for these four tubing diameters for pure hydrogen and methane for a large range of wellhead pressures (1-400 bar).

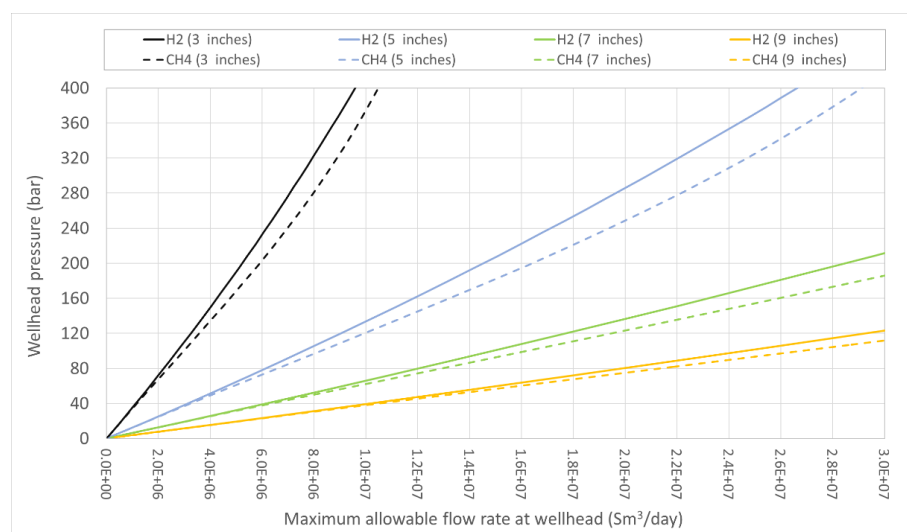


Figure 3.6: Wellhead pressure versus maximum allowable flow rate (in standard m<sup>3</sup>, Sm<sup>3</sup>) based on the 100 m/s Threshold for the erosional velocity in 3, 5, 7 and 9-inch (ID) tubings.

4. Maximum bottom-hole drawdown (wellbore - bottom-hole): Excessive drawdown (pressure drop) between the reservoir and the bottom-hole can easily lead to irreversible mechanical skin damage in the wellbore during withdrawal and/or injection operations. This damage to the rock formation can significantly reduce the reservoir permeability, causing a decrease in the well performance. The threshold for bottom-hole drawdown is determined by many factors such as petrophysical properties, fluid properties, degree of formation damage, well geometry and completion (Yildiz et al., 2006). Our GaSP-tool incorporates a user-defined threshold parameter to limit the maximum allowable bottom-hole drawdown for withdrawal and injection operations. Similar to the erosional velocity, the bottom-hole drawdown is the other important factor that can significantly limit the operational performances of a well in an underground gas storage. For this reason this factor is also considered for discussion in this study.

### 3.3.2 Input parameters

We investigate the performances of three of the four UGS in the Netherlands. The UGS of Norg, Grijskerk and Alkmaar currently provide flexibility to balance fluctuations in natural gas supply and demand, thereby substituting the swing production capacity of the giant Groningen gas field (Juez-Larré et al., 2019). Each of these reservoirs correspond to a distinct reservoir with different properties, volumes and depths (see Table 3-3). There is a fourth UGS called Bergermeer. This storage facility is mostly used for international natural gas trading and therefore it was not included in this study. In order to investigate the difference in reservoir and well performances we used two end-members gas types: pure methane and pure hydrogen. We used methane as proxy for natural gas, since it usually contains 80 to 90% of methane.

Table 3-3: Gas, reservoir and well input parameters used for the inflow/outflow calculations. (\*) Parameter assumed, (\*\*) Parameter calculated and (\*\*\*) Standard values taken from operational UGS. Note that we refer to “Sm<sup>3</sup>” as the International Standard Metric Conditions at 15°C and 1.01325 bar.

| Parameters   |                         | Grijskerk   | Norg            | Alkmaar         |
|--|-------------------------|---|-----------------|-----------------|
| <b>GAS</b>   |                         |   |                 |                 |
| Type gas (dry*) / flow*  | -                       | Pure hydrogen or methane / radial flow  |                 |                 |
| Type gas (energy contents)   | -                       | H <sub>2</sub> : 10.2 MJ/Sm <sup>3</sup> (LHV); CH <sub>4</sub> : 37.5 MJ/Sm <sup>3</sup> |                 |                 |
| Type storage operation   | -                       | Withdrawal (send-out) or injection (send-in)  |                 |                 |
| <b>RESERVOIR</b>   |                         |   |                 |                 |
| Reservoir formation  | -                       | Rotliegend Sst.   | Rotliegend Sst. | Zechstein Carb. |
| Reservoir depth (mid res. thickness)                                 | m TVD                   | 3420  | 2895            | 2125            |
| Gas-Initially-In-Place (GIIPvol)(CH <sub>4</sub> /H <sub>2</sub> **) | billion Sm <sup>3</sup> | 10.8/9.9  | 29.4/24.7       | 3.8/3.2         |
| Initial reservoir pressure   | bar                     | 393   | 327             | 218             |
| Expansion factor ratio (CH <sub>4</sub> /H <sub>2</sub> )**          | -                       | 0.92  | 0.84            | 0.84            |
| Initial reservoir temperature  | °C                      | 117   | 100             | 83              |
| Reservoir permeability (avg.)  | mD                      | 25  | 176             | 34              |
| Reservoir thickness (average)  | m                       | 180   | 150             | 50              |
| Type reservoir   | -                       | Single layer (implicit in the inflow equation)  |                 |                 |
| Fraction reservoir perforated*                                       | fraction                | 1 (full reservoir perforation)  |                 |                 |
| Drainage radius*   | m                       | 1500  |                 |                 |
| Dietz reservoir shape factor*  | -                       | 31.62 (circular reservoir with a centered well)   |                 |                 |
| <b>WELLBORE &amp; WELL***</b>  |                         |   |                 |                 |
| Tubing length (mid-res.depth)  | m TVD                   | 3420  | 2895            | 2125            |
| Tubing internal diameter (ID)*                                       | inches                  | 7 and 9 (Note: outer diameter equals to 7 <sup>5/8</sup> and 9 <sup>5/8</sup> )           |                 |                 |
| Angle production tubing*   | degrees                 | 0° (vertical)   |                 |                 |
| Production tubing roughness*   | m                       | 0.00005   |                 |                 |
| Wellbore radius*   | inches                  | 8 <sup>3/8</sup> (+2" for the case with a 9 <sup>5/8</sup> -inch tubing)                  |                 |                 |
| Mechanical skin (damage) factor*                                     | -                       | +1  |                 |                 |
| Beta (Kinetic factor)  | 1/m                     | 4.1e11 (from Friedel and Voigt, 2006)   |                 |                 |
| Wellhead pressure*   | bar                     | 1 up to the reported initial reservoir pressure (when possible)                           |                 |                 |
| Cut-off rate*  | mlnSm <sup>3</sup> /d   | 1   |                 |                 |

In order to compare differences in withdrawal and injection performances for a single well with no interferences, we used the same well configuration for all three reservoirs investigated. Besides the length of the tubing, which depends on the mid-depth reservoir, the rest of the wellbore and well parameters we used were taken from standard UGS wells in the Netherlands. We chose the Grijpskerk-UGS as a reference storage to carry out more detail sensitivity analyses. Grijpskerk is a smaller gas buffer relative to Norg, but larger than the Alkmaar peak-shaver storage. Table 3-3 shows the different reservoir parameters we used for each storage, as well as the parameters assumed for the inflow/outflow calculations.

### 3.3.3 Validation GaSP-tool

We validated the test results from our inflow/outflow calculations against two different petroleum engineering software. For the inflow curve we used the Saphir software from Kappa Company. This software contains an IPR module to generate inflow performance curves. Similarly, for the outflow curve we compared our results with those from the dynamic multiphase flow simulator OLGA from Schlumberger. In both cases we obtained a very good match for hydrogen and methane. We also validated our inflow/outflow estimates on performances against real production data. For that we try to reproduce the maximum realized withdrawal rates from a single well, and the reported working volume, for each of the three UGS case studies. We obtained data on the working volumes and withdrawal and injection rates from public documents ([www.nlog.nl](http://www.nlog.nl)) and the operator NAM (see Table 3-4). For the reservoir properties, and some details on the well configuration, we used average values also reported by the operator in the production licenses applications (see Table 3-3). Unfortunately we had no detailed information on some key operational parameters such as the wellhead pressures corresponding to the maximum withdrawal rates, and the lowest reservoir pressure related to the cushion volume. For that we ran several scenarios covering the large range of possible wellhead pressures.

As previously mentioned we used pure methane as a proxy for natural gas. High or low calorific natural gas contains large amounts of methane of about 89% and 81% (mole %), respectively. Juez-Larré et al. (2016) shows that slight changes in the natural gas composition have limited effect on the withdrawal rates. Pure methane gives withdrawal rates that are less than 5% and 10% higher than those from high and low calorific natural gas, respectively.

Table 3-4: Reported performances of the three UGS in the Netherlands from public production licenses applications and operator NAM. Indicator “(n.a.)” is used when rates not available or further analysis is required to generate a good estimate.

| UGS (natural gas)                                   |                         | Grijpskerk     | Norg            | Alkmaar           |
|---|-------------------------|----------------|-----------------|-------------------|
| Maximum realized single well injection rate (year)  | mIn Sm <sup>3</sup> /d  | ~5.5<br>(2013) | ~9.0<br>(2019)  | n.a.              |
| Maximum realized single well withdrawal rate (year) | mIn Sm <sup>3</sup> /d  | ~8.5<br>(2007) | ~12.5<br>(2015) | ~4.0<br>(average) |
| Working Gas Volume (WGV)                            | billion Sm <sup>3</sup> | ~2.5           | ~6.3            | ~0.6              |
| GIIP*- WGV = Cushion gas volume                     | billion Sm <sup>3</sup> | ~8.3           | ~23.0           | ~3.3              |

Our estimates on the withdrawal rates for a single well (7-inch ID), and the corresponding wellhead pressures and bottom-hole drawdowns, are depicted in the Figure 3.7. In case the reservoirs would be at full capacity, our results show that in order to reproduce the maximum withdrawal realized (see Table 3-4), bottom-hole drawdowns had to be between 9 and 67 bar. The lowest bottom-hole drawdowns

being for the high permeability reservoir in Norg (9 bar) and Grijskerk (39 bar), and the highest bottom-hole drawdown of 67 bar for the low permeability reservoir in Alkmaar. Lower reservoir pressures would require higher bottom-hole drawdowns to reach the high withdrawal rates realized, as we show in Figure 3.7 for the case of Grijskerk. For injection in Grijskerk, and as we will discuss later, we estimated a range of bottom-hole build-ups between 9 and 36 bar for the maximum realized rate of 5.5 mln Sm<sup>3</sup>/day. This is considering reservoir pressures of 350 and 50 bar, respectively (Figure 3.17).

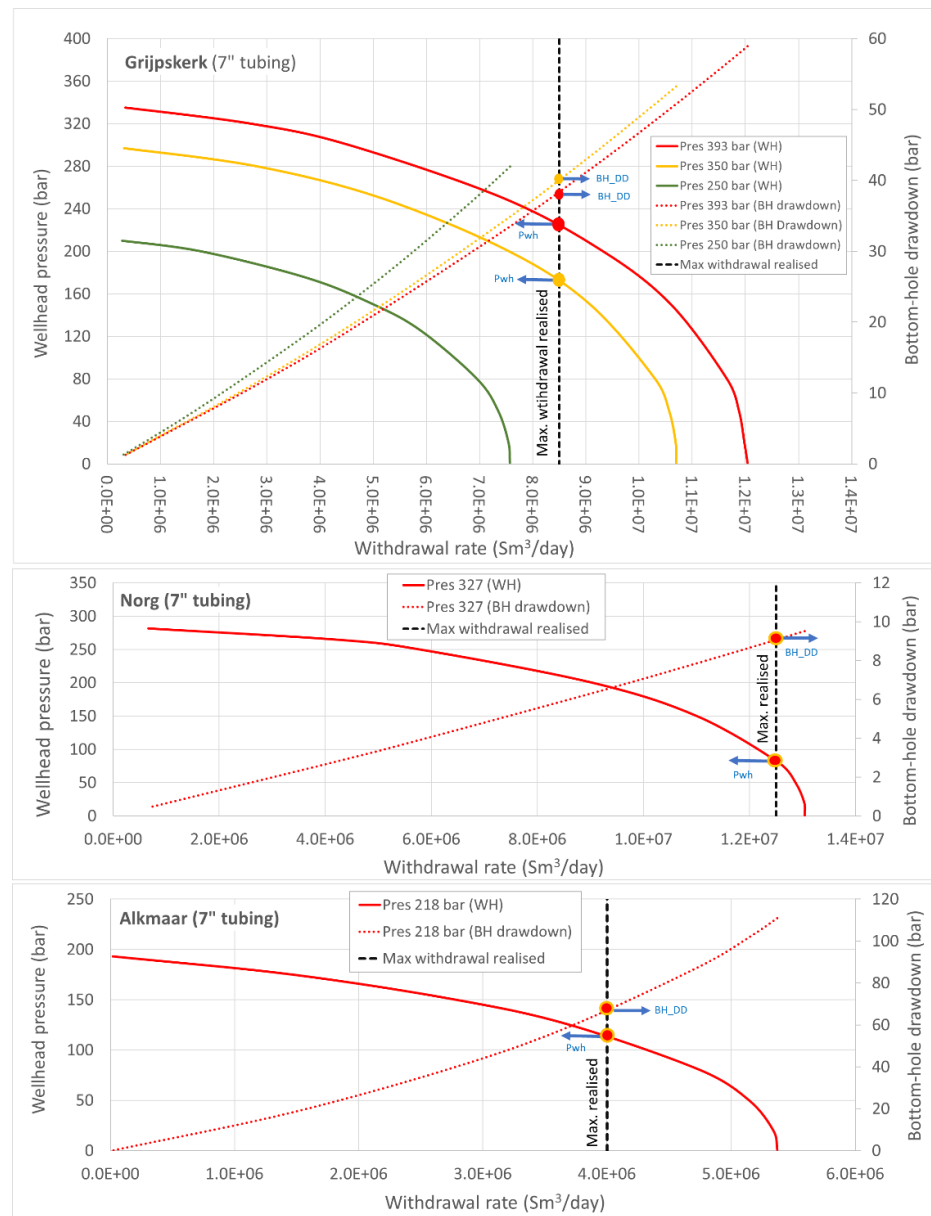


Figure 3.7: Grijskerk, Norg and Alkmaar maximum theoretical withdrawal performances versus wellhead and bottom-hole drawdown. The maximum ever realized withdrawal rate reported for a single well is depicted as a vertical black dashed line. In the case of Grijskerk three cases with different reservoir pressures are depicted for withdrawal operations at reservoir pressures from 393 bar (full), 350 bar and 250 bar. For Norg and Alkmaar only one scenario with maximum initial working reservoir pressure is shown. A 7-inch (ID) production tubing was used for all calculations since the maximum realized withdrawal rates occurred after these three fields were converted to UGS.

The range of bottom-hole drawdowns we obtain for withdrawal and injection operations falls within the common range of pressures reported for underground gas storage and conventional natural gas fields. Gas wells are often not operated to their full capacity in order to avoid any significant mechanical damage around the wellbore. Instead, the upgrade of the production or injection capacity is generally obtained by drilling additional wells. This is particularly important for UGS where the wellbore have to endure many withdrawal/injection cycles during the its life-span.

Despite we do not have precise operational data on the pressure variation in the reservoir during withdrawal and injection, we could reproduce the working volume of 2.5, 6.3 and 0.6 bcm ( $\text{Sm}^3$ ) for Grijpskerk, Norg and Alkmaar with reasonable average minimum working pressures in the reservoir of 278, 243 and 184 bar, respectively (Figure 3.15, Figure 3.21 and Figure 3.23).

#### 3.3.4 *Results performance analysis Grijpskerk, Alkmaar and Norg*

In this section we present the results of the inflow and outflow nodal analyses we carried out for the three UGS of Grijpskerk, Norg and Alkmaar. The results show how these three storages would perform in case they were to be (re)developed as UHS. Here we focus on quantifying withdrawal and injection performances and the storage capacity (working volume) for a range of operational wellheads and reservoir pressures. Results on pure hydrogen are compared to those of pure methane. It is important to understand that the withdrawal and injection rates we calculated here are those of a single well, with no interference from other nearby wells. In practice pore storages have multiple wells and the best placement of the well clusters -with the least interferences- is commonly determined by numerical modelling optimization. Despite all, our results on single-well performances can be used to rank portfolios of reservoirs, and to easily estimate the approximate number of wells that may be needed to reach a given withdrawal and injection performance.

Based on each reservoir maximum working pressure, and assuming a large range of constant wellhead pressures, we also estimated the array of potential working volumes for all three reservoirs. Each working volume -associated to a constant wellhead pressure- was calculated based on the average final reservoir pressure at the time a single-well withdrawal rate would drop below a given cut-off rate. For this study we chose a cut-off rate of 1 mln  $\text{Sm}^3/\text{day}$  of hydrogen and methane, since we considered to be a reasonable minimum performance for a single well. One million  $\text{Sm}^3$  per day of hydrogen and methane is equivalent to an energy throughput of 3 and 10 GWh/day, respectively. Based on this cut-off rate (and corresponding final average reservoir pressure) each working volume we estimated is the “ultimate storage volume”, and could not be increased by the placement of more wells. For each scenario, we also calculated the hydrogen working volume based on the minimum working pressure reported for each of the three underground natural gas storages.

The only way to increase the working volume is to increase the range between the maximum and minimum pressure. The initial reservoir pressures we used for our calculations were the reservoir pressures at the time of discovery: Grijpskerk (393 bar), Norg (327 bar) and Alkmaar (218 bar) (see Table 3-3). We did not consider the use of higher pressures since it would require a geo-mechanical study to ensure the reservoir integrity and avoid fracking and induced seismicity. Based on the historical

withdrawal and injection volumes, we estimated that at least for Grijpskerk en Norg these original pressures are the maximum pressure used for its operation as UGS.

For the case of Grijpskerk we carried out a more in depth analysis to better understand the differences in performances between hydrogen and methane. For that we ran different scenarios with different initial reservoir pressures. For each scenario we investigate the differences in flow performances and working volumes, as well as important issues regarding reservoir and well integrity such as the bottom-hole drawdown and the erosional velocity. Due to the lower energy contents of hydrogen, 3-4 times lower than that of methane, we show the results of flow performances and working volume not only in terms of volume ( $\text{Sm}^3$  and  $\text{Sm}^3/\text{day}$ ), but also in terms of thermal energy ( $\text{TWh}_t$  and  $\text{GWh}_t/\text{day}$ ). Note that for our results we refer to “ $\text{Sm}^3$ ” as the International Standard Metric Conditions at  $15^\circ\text{C}$  and 1.01325 bar. The calorific values we used for pure hydrogen and pure methane are  $10.2 \text{ MJ}/\text{Sm}^3$  and  $37.5 \text{ MJ}/\text{Sm}^3$ , respectively. The reservoir and well input parameters we used for our inflow/outflow calculations are listed in Table 3-3.

#### 3.3.4.1 Results Grijpskerk (GRK)

The Grijpskerk UGS consists of a reservoir made of well-sorted upper Permian eolian sandstone. The reservoir has an average permeability of 25 mD and thickness of around 180 m, and is located at a depth of 3420 m TVD. The GIIP reported for this reservoir is 10.8 bcm ( $\text{Sm}^3$ ) of natural gas at 393 bar and  $117^\circ\text{C}$  (see Table 3-3). The currently reported working volume for natural gas in Grijpskerk is 2.5 bcm (see Table 3-4). This is about 25% of the GIIP. Based on historical production and injection data we estimate that since the start of the UGS operations in Grijpskerk the average reservoir pressures have been fluctuating between the initial pressure of 393 bar and 200-250 bar.

In order to investigate the withdrawal and injection performance we used a standard 7-inch (ID) well (see Table 3-3), and a large range of initial reservoir pressures (393 to 50 bar) and wellhead pressures (393 to 1 bar). For the working volume we ran two scenarios with two initial reservoir pressures one at 393 bar, simulating a full reservoir, and a second one at 250 bar representing a half full reservoir. This second scenario was ran to investigate the working gas to cushion gas volume ratio (wv:cv), since for a UHS filling the reservoir to its maximum working pressure represents a high CAPEX. For both scenarios we estimated the working volume of pure methane and pure hydrogen for different degrees of reservoir pressure depletion, by again assuming a large range of constant wellhead pressures and considering a cut-off rate of  $1 \text{ mln Sm}^3/\text{day}$ . Next we present the inflow/outflow results for Grijpskerk in the following order: i) withdrawal performances, ii) drawdown and erosional velocities limitations, iii) working volumes and iv) injection performances.

##### ***Withdrawal rates - GRK***

Our inflow/outflow results provide estimates on withdrawal rates that allow us to quantify and compare the differences in well performances between hydrogen and methane at different reservoir pressures and wellhead pressures. We calculated the maximum initial theoretical withdrawal (send-out) rates for a large range of initial pressure of 393, 350, 250, 150 and 50 bar.

In general we find withdrawal rates of hydrogen to be much higher than those of methane, especially for higher reservoir pressures. This high rates are associated to higher wellhead pressures, which means lower drawdowns (Figure 3.8a). On average withdrawal rates for hydrogen are 2.4-2.7 times higher (Figure 3.9a), which although significant, they only deliver 0.7-0.8 of the energy of that of pure methane (Figure 3.9b). This is due to the 3-4 times lower energy content of hydrogen. The higher withdrawal rates we observe for hydrogen are due to its lower density and viscosity, which significantly reduces the hydrostatic pressure in the tubing and the non-Darcy flow component in the Forchheimer equation. For the pressure range we considered for Grijpskerk, hydrogen has a much lower density (8-10 times) and viscosity (1.3-3.0 times) than that of methane.

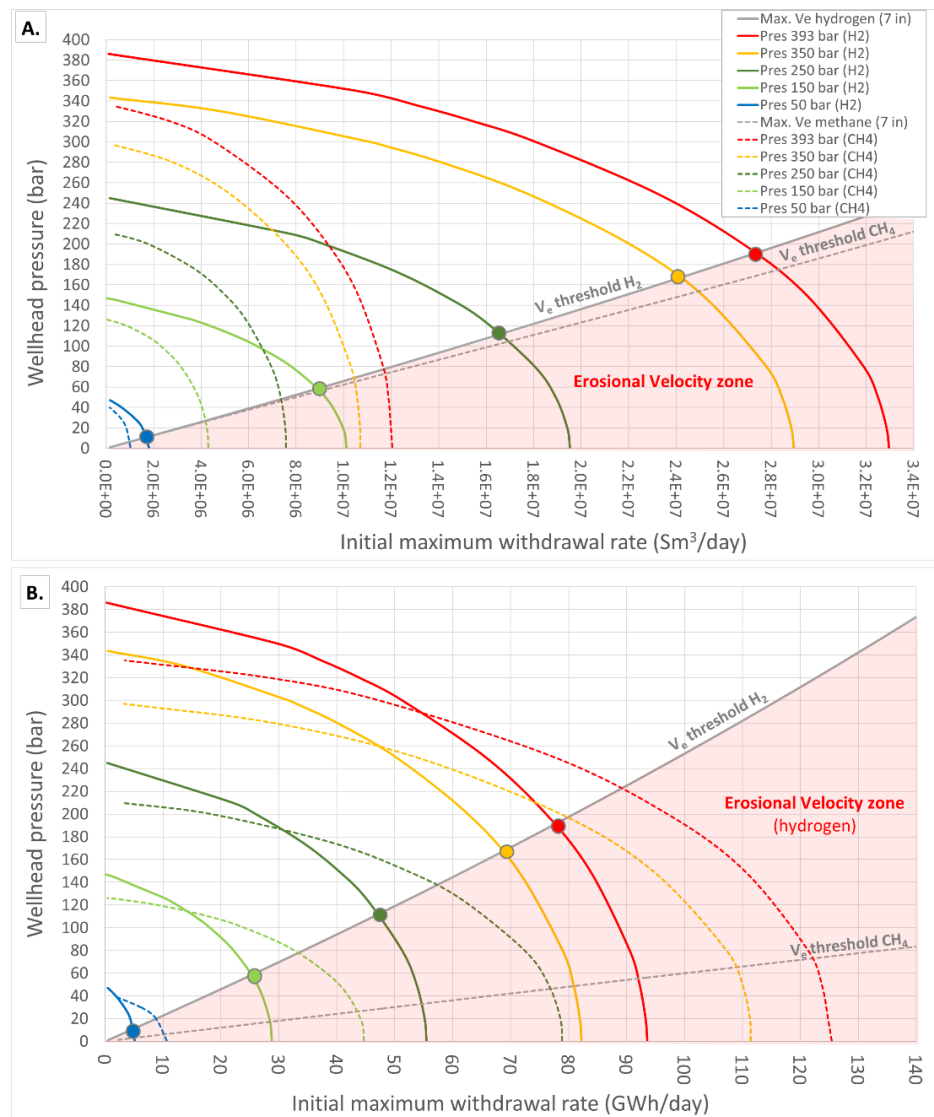


Figure 3.8: (A) Hydrogen and methane withdrawal rate (single well) versus wellhead pressures for five initial reservoir pressure for the case of a 7-inch (ID) production tubing fully perforated in the Grijpskerk reservoir. (B) Same as (A) yet in energy flow rate units (GWh). For the conversion from methane volumetric to energy flow rate we used a calorific value of 37.5 MJ/Sm<sup>3</sup> and for hydrogen a 120 MJ/kg and a density of 0.0852 kg/Sm<sup>3</sup> (International standard conditions of 15°C and 1.01325 bar). The colored dots indicate the intersection between the withdrawal rate for each reservoir pressure scenario and the Ve-threshold. The red shaded zone indicates the zone where erosion-corrosion of the production tubing may take place (see Figure 3.6).

We observed that for a given reservoir pressure, it is only at high wellhead pressures (i.e. low drawdowns) that hydrogen delivers larger amounts of energy (Figure 3.9a). This occurs when high wellhead pressure results in a too low bottom-hole drawdown that is insufficient to drive the heavier methane from the reservoir to the wellhead (Figure 3.9c, d). This leads to a drastic reduction of the withdrawal rates, and energy throughput, ratio of methane relative to hydrogen. In the case of Grijskerk this seems to occur when the bottom-hole drawdown (between reservoir and bottom-hole) drops below ~10 bar limiting the flow of methane (Figure 3.9d). Meanwhile with the same wellhead pressures the bottom-hole drawdown for hydrogen remains higher around 20 to 30 bar, allowing the less dens hydrogen to keep flowing to the wellhead (Figure 3.9c).

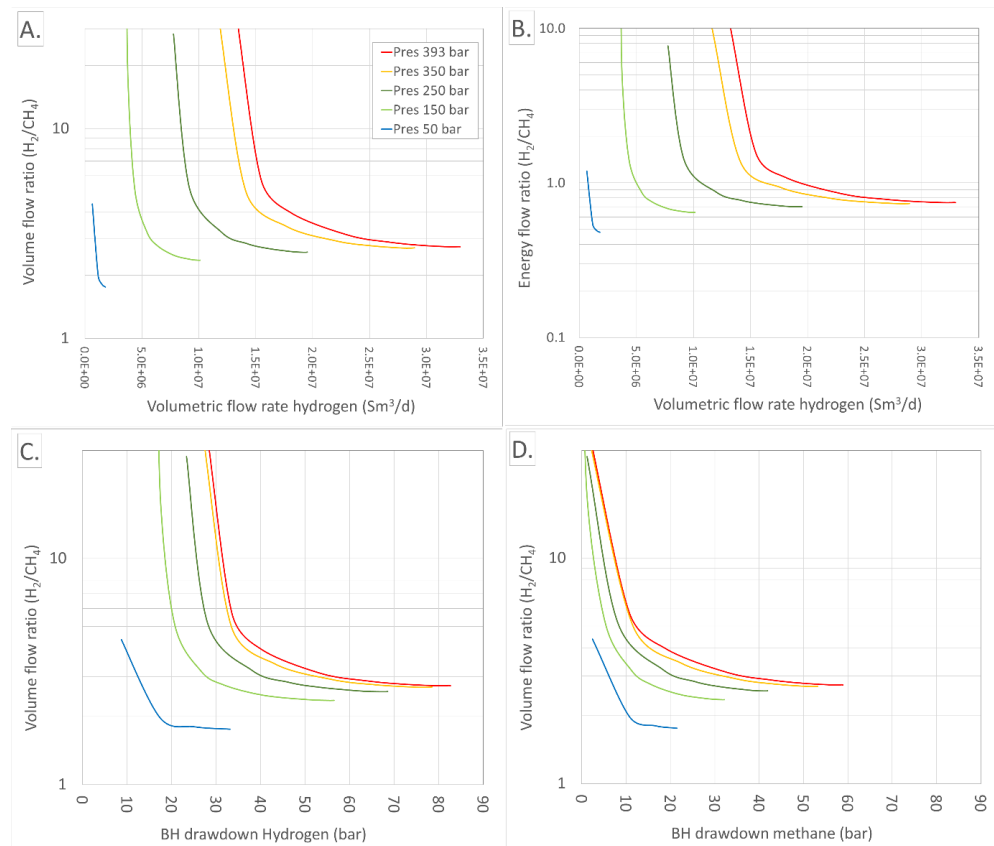


Figure 3.9: Methane and hydrogen volume and energy ratios plotted against withdrawal rates (a, b) and bottom-hole drawdown (c, d).

The withdrawal flow rates we have discussed so far referred to the maximum initial theoretical rates for a given reservoir and wellhead pressure. At a constant wellhead pressure, this maximum withdrawal rate would not remain constant and decrease in time as a result of the reservoir pressure depletion. Many UGS are strategically operated so that they can deliver a constant plateau withdrawal rate for a given period of time. In the case of the UGS in the Netherlands, this is about three months, corresponding to the three coldest winter months when the energy demand is the highest. For the Grijskerk scenario, with an initial reservoir pressure of 393 bar, we use equation (1) to calculate the plateau rate for hydrogen, a 3 months period (90 days), and a large range of initial wellhead pressures. Figure 3.10 shows that by incorporating a plateau rate the maximum withdrawal rates are reduced by 10% for rates below 15 mln  $Sm^3/day$  and up to 23% for higher withdrawal rates.



Figure 3.10: Plateau withdrawal rate of 3 months versus the maximum theoretical withdrawal rates estimated for the case of hydrogen in the Grijpskerk reservoir at 393 bar pressure (maximum working pressure), for a large range of initial wellhead pressure and using a 7-inch (ID) production tubing (see also Figure 3.8). The yellow line shows the percentual reduction of the plateau withdrawal relative to the maximum initial theoretical withdrawal rate.

### **Bottom-hole drawdown - GRK**

For an UGS it is important to estimate the maximum performances at which a single well can be operated, in order to determine the number of wells that need to be drilled. Fewer wells producing at high rate appear as one economical option to reduce costs. However, high rates can often only be achieved by increasingly higher flowing bottom-hole pressure drawdown. Pressure drawdown is the differential pressure between the far field average reservoir pressure and the flowing wellbore pressure that drives the liquid/gas from the reservoir into the bottom-hole. For a give gas/liquid type, bottom-hole drawdown is primarily determined by the wellhead pressure, and length and configuration of the tubing. For instance, for a given reservoir permeability and pressure, the lower the wellhead pressure and the larger the tubing inner diameter are, the larger the bottom-hole drawdown will be during withdrawal. On the other hand for a fixed wellhead pressure and tubing diameter, lower permeability and high reservoir pressures tend to yield larger bottom-hole pressure drawdowns. Therefore, in order to compare the performances between two different reservoirs/wells, the productivity index (PI) is used. This index determines the relation between the flow rate and drawdown at the bottom-hole:

$$PI = \frac{Q}{P^* - P_{bh}}$$

Where Q is the flow rate (mln Sm<sup>3</sup>/day), P\* the reservoir pressure and P<sub>bh</sub> the pressure at the bottom-hole. Depending of the petrophysical properties of the reservoir, fluid properties, degree of formation damage, well geometry and completion, amongst others, excessive pressure may lead to significant and irreversible mechanical damage at the wellbore as a result of collapse of the reservoir

rock material. This can significantly reduce the reservoir permeability around the wellbore drastically impairing the well productivity. Sand production damaging the production tubing is another negative effect of wellbore damage, since it can limit the flow velocity in the production tubing (i.e.  $V_e$ ).

As we have previously shown, maximum theoretical withdrawal rates for hydrogen from the Grijpskerk reservoir would be 2.4-2.7 times higher than that for methane. However, these higher flow velocities together with the lower density of hydrogen leads to higher bottom-hole drawdowns. In Figure 3.11 we show the differences in bottom-hole drawdowns associated to the range of withdrawal rates we calculated for hydrogen and methane based on the five pressure scenarios of Figure 3.8a. The highest bottom-hole drawdowns we obtained are of up to 34 to 82 bar for hydrogen and 22 to 59 bar for methane. This is on average  $\sim 1.5$  higher drawdowns for hydrogen. Note that the maximum drawdowns are associated to the extreme situation of AOF (Atmospheric Open Flow). When we plot the corresponding productivity indexes for the same scenarios, we observed PI values for hydrogen up to 2 fold higher than for methane for the reservoir pressures of 350 to 393, yet this difference significantly decreases for lower reservoir pressures (see Figure 3.12). All these calculations are made based on a mechanical skin factor of +1, which is an average value for a relatively undamaged wellbore. Higher skin factors would significantly increase the bottom-hole drawdowns and hamper the inflow performances of the reservoir. As we previously mentioned in the validation section of this report, gas operators of conventional and UGS wells often restrict the bottom-hole drawdown, which we estimate to be in the range between  $\sim 9$  to 67 bar (Figure 3.7). This means that in some cases of fast withdrawal of hydrogen, bottom-hole drawdowns could exceed the allowable operational pressures.

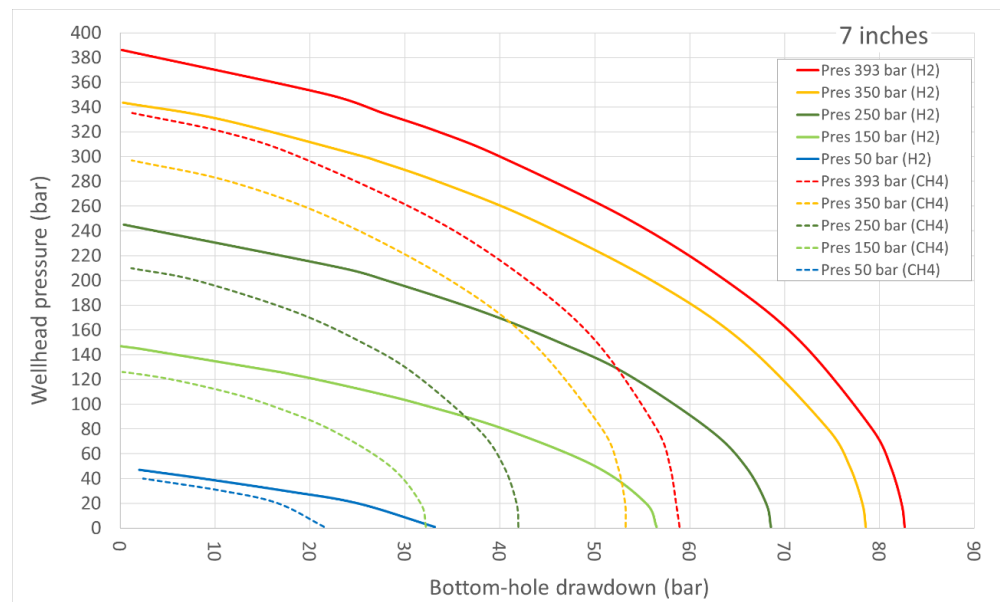


Figure 3.11: Bottom-hole drawdown for the five reservoir pressure scenarios calculated for Grijpskerk in Figure 3.8a.

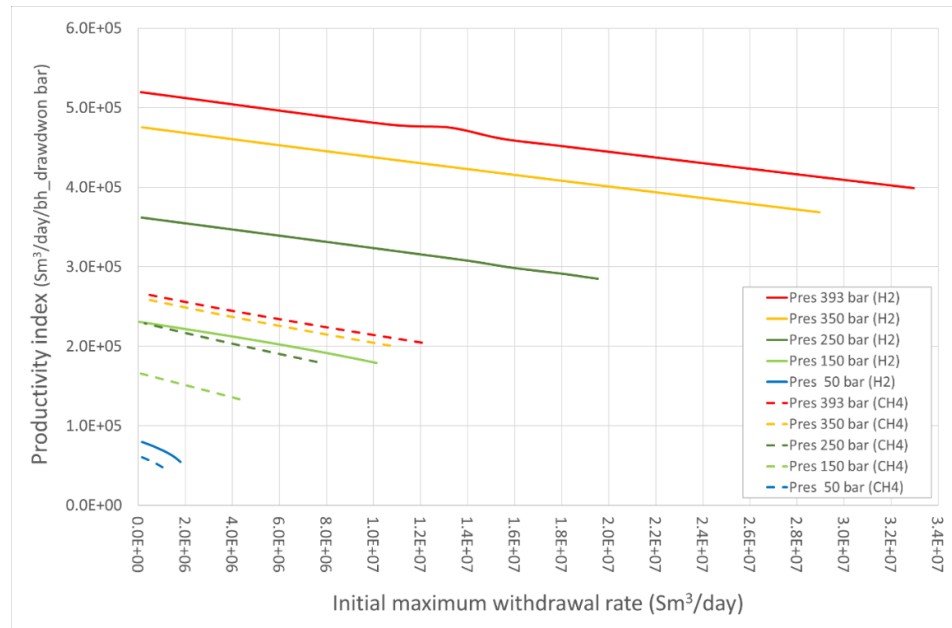


Figure 3.12: Productivity index (PI) for the five reservoir pressure scenarios calculated for Grijpskerk in Figure 3.8a for pure hydrogen and methane.

### **Erosional velocity ( $V_e$ ) - GRK**

Another limiting factor to the high withdrawal rates of hydrogen is the flow velocity in the production tubing. As previously introduced, the erosional velocity ( $v_e$ ) is the maximum flow velocity under which no erosion-corrosion is assumed to occur in the production tubing. In this study we used the conservative velocity of 100 m/s used by the Oil/Gas industry (personal communication Stefan Belfroid, TNO-Delft).

Based on the fact that during withdrawal operations the lowest pressures in the reservoir-well assembly are reached at the wellhead, this is where the gas reaches its maximum velocities as its density is the lowest. Based on 100 m/s threshold velocity, the cross-sectional area of a 7-inch (ID) tubing and the corresponding hydrogen and methane density for a large range of wellhead pressures, we calculated for each case the equivalent maximum allowable mass flow (kg/s). In Figure 3.8 we plotted the erosional threshold flow rate (in Sm<sup>3</sup>/day) on top of the ranges of theoretical hydrogen withdrawal rates we previously calculated for the Grijpskerk. Our results show a more significant velocity restrictions for the hydrogen withdrawal rates than that of methane. This is due to the hydrogen lower density, which requires high velocities to transport the same amount of mass. The highest single well theoretical withdrawal rate we estimate below the  $V_e$ -threshold for hydrogen in Grijpskerk is 27.4 mln Sm<sup>3</sup>/day (78 GWh/day). This is for a reservoir pressure at 393 bar, a well head pressure of 195 bar and a bottom-hole drawdown of 65 bar. The equivalent constant plateau rate for a three months withdrawal would be slightly lower the flow rate down to 21.9 mln Sm<sup>3</sup>/day (62 GWh/day) (Figure 3.10). Although we do not have precise information on the range of allowable drawdowns for the reservoir in Grijpskerk, the theoretical energy throughput we estimate -if feasible- it is 33% lower flowing energy than the highest flow rate realized for natural gas in Grijpskerk, which has been 8.5 mln Sm<sup>3</sup>/day with an energy throughput of 92 GWh/day (assuming a calorific value of 39 MJ/Sm<sup>3</sup> for natural gas).

Therefore the erosional velocity together the bottom-hole drawdown are two important factors to be considered for the higher withdrawal velocities of hydrogen, since they can considerably limit the operational performances and reduce the H<sub>2</sub>/CH<sub>4</sub> energy ratio throughput that we originally estimated between 0.7 and 0.8. One possible alternative to this limitation is the use of a tubing with a larger diameter. Tubings with a 9-inch (ID) internal diameter are also used in many UGS. We recalculated the withdrawal rates and erosional velocity of Figure 3.8 with a 9-inch (ID) tubing (see Figure 3.13), together with the corresponding bottom-hole drawdowns (see Figure 3.14). Figure 3.13 shows an increase of the hydrogen withdrawal rates (and energy throughput) of up to 11% and 57% relative to the 7-inch (ID) tubing for hydrogen for the reservoir pressure scenarios of 50 bar to 393 bar, respectively. However, the increase in withdrawal rates also involves a considerably increase of the bottom-hole drawdown pressure, up to 40 to 143 bar. This is a 17% to 42% increase in bottom-hole drawdowns (see Figure 3.14).

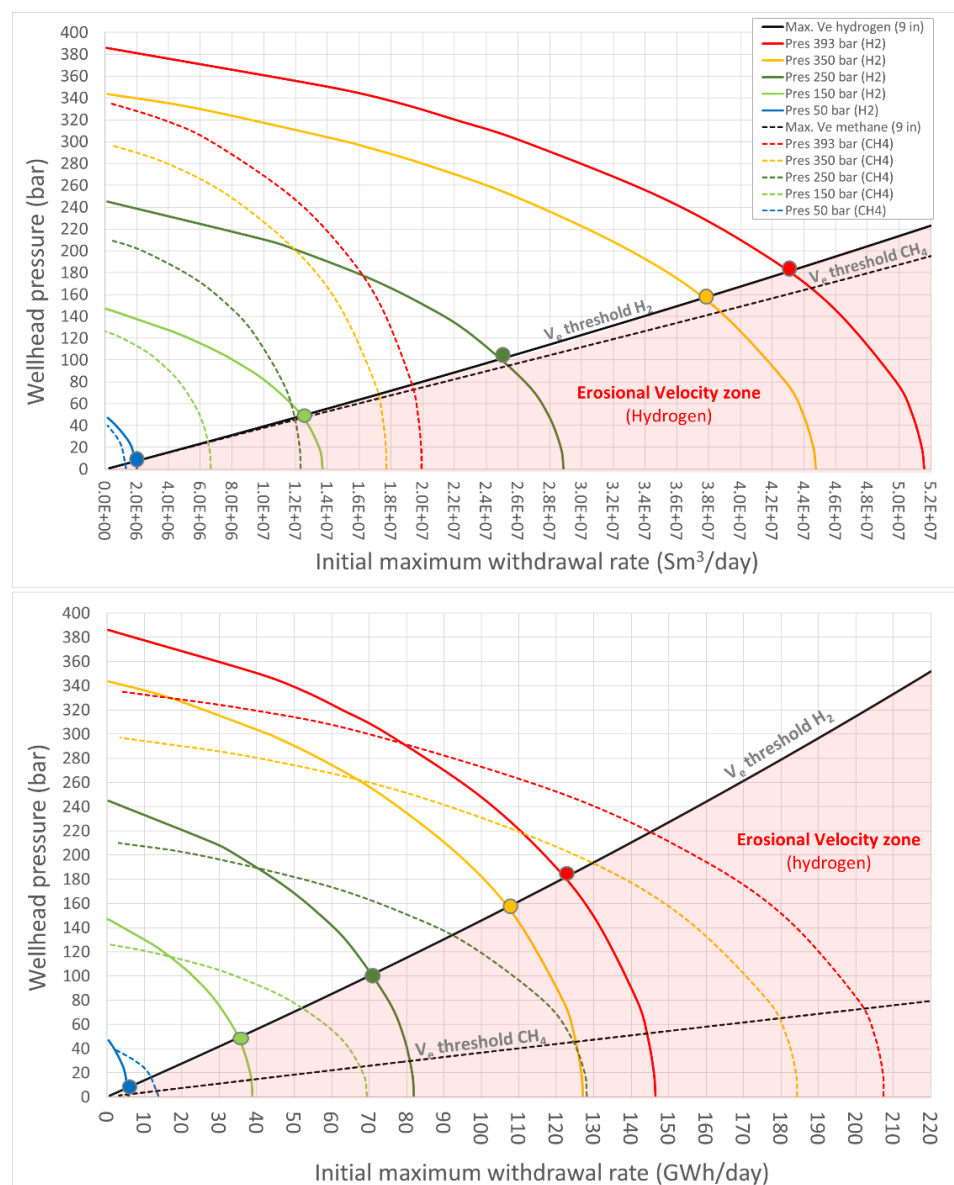


Figure 3.13: Same as Figure 3.8, yet for a 9-inch (ID) tubing.

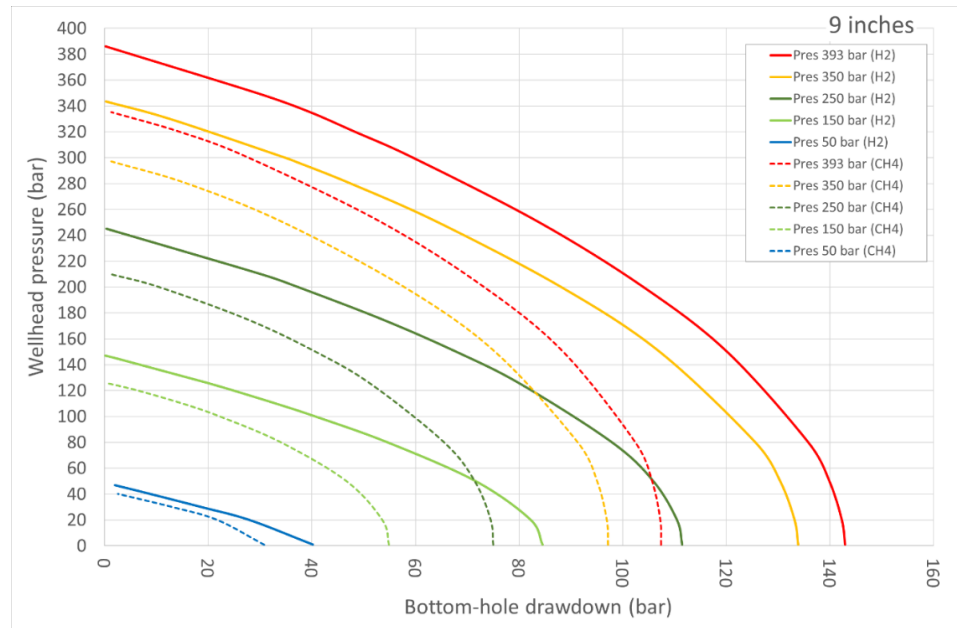


Figure 3.14: Same as Figure 3.11, but with a 9-inch (ID) tubing (see also Figure 3.13).

In conclusion we can say that the inflow/outflow methodology we present here provide important information not only on the hydrogen versus methane flow performances, but also on technical limitation in the wellbore and production tubing. Due to the higher velocities of hydrogen, this information can certainly assist in the planning and design of production strategies and operational ranges of future UHS.

#### **Working volume - GRK**

At the maximum reservoir pressure of 393 bar and 117°C the Grijpskerk reservoir contains a Gas-Initially-In-Place of 10.84 bcm. At these conditions the expansion factor ratio between hydrogen and methane is 0.92. This means that the reservoir in Grijpskerk could store up to 9.9 bcm of hydrogen. Based on these two initial Gas-Initially-In-Place, we calculated the range of possible working volumes of hydrogen and methane. We did that by applying different constant wellhead pressure to simulate different degrees of reservoir depletion (minimum working pressures) during a period of withdrawal. We also run a second scenario with a low initial reservoir pressure of 250 bar (half full reservoir). The reason why we did that is to quantify the impact that it would have on the storage capacity in a case where filling up of the reservoir to its maximum working pressure would be too costly. As for the UGS, one of the largest expenses of a UHS project would be the production and injection of the hydrogen cushion gas.

Figure 3.15 shows a range of estimated working volumes at the different degrees of reservoir pressure depletion. For a given wellhead pressure, hydrogen gives a lower final reservoir pressure than methane when reaching the cut-off rate of 1 mln Sm<sup>3</sup>/day. These differences in pressure decrease from 49 to 19 bar with increasing degree of reservoir pressure depletion. We also observed that for reservoir pressures from 393 bar to ~120 bar, the working volumes of hydrogen we estimate are larger than those of methane. These differences quickly reverse for reservoir pressures below 120 bar, where the methane working volumes becomes larger giving a H<sub>2</sub>/CH<sub>4</sub> working volume ratio around 0.96. Below reservoir pressures of 80 bar the percentage of working volume -relative to the volume at the maximum working pressure- for hydrogen and methane gases are very similar.

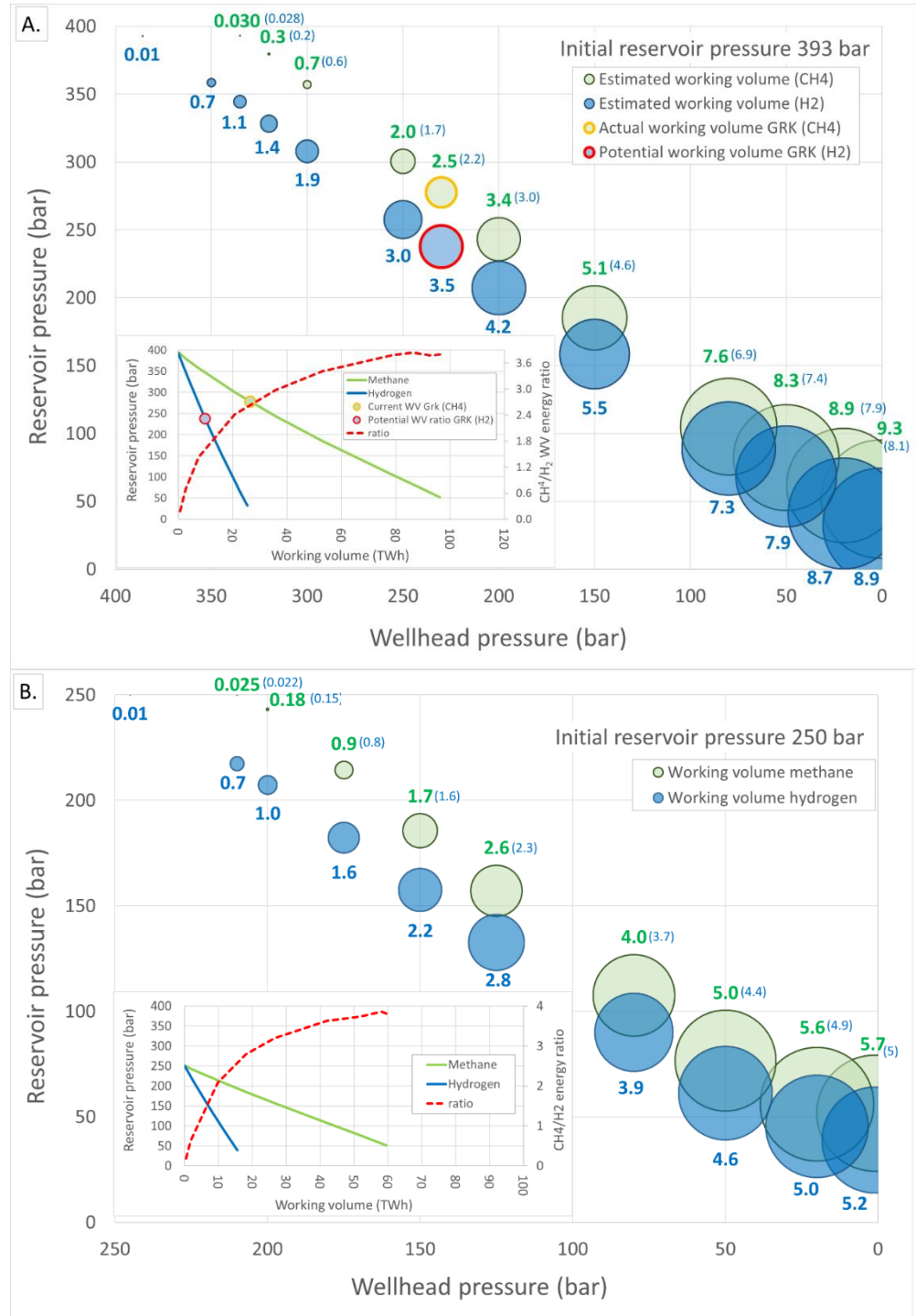


Figure 3.15: Working volumes (bubble size and values in  $\text{bcm Sm}^3$ ) estimated for two scenarios for the Grijpskerk reservoir at 393 bar (A. full reservoir) and 250 bar (B. partly depleted reservoir), considering a large range of constant wellhead pressures for the withdrawal of hydrogen (blue) and methane (green). The working volume was calculated based on a given wellhead pressure and the cut-off withdrawal rate of 1 mln  $\text{Sm}^3/\text{day}$ . Next to the value for the ww of methane, the equivalent hydrogen volume at the same temperature and pressure is given in blue between brackets. The graph at the lower left corner shows the energy content of the estimated working volumes (absolute and ratio) between hydrogen and methane.

The differences in pressure and working volume we obtained are both caused by the fact that at high reservoir pressures hydrogen can be withdrawn faster above the cut-off rate than methane due to its lower density and viscosity. This results in a faster recovery rate for hydrogen and a lower final reservoir pressure during the first stages of withdrawal. These differences become less at higher degrees of reservoir pressure depletion, in the case of Grijpskerk for reservoir pressures below the 120 bar. Despite all, even in the first stages of withdrawal the larger working volumes of hydrogen produced do not compensate for its significantly lower energy contents. The CH<sub>4</sub>/H<sub>2</sub> energy density ratio quickly increases in favor of methane since the start of a withdrawal cycle (Figure 3.15a). We obtained similar results for the scenario with a partly depleted Grijpskerk reservoir with an initial reservoir pressure of 250 bar (Figure 3.15b). However, in this scenario the CH<sub>4</sub>/H<sub>2</sub> energy contents ratio increases more quickly due to the lower reservoir pressure (Figure 3.16).

For the currently reported working volume of 2.5 bcm of natural gas in Grijpskerk we estimated a pressure depletion of the reservoir down to 278 bar from the maximum working pressure of 393 bar. At this pressure the equivalent working volume in hydrogen would be of 2.2 bcm based on a H<sub>2</sub>/CH<sub>4</sub> expansion factor ratio of 0.879. This is 24% and 22% of the total methane (10.8 bcm) and hydrogen (9.9 bcm) the reservoir could contain, respectively. This implies a considerable large cushion gas volume. On the other hand when considering the higher flow performance of hydrogen, and using the 1 mln Sm<sup>3</sup> as a cut-off rate, the working volume of hydrogen would be higher up to 3.5 bcm, this being a 35% of the total gas in the reservoir. In this case we estimate a final pressure for the reservoir of 230 bar. We run again the same scenarios of Figure 3.15a, yet this time with a 9-inch (ID), and obtained the same range of working volumes. Therefore we concluded that the tubing diameter has only an impact to rate of withdrawal, but not to the ultimate working volume.

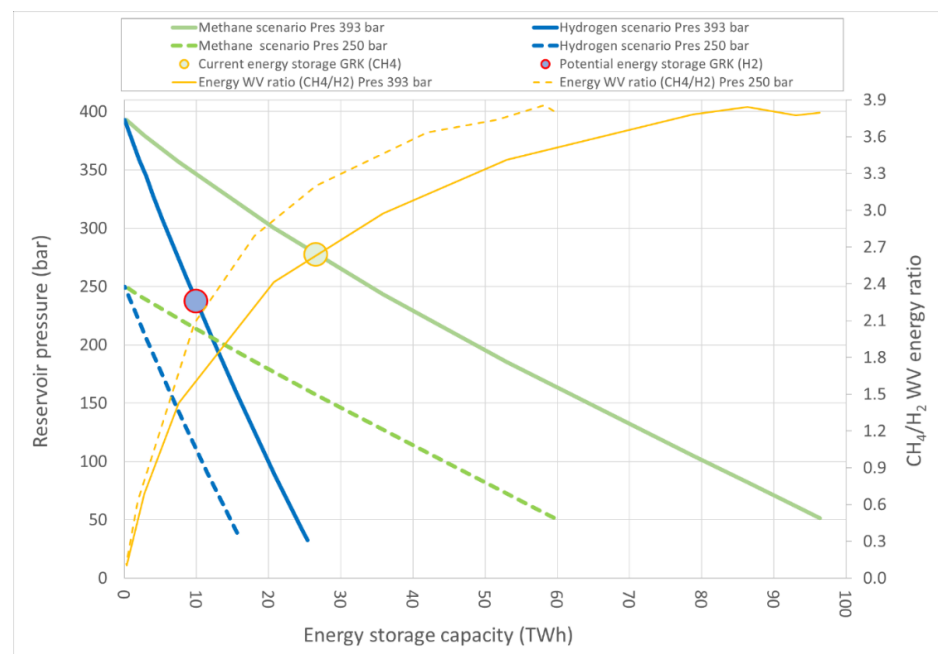


Figure 3.16: H<sub>2</sub> and CH<sub>4</sub> working volumes in energy units (TWh) versus reservoir final pressure for the two Grijpskerk scenarios with an initial reservoir pressure of 393 bar and 250 bar (Figure 3.15a ,b). The current energy stored in Grijpskerk in the form of natural gas (methane), and the potentially equivalent in hydrogen based on the cut-off of 1 mln Sm<sup>3</sup>/day, are marked with a circle.

When converting the methane working volume of 2.5 bcm to energy, this is equivalent to 26.5 TWh (Figure 3.16). Meanwhile that of hydrogen working volumes of 2.2 bcm and 3.5 bcm are about 6.3 and 9.9 TWh, respectively. This means that an UHS in Grijpskerk could only store 24% and 37% of the present energy stored as working volume relative to an UGS (methane). As we show in Figure 3.16, only the lowering of the final operational reservoir pressure could increase the amount of energy stored. However, the lowering of the minimum working pressure -for a UHS relative to an UGS- will require a new risk assessment study to investigate possible negative effects.

### ***Injection rates - GRK***

The GaSP-tool also allows calculating the injection performances of gas from a well into reservoir using the same set of formulas as those for withdrawal. The only difference is that in the outflow (tubing) equation, the gravitational term is now positive meaning it favors the flow along the tubing and into the reservoir. As we did for the withdrawal performances, we also ran a set of scenarios to investigate and compare the injection performance of hydrogen and methane. The aim is to understand how the reservoir of the Grijpskerk UGS would perform when hydrogen would be injected. The input parameters for the inflow/outflow calculation are listed in Table 3-3. We ran the same pressure scenarios for Grijpskerk, with increasing initial minimum working pressure at 50, 150, 250 and 350 bar, and used a large range of wellhead pressures (40 to 393 bar). Unlike for the withdrawal scenarios, where we assumed the gas temperature to be that of the reservoir, here we assumed a temperature of 40°C, after compression and before entering the wellhead.

Figure 3.17 shows the hydrogen and methane injection rates versus wellhead pressures for various reservoir scenarios with different initial minimum working pressures. For each scenario, we observe that lower wellhead pressures are required to inject methane at low rates (<6 mln Sm<sup>3</sup>/day). This can be explain by the fact that methane has a higher density than hydrogen, resulting in a higher hydrostatic weight that favors injectivity. However, at higher rates, involving higher wellhead pressures, the injection of methane becomes progressively lower than that of hydrogen. Although at higher pressures the density of methane increase significantly more than that of hydrogen, methane also experiences an much larger increase in viscosity. It is the higher viscosity of methane that appears to have a negative effect for injection of methane relative to hydrogen.

While the range of injection rates we obtained looks similar to that of withdrawal rates, the differential pressure between the bottom-hole and the wellbore (build-up) are slightly larger, in particular for scenarios with very low initial minimum working pressure (e.g. 50, 150 bar) (Figure 3.17). This suggests that lower wellhead (injection) pressures or a higher reservoir pressure may be required during the first stages of hydrogen injection, however, as previously discussed pressure differentials between the bottom-hole and reservoir should be kept low in other to avoid any mechanical damage to the wellbore. Furthermore it is also the lowest reservoir pressure (50 bar) that shows a different injection pattern for hydrogen. Unlike the other cases where the maximum allowable wellhead injection pressure was 393 bar, in this scenario no pressure higher that 313 bar could be calculated. This could be a limitation of the analytical method, and may require the use of numerical modelling which, together with other aspects of methane and hydrogen injectivity, may be topics of future research.

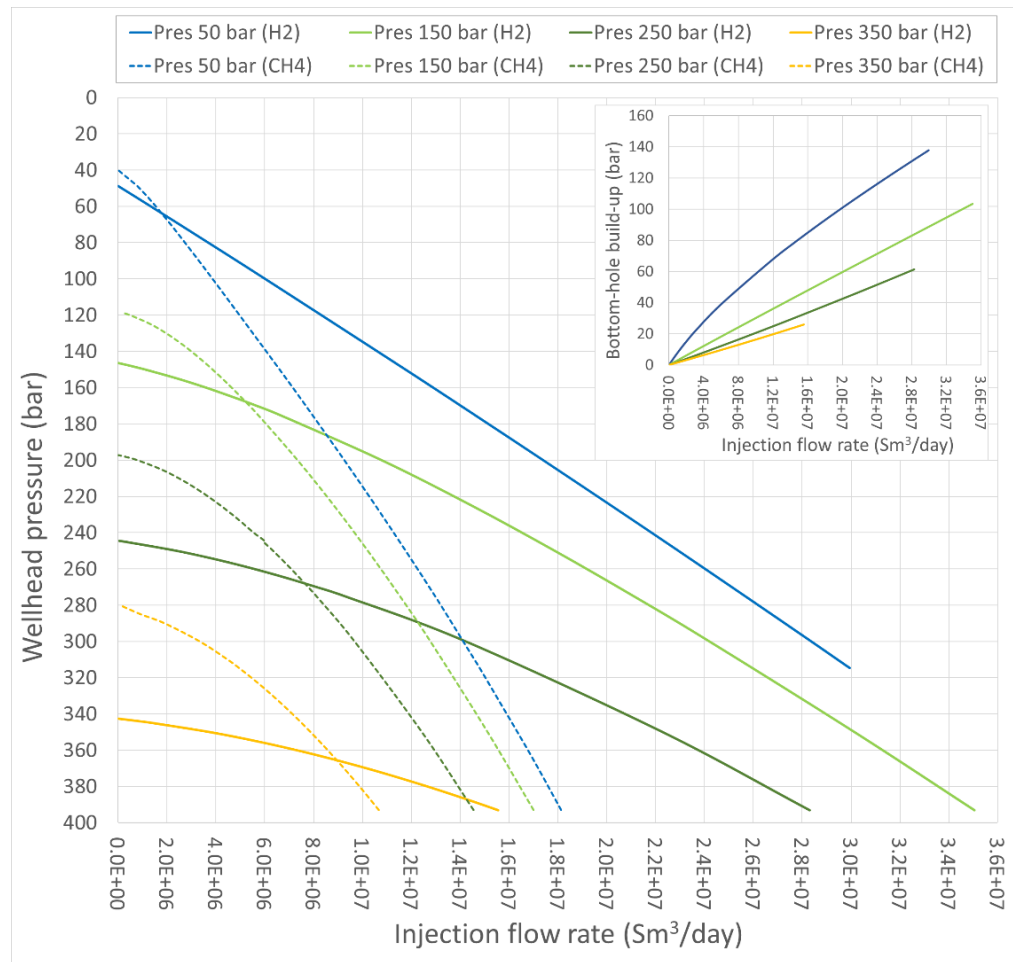


Figure 3.17 Hydrogen and methane Injection rates versus wellhead pressure for different initial reservoir pressures of the Grijpskerk underground reservoir. (upper left corner) Hydrogen bottom-hole build up for the injection rates and wellhead pressures shown in the main figure.

3.3.4.2 Results Norg (NOR) and Alkmaar (ALK), and comparison with Grijpskerk

In this section we compare the main results on single-well withdrawal performance and working volume for the Grijpskerk to those of Norg and Alkmaar. For all three reservoirs we assume a maximum working pressure of 393, 327 and 218 bar, respectively. The premises for the inflow/outflow are the same to those described for Grijpskerk. The input parameters are listed in Table 3-3.

**Withdrawal rate - NOR**

Similar to Grijpskerk, the Norg UGS consists of a reservoir made of well-sorted upper Permian eolian sandstone. The reservoir has a high average permeability of 176 mD, a thickness of 150 m and is located at a depth of 2895 m TVD. Based on the historical volumes withdrawn and injected, we estimate the pressure in the reservoir to have fluctuated between the initial 327 bar down to 210-250 bar. Despite the reservoir in Norg has a slightly lower reservoir pressure and a similar thickness to that in Grijpskerk, it is located 500 meters shallower and has an average permeability 7 times higher. Based on our inflow/outflow result we estimate for Norg an maximum theoretical withdrawal rate up to 37 mln Sm<sup>3</sup>/day (single well) at maximum working pressure (327 bar) (Figure 3.18). The restriction due to erosional velocity threshold reduces the allowable top rate below the 28.6 mln Sm<sup>3</sup>/day (81 GWh/day), which is

very similar to the 27.4 mln Sm<sup>3</sup>/day (78 GWh/day) we obtained for Grijpskerk. Yet the bottom-hole drawdown in Norg is much lower 15 bar, compare to the 65 bar in Grijpskerk. This implies that as Norg has a higher permeability, bottom-hole drawdowns are in principle a less limiting factor. This is also shown by the “productivity index” (PI). The PI we obtained for Norg is 5 times higher than that of Grijpskerk (Figure 3.20). Another important difference between the two reservoirs is the larger volume at maximum working pressure: 24.7 bcm of Norg compared to 9.9 bcm for Grijpskerk. As Figure 3.19 shows the larger volumes in Norg provide a better pressure support, which allows maintaining a higher withdrawal plateau rates for the period of three months we select. The maximum theoretical rate of 28.6 mln Sm<sup>3</sup>/day would be since reduced by about 9% in order to maintain a rate of 26.0 mln Sm<sup>3</sup>/day (74 GWh/day) for a period of 3 months.

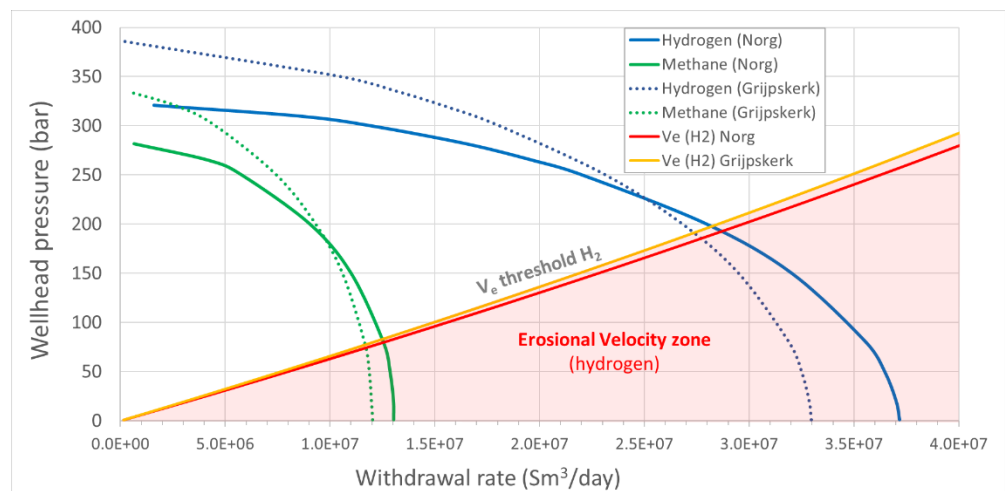


Figure 3.18 Wellhead pressure versus maximum theoretical withdrawal rate (single well) for hydrogen and methane calculated for the Norg reservoir at maximum working pressure (327 bar). The results of Grijpskerk at 3939 bar are also plotted for comparison.

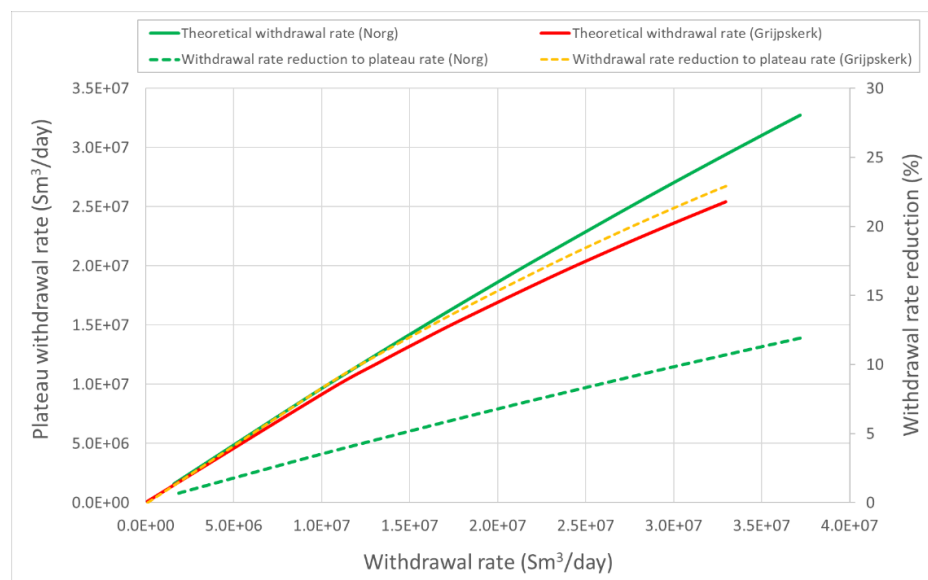


Figure 3.19 Plateau rate of 3 months versus the maximum withdrawal rates estimated for the case of Norg at maximum working pressure (327 bar) for a 7-inch (ID) production tubing. The dashed line shows the percentual reduction of the plateau withdrawal relative to the maximum initial withdrawal rate. The results of Grijpskerk (Figure 3.10) are also depicted in this graph for comparison.

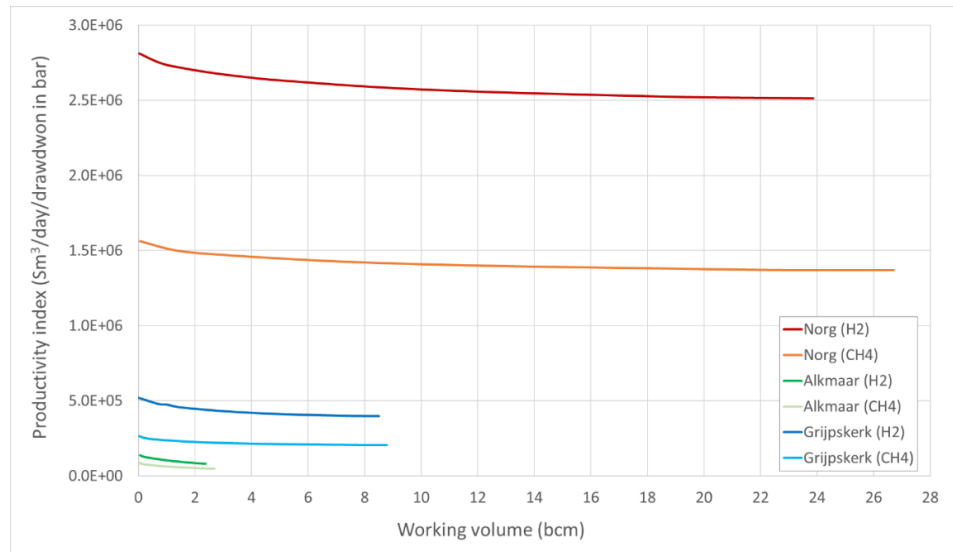


Figure 3.20 Comparison between the productivity index and working volume for hydrogen and methane in the Grijpskerk, Norg and Alkmaar reservoirs.

We estimate a single well plateau rate for Norg of 25.8 mln Sm<sup>3</sup>/day (73 GWh/day), which is higher than the 21.9 mln Sm<sup>3</sup>/day of Grijpskerk (62 GWh/day). These results show the importance of the reservoir permeability to the performance and technical limitations of an UHS.

#### **Working volume - NOR**

Similarly to Grijpskerk we calculated the working volume considering the Norg reservoir to be at its maximum working pressure (327 bar), and assuming large range of wellhead pressures. Figure 3.21 show the working volume we estimate for different degrees of reservoir depletion. We observe that for reservoir initial pressures down to ~140 bar, the working volumes of hydrogen are larger than those of methane. As we previously mentioned, this is due to the fact that in the first stages of depletion high withdrawal rates of hydrogen can be maintained above the cut-off rate, leading to a higher recovery (working volume). For the currently reported working volume of 6.3 bcm in Norg, we estimate a corresponding reservoir pressure depletion down to 243 bar. At this pressure the equivalent working volume of hydrogen would be 5.5 bcm, based on a H<sub>2</sub>/CH<sub>4</sub> expansion factor ratio of 0.872 (see Figure 3.21). For both hydrogen and methane this is 22% of the gas the reservoir could store at maximum working pressure, meaning a large volume of cushion gas is necessary for pressure support. Yet again when considering the higher flow performances of hydrogen, and using the 1 mln Sm<sup>3</sup> as a cut-off rate, the working volume of hydrogen could be slightly higher up to 7.9 bcm. This is 32% of the total gas at maximum working pressure (see Figure 3.21). In this case we estimate a minimum working pressure of 211 bar, which is 32 bar lower than that for methane for an UGS (see Figure 3.21).

When converting the methane working volume of 6.3 bcm to (thermal) energy, this is equivalent to 65.6 TWh (see Figure 3.21). Meanwhile that of hydrogen working volumes of 5.5 bcm and 7.9 bcm are about 15.6 and 22.4 TWh, respectively. This means that an UHS in Norg could only supply 24% and 34% of the present energy delivered by the Norg UGS (methane). These are very similar percentages to those of Grijpskerk.

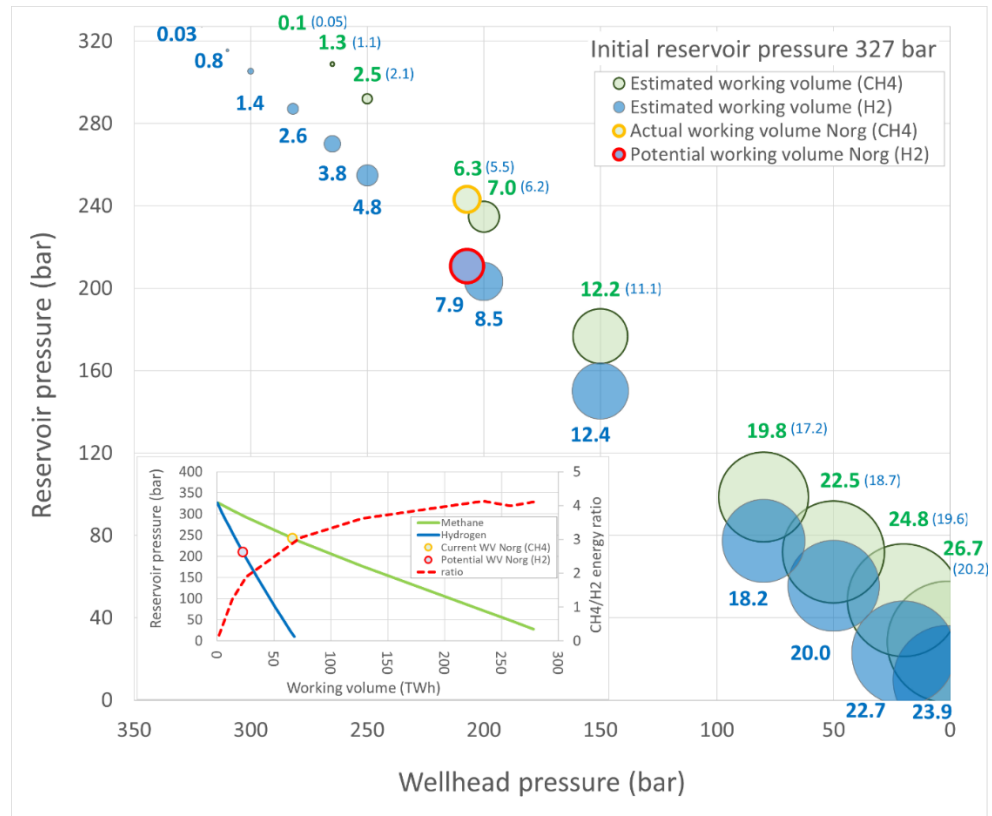


Figure 3.21 Working volumes (bubble size and values in bcm) estimated for scenario for the Norg reservoir at 327 bar (full reservoir), considering a large range of constant wellhead pressures for the withdrawal of hydrogen (blue) and methane (green). The working volume was calculated based on a given wellhead pressure and the cut-off withdrawal rate of 1 mln Sm<sup>3</sup>/day. Next to the value for the WV of methane, the equivalent hydrogen volume at the same temperature and pressure is given in blue between brackets. The graph at the lower left corner shows the energy content of the estimated working volumes (absolute and ratio) between hydrogen and methane.

As already described by Juez-Larré et al. (2016), despite the good reservoir quality of the Grijpskerk and Norg reservoirs, these reservoirs require a large cushion volume to perform due to their large size and great depth. The Grijpskerk reservoir although is smaller, its depth is much greater than that of Norg. The reason why these two conventional natural gas reservoirs were converted to UGS was -amongst other reasons- because part of the cushion gas needed had not yet been produced giving the advantage of earlier commissioning.

#### **Withdrawal rates - ALK**

The Alkmaar UGS consists of a reservoir made of upper Permian carbonates rocks. The reservoir has an average permeability of 34 mD, a thickness of 50 m, is located at a depth of 2125 m TVD and had an original pressure of 218 bars. Although the permeability is similar to that of Grijpskerk, the thickness is about 3.6 times lower and the pressure is about half. This explains why for the maximum working pressure in Alkmaar (218 bar) the withdrawal rates for hydrogen are much lower (up to 11 mln Sm<sup>3</sup>/day, i.e. 31 GWh/day) (Figure 3.22) and the productivity index is 5 times lower (Figure 3.20). Since the reservoir in Alkmaar has the lowest productivity index of all three UGS, the bottom-hole drawdowns are the highest, ranging from 22 to 140 bar for a wellhead of 190 to 1 bar. Therefore opposite to Norg, the performances of Alkmaar may be more limited, not by the erosional velocity, but by the bottom-hole drawdown (see Figure 3.22).

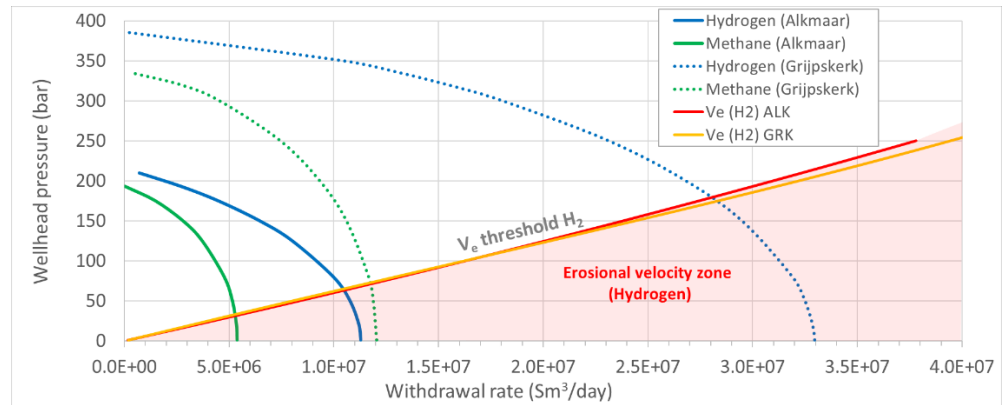


Figure 3.22 Wellhead pressure versus withdrawal rates (single well) for hydrogen and methane (single well) for the case of Alkmaar at maximum working pressure (218 bar). For comparison the curve of maximum theoretical withdrawal rates for Grijpskerk at maximum working pressure (393 bar) is also plotted for comparison.

**Working volume - ALK**

The working volume currently used in Alkmaar is 0.56 bcm (5.9 TWh) for which we estimate an associated minimum working pressure of 184 bar. This is only 15% of the 3.8 bcm (39.6 TWh) at maximum working pressure of 218 bar. Accordingly at max. and min. working pressure the reservoir in Alkmaar could contain 3.2 bcm of hydrogen (9.1 TWh) and a working volume of 0.48 bcm (1.4 TWh) (Figure 3.23).

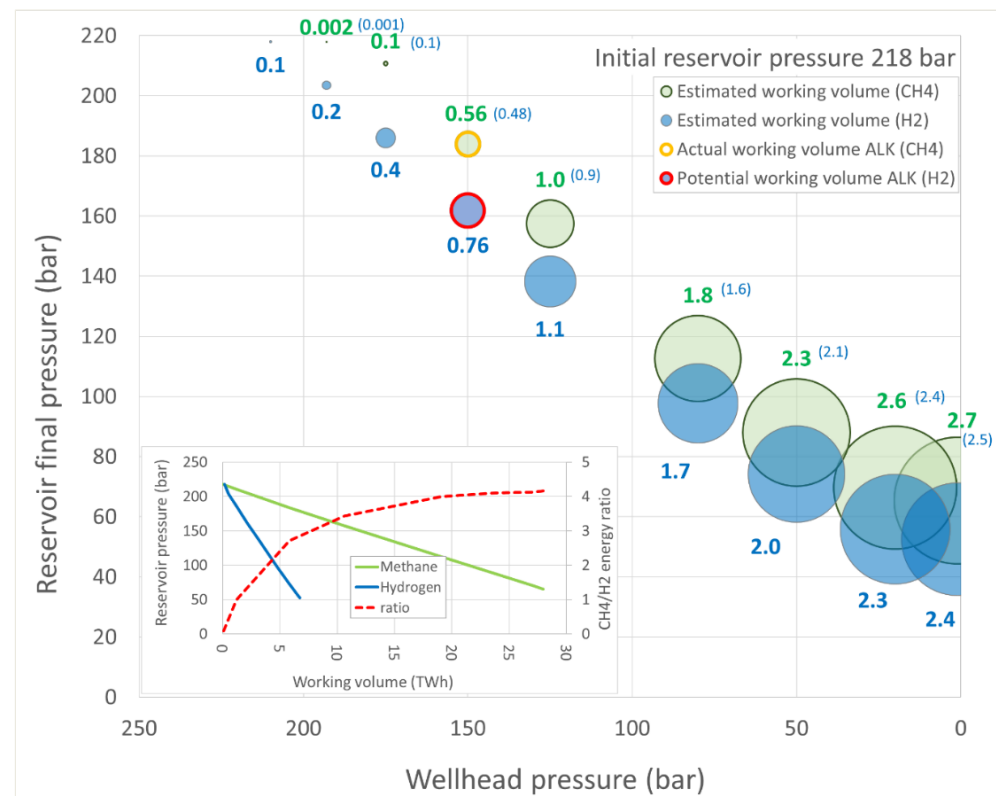


Figure 3.23 Working volumes (bubble size and value in bcm) estimated for a scenario for the Alkmaar reservoir at 218 bar (full reservoir), considering a large range of constant wellhead pressures for the withdrawal of hydrogen (blue) and methane (green). The working volume was calculated based on a given wellhead pressure and the cut-off withdrawal rate of 1mln Sm<sup>3</sup>/day. Next to the value for the ww of methane, the equivalent hydrogen volume at the same temperature and pressure is given in blue between brackets. The graph at the lower left corner shows the energy content of the estimated working volumes (absolute and ratio) between hydrogen and methane.

The use of a 1 mln Sm<sup>3</sup>/day cut-off instead would yield a large working volume of hydrogen of 0.76 bcm (2.2 TWh). This means for each hydrogen working volume the UHS in Alkmaar could deliver 23% and 37% of the energy currently contained as a working volume (methane). These percentages are again very similar to those we obtained for Grijpskerk and Norg.

### 3.3.5 Porous reservoir vs. salt cavern – comparison of withdrawal performances

In order to perform a brief assessment of the differences between the maximum theoretical withdrawal rates from a porous reservoir and that of a salt cavern (void space), we ran some simplified inflow/outflow scenarios using the GaSP-tool. For the porous reservoir and salt cavern we used the same input parameters (Table 3-5), including the same depth (1100 m TVD), dimensions (450 m height x 27 m radius) and tubing diameter (9-inch ID), which are the typical values for a salt cavern. Only a different permeability was used: 25 mD for the porous reservoir and an infinite permeability for the salt cavern. In an attempt to design a scenario that best simulates the bottom-hole restrictions of gas flowing into the well, we considered for both cases the fraction of reservoir and cavern “perforated” to be 0.1.

Table 3-5 Gas, reservoir & well input parameters used for the calculations. These parameters were collected from the storage license for Zuidwending of 11-July 2017 (<https://www.nlog.nl/field-web/rest/field/document/3361944097>). (\*) Values assumed, (\*\*) Values calculated. We refer to “Sm<sup>3</sup>” as the International Standard Metric Conditions at 15°C and 1.01325 bar.

| Parameters                                |                    | Cavern   | Reservoir  |
|---|--------------------|--|------------|
| <b>GAS</b>                                |                    |  |            |
| Type gas (dry*)                           | -                  | Pure hydrogen or methane                       |            |
| Type storage operation                    | -                  | Withdrawal (send-out)                          |            |
| Type flow*                                |                    | Radial flow                                    |            |
| <b>Underground reservoir</b>              |                    |  |            |
| Reservoir depth (mid-reservoir thickness) | m TVD              | 1100   | 1100       |
| Initial reservoir pressure                | bar                | 180 or 110                                     | 180 or 110 |
| Initial reservoir temperature             | °C                 | 45   | 45         |
| Reservoir permeability (average)          | mD                 | infinite                                       | 25         |
| Reservoir thickness or height cavern      | m                  | 450  | 450        |
| Drainage radius*                          | m                  | 27 (drainage radius)                           | 27         |
| Geometrical volume                        | mln m <sup>3</sup> | 1  | 1          |
| Type reservoir                            | -                  | Single layer (implicit in the inflow equation) |            |
| Fraction reservoir perforated*            | fraction           | 0.1  |            |
| Dietz reservoir shape factor*             | -                  | 31.62 (circular reservoir & centered well)     |            |
| <b>WELLBORE and WELL</b>                  |                    |  |            |
| Tubing length (top reservoir or cavern)   | m TVD              | 1100   |            |
| Tubing internal diameter (ID)*            | inches             | 9 (9 <sup>5/8</sup> outer diameter)            |            |
| Angle production tubing*                  | degrees            | 0° (vertical)                                  |            |
| Production tubing internal roughness*     | m                  | 0.00005  |            |
| Wellbore radius*                          | inches             | 10 <sup>3/8</sup>                              |            |
| Mechanical skin (damage) factor*          | -                  | +0   |            |
| Beta (Kinetic factor)                     | 1/m                | 4.1e11 (from Friedel and Voigt, 2006)          |            |
| Wellhead pressure*                        | bar                | 55 to 180                                      |            |

Furthermore, since the GaSP-tool does not include thermal effects, we assume adiabatic conditions in the well, cavern and reservoir. We are aware of the limitations of the choices and simplifications made, yet we regard these results as a mere first order approximation. These calculations aim at comparing the maximum theoretical withdrawal rates between a porous reservoir and a salt cavern, yet in this study we did not make any attempt to investigate the progress through time of the rates of withdrawal and the cavern pressure depletion. Figure 3.24 shows the maximum theoretical withdrawal rates for the porous reservoir and salt cavern at two different maximum working pressures of 180 bar (scenario 1) and 110 bar (scenario 2), and this for a large range of wellhead pressures down to 80 and 55 bar, respectively.

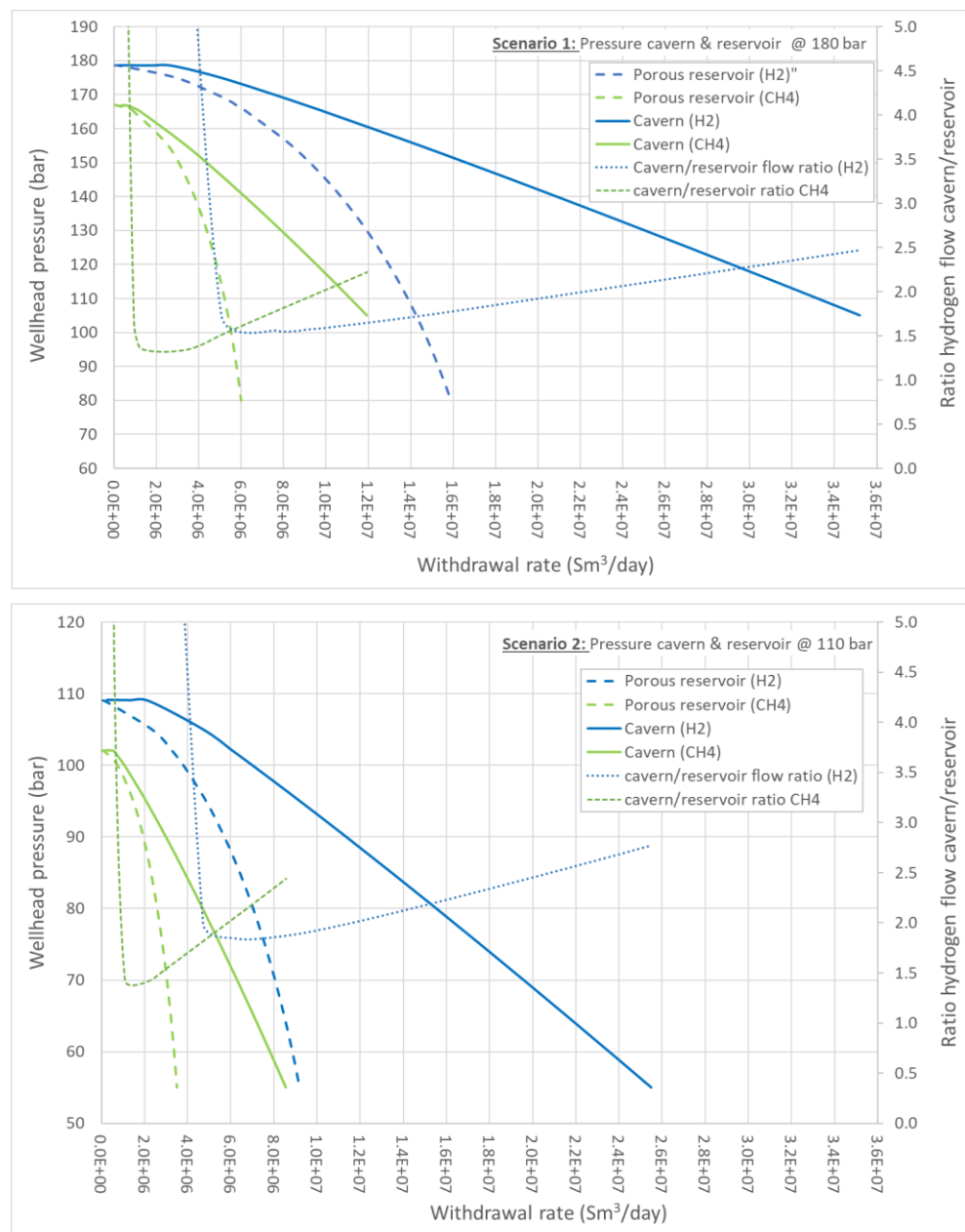


Figure 3.24 Maximum theoretical withdrawal rates versus wellhead pressure for caverns and porous reservoir at two different maximum working pressures of 180 bar (above) and 110 bar (below). The red dotted curve show the withdrawal ratio of hydrogen in a cavern and porous reservoir.

The range of pressures in scenario 1 (180-80 bar) are the common operational range for a natural gas storage in a salt cavern. Scenario 2 (110-55 bar) represents a case where the salt cavern would be operated at a much lower pressure. Results for the two pressure scenarios in a salt cavern show very high theoretical withdrawal rates for hydrogen up to 35 mln Sm<sup>3</sup>/day (scenario 1) and 25 mln Sm<sup>3</sup>/day (scenario 2), which are up to 2.5 and 2.8 times higher than those for a porous reservoir, respectively (see Figure 3.24). These withdrawal ratios are slightly lower than when the cavern and reservoir performances are compared for the case of methane (up to 2.2 and 2.4 respectively) (see Figure 3.24). We observed an exponential increase of the withdrawal ratios between caverns and porous reservoirs only for withdrawal rates lower than 5 mln m<sup>3</sup>/d (hydrogen) and 1 mln m<sup>3</sup>/d (methane). This is because for porous reservoirs larger initial wellhead drawdowns are needed to initiate and increase the rate of withdrawal (Figure 3.24).

Figure 3.25 shows pressure drawdowns, between the wellhead and the cavern, for the large range of hydrogen and methane withdrawal rates of Figure 3.24. We observed that relative to methane, hydrogen requires lower pressure drawdowns to achieve higher withdrawal rates, especially at high cavern pressures. At the same wellhead drawdown hydrogen flows 3-4 times faster. This is due to the lower density and viscosity of hydrogen. However, unlike in porous reservoirs, we find that withdrawal rates from salt cavern are mostly limited by structural integrity issues due to the maximum allowable “daily pressure depletion”.

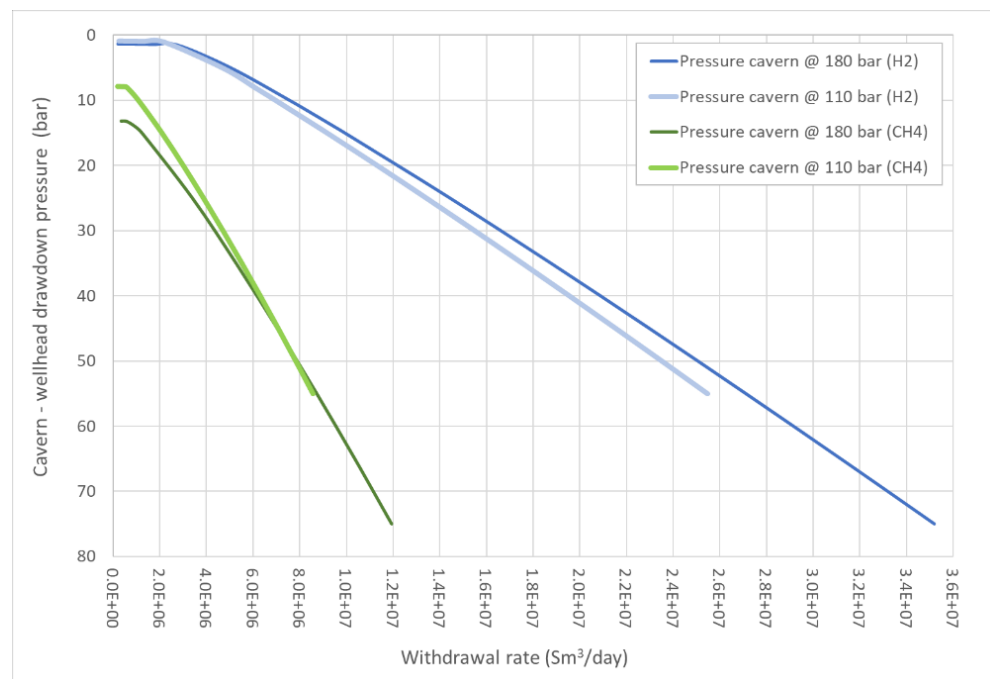


Figure 3.25 Wellhead drawdown versus the maximum theoretical withdrawal rate corresponding to the cavern scenarios 1 and 2 both for an initial cavern pressure of 180 and 110 bar (see Figure 3.24).

As example, for the salt cavern storage in Zuidwending, filled with natural gas, the operational pressure depletion is limited to 10 bar a day (Energystock, 2017). The six salt caverns in Zuidwending, each equipped with two wells, are operated as one big volume, i.e., pressure in the six caverns is varied synchronously. Assuming a maximum working pressure of 180 bar, a temperature of 45°C and a total geometric volume of 4.4 million m<sup>3</sup> for Zuidwending, an initial pressure drop of 10 bar means

that 43.5 million Sm<sup>3</sup> of natural gas can be withdrawn per day out of the total stored 0.8 billion Sm<sup>3</sup>, which equates to 7.3 million m<sup>3</sup>/day (67 GWh/day) per cavern. This is very similar to the volume and rates the operator reports, i.e. 7.6 million Sm<sup>3</sup>/day per cavern based on a reported withdrawal capacity of 1.89 million Sm<sup>3</sup>/hour for the entire facility (i.e. 45.4 mln Sm<sup>3</sup>/day) (Table 3-6). Therefore we can conclude that the maximum theoretical withdrawal rate per well we estimated for methane at ~12 mln Sm<sup>3</sup>/day, at a maximum working pressure of ~180 bar and a wellhead pressure of 105 bar, is 1.6 times higher than the allowable withdrawal rate per cavern (Figure 3.24). This clearly shows that wells in salt cavern storages are mostly operated well below their maximum theoretical performances, especially when taking into account that each cavern has two wells through which theoretically 24 mln Sm<sup>3</sup>/day could be withdrawn.

We repeated the previous calculations for Zuidwending at the same initial cavern pressures and temperatures conditions, but now for hydrogen. For an initial drop of 10 bar in one day only 31 million Sm<sup>3</sup> of hydrogen could be withdrawn out of the initial total stored volume of 0.6 billion Sm<sup>3</sup> (six caverns). This is equivalent to a 5.2 million Sm<sup>3</sup>/day (15 GWh) of hydrogen per cavern. In this case, this is about 7 times lower withdrawal rate than the theoretical 35 million Sm<sup>3</sup>/day per well from a cavern filled with hydrogen at 180 bar and wellhead of 105 bar. This shows that the withdrawal performance from a salt cavern filled with hydrogen is much more restricted than that of natural gas, since the pressure in the cavern decreases more rapidly during the withdrawal of hydrogen. In terms of energy, this means that a hydrogen storage cavern could only deliver 22% of the energy of that from a current natural gas cavern, i.e. 15 GWh/day (5.2 mln Sm<sup>3</sup>/day of hydrogen) instead of 67 GWh/day (7.3 mln Sm<sup>3</sup>/day of natural gas). It must be noted here that these are the limit rates per cavern and per day, i.e., higher withdrawal rates per well per hour are possible as long as the daily allowable pressure drop is not exceeded. Nonetheless, the daily pressure depletion restriction, which is enforced to safeguard the structural integrity of the cavern, is clearly the most limiting factor to the well performance, i.e., much more so than the bottom-hole drawdown and erosional velocity we previously discussed for porous reservoirs.

This imposed restriction also strongly limits the working volume available, since the cavern pressure has to be at all times above a minimum pressure to avoid a fast reduction of its (geometric) volume due to salt creep, the rate of which increases with increasing difference between the cavern pressure and the lithostatic pressure. As previously mentioned, the six caverns in Zuidwending are operated as one single big salt cavern, with a total geometrical volume of 4.4 mln m<sup>3</sup>, storing almost 0.8 bcm (~7.6 TWh) of natural gas (Groningen quality) (Table 3-6). The total working volume reported is of 382 mln m<sup>3</sup> (3.6 TWh) for which we estimate a minimum working pressure of 88 bar. This working volume is only ~50% of the total storage capacity. This means that the remaining 382 mln m<sup>3</sup> are used as cushion gas to provide a minimum pressure support. In case the current Zuidwending storage site would be operated at the same range of pressures of today, yet storing hydrogen instead, we estimate the total storage capacity at about 630 million m<sup>3</sup> (1.8 TWh), and a working volume of ~279 million m<sup>3</sup> (0.8 TWh). This is only 22% of the energy contained today in the natural gas working volume.

### 3.3.6 Conclusions and future research

In this study we applied the combination of the Inflow Performance Relationship (IPR) (Vogel, 1968) and the Vertical flow performances (VFP) (outflow) analysis to investigate the potential performances of Underground Hydrogen storages (UHS) relative to current Underground natural Gas Storages (UGS).

#### 3.3.6.1 Conclusions

Based on our results -especially those from Grijpskerk- we can conclude the following:

- The lower density (8-10 times) and viscosity (1.3-3 times) of hydrogen relative to methane results in 2.4 to 2.7 times higher withdrawal rates. These high rates partly compensate for the lower energy content (3-4 times lower), resulting in an energy throughput of 0.7 to 0.8 times that of methane.
- We estimated maximum theoretical withdrawal rates for hydrogen up to ~ 33 mln Sm<sup>3</sup>/day for a 7-inch tubing (ID). Yet there are various factors limiting these high rates:
  - Erosional velocity ( $V_e$ ): High flow velocities of gasses/fluids combined with solid particles can cause important erosion-corrosion to the production tubing, which can compromise well integrity. Based on the conservative velocity threshold of 100 m/s, used by many O&G consultancy companies, we lowered our estimated maximum theoretical hydrogen withdrawal rates below 27.4 mln Sm<sup>3</sup>/day (78 GWh/day).
  - Bottom-hole drawdown: High flow rates from the reservoir into the tubing can cause important mechanical damage to the wellbore, leading to a significant reduction of the flow performances. Assuming a skin factor of +1, we estimated bottom-hole drawdown pressures up to 80 bar for hydrogen and 60 bar for methane in Grijpskerk. Details on the structural integrity of the wellbore rock and fluid type -amongst others- can help to determine the degree of flow rate restriction that needs to be applied. Based on inflow/outflow calculations we carried out to match the maximum realized withdrawal rate from the three UGS, we estimate bottom-hole drawdowns between 9 and 67 bar. The highest value corresponding to the low permeability reservoir in Alkmaar (67 bar), and the lowest value to the high permeable reservoir in Norg (9 bar) and Grijpskerk (39 bar). The degree of restriction of the theoretical maximum withdrawal rate, due to an excessive bottom-hole drawdown, is progressively higher to that of the erosional velocity for lower permeable reservoirs.
  - Plateau rate: Gas storage performances are reported on the basis of the maximum theoretical flow rate that can be hold constant for a given period of time. For Grijpskerk we estimated that the maximum theoretical withdrawal rate may need to be reduced up to 25% to obtain a constant (plateau) withdrawal rate for a 3 months period (i.e. down to 21.9 mln m<sup>3</sup>/day or 62 GWh/day) (see Table 3-6).
  - The interplay between the three previous factors determines the degree of restriction of the theoretical maximum withdrawal rate for hydrogen. For the case

study of Grijpskerk, we estimated a maximum bottom-hole drawdown for methane around 39 bar for a 7-inch (ID) tubing. Based on this value, we estimate a restriction of the maximum theoretical withdrawal rate for hydrogen most likely below ~20 mln Sm<sup>3</sup>/day. This mass flow corresponds to an energy throughput of 57 GWh/day for a single well (assuming no well interferences). The use of a 9-inch (ID) tubing would significantly increase the withdrawal rate by 57%, yet also the bottom-hole drawdowns up to 140 bar (a 42% increment).

Table 3-6 Summary results of the realized natural gas and estimated (hydrogen) withdrawal and injection rates and working/cushion volumes for the three UGS and one salt cavern. For Zuidwending the realized withdrawal and injection rates for natural gas are as reported in the Zuidwending storage plan. Volumes of working gas and cushion gas for natural gas were extracted from the storage licenses www.nlog.nl. (\*) Realized daily rates are based on values reported by the operator NAM. (\*\*) Estimated range of maximum theoretical withdrawal rates for hydrogen based on bottom-hole and erosional velocity restrictions. Working gas and cushion gas volumes for hydrogen calculated using working pressure range as currently used for natural gas. (n.a.) Rates not available (realized) or further analysis are required to generate a good estimate (estimated).

| (CH <sub>4</sub> -realized*/<br>H <sub>2</sub> -est.**) |                              | Grijpskerk        |                   | Norg              |                   | Alkmaar           |                   | Zuidwending       |                   |
|---|------------------------------|-------------------|-------------------|-------------------|-------------------|-------------------|-------------------|-------------------|-------------------|
|   |                              | CH <sub>4</sub> * | H <sub>2</sub> ** |
| <b>Max. withdrawal rate</b>                             | million Sm <sup>3</sup> /day | ~8.5              | <20.0-<br>21.9    | ~12.5             | <26.0-<br>28.6    | ~4.0              | <11               | 7.6<br>(avg.)     | n.a.              |
| <b>Max. injection rate</b>                              | million Sm <sup>3</sup> /day | ~5.5              | n.a.              | ~9                | n.a.              | n.a.              | n.a.              | 4.6<br>(avg.)     | n.a.              |
| <b>Volume at max. working pressure (GIIP)</b>           | billion Sm <sup>3</sup>      | 10.8              | 9.9               | 29.4              | 24.7              | 3.8               | 3.2               | 0.76              | 0.61              |
| <b>Working Gas Volume (WGV)</b>                         | billion Sm <sup>3</sup>      | 2.5               | 3.5               | 6.3               | 7.9               | 0.56              | 0.76              | 0.38              | 0.29              |
| <b>Cushion Gas Volume (CGV)</b>                         | billion Sm <sup>3</sup>      | 8.3               | 6.4               | 23.0              | 16.8              | 3.3               | 2.4               | 0.37              | 0.32              |
| <b>WGV : CGV ratio</b>                                  | -                            | 0.3               | 0.54              | 0.27              | 0.47              | 0.18              | 0.33              | 1.02              | 0.90              |

- We calculated the working volume for the three reservoirs at their maximum working pressure (Grijpskerk 393 bar, Norg 327 bar and Alkmaar 218 bar) and for different pressure depletions. Each working volume -associated to a constant wellhead pressure- was calculated based on the average final reservoir pressure at the time when the single-well withdrawal rate dropped below a given cut-off rate. For this study we chose a cut-off rate of 1 mln Sm<sup>3</sup>/day for hydrogen and methane, since we considered to be a reasonable minimum performance for a single well. One million Sm<sup>3</sup> per day of hydrogen and methane is equivalent to an energy throughput of 3 and 10 GWh/day, respectively. Based on these results we can conclude the following:
  - We could reproduce the ratio between the current working volume and the maximum working volume (or GIIP, the amount of Gas Initially In Place in the reservoirs) (in bcm) for the three UGS facilities Grijpskerk (2.5/10.8), Norg (6.3/29.4) and Alkmaar (0.56/3.81) by depleting the reservoirs down to a pressure of 278 bar, 243 bar and 184 bar, respectively (see Table 3-6). This means the percentage of gas in these storages that is currently used as working volume is 23%, 21% and 14% of the GIIP. The corresponding working volumes of hydrogen at the same pressure (case 1) would be 2.2, 5,5 and 0.48 bcm, and slight higher, 3.5, 7.9 and 0.76 bcm, when using the 1 mln Sm<sup>3</sup>/day cut-off rate (case 2) (see Table 3-6). This means that the working volume of hydrogen would contain only 24% (case 1) and 37% (case 2) of the energy contained in the original working volume of methane. For an UHS, the option of depleting the

reservoir below the currently minimum working pressures in the three UGS, would require a reservoir integrity study to estimate the potential negative impact at the surface in the form of surface subsidence and/or induced seismicity. This is an important consideration, since the lowering of the minimum working pressure not only would increase the working volume, but also reduce the cushion volume, which is one of the most expensive elements of an UHS.

- In general we observe higher injection rates for hydrogen than for methane at higher wellhead pressures. Despite the higher density (weight) of the methane, this gas has also a higher viscosity, which at high flow rate apparently hampers injection into the reservoir. For the case of Grijpskerk we observe that only for lower injection rates, below 6 mln Sm<sup>3</sup>/day, this effect seems to decrease in favor of the gravitational pull facilitating the injection, as lower wellhead pressures are required for the injection of methane than for hydrogen. For Grijpskerk we estimate maximum theoretical injection rates for hydrogen up to 35 mln Sm<sup>3</sup>/day through a 7-inch (ID) tubing. These high injection rates will also be limited by the erosional velocity and bottom-hole build-up as previously discussed for withdrawal. Further research is needed to obtain a good estimate of the feasible maximum theoretical injection rates.
- For a standard salt cavern, such that in Zuidwending, we estimate very high theoretical withdrawal rates of hydrogen up to 35 mln Sm<sup>3</sup>/day through a well with a 9-inch tubing (ID). This is 3-4 times faster than that of well in a salt cavern filled with natural gas, and 1.5 to 2.5 times faster than a well in a porous reservoir filled with hydrogen.
- Differently from porous reservoirs though, we observe that the very high theoretical withdrawal rates and the working volumes in salt caverns are primarily limited by daily allowable pressure depletion in order to preserve the structural integrity of the cavern and reduce the loss of (geometric) volume due to salt creep. For Zuidwending the depletion is limited to less than 10 bar per day. Based on this restriction, we observe that salt caverns in the Zuidwending storage site cannot exceed the withdrawal rate of 7.3 million Sm<sup>3</sup>/day of natural gas per cavern (67 GWh/day, each cavern has two wells), which is 1.6 times lower than the 12 mln Sm<sup>3</sup>/day we estimated as the theoretical maximum rate per well. In the case of hydrogen the maximum per cavern withdrawal rate we obtained is 5.2 million Sm<sup>3</sup>/day (15GWh/day), which is almost 7 times lower than the theoretical maximum of 35 mln Sm<sup>3</sup>/day per well.
- The importance of the daily pressure depletion restriction also applies to the working volume available in a salt cavern, which in Zuidwending is currently only 50% of the total storage capacity. In case Zuidwending would be operated at the same pressure range of today, yet storing hydrogen instead of natural gas, the energy content of the hydrogen working volume would be only 22% of the 3.6 TWh available today as natural gas. This is due to the faster pressure drop in the salt cavern during the withdrawal of hydrogen.
- Despite the good quality of the Grijpskerk and Norg reservoirs, these reservoirs require a large cushion volume to deliver high performances. This is due to their large size and great depth. These reservoirs were converted to UGS because - amongst other reasons- part of the cushion gas needed had not yet been produced giving the advantage of earlier commissioning. As described by Juez-Larré et al. (2016), there are many other potential porous reservoirs in the Netherlands, which could also be good candidates for UHS.

### 3.3.6.2 Future research

- Expand the model from unary/binary gas mixtures and multi-phase component.
- Incorporate thermal effects during injection cycles as the injected gas may be at lower temperature to that of the reservoir and cushion gas. An analytical solution could be incorporated in the current GaSP-tool, which could be validated against results from a numerical modelling.
- Carry out a more detailed study on model parameters uncertainty.
- Investigate in more detail the factor influencing the injection performance.
- Study different types of well configurations to reduce the limitations of the erosional velocity thresholds.

### 3.4 Geo- and biochemistry of H<sub>2</sub> storage in depleted gasfields

Underground storage of hydrogen is currently considered as one of the potential options to store energy at a large-scale. While there is a lot of experience with storage of natural gas in salt caverns, depleted fields and aquifers, and some experience with hydrogen storage in salt caverns (in the UK and the US; see Section 3.2), the storage of hydrogen in depleted gas fields and aquifers is not a mature technology. To advance this technology towards commercial-scale implementation, several open research questions must be addressed to clarify if hydrogen can be safely and economically stored, and with no adverse effects to the environment.

One of the main uncertainties is the possibility of hydrogen-fluid-rock interactions in the storage reservoir. These reactions may:

- a. Produce toxic fluids (e.g. H<sub>2</sub>S) that pose a threat to environment, health and safety;
- b. Produce corroding fluids (e.g. H<sub>2</sub>S) that affect well integrity;
- c. Reduce the porosity and/or permeability of the reservoir by precipitation of minerals; and
- d. Lead to loss of hydrogen, e.g. by microbial activity, or degradation of purity by pollution of H<sub>2</sub> with other gases in the reservoir that are co-produced upon withdrawal from storage.

Furthermore, when storing hydrogen in a depleted field, large volumes of cushion gas will have to be injected to keep the working pressure in the reservoir above a threshold minimum value. In reservoirs used for underground (natural) gas storage, the residual gas in the reservoir upon cessation of production can serve as cushion gas, and further pressure support is provided by injecting natural gas, which constitutes an additional investment. However, in the case of underground hydrogen storage (UHS) in reservoirs, this additional investment would potentially be much higher, because of the significantly higher production costs for H<sub>2</sub> compared to natural gas. Investment costs could be significantly reduced if other gases with lower unit cost could be used as cushion gas.

In this section, we detail the results of geo- and biochemical numerical simulations to analyse the impact of a) hydrogen-fluid-rock interactions in the storage reservoir; b) interactions of hydrogen with other (cushion) gases, in particular CO<sub>2</sub> and N<sub>2</sub>, and c) potential biochemical reactions in storage reservoirs in the presence of H<sub>2</sub>. First, in subsection 3.4.1, we describe the results of a literature review on recent experimental and numerical modelling work in these fields to identify which are the main geochemical reactions and biochemical processes to focus on. Next, in subsection 3.4.2, we explain the methodology, the software (PHREEQC and TOUGHREACT-EWAGS), and the input data that were used for the analysis. In subsection 3.4.3 we present and discuss the results of geo- and biochemical simulations with PHREEQC, followed by the results of near-wellbore injection simulations with TOUGHREACT-EWAGS in subsection 3.4.4. Finally, in Section 3.4.5, we present our conclusions, discuss the implications, and make suggestions for future research.

### 3.4.1 Literature review on geo- and biochemical interactions with H<sub>2</sub> in porous reservoirs

In the early days of hydrogen storage feasibility research in the 1970's, it was already proposed that hydrogen may react with sulphide, sulphate, carbonate and oxide minerals in the host formation, while leaving the stable silicates unaffected (Carden and Paterson, 1979; Foh 1979). The main concern raised was the formation of toxic and corrosive gasses such as hydrogen sulphide (H<sub>2</sub>S). Consequently, reservoirs containing these minerals were advised not to be used as storage reservoirs.

Crotogino et al. (2010) state that microbiological or mineralogical reactions may lead to deterioration or loss of the stored hydrogen and that reaction products can plug the pore space. Reitenbach et al (2015) state that the introduction of gaseous hydrogen in the reservoir can lead to the formation of H<sub>2</sub>S (a weak acid) via reduction of sulphide minerals. Furthermore, it may lead to degassing of CO<sub>2</sub> or evaporation of water into the gaseous hydrogen phase. These effects can drive changes in pH or in solute activity which can drive mineral reactions in the reservoir and caprock such as dissolution of carbonate- and sulphate minerals, feldspars and clay minerals of the chlorite group and precipitation of illite, iron sulphide and pyrrhotite. At higher temperatures (60-90 °C) the H<sub>2</sub>/H<sub>2</sub>O redox system becomes more active as an electron donor and can support metal oxidation processes which can lead to corrosion of wellbore materials. These processes can be inhibited by minerals such as siderite, dolomite or calcite, and can be promoted by microbiological activity (Reitenbach et al., 2015). Besides the reported theoretical considerations of the effects of hydrogen storage, limited laboratory, numerical or field research has been done on hydrogen-rock-fluid interactions in storage reservoirs or salt caverns.

Results of the few modelling studies reported are not always consistent. This can partially be attributed to the formation-water specific and mineralogy-specific nature of hydrogen-water-rock reactions. Lassin et al. (2011) found that when hydrogen dissolves in the formation water, the pH could increase. Their modelling study shows an increase in pH from 7.4 to between 10 and 12 depending on the temperature (higher pH for lower temperatures). This pH change was attributed to the reaction of  $\text{SO}_4^{2-} + 4 \text{H}_2 \leftrightarrow \text{HS}^- + \text{OH}^- + 3 \text{H}_2\text{O}$ . However, if sulphate reduction is kinetically limited and the pH is buffered by rock minerals, H<sub>2</sub> will act as if it was an inert gas (Lassin et al., 2011). A PHREEQC numerical modelling study of Hemme and van Berk (2018) indicated a loss of hydrogen by bacterial conversion to methane. The authors modelled biotic and abiotic processes in one model, hence their conclusions on inorganic processes could reflect coupled processes. The predicted mineral reactions result in a small decrease of porosity. However, the reaction rate of minerals was not taken into account in the models.

Truche et al. (2010, 2013) report experiments on hydrogen and pyrite and pyrite-enriched clays at 90 to 250 °C, which showed production of sulphide (mainly H<sub>2</sub>S) in the fluid phase, with faster reaction rates at higher temperatures. The general reaction was thought to be the transformation of pyrite to pyrrhotite ( $\text{FeS}_2 + (1-x)\text{H}_2 = \text{FeS}_{1+x} + (1-x) \text{H}_2\text{S}$  with  $0 < x < 0.125$ ). This mineralogical change was observed with SEM to occur above 200 °C with variable hydrogen pressures. At 150°C a high (30 bar) H<sub>2</sub> partial pressure is required for a high degree of mineral reactions. Clay, quartz, carbonate and feldspars remained unaltered. Besides the effect of the hydrogen pressure and temperature, the initial pH largely controls pyrite dissolution. With claystone and a pH between 5 and 7, pyrrhotite only precipitated at 150 °C - 30

bar and not at lower PT conditions. In alkaline calcite-buffered systems and a pH between 8 and 10, pyrrhotite formation can already occur at 90 °C (Truche et al., 2010). Hence acidic reservoirs may be more suitable to prevent H<sub>2</sub>S formation (Truche et al, 2013).

Yekta et al., 2018 performed abiotic batch experiments with H<sub>2</sub> and sandstones at 100 to 200 °C and 10 to 50 bar. Although XRD and SEM did not show mineralogical changes, microprobe analyses indicated an iron decrease in muscovite. PHREEQC geochemical simulations showed no effect to the main minerals like quartz and feldspars, but high saturation indices for iron silicates (Yekta et al., 2018). The models predicted the reduction of Fe<sup>3+</sup> to Fe<sup>2+</sup> and a minor reaction of hematite to magnetite ( $3 \text{ Fe}_2\text{O}_3 + \text{H}_2 \leftrightarrow 3 \text{ Fe}_3\text{O}_4 + \text{H}_2\text{O}$ ). However, it was concluded that for the studied sandstones, abiotic geochemical reactions will have a minor effect on porosity and permeability (Yekta et al. 2018). The reduction of iron in mineral phases was also shown for clay by Didier et al. (2012). They measured hydrogen gas adsorption on both synthetic clays with 0 to 6.4 wt.% structural Fe(III) and Callovo-Oxfordian clay rock at 90 and 120 °C under a hydrogen partial pressure of 0.45 bar. Didier et al. (2012) showed that up to 0.11 wt. % of hydrogen is adsorbed and that up to 6% of the structural Fe(III) in synthetic clays is reduced upon adsorption of hydrogen. In potential storage reservoirs in the Dutch subsurface (reservoirs currently used for UGS, or gasfields that are nearing depletion), the temperatures are generally lower than the temperature of 150 °C for which significant reactions were observed in past experiments. However, the hydrogen partial pressure during storage will likely exceed the 30 and 50 bar pressure applied in the experiments, and this will increase reactivity.

Hematite present in the reservoir can be a small sink for hydrogen. When hematite reacts with hydrogen it is reduced to magnetite and subsequently magnetite is reduced to iron. This reaction produces water. Thüns et al. (2019) studied these processes at 200 °C showing the influence of H<sub>2</sub> pressure on the kinetic reaction rates. At higher partial pressures the conversion rates of hematite to magnetite to iron will accelerate, but the water that is produced in the first step from hematite to magnetite will inhibit the reaction of magnetite to iron. Therefore, it is expected that when hydrogen is stored in an empty gas reservoir hematite will be reduced to magnetite but reduction of magnetite to iron will not occur.

In summary, and based on the concise literature review as described, the geochemical processes that could be of concern for hydrogen storage in the Netherlands are:

- Reduction of iron minerals (pyrite) forming H<sub>2</sub>S;
- Reduction of hematite to magnetite, sequestering H<sub>2</sub> and producing H<sub>2</sub>O;
- Reduction reactions and H<sub>2</sub>S formation change the fluid composition and pH, possibly resulting in precipitation and dissolution of secondary minerals (changing the pore space);
- Reactivity of wellbore materials impacting well integrity;
- Hydrogen adsorption in clay.

Here, the first three were selected for numerical assessment, i.e., formation of toxic, corrosive agents such as H<sub>2</sub>S, mineral dissolution and precipitation, and acidification due to changes in formation water speciation and pH.

### 3.4.2 Methodology

#### 3.4.2.1 Software

A reactive transport model was developed using TOUGHREACT software Version 3 (Xu et al., 2006; Xu et al., 2014). The simulator introduces reactive chemistry into the TOUGH2 simulator on multiphase and multicomponent fluid flow in porous and fractured media (Pruess et al., 2011). Our work was aimed at using a newly acquired TOUGHREACT executable for the EWASG equation of state. The EWASG (Water-Salt-Gas) fluid property module was developed by Battistelli et al. (1997) for modelling geothermal reservoirs with saline fluids and non-condensable gas (NCG). Salt used to be the only mineral phase, but now the full chemistry can be modelled with EWASG. EWASG represents the components water, NaCl, NCG as three-phase mixtures. The choices of NCG's are CO<sub>2</sub>, air, CH<sub>4</sub>, H<sub>2</sub> and N<sub>2</sub> (one gas is selected, mixtures are not possible). The thermophysical property correlations used in EWASG are accurate for temperatures in the range from 100 to 350 °C, fluid pressures up to 80 MPa, CO<sub>2</sub> partial pressures up to 10 MPa, and salt mass fraction up to halite saturation (Pruess et al., 2011, Battistelli et al. 1997). We used the (unmodified) geochemical database Thermodem (V1.10\_06Jun2017) developed by the BRGM (Blanc et al., 2012; <http://thermoddem.brgm.fr/>).

The software PHREEQC was used for batch (0D) modelling of the geochemical interaction of minerals and hydrogen dissolved in the pore fluid. PHREEQC version 3 is a computer program provided by the US Geological Survey written in the C and C++ programming languages that is designed to perform a wide variety of aqueous geochemical calculations (Parkhurst and Appelo, 1999). Geochemical simulations require a thermodynamic database containing parameters for mineral solubility and equilibrium constants. Several databases are available for PHREEQC and can be user selected. We used the geochemical database Thermodem (V1.10\_06Jun2017) developed by the BRGM (Blanc et al., 2012; <http://thermoddem.brgm.fr/>). We modified this database to remove the redox coupling of sulphate to sulphide, which is kinetically inhibited. Similar to Truche et al., (2010) we suppressed the kinetically inhibited redox reactions involving reduced carbon species (reduction of calcite and HCO<sub>3</sub> into methane). Mineral reactions were simulated assuming instantaneous reaction to achieve a chemical equilibrium. Kinetic reaction rates were not implemented because the required fitted data was not available.

A PHREEQC model was developed in which chemical reactions are simulated in three steps:

1. Equilibrating the measured water composition with a gas phase containing methane and small amount of CO<sub>2</sub> and a formation specific set of equilibrium phases;
2. Equilibrating the formation water of step 1 with cushion gas and fast reacting minerals (carbonates and anhydrite). Reactions with the cushion gas are simulated at half the reservoir pressure (optional step);
3. Equilibrating the solution of step 2 with the reservoir minerals and a gas phase containing hydrogen and traces of CH<sub>4</sub> and CO<sub>2</sub>. Reactions are simulated at initial reservoir pressure and temperature.

### 3.4.2.2 PHREEQC model input

Dutch gas reservoirs occur at depths ranging from 500-3500 meters and therefore storage of hydrogen in those reservoirs can occur at varying temperatures and pressure, because both are a function of depth. P/T conditions associated with this depth interval were modelled. The temperature and pressure at the different depths were calculated by assuming a thermal gradient of 30 °C per km, starting at 35 °C at a depth of 500 meters (

Table 3-7). The pressure was calculated by assuming a pressure gradient of 10 bar per 100 meters. The influence of P/T was investigated by modelling three depth intervals for the different storage reservoir compositions.

Table 3-7: Modelled P/T conditions and associated depth.

| Temperature (°C) | Depth (m) | P (bar) |
|------------------|-----------|---------|
| 35               | 500       | 50      |
| 45               | 1000      | 100     |
| 60               | 1500      | 150     |
| 75               | 2000      | 200     |
| 90               | 2500      | 250     |
| 105              | 3000      | 300     |
| 120              | 3500      | 350     |

Another important parameter in this system is the presence of CO<sub>2</sub> in the reservoir. The influence of CO<sub>2</sub> is important to investigate because in many of the Dutch reservoirs CO<sub>2</sub> is already present, and hydrogen storage with CO<sub>2</sub> as cushion gas would be very attractive economically because the cushion gas that is required to support a minimum storage pressure would then not require an investment, and may even contribute to the earnings of the project because CO<sub>2</sub> has a negative value (carbon credit), i.e., storage of H<sub>2</sub> could then be combined with CO<sub>2</sub> sequestration. Therefore, the influence of CO<sub>2</sub> was investigated by modelling the gas-fluid-rock interactions with hydrogen gas and saturated with CO<sub>2</sub>.

Four case studies representative for the Dutch subsurface were modelled. The majority of the gas reservoirs are in in the Buntsandstein, Rotliegend and Zechstein formations (see Figure 3.26; Juez-Larré et al., 2016). Therefore these cases were studied as well as a Delft sandstone case. Mineralogical data for these four reservoirs was collected from earlier projects as well as from literature (see Table 3-8). Formation water data from wells that were drilled in each reservoir were taken from an internal formation water data-set (see Table 3-9). It must be noted here that the fluid composition and rock composition were not always in equilibrium. Several minerals were added to the measured composition because they were predicted to be oversaturated and are assumed to be expected in these reservoirs. The minerals of interest for hydrogen-rock interaction (pyrite and hematite) were included in equal amounts in all models for easy comparison of the model results. The volume of water after gas storage is calculated as filling 20% of the porosity, assuming a gas saturation of 0.8. Concentrations of minor elements for which no data was present are calculated in equilibrium with the minerals. Sulphate and sulphide concentrations were also calculated in equilibrium with the minerals to achieve the right relative concentrations.

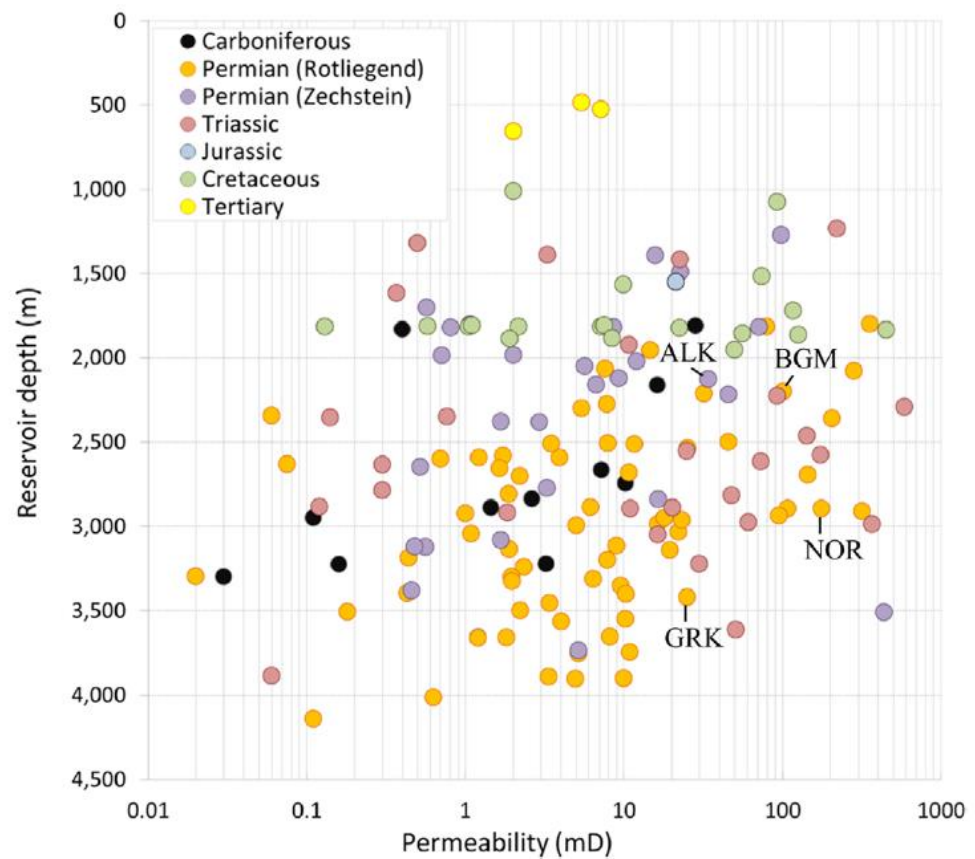


Figure 3.26: Depth and permeability distribution of gas reservoirs per formation (Buntsandstein is Triassic) (Juez-Larré et al.2016)

Table 3-8: Mineralogical data from the Buntsandstein, Rotliegend, Delft and Zechstein formation. In the calculations an average porosity of 20% is assumed.

| <b>Buntsandstein</b>                                   | <b>Mass fraction</b>        | <b>Mol in 1 dm<sup>3</sup> medium</b> |
|--|-----------------------------|---------------------------------------|
| Quartz   | 0.74                        | 26.09                                 |
| Microcline   | 0.125                       | 0.92                                  |
| Muscovite/Illite–Smectite<br>(Smectite(MX80:3.989H2O)) | 0.06                        | 0.36                                  |
| Dolomite   | 0.05                        | 0.62                                  |
| Siderite   | 0.02                        | 0.54                                  |
| hematite   | 0.005                       | 0.2                                   |
| <b>Rotliegend</b>                                      | <b>Mass fraction</b>        | <b>Mol in 1 dm<sup>3</sup> medium</b> |
| Calcite  | 0.03                        | 0.65                                  |
| Dolomite   | 0.06                        | 0.75                                  |
| Anhydrite  | 0.04                        | 0.70                                  |
| Quartz   | 0.7                         | 24.68                                 |
| Albite (low)   | 0.06                        | 0.48                                  |
| Kaolinite  | 0.03                        | 0.24                                  |
| Illite (Al)  | 0.05                        | 0.29                                  |
| Clinocllore  | 0.02                        | 0.08                                  |
| Pyrite_sg  | added because oversaturated | 0.1                                   |
| Barite_sf  | added because oversaturated | 0.1                                   |
| Hematite   | added because oversaturated | 0.2                                   |
| Siderite   | added because oversaturated | 0.1                                   |
| <b>Zechstein</b>                                       | <b>Mass fraction</b>        | <b>Mol in 1 dm<sup>3</sup> medium</b> |
| Quartz   | 0.46                        | 16.22                                 |
| Illite (Al)  | 0.16                        | 0.92                                  |
| Microcline   | 0.02                        | 0.15                                  |
| Albite(low)  | 0.04                        | 0.32                                  |
| Calcite  | 0.11                        | 2.38                                  |
| Dolomite   | 0.21                        | 2.61                                  |

| Delft sandstone                      | Mass percentage             | Mol in 1 dm <sup>3</sup> medium |
|--------------------------------------|-----------------------------|---------------------------------|
| Quartz(alpha)                        | 81.3                        | 108.5                           |
| Calcite                              | 13.6                        | 10.9                            |
| Siderite                             | 0.5                         | 0.35                            |
| Pyrite_sg                            | 0.1                         | 0.1                             |
| Kaolinite                            | 2.4                         | 0.75                            |
| Smectite(MX80:3.989H <sub>2</sub> O) | 1.7                         | 0.36                            |
| Hematite                             | added because oversaturated | 0.2                             |

Table 3-9: Formation water composition (mg/l) used as input data

| Well<br>Formation              | L08-10-S1<br>Buntsandstein | P05-02<br>Rotliegend | SLD-01<br>Zechstein | Delft SS |
|--------------------------------|----------------------------|----------------------|---------------------|----------|
| Initial pH                     | 6.4                        | 6                    | 6.4                 | 6.2      |
| Temp (°C)                      | 20                         | 20                   | 18                  | 20       |
| Na (Sodium)                    | 70300                      | 43240                | 51520               | 38800    |
| K (Potassium)                  | 1170                       | 21200                | 3970                | 458      |
| Ca (Calcium)                   | 8700                       | 345                  | 9520                | 6190     |
| Mg (Magnesium)                 | 1400                       | 48400                | 580                 | 983      |
| Ba (Barium)                    | 30                         | 0.03                 |                     | 8.24     |
| Fe (Iron)                      | 46                         | 86                   |                     | 72.1     |
| Cl (Chloride)                  | 118000                     | 214490               | 102820              | 75710    |
| SO <sub>4</sub> (Sulphate)     | 1060                       | 17800                | 880                 | 200      |
| HCO <sub>3</sub> (Bicarbonate) | 98                         | 195                  | 120                 | 151      |
| SiO <sub>2</sub> (Silica)      | 26.1                       |                      |                     | 118.4    |

### 3.4.3 Simulation results PHREEQC

#### 3.4.3.1 Hydrogen interaction for different geological formations

The hydrogen-induced reactions are compared for four geological formations in the Dutch subsurface that may have potential to be used for hydrogen storage: the Zechstein, Buntsandstein, Rotliegend and Delft geological formations. All have different mineralogical compositions and water compositions. The water and mineral compositions that equilibrated at reservoir conditions were brought in contact with a gas phase containing hydrogen and trace amounts of CH<sub>4</sub> and CO<sub>2</sub>. The predicted H<sub>2</sub>-water-rock interactions for two of the four formations are characterised by pyrite (FeS<sub>2</sub>) dissolution and pyrrhotite (FeS) precipitation, in particular for the pyrite-containing rocks of the Rotliegend and Delft formations (Figure 3.27, left column of graphs). In this modelling exercise it is assumed that the kinetics of the reaction is not limiting the reaction. The pyrite to pyrrhotite reduction will create H<sub>2</sub>S in the aqueous phase that will result in the partitioning of H<sub>2</sub>S in the gas phase to form H<sub>2</sub>S gas. For the Rotliegend, 1.55 ppm H<sub>2</sub>S is formed and for the Delft sandstone 0.01 ppm H<sub>2</sub>S (at 3000m depth P/T; see Table 3-10). No H<sub>2</sub>S is formed in the Zechstein and Buntsandstein cases since there was no pyrite in the measured mineralogical composition. It is possible that pyrite was present in concentrations below the detection limit. Note that these predictions may not be true for the formations in general since mineralogical compositions are variable.

The concentration is of H<sub>2</sub>S in the gas phase related to H<sub>2</sub>S generated by pyrite reduction also depends on the kinetic rate of the mineral reactions and on the presence of H<sub>2</sub>S scavenging minerals, currently not modelled. The understanding of the kinetic rate constants is limited, especially at high H<sub>2</sub> partial pressure and will require future research.

These modelling results show that pyrite reduction as a result of H<sub>2</sub> storage may occur, leading to H<sub>2</sub>S formation in the gas phase, which may affect safety, materials selection, facility design and economics. Further efforts into the most accurate prediction of in-reservoir H<sub>2</sub>S concentrations will require incorporation of kinetic rates at high temperatures and high H<sub>2</sub> partial pressures, as well as H<sub>2</sub>S scavenging reactions and transport in the reservoir.

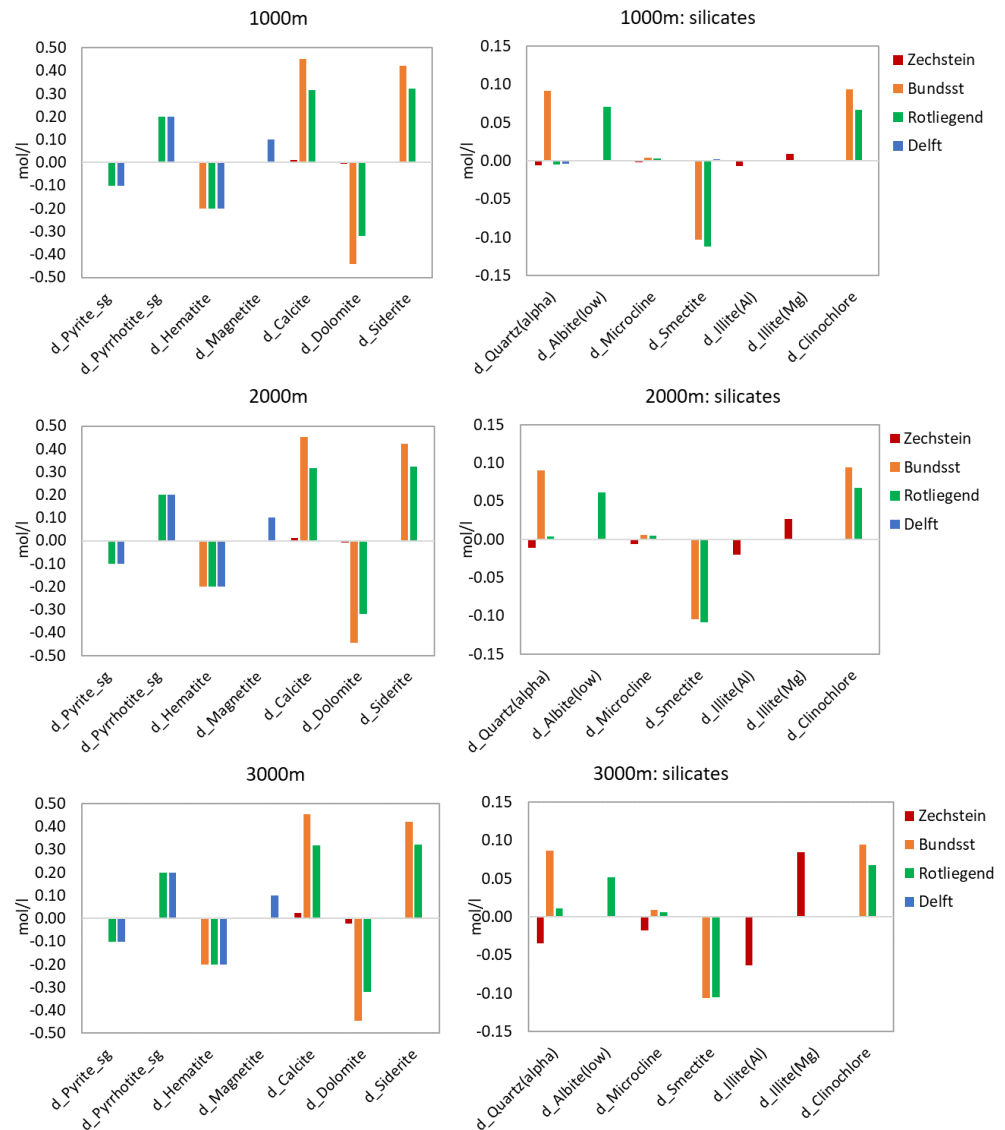


Figure 3.27: Mineral reactions due to hydrogen storage at different depths.

Besides pyrite, hematite dissolves in contact with dissolved hydrogen. The Delft sandstone shows the hematite (Fe<sub>3</sub>O<sub>3</sub>) to magnetite (Fe<sub>3</sub>O<sub>4</sub>) reaction (Figure 3.27, left column of graphs). The Rotliegend and Buntsandstein cases predict hematite dissolution and the precipitation of iron containing siderite (FeCO<sub>3</sub>) which appears to be preferred over magnetite formation. The cases with hematite dissolution show an increase of water content as expected for the reduction of hematite. For the Buntsandstein case at 2000 m, interaction with hydrogen results in a water mass increase from 0.04 l to 0.046 l.

The Rotliegend and Buntsandstein contain dolomite ( $\text{CaMg}(\text{CO}_3)_2$ ) which dissolves to form the siderite as well as calcite ( $\text{CaCO}_3$ ). The dissolution of dolomite releases magnesium in solution which causes a tendency for clay transformations. For the Zechstein this is expressed by aluminium-illite dissolution and magnesium-illite precipitation (Figure 3.27, right column of graphs). For the Buntsandstein and Rotliegend cases, the aluminium, magnesium and iron containing smectite dissolves and the magnesium richer clinocllore ( $\text{Mg}_5\text{Al}(\text{AlSi}_3)\text{O}_{10}(\text{OH})_8$ ) forms. For the Buntsandstein case this reaction is accompanied by quartz precipitation and for the Rotliegend case, albite precipitation is predicted. The Rotliegend contains anhydrite and barite which show minor (too small to visualize) precipitation and dissolution respectively.

### 3.4.3.2 Depth dependence of H<sub>2</sub>-water-rock reactions

Geochemical reactions were simulated at different depths to investigate the effect of pressure and temperature on hydrogen-water-rock interactions. The main reactions are the same at 1000, 2000 and 3000m, with full dissolution of pyrite and hematite at all depths (Figure 3.27, left column of graphs). There are small increases in precipitation and dissolution with depth. For example, the Zechstein case shows an increase of calcite precipitation with depth from 1.03E-02 and 1.11E-02 to 2.35E-02 mol. The most pronounced difference with depth is the increasing illite transition from aluminium to magnesium-rich as observed for the Zechstein mineralogy (Figure 3.27, right column of graphs). Although the same amount of pyrite dissolves at all depths, the amount of H<sub>2</sub>S increases with depth as the partial pressure increases (Table 3-10). The large increase of released H<sub>2</sub>S gas is illustrated for the Rotliegend case, showing results simulated for depths between 500 and 3500 m (Figure 3.28).

Table 3-10: Partial pressure and amount of H<sub>2</sub>S for different depths.

|            |                   | 1 km  | 2 km  | 3 km  |                           | 1 km   | 2 km   | 3 km  |
|------------|-------------------|-------|-------|-------|---------------------------|--------|--------|-------|
| Delft      | pH <sub>2</sub> S | 4.66E | 3.67E | 3.21E | H <sub>2</sub> S<br>(ppm) | 4.66E- | 1.84E- | 0.011 |
|            |                   | -08   | -07   | -06   |                           | 04     | 03     |       |
| Rotliegend | pH <sub>2</sub> S | 1.86E | 9.35E | 4.64E | H <sub>2</sub> S<br>(ppm) | 0.186  | 0.467  | 1.55  |
|            |                   | -05   | -05   | -04   |                           |        |        |       |

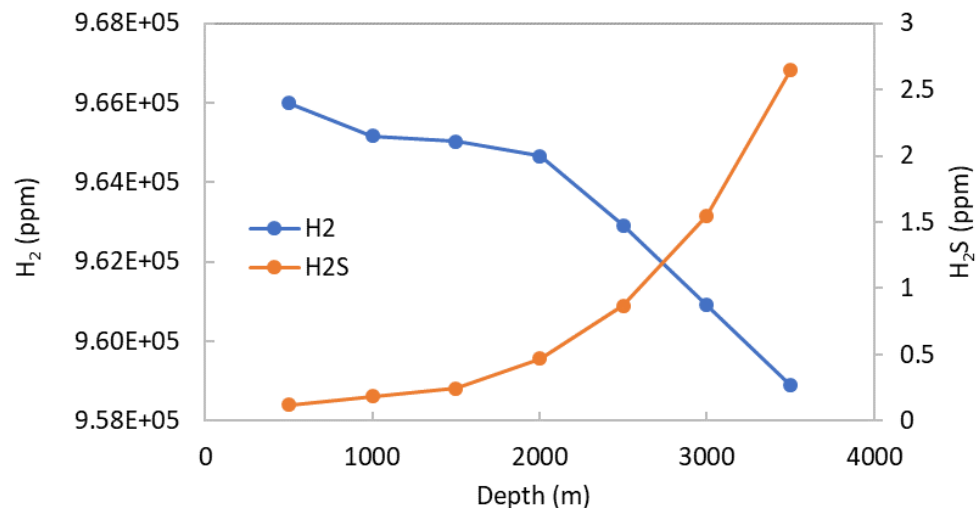


Figure 3.28: H<sub>2</sub> and H<sub>2</sub>S amount with depth for the Rotliegend case

### 3.4.3.3 Effect of pyrite and siderite content on H<sub>2</sub>S formation

The model results of the Delft and Rotliegend sandstones show that all pyrite is consumed when the minerals interact with stored hydrogen. With more pyrite present, the amount of H<sub>2</sub>S formed can be higher. The Rotliegend mineralogy model is run with increasing pyrite content at conditions corresponding to a depth of 2000m. The models predict that below a pyrite content of 0.5 mol/dm<sup>3</sup> medium, the amount of H<sub>2</sub>S formed slightly increases from 0.464 to 0.468 ppm as H<sub>2</sub> is consumed (Figure 3.29). The amount of siderite formed also decreases. With higher pyrite concentrations, all siderite is consumed, H<sub>2</sub>S scavenging by siderite no longer occurs and a large rise in the H<sub>2</sub>S amount to 368 ppm is predicted. Maximum H<sub>2</sub>S formation is reached with more than 0.6 mol/dm<sup>3</sup> medium. With more pyrite, the pyrite is no longer fully consumed, H<sub>2</sub>S remains constant, and an equilibrium is reached characterised by a very low iron solubility and high amounts of sulphide in solution.

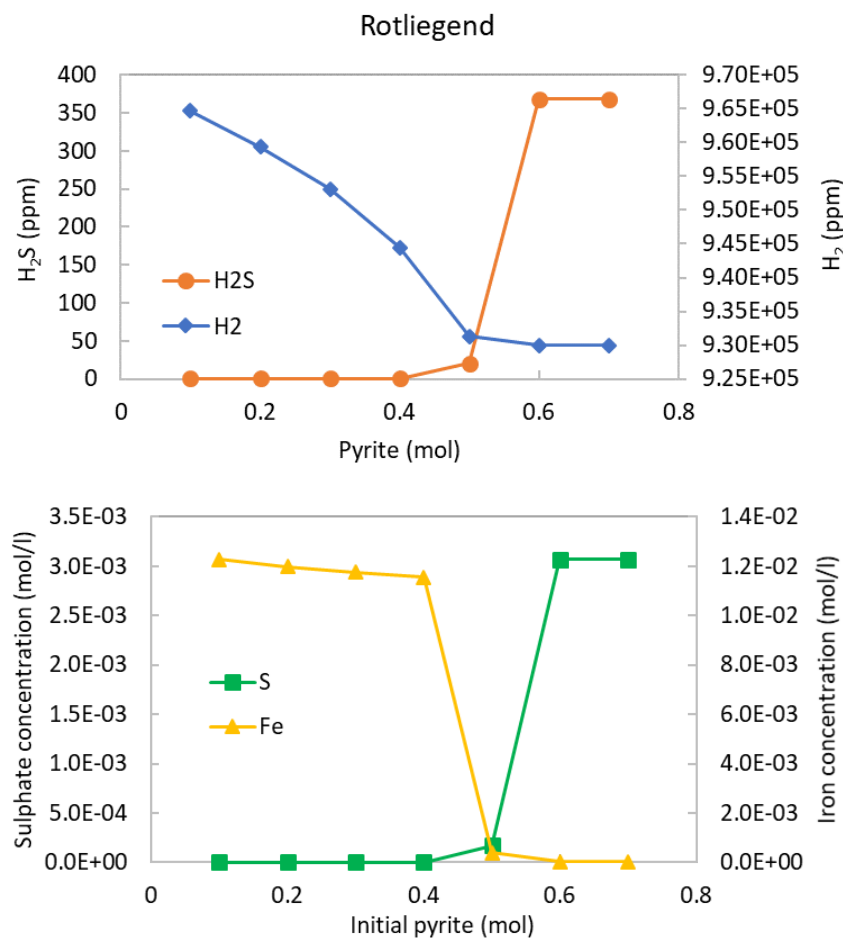


Figure 3.29: a) H<sub>2</sub> and H<sub>2</sub>S amount, b) Dissolved iron and sulphate concentrations with different initial pyrite contents for the Rotliegend case.

The increasing pyrite to pyrrhotite reaction is visible in Figure 3.30. With higher pyrite content and H<sub>2</sub>S release, the carbonate reactions change. With less siderite formed the dolomite to calcite reaction decreases and even reverses. It appears that carbonate is a less favourable sink for iron. With less dolomite dissolution and released magnesium available, the amount of clinocllore precipitated is lower. With high pyrite content and the related low iron in solution, clinocllore dissolution is triggered. This yields an increases in the predicted quartz and albite precipitation.

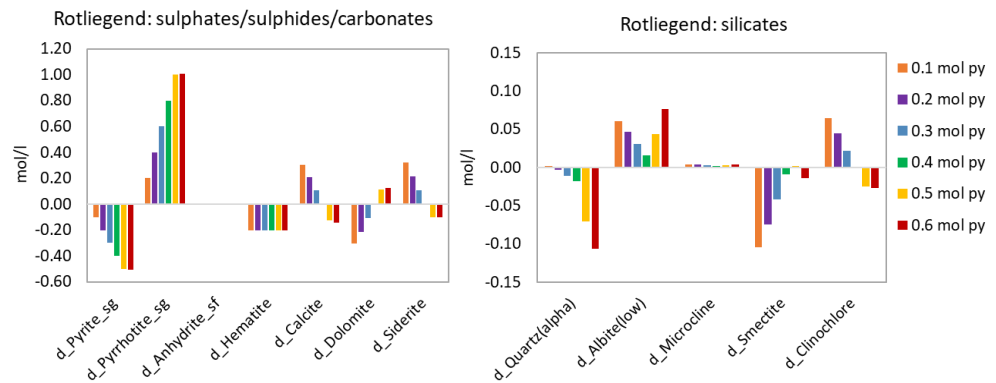


Figure 3.30: Dependence of mineral reactions on amount of pyrite initially present

### 3.4.3.4 CO<sub>2</sub> as cushion gas

CO<sub>2</sub> could be used as a cushion gas for hydrogen storage and is often naturally present in gas fields. Using CO<sub>2</sub> as cushion gas does not directly change the reactions of pyrite and hematite (Figure 3.31). There are only small changes in the reactions, this could be because CO<sub>2</sub> was already present in the models with and without CO<sub>2</sub> cushion gas. There is a slightly larger tendency for siderite formation which is now also observed for the Delft case (compare the two graphs at the top in Figure 3.31 with the two graphs at the bottom). The amount of H<sub>2</sub>S formed is less than one percent different between the cases with and without CO<sub>2</sub>.

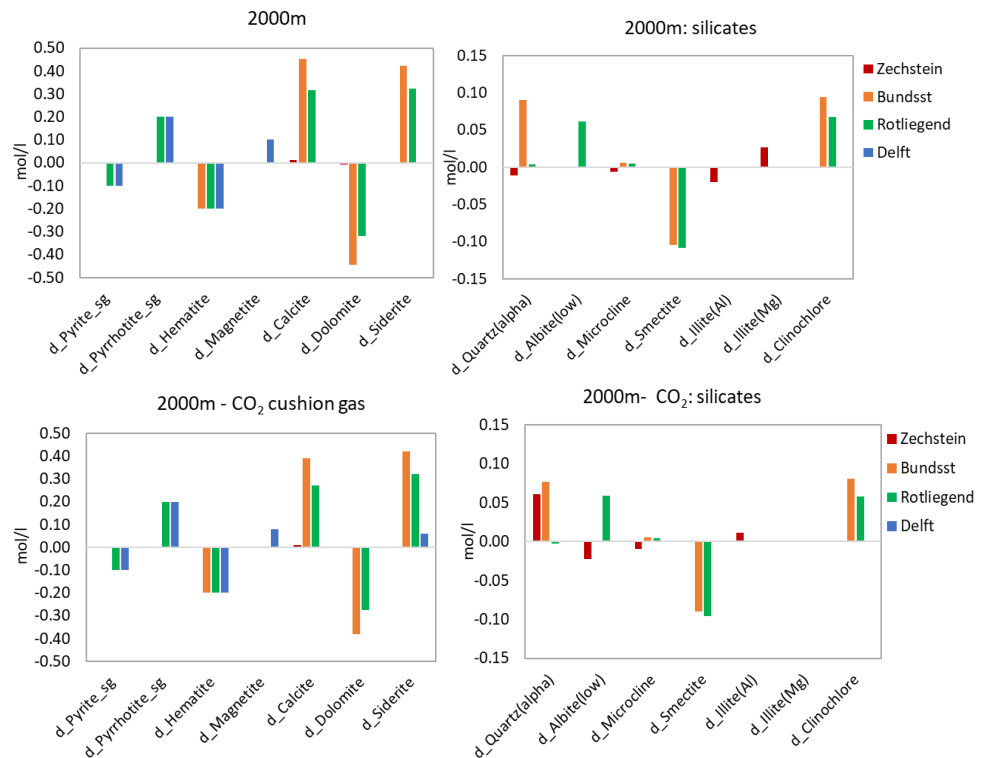


Figure 3.31: Mineral reactions in presence of CO<sub>2</sub> (cushion gas) for different geological formations at 2000m depth. The two graphs at the bottom are the results with CO<sub>2</sub> cushion gas, while the two graphs at the top are base case results, repeated from Figure 3.27 for comparison.

### 3.4.3.5 N<sub>2</sub> as cushion gas

Nitrogen is already widely used as cushion gas in natural gas reservoirs (Laille et al. 1988; Misra et al. 1988) to improve productivity when production rates decline due to lowering of pressure in the reservoir. Similarly, hydrogen storage requires a certain amount of cushion gas to maintain the pressure level in the reservoir such that a certain withdrawal rate can be maintained. Instead of using hydrogen itself as cushion gas, which is very costly, nitrogen could be an interesting option, because it is widely available, cheaper than hydrogen and relatively inert to chemical reactions (Oldenburg, 2003; Oldenburg and Pan, 2013). To explore the geochemical interactions of nitrogen with rocks and fluids in a reservoir used for hydrogen storage, a base case nitrogen model was created in PHREEQC. In this model the sandstone mineralogy from Table 3-11 was used with the addition of calcite. The aim of the model was to investigate any possible influence nitrogen could have on mineral precipitation/dissolution and chemical processes in the reservoir. The simulation was run at a depth of 1000, 2000 and 3000 meters (Table 3-12).

Table 3-11: Sandstone mineralogy used in simulations with N<sub>2</sub> cushion gas

| Sandstone           |   | Vol. Frac. | Mol   |
|---------------------|---|------------|-------|
| 'Hematite'          | Fe <sub>2</sub> O <sub>3</sub>  | 0          | 0     |
| 'Anhydrite'         | CaSO <sub>4</sub>   | 0          | 0     |
| 'Quartz,alpha'      | SiO <sub>2</sub>  | 0.52       | 18.79 |
| 'Albite_low'        | NaAlSi <sub>3</sub> O <sub>6</sub>  | 0.061      | 0.5   |
| 'Microcline'        | K(AlSi <sub>3</sub> )O <sub>8</sub>   | 0.066      | 0.498 |
| 'Smectite MX80_des' | *   | 0.165      | 1.003 |
| 'Clinocllore'       | Mg <sub>5</sub> Al(AlSi <sub>3</sub> )<br>O <sub>10</sub> (OH) <sub>8</sub> | 0          | 0     |
| 'Kaolinite'         | Al <sub>2</sub> Si <sub>2</sub> O <sub>5</sub> (OH) <sub>4</sub>            | 0.085      | 0.702 |
| 'Pyrite'            | FeS <sub>2</sub>  | 0.003      | 0.1   |
| 'Pyrrhotite'        | FeS   | 0          | 0     |
| 'Magnetite'         | Fe <sub>3</sub> O <sub>4</sub>  | 0          | 0     |

Table 3-12: Temperature, depth and pressure used in PHREEQC simulations

| Temperature (°C) | Depth (m) | P (bar) |
|------------------|-----------|---------|
| 45               | 1000      | 100     |
| 75               | 2000      | 200     |
| 105              | 3000      | 300     |

### **Results N<sub>2</sub> as cushion gas**

A first round of simulations was run for the three different depths, and it made clear that the Thermoddem database that was used for the simulations did not work properly. During the simulations the nitrogen and hydrogen were combined to create ammonia. This process is similar to the Haber process and should not occur at reservoir conditions. The Haber process is the process in which ammonia is synthesised, and even though this process occurs at low temperature and high pressure, N<sub>2</sub> and H<sub>2</sub> will only react at temperatures above 1000 °C. In the presence of an iron catalyst this temperature is lowered to 250 to 400 °C (Modak, 2002). This is still well above our maximum reservoir temperature of 105 °C and therefore will not take place. Therefore, it was chosen to add a new nitrogen phase to the model which behaves inert with hydrogen and run the simulation without the ammonia reactions. Therefore, the difference between the N<sub>2</sub> cushion and N<sub>2</sub> inert is that the inert nitrogen will not react with hydrogen.

Figure 3.32, Figure 3.33, and Figure 3.34 show the results of the simulations with inert nitrogen. These results are much more realistic since nitrogen will not be

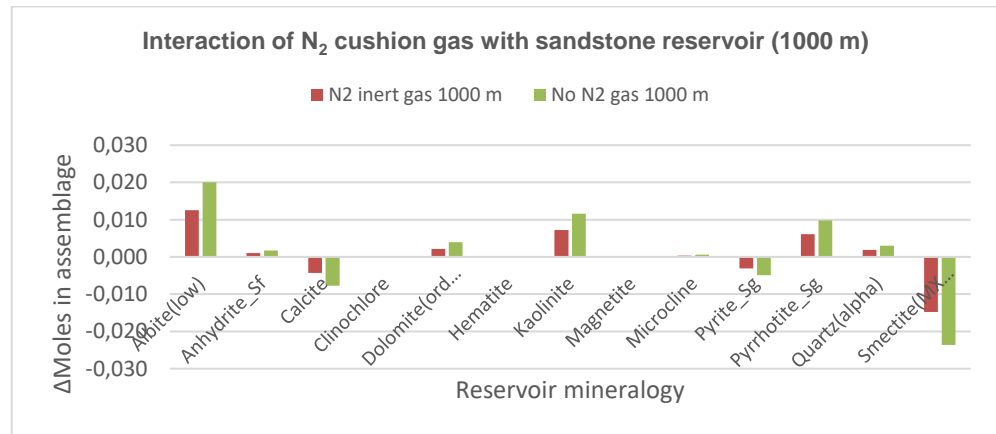


Figure 3.32: Mineral dissolution and precipitation at 1000 meter depth, when H<sub>2</sub> is stored in a natural gas reservoir. In red hydrogen storage with the addition of an inert N<sub>2</sub> gas. In green, for comparison the model without addition of nitrogen gas

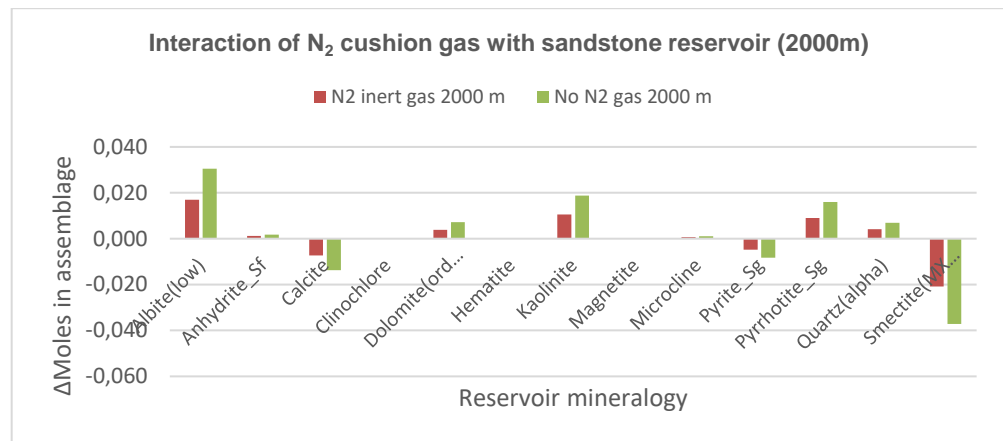


Figure 3.33: Mineral dissolution and precipitation at 2000 meter depth, when H<sub>2</sub> is stored in a natural gas reservoir. In red hydrogen storage with the addition of an inert N<sub>2</sub> gas. In green, for comparison the model without addition of nitrogen gas.

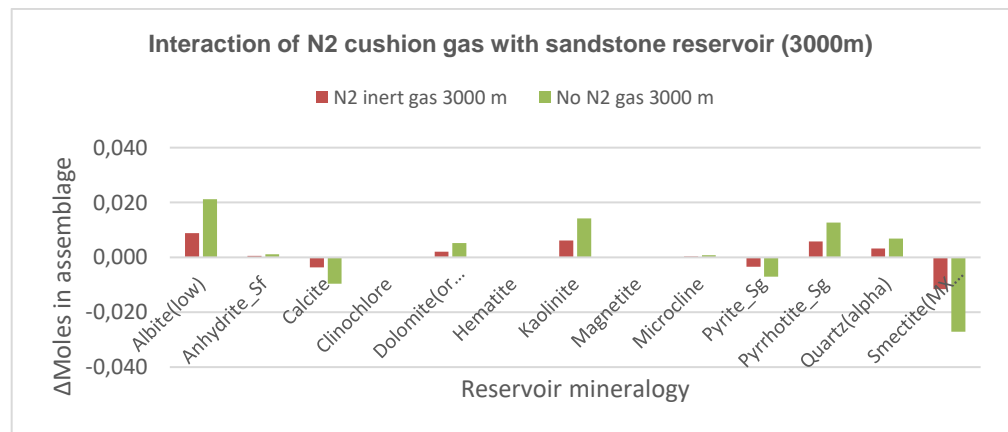


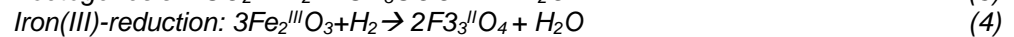
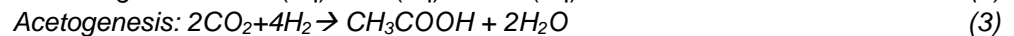
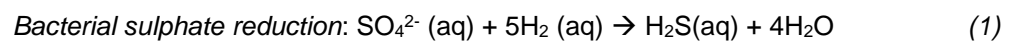
Figure 3.34 Mineral dissolution and precipitation at 3000 meter depth, when H<sub>2</sub> is stored in a natural gas reservoir. In red hydrogen storage with the addition of an inert N<sub>2</sub> gas. In green, for comparison the model without addition of nitrogen gas.

reactive at reservoir conditions and therefore there should be no changes in the reactions occurring with or without nitrogen. The simulations with nitrogen show lower amounts of mineral dissolution and precipitation. This is caused by the presence of nitrogen which will lower the hydrogen partial pressure in the gas phase and therefore lower the reactivity.

### 3.4.3.6 Biochemical reactions with H<sub>2</sub> in reservoirs

Storage of H<sub>2</sub> in (depleted) gas fields could create several risks. In addition to the risks of chemical reactions between H<sub>2</sub> and reservoir rock, the risks associated with conversion of H<sub>2</sub> to CH<sub>4</sub> and H<sub>2</sub>S due to microbial activity also need to be assessed. Microbial reactions with H<sub>2</sub> can occur when microorganisms act as catalysts, which is likely because H<sub>2</sub> is a universal electron donor for the metabolism of different anaerobic microbial species that are present in the subsurface (Hagemann et al., 2016). In addition, microbial reactions under high H<sub>2</sub> partial pressure and elevated temperatures and pressures have been scarcely investigated and could use more research to verify the occurrence of extremophiles as risks for H<sub>2</sub> storage.

There are 4 relevant microbial processes recognized in literature (Hagemann et al., 2016):



The biochemical processes that pose the greatest risks for underground hydrogen storage are sulphate reduction and methanogenesis. In these processes H<sub>2</sub> is microbially catalysed by bacteria and converted to aqueous H<sub>2</sub>S and CH<sub>4</sub>.

#### ***Bacterial sulphate reduction***

Bacterial sulphate reduction is an already occurring issue in the hydrocarbon industry (Bernardez, 2013; Hemme & Van Berk, 2018). Bacterial sulphate reduction occurs in aqueous anoxic environments and produces highly toxic and corrosive H<sub>2</sub>S. The bacteria use sulphate as an electron acceptor to oxidize hydrogen. During this process sulphide-S is generated which can then be available as S<sup>2-</sup> (aq), HS<sup>-</sup>(aq), and aqueous or gaseous H<sub>2</sub>S, depending on the pH (Bernardez, 2013). Important for this process is the availability of sulphate, which comes from the aqueous dissolution of mineral phases containing sulphate such as anhydrite, barite, pyrite. Other parameters that are important for this process are the pH (near-neutral) and temperature (Hemme & Van Berk, 2018; Bernardez 2013). Even though the bacteria prefer lower temperatures (38 °C) than the average temperature in natural gas reservoirs, they can also be active in more extreme conditions, ranging from 0 °C up to 110 °C (Jorgensen, 1992; Machel, 2001; Postgate, 1984).

#### ***Methanogenesis***

Methanogenesis is a chemical reaction between CO<sub>2</sub> (or acetate) and H<sub>2</sub>, caused by methanogenic archaea (microbes). In this process H<sub>2</sub>(aq) acts as the electron donor and CO<sub>2</sub>(aq) is the acceptor. Subsequently these are reduced to form aqueous CH<sub>4</sub> (Panfilov, 2010). Methanogenic archaea live at anaerobic conditions and temperatures up to 110°C (J.F. Holden, 2009; Gusev and Mineeva, 1992). Besides temperature and pH, the activity of the bacteria depends on the availability of acetate or carbon dioxide (Hemme & Van Berk, 2018). Loss of hydrogen is the main risk of methanogenesis. It has already been observed in underground storage of town gas (a mix of hydrogen, carbon monoxide, carbon dioxide, methane, nitrogen and volatile hydrocarbons), where after a storage cycle of seven months the initial volume % of H<sub>2</sub> decreased by 17% (from 57% to 40%) and the concentration of CH<sub>4</sub> increased by 18% (Greksák et al., 1990), and was also identified in experiments from the Underground Sun Storage project (2017) where 10% hydrogen was stored in a natural gas blend

### **Modelling biochemical reactions related to underground hydrogen storage**

Hemme and Van Berk (2018) developed a 1D reactive transport model in PHREEQC version 3. In this study, transport is not considered, and therefore the model of Hemme and Van Berk (2018) was modified to obtain a 1D kinetic model with no transport. Since sulphate to sulphide reduction being simulated in the biochemical models the database used in the other simulations in which the sulphate to sulphide reduction is uncoupled cannot be used for these simulations. Therefore the PHREEQC.dat database as used in the study of Hemme and Van Berk (2018) was used for the simulations.

The simulation calculated equilibria for the gas-water-rock interactions and performed kinetic reactions for the two biochemical processes (bacterial sulphate reduction and methanogenesis). The input for the equilibrium phases is a wide range of minerals representative for the Dutch reservoirs (see Table 3-13). The gas mixture used by Hemme and Van Berk (2018) was kept the same. The mixture consists of 10% residual gas and 90% stored hydrogen gas. The residual gas consists of 89% CH<sub>4</sub>, 10% N<sub>2</sub> and 1% CO<sub>2</sub>. The stored gas consists of 96% hydrogen and 4% CO<sub>2</sub>.

The reactions catalysed by the bacteria are kinetically controlled. The maximum specific growth rates for methanogenesis and bacterial sulphate reduction were calculated using the Monod equation. This is a mathematical model which calculates the growth of microorganisms (Liu, 2017). This model calculates the growth rate by considering limiting substrates (CO<sub>2</sub> for methanogenesis and sulphate for bacterial sulphate reduction), the maximum specific growth rate and the half-velocity constant. Availability of other nutrients is not considered. From this a growth rate of  $2.3 \cdot 10^{-9}$  mol/kgw/s for methanogenesis and  $9.26 \cdot 10^{-8}$  mol/kgw/s for bacterial sulphate reduction was calculated. Both rates are at optimal growth temperatures of 37 °C for methanogenesis and 30°C for bacterial sulphate reduction (Hemme & Van Berk, 2018). The model uses the maximum growth rate at these optimal growth temperatures and keeps the bacterial concentrations constant which will create a worst-case scenario. This simplification causes the influence of higher temperatures on bacterial activity to not be part of the simulations.

Table 3-13: Equilibrium phases used in the biochemical simulations

| Equilibrium phase | Mol/kgw |
|-------------------|---------|
| Anhydrite         | 0.132   |
| Barite            | 0.001   |
| Calcite           | 4.820   |
| Dolomite          | 0.030   |
| Goethite          | 0.002   |
| Illite            | 28.880  |
| Kaolinite         | 3.730   |
| K-feldspar        | 103.900 |
| Pyrite            | 7.390   |
| Quartz            | 866.390 |

### Results biochemical simulations

The results of the three simulations are shown in Figure 3.35 and Figure 3.36. Figure 3.37 shows the changes in mineralogy at different depths. The process of methanogenesis is controlled by the availability of CO<sub>2</sub>. This is initially present in the gas but can also come from dissolving carbonate phases. The simulation was run over 30 years at three different depths.

For all three simulations the amount of hydrogen decreases over time, but the rate becomes larger at greater depth (see Table 3-14). The simulation at 3000 meters even shows that after 30 years all hydrogen will be consumed. This is likely caused by a higher amount of calcite dissolution at greater depths which will increase the amounts of available CO<sub>2</sub> (see Figure 3.37). Figure 3.35 shows the amounts of methane in gas phase produced during the simulations. At all depths the amount of methane increases. However, these are results for the worst case scenario and that even if a higher temperature will increase the available CO<sub>2</sub>, it will negatively impact the activity of the bacteria since their optimal temperature is 37 °C. At temperatures above 80°C it is unlikely, yet not impossible, that methanogenic and sulphate reducing bacteria are still active, which is the case in the simulation at 3000 meters (105°C) (Hemme & Van Berk, 2018).

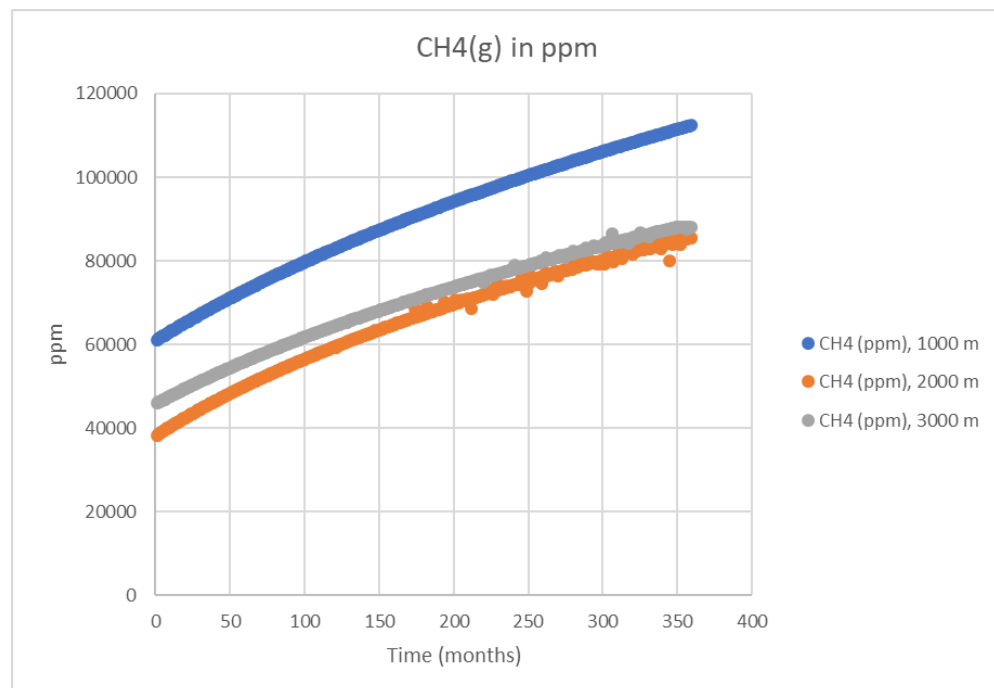


Figure 3.35: Amount of methane gas (ppm) produced through time in simulations at 1000, 2000 and 3000 meter depth.

Table 3-14: Initial and final hydrogen (gas) and mole fraction of consumed hydrogen after 30 years

|                               | H <sub>2</sub> (g)<br>1000 meter | H <sub>2</sub> (g)<br>2000 meter | H <sub>2</sub> (g)<br>3000 meter |
|-------------------------------|----------------------------------|----------------------------------|----------------------------------|
| <b>Moles initial</b>          | 4.28                             | 4.28                             | 4.28                             |
| <b>Moles final</b>            | 1.81                             | 0.03                             | 0.00                             |
| <b>Mole fraction consumed</b> | 0.58                             | 0.99                             | 1.00                             |

The results also show that significant amounts of H<sub>2</sub>S are formed in the reservoir (see Figure 3.36). At larger depths the amount of H<sub>2</sub>S increases, this is caused by the larger amounts of mineral dissolution/precipitation that occurs at larger depths, making more sulphate available. Figure 3.37 does show dissolution of pyrite, but also shows precipitation of anhydrite. To which extend these processes will influence the amount of available sulphate, cannot be concluded from these simulations.

Based upon these simulations, both sulphate reduction and methanogenesis may take place, where methanogenesis is more dominant compared to sulphate reduction, as sulphate reduction is limited by sulphate availability. The extent of sulphate reduction modelled however leads to alarming levels of H<sub>2</sub>S. How likely these amounts of H<sub>2</sub>S are to develop will require further research.

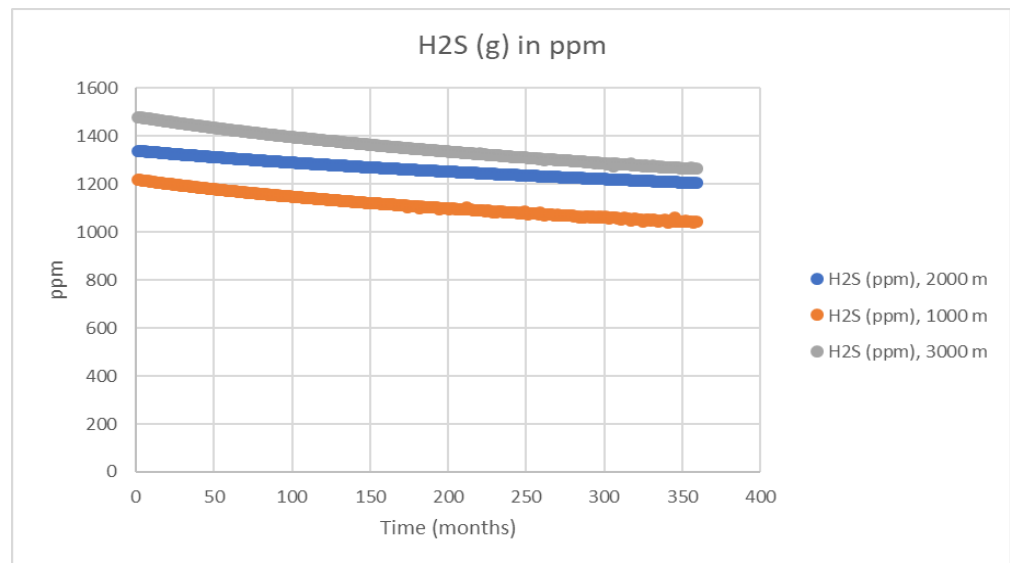


Figure 3.36: Amount of H<sub>2</sub>S gas (ppm) produced through time in simulations at 1000, 2000 and 3000 meter depth.

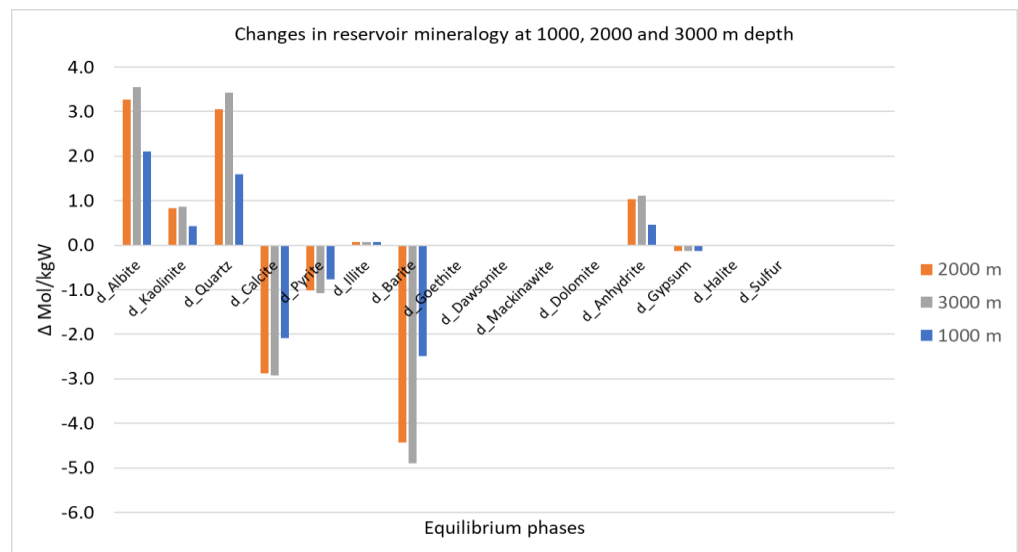


Figure 3.37: Mineral dissolution and precipitation at 1000, 2000 and 3000 meters depth.

#### 3.4.4 *Simulating Hydrogen storage with TOUGHREACT – EWAGS*

The aim of the work with TOUGHREACT was primarily to investigate the use of the newly acquired executable for the EWAGS equation of state and its applicability for hydrogen storage in depleted reservoirs. For comparison with PHREEQC, we used the geochemical database Thermoddem (V1.10\_06Jun2017) and not the default TOUGHREACT database. Both 0D batch models and 2D injection models have been developed.

Although the basic trends of mineral reactions are the same for PHREEQC and TOUGHREACT we encountered several constraints for the use of TOUGHREACT EWAGS. These limitations led us to conclude that TOUGHREACT EWAGS is not suitable for modelling hydrogen storage in depleted gas fields. However, it must be noted that we did not implement the sulphate/sulphide redox uncoupled database in TOUGHREACT. The different constraints of the software will be described in the following section. Because the model results are not reliable, these are not reported.

- In TOUGHREACT, the chemical calculations are coupled to the physical behaviour of hydrogen by an equation of state (EOS). This should better calculate the hydrogen solubility and phase changes, but it also means that only one gas can be selected (next to water and NaCl phases). Consequently, residual methane, CO<sub>2</sub> as a cushion gas or released gaseous H<sub>2</sub>S cannot be simulated. Hence, only hydrogen storage in water saturated aquifers can be simulated with this EOS.
- EWAGS is accurate for temperatures in the range of 100 °C to 350 °C. This excludes cooler (shallower) reservoirs and situations where the reservoir will be cooled below 100 °C due to injection of colder hydrogen.
- There is a coupling possible of hydrogen and/or of water between the flow and chemical models. The coupling of hydrogen is required for reactive transport of hydrogen. However, the coupling of water yielded unexpected large amounts of water production. The mass balance issues have not been solved or explained and this coupling had to be disabled.
- Model development is required to fix the convergence issues with non-isothermal injection and reaction. Non-convergence could be either software related or due to the selected input chemistry and boundary conditions.
- The models showed that injection of dry hydrogen in the saline aquifer results in significant salt precipitation. To prevent salt precipitation, minimal water can be injected together with the hydrogen to simulate injection of wet hydrogen. However, the balance proved difficult resulting in either drying or wetting of the reservoir.
- Injection of hydrogen in an aquifer results in a hydrogen plume, however the gas saturation remains low in the plume except for the near-well area. Only in the near-well zone, the partial pressure is high enough to yield hydrogen dissolution and chemical reactions. The low gas saturation and low partial pressure of hydrogen in the reservoir has not been explained.

#### 3.4.5 *Conclusions and future research*

While the interest in storage of hydrogen is continuously growing as one of the potential options to add flexibility to the sustainable energy system, a range of technical questions need to be answered to make implementation of this technology

successful. An important technical challenge is related to the reactivity of hydrogen in the subsurface, which may affect the integrity of the well-reservoir-caprock system and the quality of the back-produced hydrogen gas during cyclic storage. Based on a literature study we see that abiotic geochemical reactions in sandstone reservoirs are expected to have a minor effect on the reservoir quality. However, the presence of sulphur-containing minerals in combination with high temperatures can lead to chemical modifications and release of H<sub>2</sub>S, which is toxic and highly corrosive.

#### Reservoir reactivity

The geochemical model was successful in simulating the dominant expected hydrogen-water-rock reactions:

- Reduction of pyrite forming pyrrhotite and H<sub>2</sub>S. The modelling results show that pyrite reduction as a result of H<sub>2</sub> storage may occur, leading to H<sub>2</sub>S formation in the gas phase, which may affect safety, materials selection, facility design and economics. H<sub>2</sub>S release increases with depth (as the partial pressure increases), and with the amount of initial pyrite in the reservoir, as is illustrated by the results of the Rotliegend sandstone.
- Reduction of hematite to magnetite, sequestering H<sub>2</sub> and producing H<sub>2</sub>O. While the Delft sandstone case predicts dissolution of hematite (Fe<sub>2</sub>O<sub>3</sub>) and precipitation of magnetite (Fe<sub>3</sub>O<sub>4</sub>), the Rotliegend and Buntsandstein cases predict hematite dissolution and the precipitation of (iron-containing) siderite (FeCO<sub>3</sub>) as well as calcite (CaCO<sub>3</sub>). The preference for the hematite to siderite reaction in the Rotliegend and Buntsandstein cases is due to the presence of dolomite (CaMg(CO<sub>3</sub>)<sub>2</sub>) in these reservoir rocks. Furthermore, the cases with hematite dissolution show an increase of water content, which is as expected for the reduction of hematite.
- Precipitation and dissolution of secondary minerals depending on the initial mineralogical composition. Carbonate and clay transformations can be triggered by changes in fluid composition.

On the reduction of pyrite to pyrrhotite, it must be noted that kinetic rates for this reaction were not available at our reservoir conditions and hence the kinetic effects were not taken into account. As such, the model results reflect a worst case scenario.

To accurately assess the risk of H<sub>2</sub>S formation in hydrogen storage reservoirs it is of the utmost importance to improve the predictive power of the geochemical models by incorporating kinetic rates at high temperatures and high H<sub>2</sub> partial pressures. Accurate predictions also require detailed knowledge of the concentrations of iron-containing minerals in reservoir rocks, which can be below detection limit of techniques such as XRD. This is important to determine the amount of H<sub>2</sub>S producing pyrite as well as the presence of H<sub>2</sub>S scavenging minerals such as siderite.

#### Effect of depth and temperature on reactivity

In general reactivity of minerals increases with higher temperatures. Besides the temperature, a higher H<sub>2</sub> partial pressure increases reactivity in the reservoir. Hence deeper reservoirs will have a higher potential for hydrogen-induced reactions. The temperature in the reservoir will also depend on the temperature of the hydrogen when injected. The produced hydrogen is probably relatively cold (<60 °C) but it might

be required to heat up the hydrogen before injection to prevent a cooling effect. This needs to be better constrained for future feasibility studies.

#### CO<sub>2</sub> as cushion gas

Using CO<sub>2</sub> as cushion gas does not directly change the reactions of pyrite and hematite. Only small changes in the reactions are observed, this could be because CO<sub>2</sub> was already present in the models with and without CO<sub>2</sub> cushion gas. The amount of H<sub>2</sub>S formed is less than one percent different between the cases with and without CO<sub>2</sub>.

#### N<sub>2</sub> as cushion gas

Initial model results showed that the THERMODDEM database is not ideal for this type of models, since it predicts the occurrence of the Haber process (ammonia synthesis, i.e., combining H<sub>2</sub> and N<sub>2</sub>) that does not occur at our defined reservoir conditions, and therefore produces unrealistic results. However, when nitrogen is introduced as a hydrogen-inert gas (i.e., not reacting with hydrogen) the model runs well. The results show that nitrogen has no impact on rock-gas-water reactions, which is similar to results in literature ((Laille et al. 1988; Misra et al 1988). The only effect is the change in hydrogen partial pressure when nitrogen is present as cushion gas which causes lower reactivity of hydrogen in the reservoir. Therefore, with respect to geochemistry nitrogen would potentially be suitable for use as a cushion gas for hydrogen storage.

#### Biochemical PHREEQC simulations

The literature study in combination with the simulation results show that the two bacterial processes that were modelled in this research, bacterial sulphate reduction and methanogenesis, may both pose a risk for underground hydrogen storage. However, in this study, microbial activity is assumed similar to optimum temperatures, while it is expected that the reservoir conditions are not optimum conditions therefore our results will tend to over-estimate the impact of microbiological activity. Although microbial reaction rates are expected to be limited at the prevailing temperatures >80°C in potential reservoirs for hydrogen storage in the Dutch subsurface, some hyperthermophiles living up to 110 °C have been observed. The unique circumstances that would be created when storing hydrogen in a reservoir, with high concentrations of hydrogen, a very good electron donor for microbes, warrants further research before this can be dismissed as a relevant process, especially since H<sub>2</sub>S already posers a serious threat in minor amounts.

#### Future research

- Experimental studies of hydrogen interaction with reservoir, caprock and wellbore materials are required and envisaged for next year, the results of which can be used for validation of geochemical models.
- To accurately assess the risk of H<sub>2</sub>S formation the predictive power of geochemical models has to be improved. This can be done by incorporating kinetic rates at high temperatures and high H<sub>2</sub> partial pressures (experimental data).
- With respect to the reservoir mineralogy it is important for accurate predictions of H<sub>2</sub>S formation to further investigate H<sub>2</sub>S producing pyrite as well as H<sub>2</sub>S scavenging minerals such as siderite.

### 3.5 Geomechanical effects of H<sub>2</sub> storage in salt caverns

Cyclic injection and withdrawal of gas (air or hydrogen in this study) causes variations in the internal cavern pressure and temperature, which in turn could have adverse effects on the mechanical integrity and stability of the salt cavern. To assess these effects, and the extent to which they affect cavern integrity, geomechanical numerical simulations were conducted of a salt cavern subjected to cycles of injection and withdrawal that are typical for Compressed Air Energy Storage (CAES) and Underground Hydrogen Storage (UHS).

Our focus in this geomechanical modeling study was on analyzing the cavern wall convergence and the thermo-mechanical effects of cycling loading on the rock salt surrounding the salt cavern. For this purpose, two single-cavern geomechanical models were developed: (i) a model of a salt cavern used for storage of air for CAES and (ii) a model of a salt cavern used for storing hydrogen for UHS.

For a description of the numerical model developed for UHS, and the input data for the geomechanical numerical simulations, the reader is referred to subsection 2.5.1 of this report, where this is provided in combination with CAES. Here, we limit ourselves to describing the load cases used for UHS in subsection 3.5.1. In Section 3.5.2 we present and discuss the results of the model simulations for UHS. Conclusions and recommendations for further research on geomechanical effects of cyclic injection and withdrawal on caverns (and well systems) used for UHS are given in subsection 3.5.3.

#### 3.5.1 Numerical model

Numerical simulations were conducted to evaluate the geomechanical effects of hydrogen energy storage (UHS) in salt caverns. For a description of the model geometry, the constitutive models and material properties used, and the approach to initializing the model and simulating the effects during the leaching phase when the cavern is developed, the reader is referred to subsection 2.5.1. Here, we continue with describing the load cases for UHS.

##### 3.5.1.1 Load cases for UHS

Similar as for CAES loading, for UHS cavern debrining was assumed to take place immediately after the leaching phase. During a debrining phase of 30 days, brine was removed from the cavern by injecting H<sub>2</sub>. During this phase, cavern pressures were gradually decreased from an initial halmostatic static pressure gradient to a uniform pressure of 80 bar at the start of UHS cycling (empty working volume).

For UHS, five scenarios for injection and withdrawal cycles were assumed, based on the literature and considerations of current and possible future upscaling of energy storage operations. For every scenario, the response of the rocks in terms of wall convergence, temperature and stress evolution was analysed, using either the power-law creep model (ZwdNLC law), or combined power-law and low-linear-creep model (ZwdNLCLLC law). For all cases, pressures during cycling were assumed to vary linearly between 80 bar (end withdrawal / start injection) and 180 bar (end of injection / start production). Duration of the injection and withdrawal cycles was varied between weekly, monthly and yearly cycles. For the scenarios of weekly and monthly cycling, a total of 10 cycles was modelled. For the scenario of yearly cycling, due to

longer computation times, only 5 cycles were modelled. In contrast to CAES pressure cycling, no idle time was modelled for UHS. Temperature variations of the H<sub>2</sub> gas in the cavern during cycling were based on literature values (Nieland, 2008); a temperature change of 0.5°C/bar pressure change was assumed for the shorter weekly cycles, whereas a smaller change of 0.2°C/bar, resp. 0.06°C/bar was used to simulate the temperature evolution during the longer monthly and yearly cycles. Well head injection temperature was varied between 15°C and 50°C. Scenario's for UHS P,T cycles are summarized in Table 3-15 and Figure 3.38. Furthermore, it must be noted here that contrary to CAES, no scenarios were run that include a maintenance period during which the cavern pressure is atmospheric (1 bar), because we assume that in the case of hydrogen, for economic reasons, maintenance will occur under pressure, i.e., with the hydrogen in the cavern.

Table 3-15: Overview of UHS simulation scenarios. I: injection period, P: withdrawal period, WHT: wellhead temperature.

|       | Cycle duration (days) | Pressure (bar) | Temperature cycles (°C) | Nr. of cycles | Creep law |
|-------|-----------------------|----------------|-------------------------|---------------|-----------|
| Run01 | I: 3.5<br>P: 3.5      | 80-180         | WHT: 15<br>15-65        | 10            | ZwdNLC    |
| Run11 | I: 3.5<br>P: 3.5      | 80-180         | WHT: 15<br>15-65        | 10            | ZwdNLCLLC |
| Run02 | I: 22.5<br>P: 7.5     | 80-180         | WHT: 15<br>15-35        | 10            | ZwdNLC    |
| Run12 | I: 22.5<br>P: 7.5     | 80-180         | WHT: 15<br>15-35        | 10            | ZwdNLCLLC |
| Run03 | I: 15<br>P: 15        | 80-180         | WHT: 15<br>15-35        | 10            | ZwdNLC    |
| Run13 | I: 15<br>P: 15        | 80-180         | WHT: 15<br>15-35        | 10            | ZwdNLCLLC |
| Run04 | I: 22.5<br>P: 7.5     | 80-180         | WHT: 50<br>50-70        | 10            | ZwdNLC    |
| Run14 | I: 22.5<br>P: 7.5     | 80-180         | WHT: 50<br>50-70        | 10            | ZwdNLCLLC |
| Run05 | I: 273.75<br>P: 91.25 | 80-180         | WHT: 15<br>15-21        | 5             | ZwdNLC    |
| Run15 | I: 273.75<br>P: 91.25 | 80-180         | WHT: 15<br>15-21        | 5             | ZwdNLCLLC |

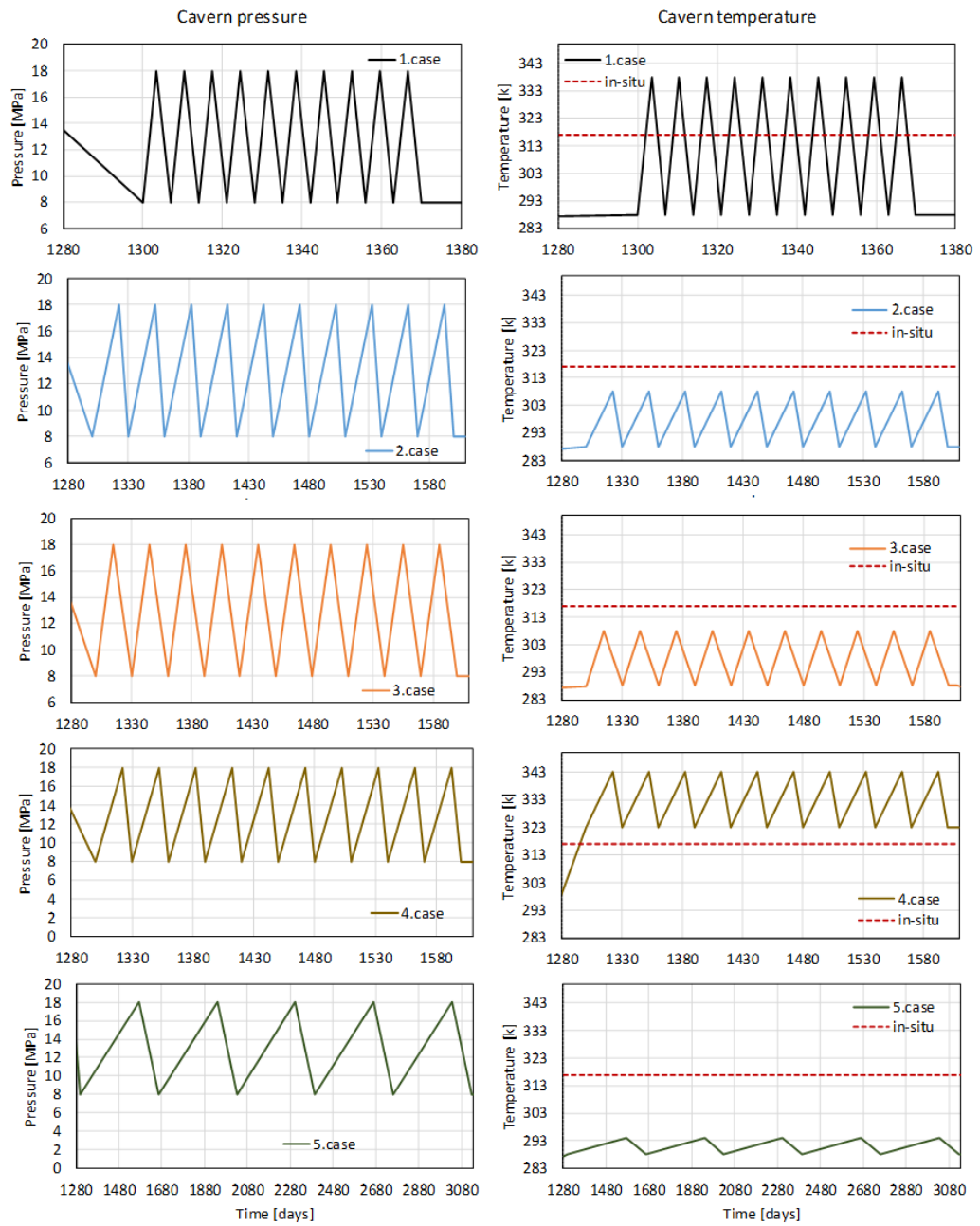


Figure 3.38: Scenarios for modelling UHS. Pressure and temperature evolution during UHS cycling. For description of cyclic characteristics, see Table 3-15.

### 3.5.2 Results UHS simulations

For every scenario, the response of the rocks in terms of displacements (wall convergence), temperature and stress evolution was analyzed. Displacements and stresses, and the potential of tensile failure and dilatant behavior in the rock salt were monitored close to the cavern wall, at a depth of 1375m (mid-height of the cavern). In addition, temperature changes were monitored at a depth of 1375m (cavern mid-height) up to 25 m into the cavern wall at different stages of the injection/withdrawal cycles, i.e. at the end of cavern leaching, at the end of the 1<sup>st</sup> injection- and withdrawal period and at the end of the last injection- and withdrawal cycle. Results for the different scenarios are presented in Figure 3.39 to Figure 3.43.

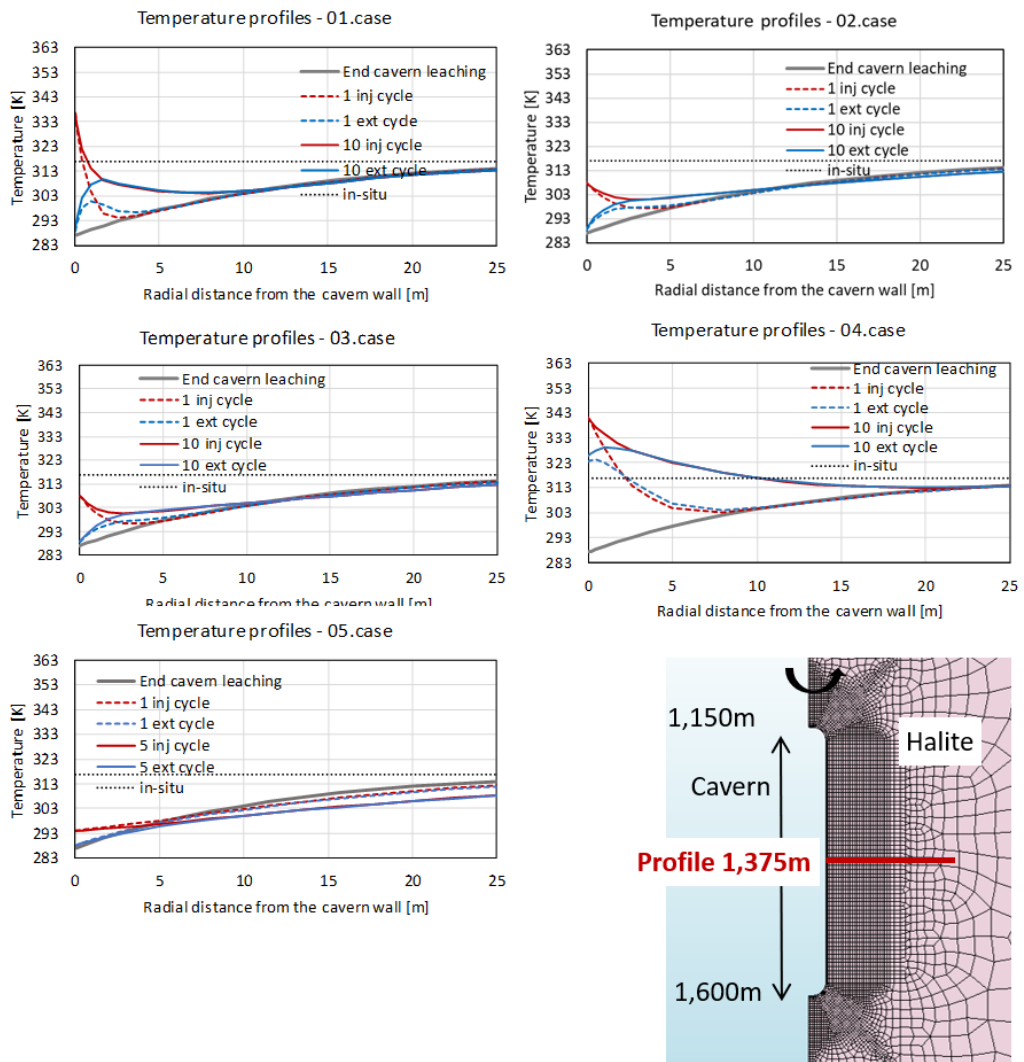


Figure 3.39: Temperature changes at the end of cavern leaching and during injection and withdrawal cycles, for the 5 UHS scenarios. Temperatures are monitored along a horizontal profile at a depth of 1375m (mid-height cavern).

Figure 3.44 presents the ‘geological tightness’ of the salt cavern, during different stages of UHS operations for scenario 1 and scenario 3, assuming a ZwdNLC salt creep law. The geological tightness of a salt cavern is guaranteed, if at maximum injection pressure  $P_{max}$  (= 180 bar), the cavern is enclosed by a zone of at least 25m where the minimum principal stress is 10% higher than the maximum cavern pressure:

$$1.1 P_{max} \leq \sigma_{min}$$

From Figure 3.44 it can be seen that the criterium for geological tightness is met at all stages of the modelled UHS operations.

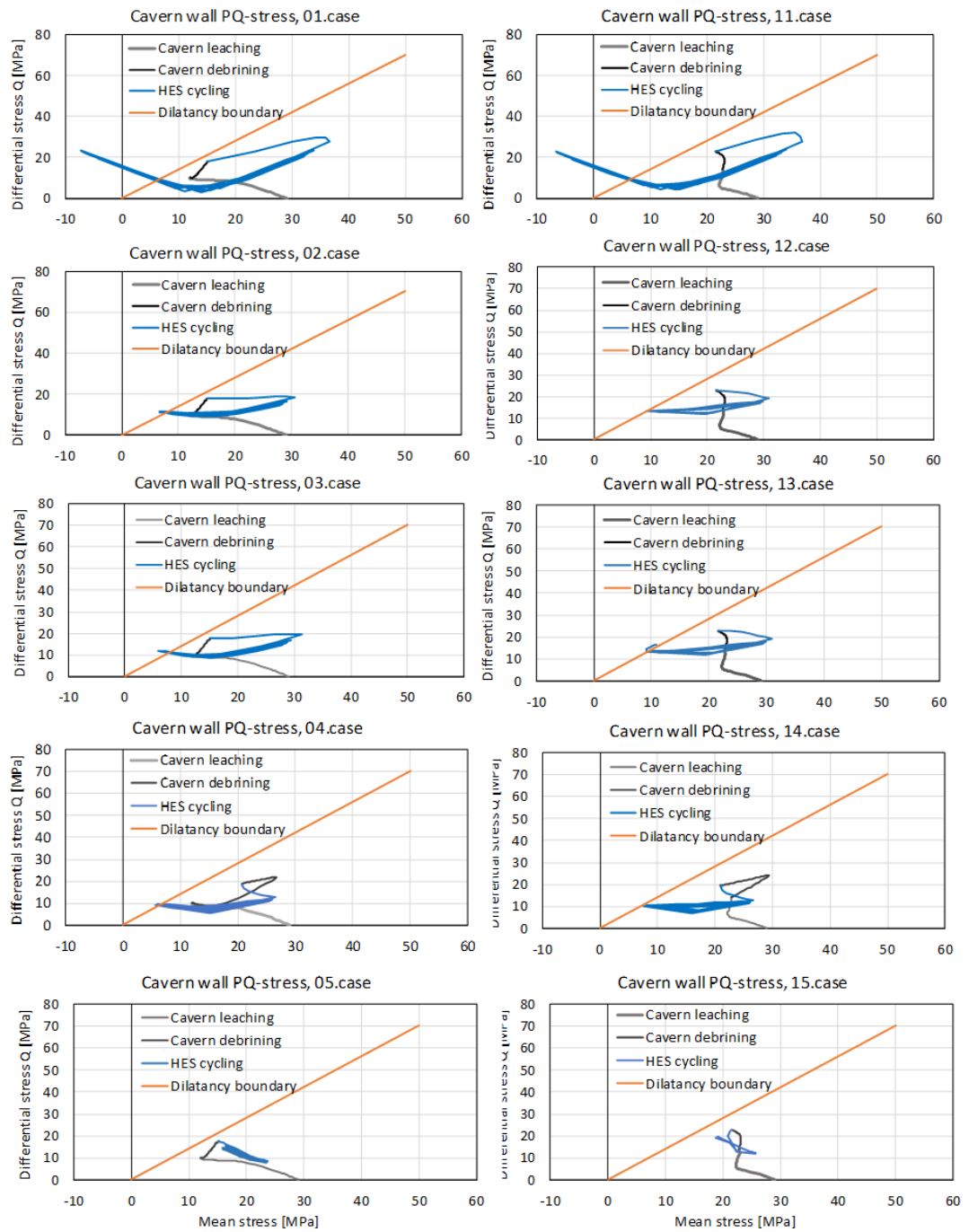


Figure 3.40: P-Q stress path versus dilation boundary based on Ratigan dilation criterion, for 5 injection – withdrawal scenarios. Left column: for ZwdNLC law creep law, right column for ZwdNLCLCC creep law. P,Q evolution plotted at location of cavern wall at a depth of 1375m (cavern mid-height).

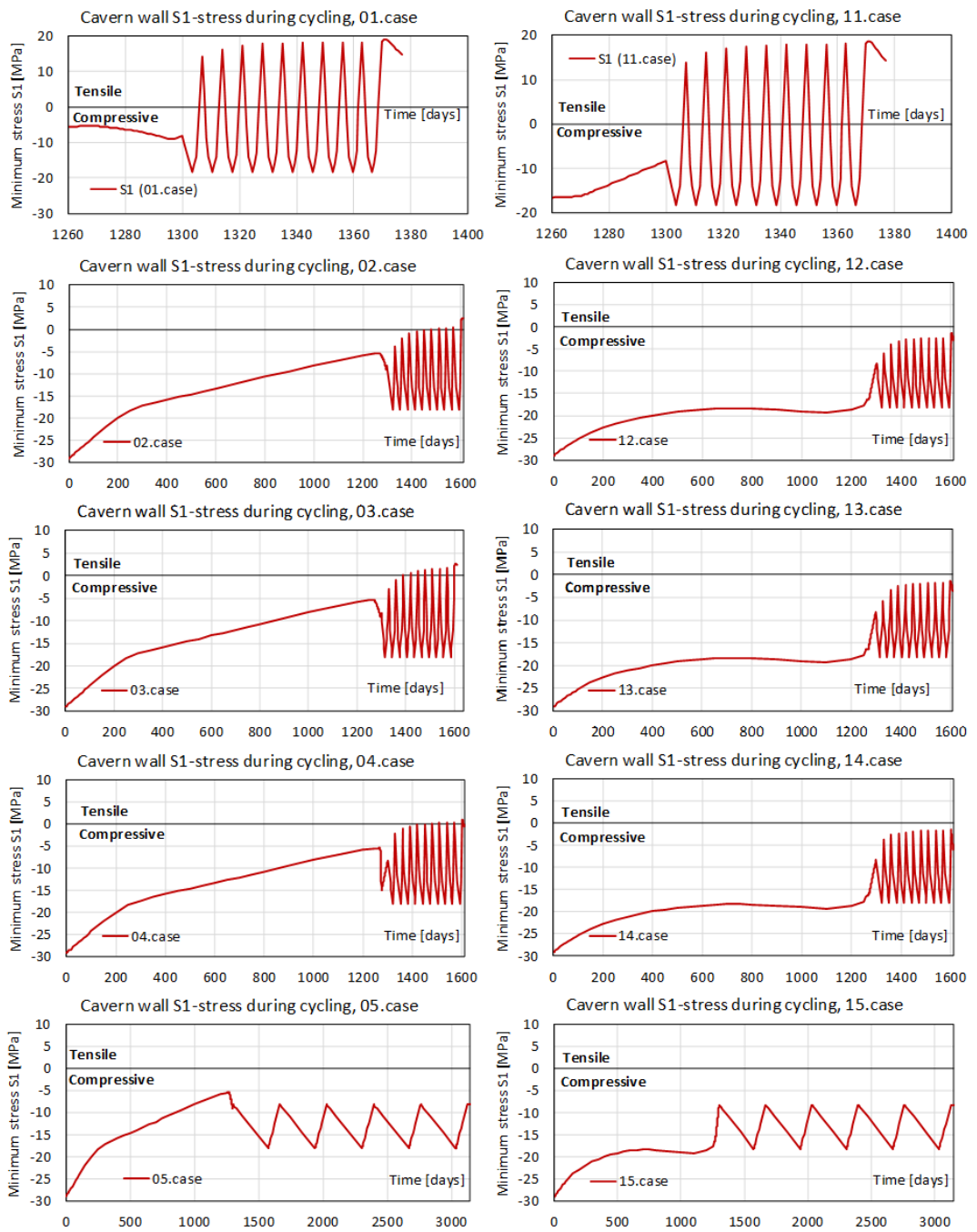


Figure 3.41: Minimum principal total stress near the cavern wall, at a depth of 1375m (cavern mid-height) for the 5 UHS scenarios.

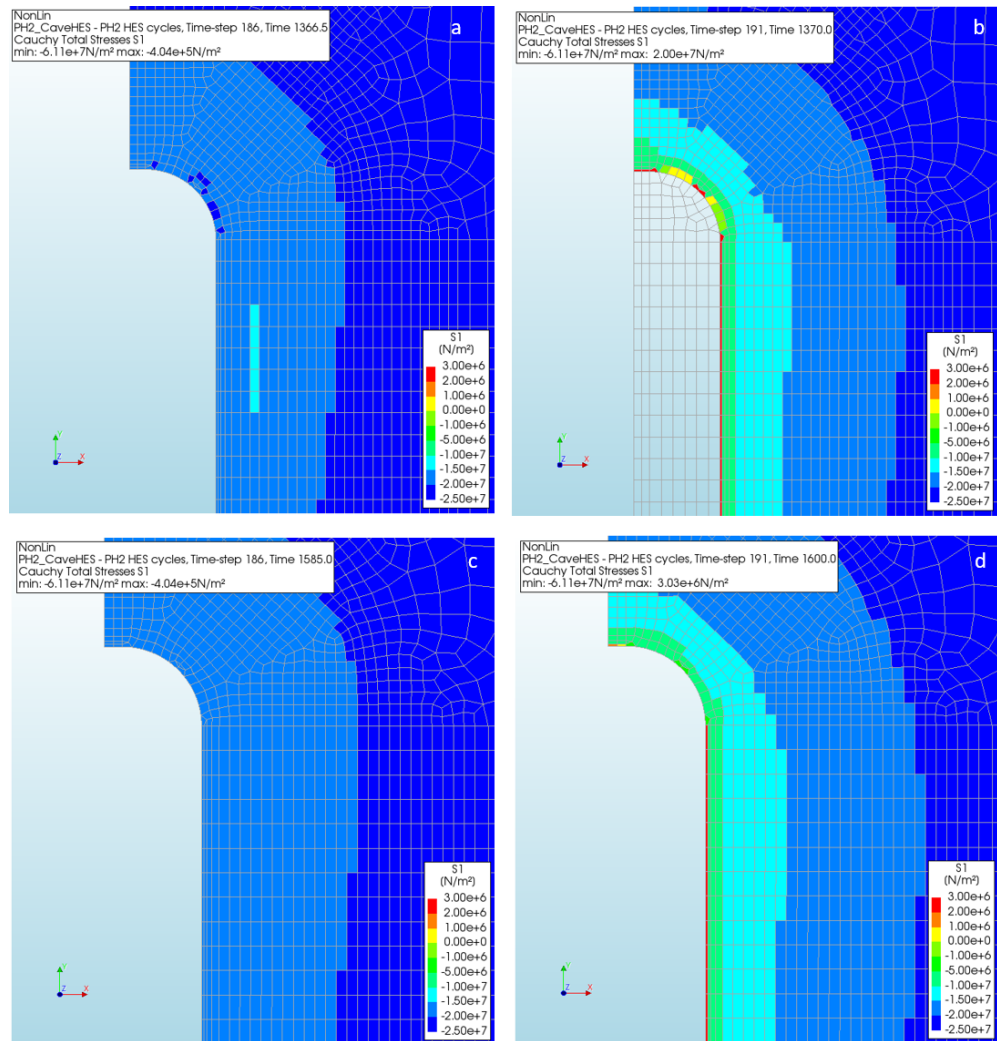


Figure 3.42: Minimum total stress for case-01 and case-03 around the cavern wall. (a) Case 01 after 10<sup>th</sup> injection cycle; (b) case 01 after 10<sup>th</sup> production cycle; (c) case 03 after 10<sup>th</sup> injection cycle; (d): case 03 after 10<sup>th</sup> production cycle. Contour plots show that the extent of tensile failure is limited to the rocks near the cavern wall (<1m distance from cavern wall).

Based on the evolution of temperatures, stresses and displacements in the cavern wall as shown in Figure 3.39 to Figure 3.44, the following conclusions can be drawn for UHS:

Effect of injection and gas withdrawal on temperature changes in the cavern wall:

- A significant cooling of the rock salt some tens of meters into the cavern wall occurs during cavern leaching.
- This effect is partially annihilated during UHS cycling, specifically for shorter weekly cycles (scenario 1) and high wellhead temperature (scenario 4)
- In case of weekly UHS cycling (scenario 1), cavern wall temperatures may increase above in-situ temperatures; this effect is observed within a distance of 1 m into the cavern wall.
- In case of a high wellhead injection temperature of 50°C (i.e. higher than in-situ temperatures in the salt rock at mid-height of the cavern, scenario 4), temperatures in the salt may increase above in-situ temperatures during both the injection and withdrawal cycles; after 10 cycles this effect has penetrated several meters into the cavern wall.

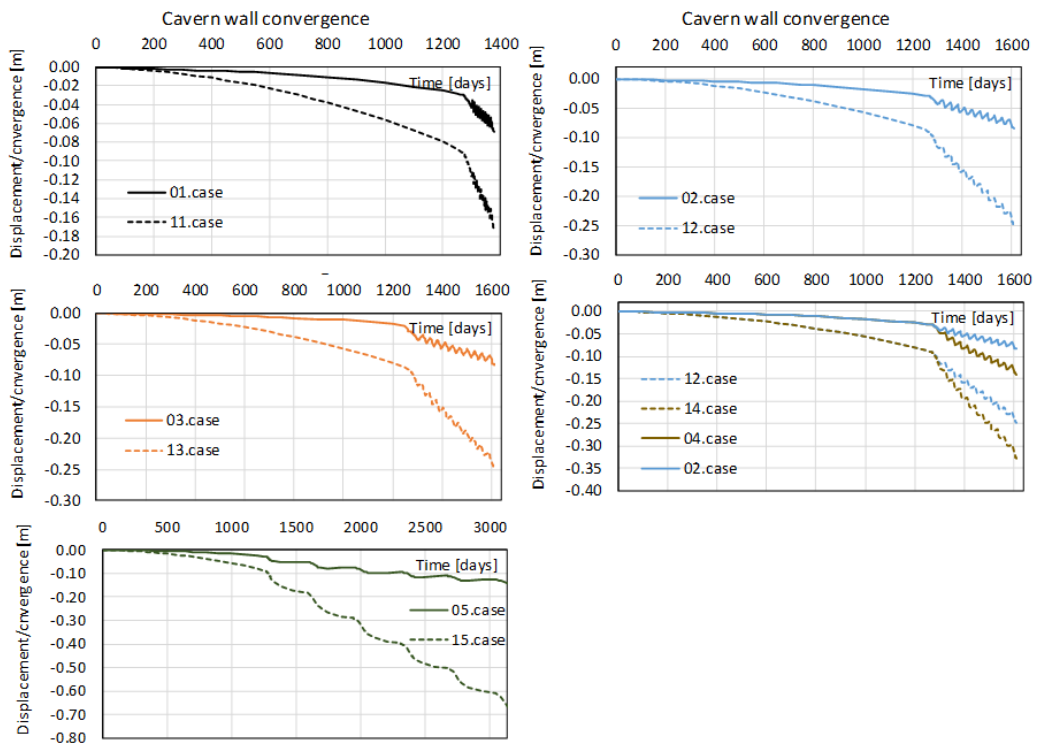


Figure 3.43: Radial displacements (cavern wall convergence) of the cavern wall at a depth of -1375m (cavern mid-height) for the 5 UHS scenarios.

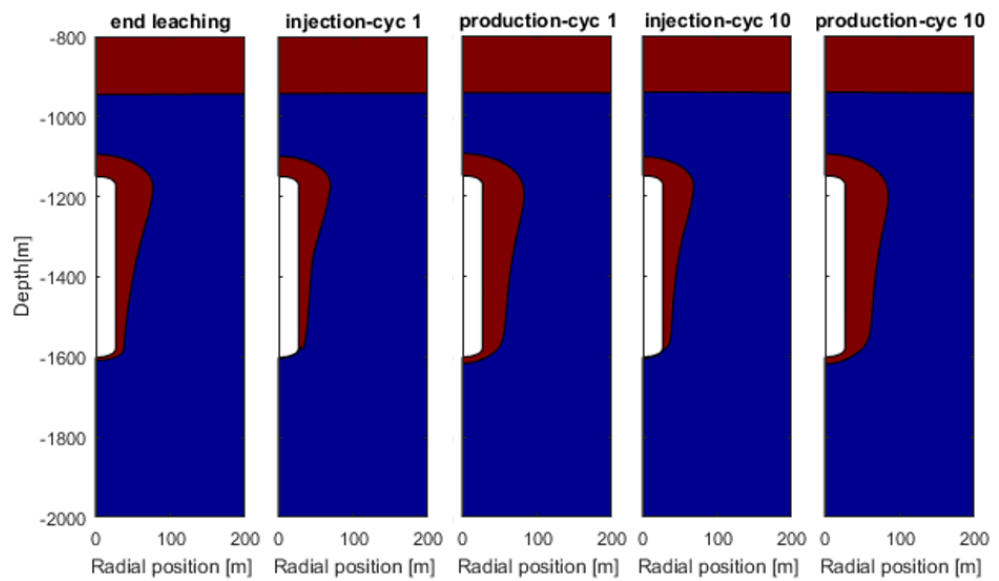


Figure 3.44: Geological tightness for scenario 3, at the end of cavern leaching, end of 1<sup>st</sup> injection and production cycle and at end of 10<sup>th</sup> injection and production cycle. The cavern is tight as it is enclosed by a zone of at least 25m in which the geological tightness criterion is fulfilled (red colored zone around the cavern; see text for further details).

Effect of the length of the injection and withdrawal cycles for UHS on dilation and tensile failure:

- For weekly cycles, a significant potential for dilation and tensile stressing in the cavern wall is observed (scenario 1).

- For monthly cycles, some potential for dilation & tensile stressing in the cavern wall is observed, specifically during the later cycles (scenario 2-4), and when linear creep plays a minor role.
- For yearly cycles, the potential for dilation and tensile stressing in the cavern wall is small (scenario 5).
- Hence, shorter cycles promote the potential for tensile failure and dilation of the rock salt (very) close to the cavern wall.
- Dilation and tensile failure is only observed at very short distances from the cavern wall (<1m)

Effect of the wellhead temperature (scenario 2 versus scenario 4):

- Higher wellhead temperature only slightly changes the potential for tensile failure and dilation in the cavern wall.

Effect of 'asymmetry' of injection versus withdrawal period (scenario 2 versus scenario 3):

- A longer production cycle (15 days versus 7.5 days) slightly promotes tensile stressing and dilation in the cavern wall.

Effect of salt creep rates:

- Higher creep rates (resulting from a combination of linear and nonlinear creep, i.e. ZwdNLCLLC ) result in a significantly larger convergence of the cavern wall
- Higher creep rates specifically reduce the potential for tensile failure and dilation during the cavern leaching and cavern debrining period.
- Higher creep rates also (but to a lesser extent) reduce the potential for tensile failure and dilation in the cavern wall during UHS cycling.

### 3.5.3 *Conclusions and future research*

#### 3.5.3.1 Conclusions

Based on the results of the geomechanical assessment, the following can be concluded regarding the effects of cyclic injection and withdrawal of hydrogen during UHS operation, and the extent to which they affect cavern stability and integrity:

- During cavern leaching, a gradual temperature decrease (up to 30°C lower than the initial temperature) is observed in the rock salt around the salt cavern, which extends up to a distance of 30m from the cavern wall.
- During UHS injection and withdrawal cycles temperatures in the near-wall area are raised again, with a local increase of temperatures above original in-situ temperatures when injection cycles are short (week) or wellhead injection temperatures are high.
- Modelling shows that the geological tightness of the cavern is not jeopardized during UHS cycling operations.
- Dilation of rock salt and tensile failure is only observed at short distances from the cavern wall (<1m), when cavern pressures are low (end production – start injection).
- Tensile failure may cause formation of fractures at short distances from the cavern wall (<1m), within zones under tensile stress. These fractures are short and could lead to spalling, but they do not pose a real threat to cavern integrity due to the limited depth of penetration in the cavern wall.

- Differences between stress paths and convergence for different salt constitutive behavior (ZwdNLC and ZwdNLCLLC creep laws) are significant for the cavern leaching phase, but are less pronounced for the UHS cycling phase (i.e. elastic deformation dominates during the relatively short UHS cycles).

#### 3.5.3.2 Future research

In the presented study, the focus was on assessing the effects of cyclic injection and withdrawal of hydrogen during UHS operation on cavern stability and integrity. Although this is an important aspect of salt cavern storage, experience from previous incidents at underground storage facilities suggests that the biggest risks arise from well problems (Evans, 2008), i.e., the integrity of the well is compromised, which leads to leakage of stored product. A logical follow-up would therefore be to extend the geomechanical assessment to the well system through which the hydrogen is injected and withdrawn from the cavern. For this purpose, a geomechanical model of the wellbore and near well area could be developed to simulate the effects cyclic hydrogen injection and withdrawal on durability and integrity of wells. In particular, the formation of micro-annuli (i.e. circumferential fractures) at interfaces between the salt and well (at the last cemented casing shoe and along the wellbore) could then be examined, as well as the potential for leakage of hydrogen along those micro-annuli and through annular cement.

### 3.6 Economic assessment of underground H<sub>2</sub> storage in salt caverns

In this section, the results are detailed of the economic modelling that was done to analyse the business case of Underground Hydrogen Storage (UHS). The business case for Compressed Air Energy Storage (CAES), which was explored as part of the same effort, is detailed in Section 2.6.

#### 3.6.1 *Goals and scope*

A comparison is made between the economics of continuous hydrogen production asset without storage and the economics of a flexible hydrogen production asset with storage in a salt cavern. The hydrogen is produced by water electrolysis. In the case of continuous hydrogen production, the electrolyser produces a constant amount of hydrogen during every hour of a year. In the case of flexible hydrogen production, hydrogen is only produced at full capacity when electricity prices are low. Production costs are minimized by making use of the volatility in electricity prices (EPEX market). Assuming a continuous market demand for hydrogen, a storage facility is needed in case of flexible production. Other potential revenues, as listed in Table 3-16, are left out of scope.

The goal of the business case analysis is to get insight into:

- Economic value and feasibility of UHS;
- The potential role and behaviour of UHS assets in the electricity system by market simulations;
- The main cost and revenue drivers of a UHS assets;
- Sensitivities and risks in the business cases of UHS.

In subsections 2.6.2 and 2.6.3, the methodologies and tools used for the analysis, and the assumptions on energy system scenarios and costs for the years 2030 and 2050 have already been described. Here, we only present and discuss the results of the business case analysis for UHS and its sensitivities in subsection 3.6.2, followed by conclusions in subsection 3.6.3.

#### 3.6.2 *Economic cost comparison UHS*

In this subsection, the business case for UHS is elaborated. First, the basic structure and assumptions are described, followed by the results of the analysis.

##### 3.6.2.1 Basic structure and assumptions

###### ***Cost modelling methodology***

Costs consist of CAPEX (capital expenditure, investments) and OPEX (constant and variable operational expenditure). CAPEX consists of investment in the production asset. Planning, engineering and construction of the assets will in practice take several years, but for simplicity all CAPEX is assumed to be spent in 2025.

OPEX consists of the following cost items:

- Electricity consumption costs (determined by EYE simulation);
- Electricity grid connection costs (TSO costs);
- Operation & maintenance for the production and storage asset;

Details and amounts of the CAPEX and OPEX cost items can be found in 3.6.2.2.

### **Business model of UHS assets**

Business models of both assets are based on electricity market prices (EPEX market) and the volatility of those prices: when electricity prices are low, the storage is charged/filled. At moments of high prices, the storage is discharged/emptied. The differences in electricity prices are the revenue generator in this study. The times of charging and discharging are determined by an hour price scenario for electricity, that results from the EYE modelling. More details on the specific business model and the underlying production strategy of both cases can be found in 3.6.2.2.

Besides a business model based on volatility of electricity prices, also other business models are possible for UHS. Benefits of storage are for example:

- Offering flexibility to the electricity system (TSO and DSO), e.g. by services like aFRR and FCR from TenneT, the Dutch TSO;
- Offering security of electricity supply by storage of electricity as hydrogen;
- Avoid or reduce investments in grid capacity extension by TSO and DSO;
- Utilisation of waste heat generated by the asset (electrolyser). Waste heat can be used for example in the industry or built environment.

These values offer possible additional revenue streams, but are not within the scope of the business case analysis in this study. Table 3-16 summarizes the business models in and out of scope in this study.

Table 3-16 Scope of business models analysed in the economic assessment of UHS

| <b>Business model in scope</b>  | <b>Business model out of scope</b>  |
|---|---|
| Hydrogen production based on electricity price volatility on the day-ahead wholesale market of the Netherlands. Continuous hydrogen supply and constant hydrogen price. | Hydrogen production based on electricity price volatility on the European day-ahead wholesale market. Continuous hydrogen supply and constant hydrogen price. |
|   | Seasonal supply of hydrogen   |
|   | Rental of storage capacity through private agreements   |

### **Business case analysis assumptions**

For the business case, the following financial parameters are assumed:

- A WACC (Weighted average cost of capital) of 5% is applied.
- The time period for the business case is from 2025-2060:
  - Investments and construction of assets from 2025-2029;
  - Asset is operational from 2030-2060
  - Decommissioning costs are left out of scope
- In the EYE simulation, an hour price scenario for 2030-2049 is determined, based on simulation of 2030; and a price scenario for 2050-2060 based on simulation of 2050.

### **Sensitivity analysis scenarios**

The assumptions of the future energy scenario and the techno-economic asset parameters are stretched by means of a sensitivity analysis to assess the robustness of the results of the business case analysis. Six sensitivity scenarios are defined. Table 3-17 describes the parameters that are varied and the values assumed to conduct this analysis. The scenarios are chosen such, that the main driver over this economic assessment, the electricity price, is subjected to potential changes to test

the robustness of the market price in 2030 and 2050. Both the capacity or primary input variables of flexible power sources (S1, S3, S5, S6) and the inflexible power sources (S2) are aggressively stretched. The aggressive sensitivity analysis aims to yield insights on the energy system behaviour and the subsequent responses the storage assets. A rapid technological development is included to explore the benefits from lower electrolyser investment costs and better hourly performance (S4). The values of varied parameters can be found in Appendix B: Detailed sensitivity analysis description.

Table 3-17: Definition of six sensitivity scenarios

| Sensitivity scenarios |   | Varied parameter(s)      |
|-----------------------|---|--------------------------|
| S1                    | Maximum natural gas-fired power plant [GW]  | +3.2 GW operational      |
| S2                    | Installed capacity solar (PV) [GW]          | 200% Solar <2050         |
|                       | Installed capacity offshore wind farms [GW] | 200% OWF >2050           |
| S3                    | Natural gas price [EUR/MWh]                 | 200% NG price            |
|                       | CO2 price [EUR/ton]                         | 200% CO2 price           |
| S4                    | Electrolyser power of P2G asset [MW/h]      | 200% production capacity |
|                       | Cavern charge rate of UGS asset [MW/h]      | 200% charge capacity     |
|                       | Electrolyser efficiency [%]                 | +10% efficiency          |
|                       | Electrolyser investment costs [EUR/MW]      | -20% investment cost     |
|                       | TSO costs flex [EUR/MW]                     | 50% TSO costs            |
| S5                    | Hydrogen price [EUR/kg (EUR/MWh)]           | 50% H2 price             |
| S6                    | Hydrogen price [EUR/kg (EUR/MWh)]           | 500% H2 price            |

### 3.6.2.2 Business case flexible hydrogen production and storage

The business case analysis of the flexible hydrogen production and storage case study is presented in this paragraph. The business case of flexible hydrogen production and underground hydrogen storage (UHS) is compared to a continuous production asset. If the delta between these two business cases is in favour of the flexible production asset with storage, the storage creates sufficient value to justify the higher investment and operation costs of the flexible production asset.

First, the production strategy and techno-economic parameters are discussed. Subsequently, the results and sensitivity analysis of both the EYE market simulation and the economic cost modelling are presented. Finally, conclusions regarding the case study are drawn based on these results.

#### ***Production strategy flexible versus continuous hydrogen production***

A continuous amount of hydrogen is to be supplied by both the continuous and flexible hydrogen production asset. This continuous demand is equal to the maximum production capacity of the continuous production asset: 600 MW<sub>H<sub>2</sub>LHV</sub>. The hydrogen production capacity of the flexible asset is 150% of the continuous asset capacity. The flexible asset is thereby able to produce and store excessive hydrogen when electricity prices are low, and switch off hydrogen production to rely on the supply of hydrogen from storage when electricity prices are high. An operational strategy is required to benefit from this operational expenditure reduction mechanism. This strategy is described in the four steps below:

1. A virtual electricity market is simulated excluding all non-must run assets (including competing storage assets such as batteries, flexible Power-2-gas assets, D-CAES and AA-CAES assets). This virtual market can be considered a perfect forecast of future hourly prices.

2. Participation of the flexible hydrogen asset on the electricity market depends on the following logic: the flex hydrogen asset checks first if there is enough hydrogen stored in the salt cavern to supply the hourly demand of hydrogen. If there is not enough hydrogen available, the asset places a bid into the electricity market to purchase the electricity required to produce hydrogen. If there is enough hydrogen available, the asset continues with step 3.
3. The asset compares the hourly virtual market price to the yearly average to define whether it is economically attractive to produce and store hydrogen, based on its operational costs.
4. It is assumed that the asset can only run at full load or stand-by load. The stand-by load is assumed to be required for the PEM electrolyser to remain active. The electrolyser should be 'on' at all time at 34 MWe capacity. Therefore, the stand-by load results in a minimal bid into the electricity market.

The above mentioned operational strategy fully relies on the hourly electricity market volatility to achieve operational cost reduction. In addition to this *use case* of hydrogen storage, additional storage use cases can be identified. Other use cases are however out of the scope of this research.

#### ***Techno-economic parameters flexible hydrogen production***

The flexible and continuous hydrogen production assets are defined by the technological and economic parameters described in this paragraph. A selection of the most relevant parameters is found in Table 3-18 and Table 3-19. A detailed list of asset parameters can be found in Appendix A: Techno-economic parameters.

The increased production rate of the flexible electrolyser is chosen such that a an observable change in the operational profile can be expected, while acknowledging the technology readiness level of large capacity PEM electrolysers. A significantly larger capacity difference of 300% is considered in the sensitivity analysis of this study.

Table 3-18: Technological parameters flexible hydrogen production

| <b>Technological parameter</b>              | <b>Unit</b>           | <b>Flexible</b> | <b>Continuous</b> |
|---|-----------------------|-----------------|-------------------|
| P2G PEM Production capacity                 | MW <sub>e</sub>       | 1,500           | 1000              |
| P2G PEM Production capacity stand-by        | MW <sub>e</sub>       | 34              |                   |
| P2G PEM Efficiency                          | %                     | 60              | 60                |
| P2G PEM lifetime                            | year                  | 30              | 30                |
| P2G PEM Stack lifetime hours                | hours                 | 50,000          | 50000             |
| UHS Storage capacity                        | MWh <sub>H2 LHV</sub> | 163,150         |                   |
| UHS Storage capacity volume                 | Nm <sup>3</sup>       | 54,500,000      |                   |
| UHS Storage capacity volume                 | ton                   | 4,895           |                   |
| UHS Charge efficiency                       | %                     | 100             |                   |
| UHS max charge rate                         | MWh <sub>H2 LHV</sub> | 900             |                   |
| UHS max charge flow                         | ton/h                 | 27              |                   |
| UHS max discharge rate                      | MWh <sub>H2 LHV</sub> | 606             |                   |
| UHS max discharge flow                      | ton/h                 | 18              |                   |
| UHS Discharge efficiency                    | %                     | 99              |                   |
| Ratio working gas volume/cushion gas volume | -                     | 3/2             |                   |
| Required cushion gas volume                 | Nm <sup>3</sup>       | 36,333,333      |                   |
| Required cushion gas volume ton             | ton                   | 3303            |                   |

Table 3-19: Economic parameters flexible hydrogen production

| Economic parameter                              | Unit                  | Flexible    | Continuous  |
|---|-----------------------|-------------|-------------|
| Investment costs P2G PEM                        | EUR/MW                | € 1,000,000 | € 1,000,000 |
| Investment costs stack replacement              | EUR/MW                | € 184,000   | € 184,000   |
| Investment costs Balance of plant <sup>26</sup> | EUR/MW                | € 500,000   | € 500,000   |
| Investment costs Compressor (+drying)           | EUR/ton/h             | € 4,200,000 |             |
| Investment costs UHS cavern                     | EUR/ton               | € 4,800     |             |
| Investment costs Expander gas treatment         | EUR/ton               | € 2,520,000 |             |
| Electricity consumption P2G PEM                 | MWh <sub>e</sub> /ton | 55.56       | 55.56       |
| Electricity consumption Balance of plant        | MWh <sub>e</sub> /ton | 0           | 0           |
| Electricity consumption Compressor (+drying)    | MWh <sub>e</sub> /ton | 1.1         |             |
| Electricity consumption UHS cavern              | MWh <sub>e</sub> /ton | 0           |             |
| Electricity consumption Expander gas treatment  | MWh <sub>e</sub> /ton | 0.1         |             |
| Constant O&M costs P2G PEM                      | CAPEX/year            | 2.5%        | 2.5%        |
| Constant O&M costs Balance of plant             | CAPEX/year            | 1%          | 1%          |
| Constant O&M costs Compressor                   | CAPEX/year            | 7%          |             |
| Constant O&M costs UHS cavern                   | CAPEX/year            | 4,5%        |             |
| Constant O&M costs Expander gas treatment       | CAPEX/year            | 4%          |             |
| TSO grid connection costs                       | EUR/MW/year           | € 37,000    | € 37,000    |

### Modelling results flexible hydrogen production

Simulating the energy market in 2030 and 2050, assuming the energy system characteristics discussed in subsection 2.6.3.3, yields systemic and asset-specific results as discussed below.

Price duration curve: The hourly electricity price throughout the year is rearranged to the *price duration curve* below in Figure 3.45. The electricity price ranges from 0 to 84.8 €/MWh in the 2030 simulation, and ranges from 0 to 84.2 €/MWh in 2050.

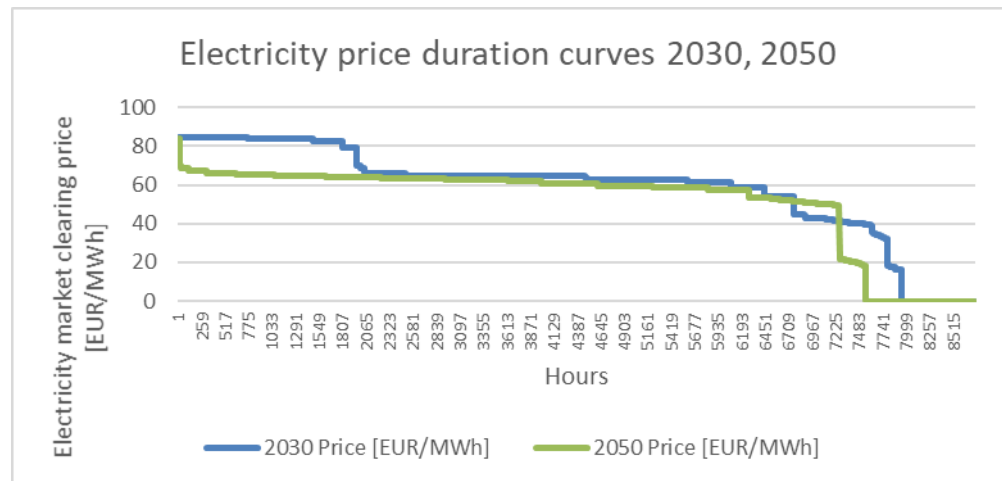


Figure 3.45: Price duration curve results 2030, 2050

<sup>26</sup> The balance of plant of the electrolyser stacks consists of the following subsystems: power supply subsystem, water management subsystem, hydrogen production subsystem, cooling subsystem and control subsystem

Annual fill level profile flexible P2G: The charge and discharge behaviour of the flexible P2G asset, rooted in its production strategy logic, leads to the fill level profiles depicted in Figure 3.46 and Figure 3.47 for the year 2030 and 2050 respectively. The figures provides insights when, and how much hydrogen is stored annually.

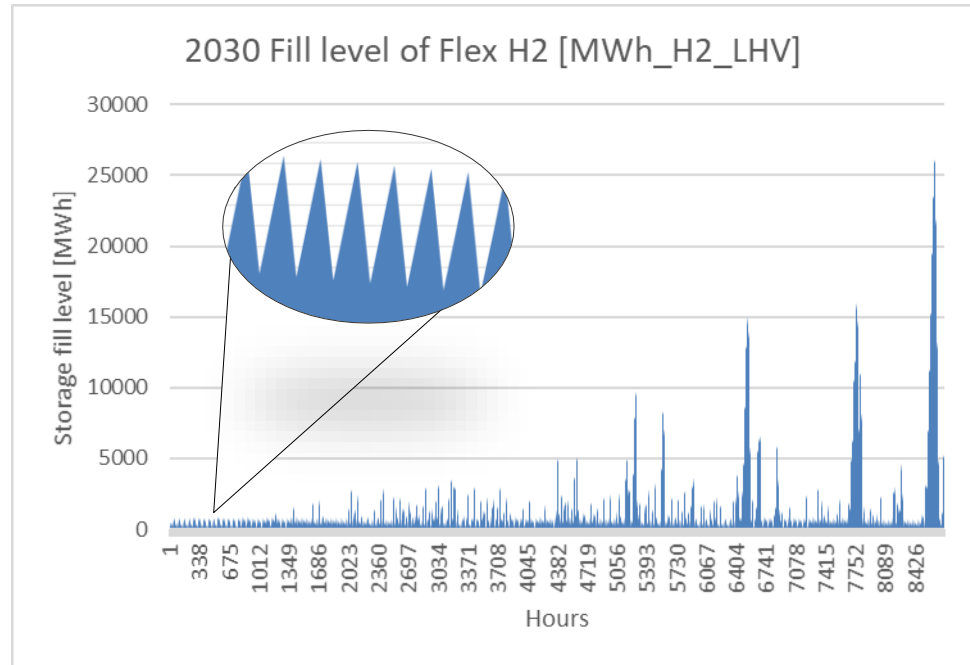


Figure 3.46: Hourly fill level of flexible hydrogen storage 2030

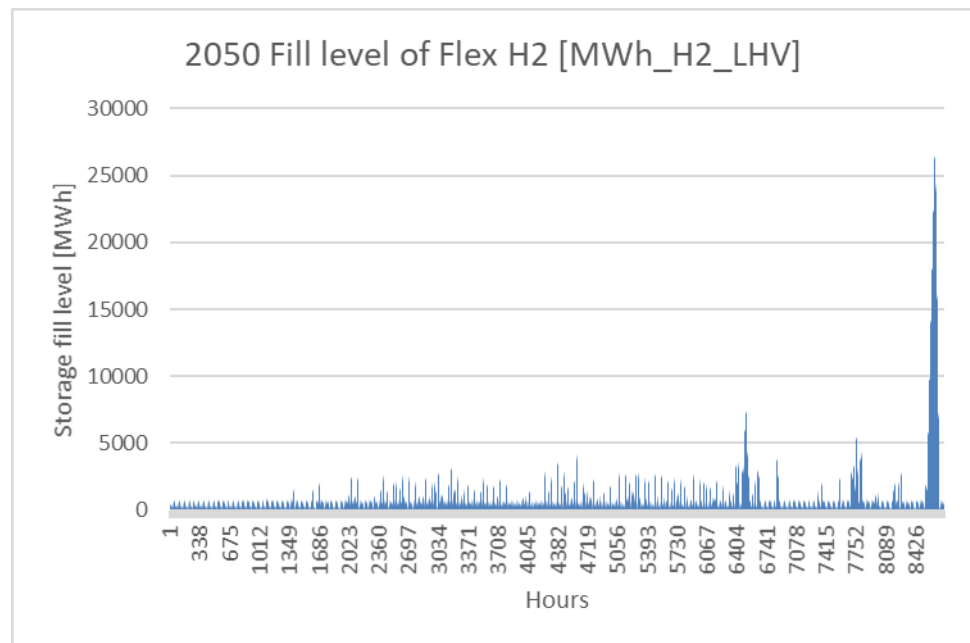


Figure 3.47: Hourly fill level of flexible hydrogen storage 2050

Load duration curve flexible P2G: The load duration curve of the flexible hydrogen production asset gives insight in the relation between the capacity requirements and capacity utilization throughout one year (see Figure 3.48).

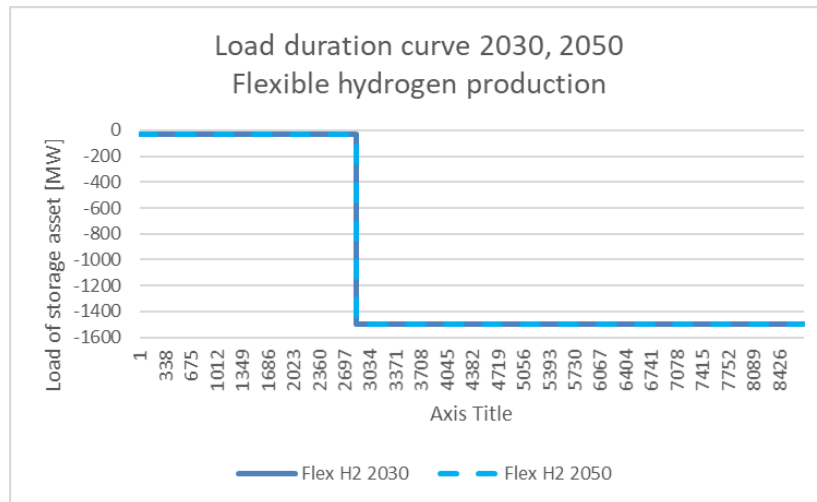


Figure 3.48: Load duration curves flexible hydrogen production 2030, 2050

The operational profiles of the flexible P2G, together with the hourly electricity price, results in the yearly electricity consumption costs. This operational cost is integrated in the economic cost model to calculate the cost breakdown and net present value per asset.

Cost breakdown flexible and continuous P2G: The total cost breakdown adds up the yearly revenue, constant and variable operational costs and investment costs (see Figure 3.49). The revenue, OPEX and CAPEX of 2030 are assumed to be representative for the years 2030 up to 2050. The revenue, OPEX and CAPEX of 2050 is representative for 2050- 2060. The cost and revenues in full detail can be found in Appendix C: Business case details 2025, 2030, 2050.

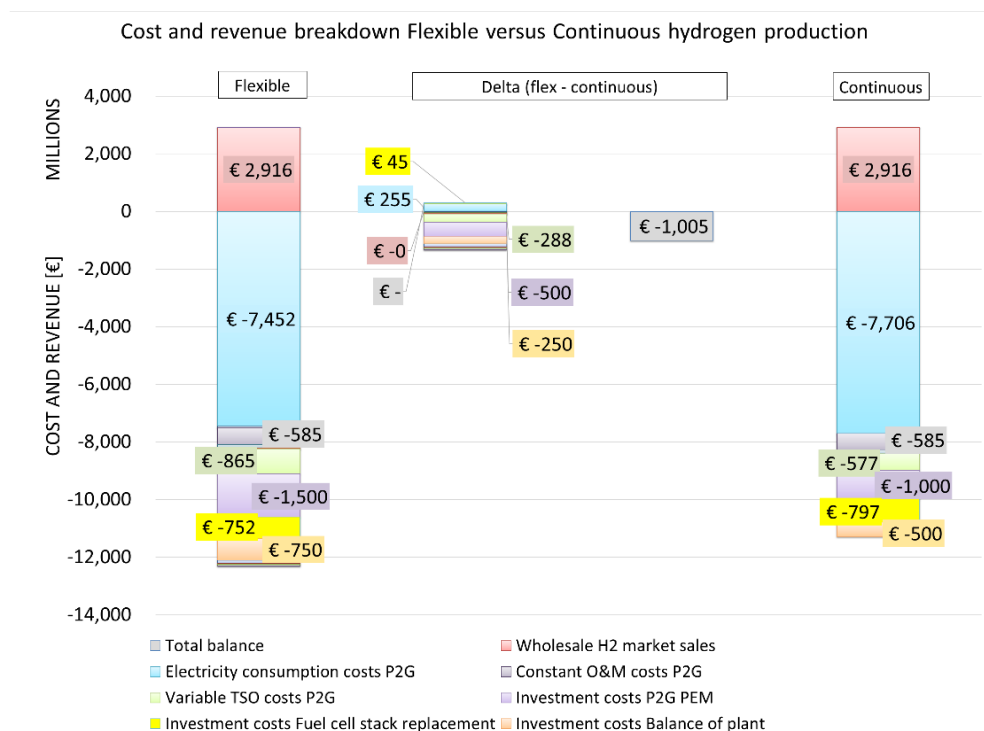


Figure 3.49: Cost and revenue breakdown flexible hydrogen production

**NPV difference flexible versus continuous P2G:** The cash flow, cumulative cash flow and cumulative discounted cash flow difference of the flexible and continuous P2G production is depicted in Figure 3.50.

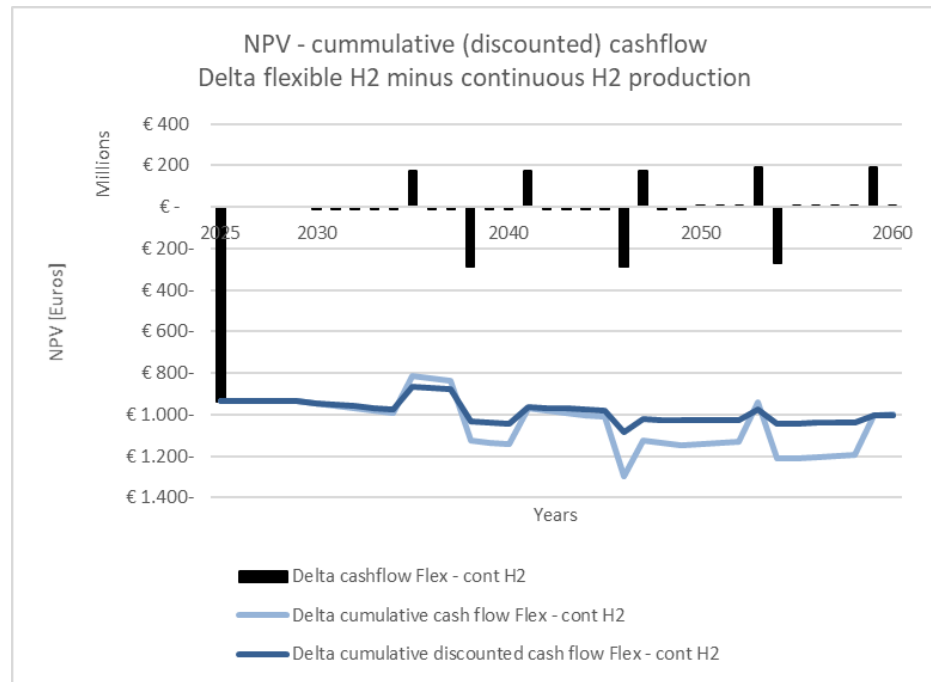


Figure 3.50: NPV and cash flow flexible hydrogen production

**Sensitivity analysis of results**

The robustness of the base case modelling results are challenged through a variety of extreme scenarios. Those scenarios are described in Table 3-17. In Figure 3.51, the cumulative discounted cashflow per scenario is visualized.

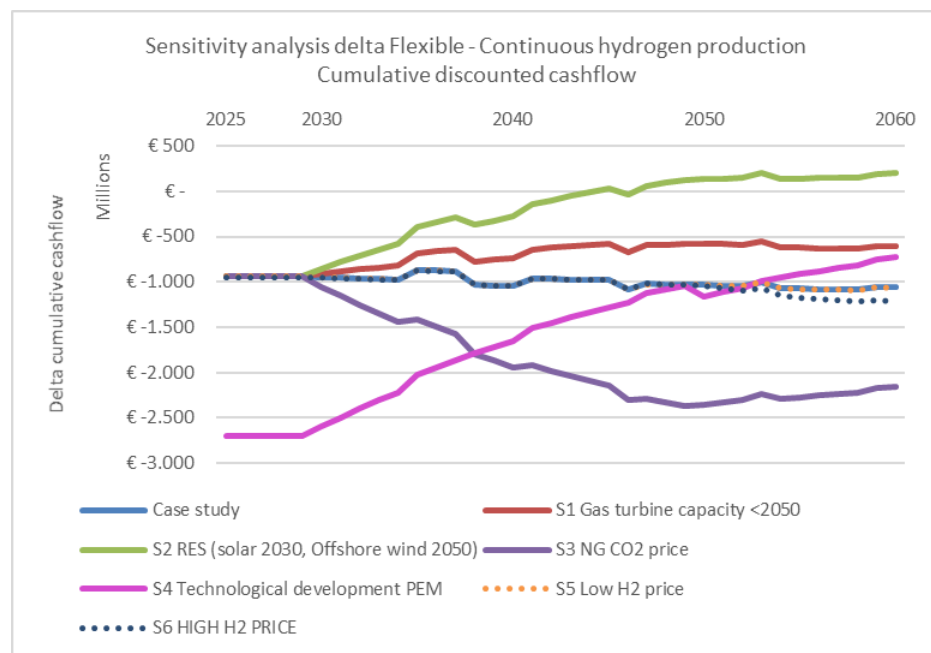


Figure 3.51: Sensitivity of NPV results flexible hydrogen production

### Discussion cost modelling flexible hydrogen production

When observing the results presented in Figure 3.49, Figure 3.50 and Figure 3.51 and considering the operational strategy of the flexible production asset, the following analysis is concluded upon:

The load duration curve indicates clearly that the flexible asset is offline 33% of the yearly operational hours. The overproduction capacity of 33%, compared to the continuous production asset, is thus fully utilized. And observing the hydrogen production profile in detail, one can identify a sawtooth-like storage fill level profile (see Figure 3.46). Furthermore, the storage fill level is rarely utilized to more than 10% of the full 163 GWh storage capacity.

Three prominent assumptions in the modelling of the flexible hydrogen production asset on the electricity market explain of this behaviour: (1) the annual hydrogen supply is equal for both the continuous and flexible production assets: 600 MW<sub>H<sub>2</sub> LHV</sub>; (2) the electrolyser start-stop decision is made per hour and has no minimum or maximum constraints; (3) the electrolyser operates either on full load capacity (900 MW<sub>H<sub>2</sub> LHV</sub> per hour) or stand-by mode (20 MW<sub>H<sub>2</sub> LHV</sub> per hour).

The operational decision logic of the asset, visualized in Figure 3.52, explains the short-term charge and discharge behaviour.

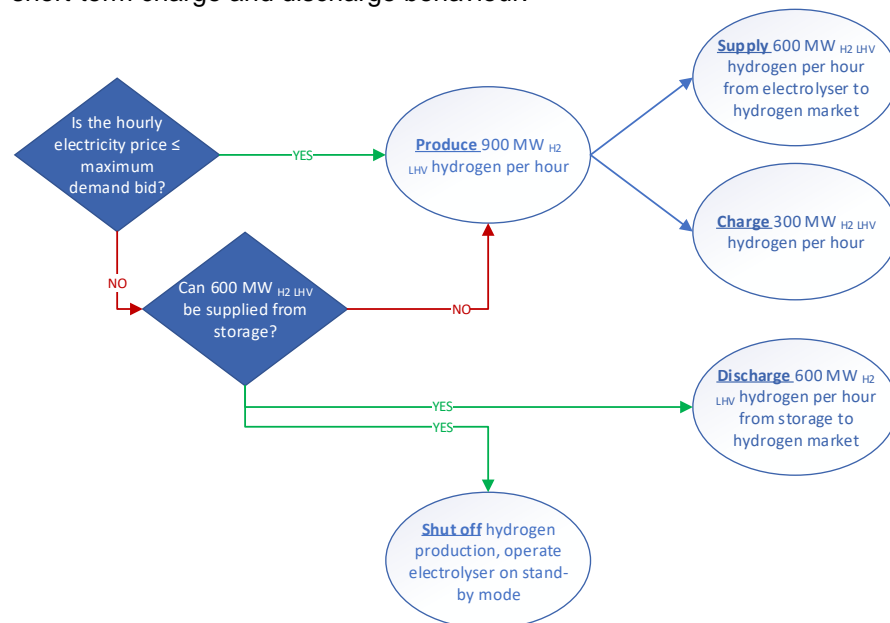


Figure 3.52: Flexible hydrogen production and storage decision tree

Given the PEM efficiency of 60%, the maximum flexible hydrogen production capacity is 900 MW<sub>H<sub>2</sub> LHV</sub> per hour. Due to the continuous demand of 600 MW<sub>H<sub>2</sub> LHV</sub> per hour, 300 MW<sub>H<sub>2</sub> LHV</sub> per hour can be stored when the flexible electrolyser is in operation. When the electricity price is such that the flexible asset production cost arrives at the break-even point with hydrogen wholesale revenue, the asset produces hydrogen. In terms of hourly electricity market bids, this implies that the electricity price needs to be equal to or lower than the maximum demand bid. When the electricity price is higher than the maximum demand bid price of the asset, the asset switches to hydrogen supply by discharging the stored hydrogen if the required amount of hydrogen is available. In case of an empty storage, two hours of full load production thus allows the electrolyser to switch off for one hour.

The mechanism described above leads to both the operational profiles of 2030 and 2050. A 14-day period of time in September 2030 (see Figure 3.53:) is depicted to illustrate the behaviour in more detail. The fill level profile in Figure 3.53: indicates that the flexible hydrogen production asset switches off and supplies stored hydrogen when electricity prices are above 58.5 €/MWh. However, due to the continuous hydrogen demand, hydrogen production against higher prices is required when the storage is empty.

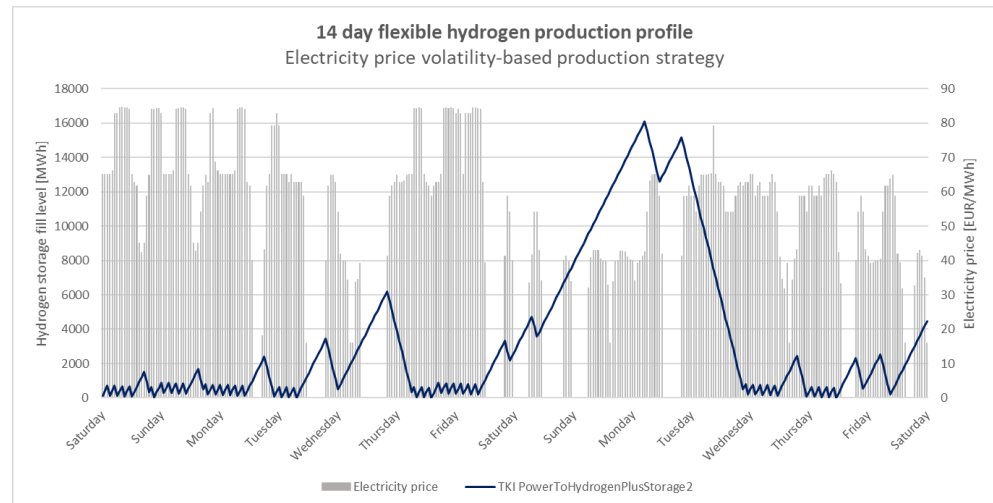


Figure 3.53: 14-day example of operational profile and electricity market volatility for flexible hydrogen production

The production strategy in this study is based on the volatility of the electricity price. The hourly electricity price is the basis to minimize operational costs. Due to the immature hydrogen market, simplified hydrogen demand assumptions are introduced in this economic assessment. Due to the constant hydrogen demand and a constant hydrogen price (36,43 €/MWh<sub>2,LHV</sub> in 2030, 32,22 €/MWh<sub>2,LHV</sub> in 2050), no hydrogen price volatility is introduced in the economic assessment. Consequentially, the operational strategy of the flexible hydrogen asset does not include a potentially larger amount of economically viable operational hours due to the increase in wholesale revenue per hour. When both the electricity price volatility and hydrogen price volatility are considered simultaneously, different operational behaviour can be expected.

The electrolyser that operates flexible has less yearly operational hours than electrolyser that produces hydrogen continuously. Consequently, the stack replacements for flexible operation need to be replaced every 8,5 years, while stacks with continuous operation need a replacement every 5,7 years. While less replacement saves costs, the replacement of the flexible stacks is more costly due to its increased capacity. The stack replacement cost difference explains the large jumps in the cash flow delta (see Figure 3.50).

The flexible production asset with storage appears to have lower electricity costs (€255 mln), due to its ability to make use of electricity market price volatility. These lower costs for electricity are however more than annihilated by the higher investment costs for the hydrogen plant (delta of €500 mln for electrolyser and €250 mln for Balance of Plant) and higher TSO costs (€288 mln extra TSO costs per year), among others. This means that, in the base case, the value the enabled flexibility by

introducing storage is not enough to justify the higher costs of the flexible production asset, compared to continuous production. The costs for the storage asset (salt cavern, compressor, gas treatment and cushion gas) have just a small stake in total investment costs.

The business case of flexible hydrogen production and storage is, however, sensitive to the deviations in the scenarios. Especially an increase in the amount of low price hours per year due to, for example, higher integration of renewable energy sources leading to more frequent surplus of electricity on the market (solar and offshore wind, S2) gives a perspective on a positive NPV. Also further developments in PEM technology (S4) favours the business case of flexible hydrogen production and storage: the increase in electrolyser efficiency is reduces the OPEX, while a lower investment cost per electrolyser capacity lowers the initial investment.

### 3.6.3 *Conclusions and future research*

#### 3.6.3.1 Conclusions

Based on the results of the economic analysis as presented, the following conclusions can be drawn regarding the business case of flexible hydrogen production with underground hydrogen storage (UHS) in a salt cavern vs. that of a continuous production asset:

- The lower electricity costs in the business case for the flexible production asset, due to reaped benefits from the volatility in electricity prices, appears insufficient to compensate for the extra investments in a larger electrolyser, the storage and the related equipment, and the higher operational costs.
- The business case of flexible hydrogen production and storage is, however, sensitive to the deviations in the scenarios. Especially an increase in the amount of hours with low electricity prices (solar and offshore wind, S2) gives a perspective on a positive NPV. Also further developments in PEM technology (S4) favours the business case of flexible hydrogen production and storage.

A perspective on a future positive business case is offered by the following developments:

- Additional revenue streams can be generated by including alternative benefits of storage in the business model, that were outside the scope of this study, for example:
  - Offering flexibility to the electricity system with the up- and down-regulating capacities of the electrolysers (TSO and DSO), e.g. by services like aFRR and FCR from TenneT, the Dutch TSO;
  - Offering security of supply by storage of hydrogen;
  - Avoid or reduce investments in grid capacity expansion by TSO and DSO;
  - Utilisation of waste heat generated by the asset (electrolyser). Waste heat can be used for example in the industry or built environment.
- On the cost side, further reductions may appear possible, for example on the following items:

- Efficiencies of the assets may turn out to be better than assumed in the business cases, due to further technical development than currently foreseen.
- CAPEX of the assets may turn out to decrease in the future, due to technical developments and economies of scale.
- OPEX may decrease, especially for TSO costs. The relatively high connection costs for flexible assets, that are supportive to the energy system, are subject of debate already.

An increase of renewable energy sources, on top of the scenarios currently foreseen, will favour the business case of flexible storage assets.

#### 3.6.3.2 Future research

Complementary revenue streams are needed to make investments in flexible hydrogen production with underground hydrogen storage (UHS) in a salt cavern pay back. Further research could focus on the potential value and business models of the additional revenue streams named above. Also, the role of interconnection and its influence on electricity prices should be further studied. Finally, the development of a hydrogen market model (e.g. as an addition to the EYE model) would enable the use of more realistic demand profiles. Rather than assuming a continuous demand, as was done in this study, the demand profiles would be influenced by the need for hydrogen in different sectors, the volatility in electricity and hydrogen prices, and import (of hydrogen, LOHC, fuels) versus local production. It would allow us to study the impact of these influences on flexible hydrogen production behaviour.

## 4 Conclusions

In this work package, we investigated the techno-economic feasibility of two technologies for storage of energy at large-scale in the subsurface: CAES in salt caverns and UHS in salt caverns and depleted fields. Based on the results of the investigations, the following can be concluded:

### 4.1 Conclusions on CAES

#### 4.1.1 *On the technology concept(s) and deployment status of CAES*

- There are two main CAES concepts, which mainly differ in how they deal with the temperature change of the air during compression and expansion: diabatic CAES (D-CAES) and advanced adiabatic CAES (AA-CAES). In both concepts, electrical energy is stored in mechanical form by compressing air, and storing the air in salt caverns. Electricity is regenerated by using the compressed air to drive a turbo-expander/turbine.
- In a D-CAES system, because the heat that is generated on compression of the air is not stored, an external fuel must be combusted at time of generation to heat up the air prior to driving the turbine. Natural gas is conventionally used, but its combustion causes CO<sub>2</sub> emissions. Hydrogen is emerging as an alternative, in particular because combustion of hydrogen does not emit CO<sub>2</sub>, and it can be produced from renewable electricity (also without emitting CO<sub>2</sub>). Worldwide, two CAES plants have been commercially operational for many years, one in Germany (Huntorf, 321MW/2.5GWh) and one in the US (McIntosh, 110MW/2.6GWh), both of which are based on the relatively mature D-CAES concept (TRL 7-8). Round-trip efficiencies of up to 60% are deemed feasible with efficient utilization of waste.
- In an AA-CAES system, the heat of compression is stored in a TES (Thermal Energy Storage device) and re-used during the discharging process, which eliminates the need to combust a fuel. With this method higher round-trip (power-to-power) efficiencies of up to 70% can be reached. However, efficient thermal storage of heat at the very high temperatures involved (up to 580°C) is challenging and costly, and the TRL of this technology (TRL 5) is currently not high enough to be commercially applied.
- In recent years, several demonstration and (commercial) development projects have been conducted and/or are ongoing, which indicates a strong renewed interest in CAES, probably sparked by the increasing need for flexibility services to integrate the growing share of variable renewables (wind, solar). Most recently, project developer Corre Energy Storage announced its intention to develop a 320-MW D-CAES plant in The Netherlands<sup>27</sup> with a storage capacity of 3-4GWh. The project obtained the status of European Project of Common Interest (PCI) in 2017 and receives financial support from the Connected Europe Facility fund, which can be considered a recognition of the potential value of this technology in providing flexibility to the increasingly renewables-based European energy

---

<sup>27</sup> <https://correenergystorage.nl/caes-the-project/>

system. A unique aspect of this project is that its two 160MW turbines will be designed to ultimately run on 100% (renewable) hydrogen.

#### 4.1.2 *On the technical performance characteristics of CAES*

- CAES systems are designed to be competitive in delivering a suite of flexibility services that are valued by utility companies, owners of generation assets, and grid operators. They can generate revenue from two main groups of services: 1) arbitrage, i.e., providing electricity traders a means to earn money by leveraging the hourly price differences on electricity markets; and 2) Ancillary services, such as frequency regulation, reserve power, black start, load following, and synchronous inertia, that are procured by grid operators and asset owners of generation assets to manage grid stability.
- CAES systems are classified by two performance parameters: 1) their generation capacity at full load (power output in MW), and 2) the duration (in hours) over which this power can be delivered. By multiplying one with the other, the electricity production capacity (in MWh) is obtained. Typically, the power range of CAES systems is between 100-500MW, and the duration over which this power can be delivered ranges from hours to a day.
- Start-up times of CAES plants in normal situations are below 15 minutes and this enables them to provide secondary (and tertiary) reserve power to grid operators for frequency restoration. Also, in an emergency situation, they can provide black-start services to grid operators to contribute to the process of recovering a power station to operation, because they can start main blocks of generation onsite without having to rely on an external power source.

#### 4.1.3 *On the design of caverns for CAES*

- In general, salt caverns designed for CAES range in volume from 100,000 m<sup>3</sup> to 1,000,000 m<sup>3</sup>. Solution mining, the technique by which they are created, has been practiced for many decades, and the techniques and procedures to ensure that a cavern develops according to the design specifications in terms of location, depth, dimensions, and volume have seen continuous improvement. To ensure the geomechanical stability and integrity of caverns, design and operational criteria must be adhered to, and this must be accounted for in spatial planning.

#### 4.1.4 *On geomechanical effects of CAES on cavern stability and integrity*

- Effects of cyclic injection and withdrawal of air during CAES operation do not jeopardize cavern stability and integrity. Although temperature fluctuations are observed that may lead to the creation of fractures in a thin skin at the cavern wall (<1m thick damage zone), they do not pose a real threat to cavern integrity due the limited depth of penetration in the cavern wall. Even during maintenance periods, or in extreme cases, when the cavern would experience atmospheric conditions for a prolonged period (months), although the width of the damage zone would be larger, the results suggest that it would not jeopardize cavern stability and integrity. However, due to the large difference between the pressure inside the cavern, and the pressure in the salt surrounding the cavern, salt creep will accelerate, leading to accelerated cavern convergence and subsidence.

#### 4.1.5 *On the economics of an arbitrage-only business model for CAES*

- An exploratory economic analysis indicates that a price arbitrage-only business case for D-CAES may not be viable. Due to a significant price spread requirement to break-even operationally, in the analysis D-CAES only charges at a very low electricity price, which results in a very limited number of operational hours, and thus limited revenues. Although the business case for AA-CAES shows more operational hours than for D-CAES, due to a less severe price spread requirement, revenues are not sufficient to realise a positive NPV. Additional (complementary) revenue streams are therefore required (e.g. from ancillary services such as grid balancing, redispatch, black start, etc.) and/or investment and operational costs must decrease to make investments in D-CAES and AA-CAES pay back.
- An important limitation in the analysis is the assumption of full-load only operation mode. Together with the hourly decision-logic and minimal risk acceptance level, the fill level of both the D-CAES and AA-CAES therefore shows economically suboptimal asset operation. Power discharge occurs as soon as the required marginal price spread is met. Subsequently, the stored energy is sold for the electricity price that generates minimum revenue. Furthermore, our analysis excludes a multi-year stochastic analysis of the variability of renewables feed-in and its influence on electricity prices is not included.
- Several recent studies (Heuberger et al., 2017; Guerra et al., 2020; van Hout et al., 2014) show the basis of a positive business case and the importance of co-optimising energy revenues with ancillary services. To be able to conclude on the economic viability and business case of the D-CAES and AA-CAES technology, additional key business models should therefore be assessed in addition to the day-ahead wholesale market business model of this study, based on multi-year stochastic analysis of the variability of renewables feed-in.

## 4.2 **Conclusions on UHS**

### 4.2.1 *On the technology concept(s) and deployment status of UHS*

- Hydrogen is currently stored in pure form in large quantities (10-100 million m<sup>3</sup>) in salt caverns in the US and in the UK. Practical experience with these sites has shown that hydrogen can be safely stored in this way for long periods of time. No issues (biological and/or chemical degradation, etc.) are reported in literature with respect to storage in salt caverns. On account of the fact that four storage facilities are currently operational in the world, hydrogen storage in salt caverns could be considered mature. However, these storages are designed to provide security of supply of feedstock to the chemical industry, where demand profiles are typically very static, reflecting the continuous mode operation of chemical production processes. In contrast, to cancel out supply-demand imbalance caused not only by variations on the demand side but also by large weather-controlled variations in supply, injection and withdrawal are expected to occur much more frequently and cyclically, and at higher volumetric rates. This kind of

fast-cycle operation brings with it specific challenges that must be addressed, in particular in relation to the integrity and durability of wellbore materials and interfaces. Hence the TRL must be considered to be lower. Several pilot- and demonstration projects are being prepared in Europe to raise the TRL to 7, one of which in the Netherlands by Energystock (a subsidiary of Gasunie).

- Hydrogen can also potentially be stored in depleted gas reservoirs, similar to natural gas. Natural gas is already safely stored in large quantities in depleted gas fields in the Dutch subsurface ( $\approx 14$  billions of  $m^3$ ), and that of many other countries in Europe. No sites exist however where pure hydrogen is stored, and there are open questions regarding the influence of geochemical processes and biochemical interactions of hydrogen with rocks, fluids and micro-organisms in depleted gas reservoirs and the potential (technical, environmental, economic) risks associated with these interactions, in particular the formation of hazardous and/or corrosive fluids, and the degradation of injection and/or withdrawal performance.
- Recent demonstration projects in Argentina and Austria with injection of up to 10% of hydrogen in a mix with natural gas into a depleted gas field have shown that hydrogen can be safely stored without adverse effects to installations and the environment. However, not all hydrogen was recoverable due to diffusion, solution and conversion to methane. Furthermore, in the past, town gas, containing 50-60% of hydrogen, was stored underground in salt caverns, depleted fields and aquifers. No major HSE (health, safety, environment) issues with these storages are reported in literature, but little research was done regarding conversion to methane or other processes (e.g. trapping of hydrogen in the reservoir) that adversely affect the amount and quality of the hydrogen that can be recovered. As such, it is clear that significant gas treatment (purification, drying) will be required when withdrawing hydrogen from a depleted field, even when injecting it in pure form, which will impact the economics.

#### 4.2.2 *On the technical performance of UHS in salt caverns and reservoirs*

- A technical performance analysis to investigate the potential performances of UHS relative UGS reveals that the lower density (8-10 times) and viscosity of hydrogen relative to methane results in 2.4 to 2.7 times higher withdrawal rates. These high rates partly compensate for the lower energy content (3-4 times lower), resulting in an energy throughput of 0.7 to 0.8 times that of methane.
- Although maximum withdrawal rates for hydrogen up to  $\approx 33$  mln  $Sm^3/day$  (99GWh/day, or  $\approx 4.1$ GW energy throughput) for a well with a 7-inch (ID) tubing are theoretically possible, there are several factors (erosional velocity limit, bottomhole drawdown, 3-month plateau rate period) that limit the practical withdrawal rate. For example, for the Grijpskerk UGS, the withdrawal rate would drop to just below 20 mln  $Sm^3/day$  (57GWh/day, or  $\approx 2.3$ GW energy throughput) for a well with a 7-inch (ID) tubing. Use of a 9-inch (ID) tubing would increase the withdrawal rate by 57% for the Grijpskerk UGS, yet also the bottom-hole drawdowns by 42%, which increases the risk of mechanical damage to the wellbore, and a significant reduction of the flow performances.

- In general we observe higher injection rates for hydrogen than for methane at higher wellhead pressures. Despite the higher density (weight) of the methane, this gas has also a higher viscosity, which at high flow rate apparently hampers injection into the reservoir. For Grijpskerk we estimate maximum theoretical injection rates for hydrogen up to 35 mln Sm<sup>3</sup>/day through a 7-inch (ID) tubing. These high injection rates will also be limited by the erosional velocity and bottom-hole build-up as previously discussed for withdrawal. Further research is needed to obtain a good estimate of the feasible maximum theoretical injection rates.
- By depleting the reservoirs down to a pressure of 278 bar (Grijpskerk), 243 bar (Norg) and 184 bar (Alkmaar), respectively, we were able to reproduce the ratio between the current working and the maximum working volume (= GIIP, the amount of Gas Initially In Place in the reservoirs) for natural gas (in bcm) for the UGS facilities of Grijpskerk (10.8/2.5), Norg (29.4/6.3) and Alkmaar (3.81/0.56). This means the percentage of gas in these storages that is currently used as working volume is 23%, 21% and 14% of the GIIP. When applying the same depletion pressure, the working volumes of hydrogen would be 2.2bcm for Grijpskerk, 5,5 bcm for Norg and 0.48 bcm for Alkmaar, i.e. they would only contain 24% of the energy content in the original working volume of methane.
- At low(er) wellhead/bottom-hole drawdowns hydrogen can still flow while the heavier methane can not longer flow at these conditions, which potentially allows the use of lower minimum working pressures. If lower working pressures are adopted, i.e., down to a level where the cut-off withdrawal rate of 1 mln Sm<sup>3</sup>/day is reached, the working volumes of hydrogen would be slightly higher - 3.5 for Grijpskerk, 7.9 for Norg and 0.76 bcm for Alkmaar – and would contain 37% of the energy content in the original working volume of methane. Hence a lowering of the minimum working pressure in the Grijpskerk, Norg and Alkmaar UGS is potentially an attractive option to increase their working volume of hydrogen, and decrease the required volume of (hydrogen) cushion gas. However, the risks of surface subsidence and induced seismicity need to be investigated, because the reservoirs would be depleted below the current pressures.
- For a standard salt cavern, such that in Zuidwending, we estimate very high theoretical withdrawal rates of hydrogen up to 35 mln Sm<sup>3</sup>/day through a well with a 9-inch tubing (ID). This is 3-4 times faster than that of well in a salt cavern filled with natural gas, and 1.5 to 2.5 times faster than a well in a porous reservoir filled with hydrogen.
- Differently from porous reservoirs though, we observe that the very high theoretical withdrawal rates and the working volumes in salt caverns are primarily limited by daily allowable pressure depletion in order to preserve the structural integrity of the cavern and reduce the loss of (geometric) volume due to salt creep. For Zuidwending the depletion is limited to less than 10 bar per day. Based on this restriction, we observe that salt caverns in the Zuidwending storage site cannot exceed the withdrawal rate of 7.3 million Sm<sup>3</sup>/day of natural gas per cavern (67 GWh/day, each cavern has two wells), which is 1.6 times lower than the 12 mln Sm<sup>3</sup>/day we estimated as the theoretical maximum rate per well. In the case of hydrogen the maximum per cavern withdrawal rate we obtained is 5.2 million Sm<sup>3</sup>/day (15GWh/day), which is almost 7 times lower than the theoretical maximum of 35 mln Sm<sup>3</sup>/day per well.

- The importance of the daily pressure depletion restriction also applies to the working volume available in a salt cavern, which in Zuidwending is currently only 50% of the total storage capacity. In case Zuidwending would be operated at the same pressure range of today, yet storing hydrogen instead of natural gas, the energy content of the hydrogen working volume would be only 22% of the 3.6 TWh available today as natural gas. This is due to the faster pressure drop in the salt cavern during the withdrawal of hydrogen.
- Despite the good quality of the Grijpskerk and Norg reservoirs, these reservoirs require a large cushion volume to deliver high performances. This is due to their large size and great depth. These reservoirs were converted to UGS in part because they were undepleted natural gas fields where the cushion gas was already available. As described by Juez-Larré et al. (2016), there are many other potential porous reservoirs in the Netherlands, which could also be good candidates for UHS.

#### 4.2.3 *On geo- and biochemistry of UHS in depleted gasfields*

- A concise literature review indicates that the geochemical processes that could be of concern for hydrogen storage in the Netherlands are:
  - a. Reduction of iron minerals (pyrite) forming  $H_2S$ ;
  - b. Reduction of hematite to magnetite, sequestering  $H_2$  and producing  $H_2O$ ;
  - c. Reduction reactions and  $H_2S$  formation change the fluid composition and pH, possibly resulting in precipitation and dissolution of secondary minerals (changing the pore space);
  - d. Reactivity of wellbore materials impacting well integrity;
  - e. Hydrogen adsorption in clay.
- To simulate the mineral reactions a-c, a geo- and biochemical modeling study was performed with the geochemical model PHREEQC assuming instantaneous reaction to achieve a chemical equilibrium (no kinetics included). Four cases were modelled representative of storing hydrogen in reservoirs in the Buntsandstein, Rotliegend, Zechstein and Delft Sandstone formations in the Dutch subsurface.
- The modelling results indicate that pyrite reduction as a result of  $H_2$  storage may occur, leading to  $H_2S$  formation in the gas phase, which may affect safety, materials selection, facility design and economics.  $H_2S$  release increases with depth (as the partial pressure increases), and with the amount of initial pyrite in the reservoir, as is illustrated by the results of the Rotliegend sandstone. However, because kinetic effects were not taken into account, the model results reflect a worst case scenario.
- Furthermore, results indicate that reduction of hematite to magnetite may occur, sequestering  $H_2$  and producing  $H_2O$ . While the Delft sandstone case predicts dissolution of hematite ( $Fe_2O_3$ ) and precipitation of magnetite ( $Fe_3O_4$ ), the Rotliegend and Buntsandstein cases predict hematite dissolution and the precipitation of (iron-containing) siderite ( $FeCO_3$ ) as well as calcite ( $CaCO_3$ ). The preference for the hematite to siderite reaction in the Rotliegend and Buntsandstein cases is due to the presence of dolomite ( $CaMg(CO_3)_2$ ) in these reservoir rocks.

- Results also show that precipitation and dissolution of secondary minerals depends on the initial mineralogical composition, and that carbonate and clay transformations can be triggered by changes in fluid composition.
- In general reactivity of minerals increases with higher temperatures. Besides the temperature, a higher H<sub>2</sub> partial pressure increases reactivity in the reservoir. Hence deeper reservoirs will have a higher potential for hydrogen-induced reactions. The temperature in the reservoir will also depend on the temperature of the hydrogen when injected. The produced hydrogen is probably relatively cold (<60 °C) but it might be required to heat up the hydrogen before injection to prevent a cooling effect. This needs to be better constrained for future feasibility studies.
- On the presence CO<sub>2</sub> in reservoirs (either by natural origin, or as cushion gas), geochemical modelling indicates that it does not directly change the reactions of pyrite and hematite. Only small changes in the reactions are observed, this could be because CO<sub>2</sub> was already present in the models with and without CO<sub>2</sub> cushion gas. The amount of H<sub>2</sub>S formed is less than one percent different between the cases with and without CO<sub>2</sub>.
- On the use of nitrogen as cushion gas, geochemical modelling indicates that nitrogen has negligible impact on rock-gas-water reactions, which conforms with results reported in literature. The only effect is the change in hydrogen partial pressure when nitrogen is present as cushion gas which causes lower reactivity of hydrogen in the reservoir. Therefore, nitrogen would be suitable to use as a cushion gas for hydrogen storage at least from a geochemical perspective.
- Biochemical simulations with PHREEQC indicate that bacterial sulphate reduction and methanogenesis, may both pose a risk for underground hydrogen storage, which is also reported in literature. In this study however, maximum growth rates are assumed that occur at temperatures of 37 °C for methanogenesis and 30°C for bacterial sulphate reduction, which will create a worst-case scenario. In fact, the temperature in potential reservoirs for hydrogen storage in the Dutch subsurface is considerably higher (>80°C), and because this simplification causes the influence of such higher temperatures on bacterial activity to not be part of the simulations, the results will tend to over-estimate its impact.
- Although microbial reaction rates are expected to be limited at the above-mentioned prevailing temperatures, some hyperthermophiles living up to 110 °C have been observed. The unique circumstances that would be created when storing hydrogen in a reservoir, with high concentrations of hydrogen, a very good electron donor for microbes, warrants further research before this can be dismissed as a relevant process, especially since H<sub>2</sub>S already poses a serious threat in minor amounts.
- To accurately assess the risk of H<sub>2</sub>S formation in hydrogen storage reservoirs it is of the utmost importance to improve the predictive power of the geochemical models by incorporating kinetic rates at high temperatures and high H<sub>2</sub> partial pressures, which can be obtained with laboratory experiments. Accurate predictions also require detailed knowledge of the concentrations of iron-

containing minerals in reservoir rocks, which can be below detection limit of techniques such as XRD. This is important to determine the amount of H<sub>2</sub>S producing pyrite as well as the presence of H<sub>2</sub>S scavenging minerals such as siderite.

#### 4.2.4 *On the geomechanical effects of UHS on cavern stability and integrity*

- Effects of cyclic injection and withdrawal of hydrogen during UHS operation do not jeopardize cavern stability and integrity. Temperature fluctuations of up to 40 C° are simulated within a distance of 1 m into the cavern wall, in particular when injection cycles are short (weekly) or wellhead injection temperatures are high. Although such temperature fluctuations may lead to the creation of fractures in a thin skin at the cavern wall (<1m thick damage zone), they do not pose a real threat to cavern integrity due the limited depth of penetration in the cavern wall.
- Furthermore, cavern wall displacement of 35 cm are simulated in monthly cycling scenario with 23 days injection (3 weeks) and 7 days production (1 week). However, the geological tightness of the cavern and cavern integrity are not jeopardized during UHS normal cycling operations.

#### 4.2.5 *On the economics of UHS in salt caverns vs. continuous H<sub>2</sub> production*

- The lower electricity costs in the business case for the flexible production asset, due to reaped benefits from being able to “overproduce” (and store) hydrogen at low electricity prices, appears insufficient to compensate for the extra investments in a larger electrolyser, the storage and the related equipment, and the higher operational costs.
- Especially an increase in the amount of hours with low electricity prices (due to a larger installed capacity of solar and offshore wind) and further developments in PEM technology favour the business case of flexible hydrogen production and storage, and provide perspective on a positive NPV.
- Additional revenue streams (to selling hydrogen) can be generated by including alternative benefits of storage in the business model, that were outside the scope of this study, for example:
  - Offering flexibility to the electricity system with the up- and down-regulating capacities of the electrolysers (TSO and DSO), e.g. by services like aFRR and FCR from TenneT, the Dutch TSO;
  - Offering security of supply by storage of hydrogen;
  - Avoid or reduce investments in grid capacity expansion by TSO and DSO;
  - Utilisation of waste heat generated by the asset (electrolyser). Waste heat can be used for example in the industry or built environment.

## References

- Barbour, E., Mignard, D., Ding, Y., Li, Y., 2015. Adiabatic compressed air energy storage with packed bed thermal energy storage. *Applied Energy*, 2015, 155, 804–815. <https://doi.org/10.1016/j.apenergy.2015.06.019>
- Bartela L., 2020. A Hybrid energy storage system using compressed air and hydrogen and the energy carrier. *Energy*, 196, 117088. <http://dx.doi.org/10.1016/j.energy.2020.117088>
- Battistelli A., Calore C., Pruess K., (1997) The simulator TOUGH2/EWASG for modelling geothermal reservoirs with brines and non-condensable gas, *Geothermics*, Volume 26, Issue 4, Pages 437-464.
- Bell, I. H. and Wronski, J., Quoilin, S., Lemort, V. [2014]. Pure and Pseudo-pure Fluid Thermophysical Property Evaluation and the Open-Source Thermophysical Property Library CoolProp. *Industrial & Engineering Chemistry Research* 53 (6), 2498-2508.
- Benedikt Lunz, Matthias Leuthold and Dirk Uwe Sauer Georg Fuchs, "Overview of Nonelectrochemical Storage Technologies," in *Electrochemical Energy Storage for Renewable Sources and Grid Balancing*. Durham, United States: Elsevier, 2014, vol. 1, pp. 89-102.
- Berenschot and Kalavasta, 2020. [Klimaatneutrale energiescenario's 2050](#). Scenariostudie ten behoeve van de integrale infrastructuurverkenning 2030-2050. Bert den Ouden, John Kerkhoven, Jan Warnaars, Rob Terwel, Max Coenen, Thijs Verboon, Tuuli Tiihonen & Anne Koot, 2020.
- Bernardez, L. A., De Andrade Lima, L. R., De Jesus, E. B., Ramos, C. L., Almeida, P. F. (2013). A kinetic study on bacterial sulfate reduction. *Bioprocess and Biosystems Engineering*, 36(12), 1861-1869. doi:10.1007/s00449-013-0960-0
- Blanc Ph., Lassin A., Piantone P., Azaroual M., Jacquement N., Fabbri A., Gaucher, E.C., (2012) Thermoddem: A geochemical database focused on low temperature water/rock interactions and waste materials, *Applied Geochemistry*, 27, 2107-2116.
- Bonté, D., J.-D. van Wees, and J.M. Verweij. 2012. Subsurface temperature of the onshore Netherlands: new temperature dataset and modelling. *Netherlands Journal of Geosciences*. 91(4): 491-515.
- Budt, M., Wolf, D., Span, R., Yan, J., 2016. A review on compressed air energy storage: Basic principles, past milestones and recent developments. *Applied Energy*, 170, 250-268. <http://dx.doi.org/10.1016/j.apenergy.2016.02.108>
- Caglayan, D., Weber, N., Heinrichs, H., Linßen, J., Robinius, M., Kukla, P., & Stolten, D. (2020). Technical Potential of Salt Caverns for Hydrogen Storage in Europe. *International Journal of Hydrogen Energy*.
- Carden, P., Paterson, L., 1979. Physical, chemical and energy aspects of underground hydrogen storage. *Int. J. Hydrogen Energy* 4, 4–8.
- Chen, L., Zheng, T., Mei, S. et al., 2016. Review and prospect of compressed air energy storage system. *J. Mod. Power Syst. Clean Energy* 4, 529–541. <http://dx.doi.org/10.1007/s40565-016-0240-5>
- Crotogino F, Donadei S, Büninger U, Landinger H. Large-scale hydrogen underground storage for securing future energy supplies. *Proceedings of 18th World Hydrogen Energy Conference (WHEC2010)*, Essen, Germany; May 16e21, 2010. p. 37e45.
- Crotogino, F., Mohmeyer, K., Scharf, R., 2001. Huntorf CAES. More than 20 years of successful operation. In: *Proc of SMRI Spring Meeting*, Orlando, Florida, USA, April, p. 351-362.
- DBI-GUT, ["Final report for executing a study of the effects of hydrogen injection in natural gas networks for the Dutch underground storages"](#), 2017.

DeVries, K.L. 2006. Geomechanical analyses to determine the onset of dilation around natural gas storage caverns in bedded salt. In Proceedings of the SMRI (Solution Mining Research Institute) Spring 2006 Conference, 30 April - 3 May 2006, Brussels, Belgium.

DIANA FEA. 2019. Finite element program and Users documentation, version 10.3. <https://dianafea.com>.

Didier, M., Leone, L., Greneche, J.-M., Giffaut, E., Charlet, L., (2012) Adsorption of hydrogen gas and redox processes in clays. *Environ. Sci. Technol.* 46, 3574–3579.

DOE, NETL., 2014. Final environmental assessment for the pacific gas and electric company (PG&E) compressed air energy storage (CAES) compression testing phase project. San Joaquin County, California. (DOE/EA-1752).

Düsterloh, U. and K.-H. Lux. 2010. Some geomechanical aspects of compressed air energy storage (CAES) in salt caverns. In Proceedings of the SMRI (Solution Mining Research Institute) Fall 2010 Conference, 3 - 6 October 2010, Leipzig, Germany.

Eckroad, S., Gyuk, I., 2003. EPRI-DOE handbook of energy storage for transmission & distribution applications. Washington, DC, Department of Energy.

Energystock, "Aanvraag Instemming Wijziging Opslagplan Zuidwending", 2017.

Energy Storage Association (ESA), 2020. Why Energy Storage – technologies. <https://energystorage.org/>

Evans, D.J., 2008. Accidents at UFS sites and risk relative to other areas of the energy supply chain, with particular reference to salt cavern storage. British Geological Survey, Nottingham, England. SMRI Fall 2008 Technical Conference, 13-14 October 2008, Galveston, Texas, USA

Finkenrath, M., Pazzi, S., d'Ercole, M., 2009. Status and technical challenges of advanced compressed air energy storage (CAES) technology. Proceedings of international workshop on environmental and alternative energy, Munich, Germany.

Foh, S., Novil, M., Rockar, E.Randolph, P., 1979. Underground Hydrogen Storage. Final Report. Institute of Gas Technology, Chicago, issued as BNL51275: 6-14.

Fokker, P.A. 1995. The behaviour of salt and salt caverns. PhD thesis, Delft University of Technology.

Forchheimer, P., 1901. Wasserbewegung durch boden. *Zeitschrift des Vereines Deutscher Ingenieur*, 45 edition: 1782-1788.

Friedel, T., Voigt, H., 2006. Investigation of non-Darcy flow in tight-gas reservoirs with fractured wells. *Journal of Petroleum Science and Engineering* 54: 112-128.

Gasunie and Tennet, 2018. [Infrastructure Outlook 2050](#) - A joint study by Gasunie and TenneT on integrated energy infrastructure in the Netherlands and Germany.

Greksák, M., Šmigáň, P., Kozánková, J., Buzek, F., Onderka, V., & Wolf, I. (1990). Methanogenic bacteria and their activity in a subsurface reservoir of town gas. *Microbiology and Biochemistry of Strict Anaerobes Involved in Interspecies Hydrogen Transfer*, 381-383. doi:10.1007/978-1-4613-0613-9\_39

Guerra, O.J., Zhang, J., Eichman, J., Denholm, P., Kurtz, J., & Hodge, B. (2020). The Value of Seasonal Energy Storage Technologies for the Integration of Wind and Solar Power. *Energy and Environmental Science*.

Gusev, M. V., & Mineeva, L. A. (1992). *Microbiology*. Moscow, Russia.

Hagemann, B., Rasoulzadeh, M., Panfilov, M., Ganzer, L., & Reitenbach, V. (2016). Hydrogenization of underground storage of natural gas - Impact of hydrogen on the hydrodynamic and bio-chemical behavior. *Comput. Geosci.* (2016) 20:595–606. doi: 10.1007/s10596-015-9515-6

Hemme, C., & Van Berk, W. (2018). Hydrogeochemical modeling to identify potential risks of Underground hydrogen storage in depleted gas fields. *Applied Sciences*, 8(11), 2282. doi:10.3390/app8112282

Clara F. Heuberger, Iain Staffell, Nilay Shah, Niall Mac Dowell (2017). A systems approach to quantifying the value of power generation and energy storage technologies in future electricity networks, *Computers & Chemical Engineering*, Volume 107, 2017, Pages 247-256.

HyUnder D3.1, "Overview on all Known Underground Storage Technologies for Hydrogen", 2013.

IfG report 11/2007, 2007. Rock Mechanical Investigations on Rock Salt from the Zuidwending Gas Storage Site. IfG Institut für Gebirgsmechanik GmbH, Report B IfG 11/2007. Downloadable via [link](#).

IfG, 2008. Rock-mechanical appraisal on the positioning of caverns in a salt dome and safety distances between gas storage caverns. Appendix to the 2012 storage plan of the Zuidwending natural gas storage facility of Energystock. IfG Institut für Gebirgsmechanik GmbH, 2008.

IfG report 49/2011, 2011. Case Studies for Cyclic Operated Storage Caverns 'Aardgasbuffer Zuidwending' NL. IfG Institut für Gebirgsmechanik GmbH, Report B IfG 49/2011. Downloadable via [link](#).

IGU Natural Gas Information, 2016. <https://www.igu.org/>

Iverson, W. P. (1980). The sulphate-reducing bacteria: John R. Postgate. Cambridge University press, Cambridge, England, 1979, 151 P., \$29.50. *International Journal of Systematic Bacteriology*, 30(3), 602-602. doi:10.1099/00207713-30-3-602

John, F., 2013. FirstEnergy postpones project to generate electricity with compressed air.

Jorgensen, B. B., Isaksen, M. F., & Jannasch, H. W. (1992). Bacterial sulfate reduction above 100 C in deep-sea hydrothermal vent sediments. *Science*, 258(5089), 1756-1757. doi:10.1126/science.258.5089.1756

Juez-Larré, J., Remmelts, G., Breunese, J., Van Gessel, S., Leeuwenburgh, O. (2016) Using Underground gas Storage to replace the swing capacity of the giant natural gas field of Groningen in The Netherlands. A reservoir performance feasibility study", *Journal of Petroleum Geosciences and Engineering* 145, pp 34-53, 2016.

Juez-Larré, J., van Gessel, S., Dalman, R., Remmelts, G., Groenenberg, R., (2019). Assessment of underground energy storage potential to support the energy transition in the Netherlands. *First Break* volume 37 (7), 57-66pp. European Association Geoscientist and Engineers.

Khaitan, S.K., Raju, M., 2012. Dynamics of hydrogen powered CAES based gas turbine plant using sodium alanate storage system. *International Journal of Hydrogen Energy*, 37, 18904-18914. <http://dx.doi.org/10.1016/j.ijhydene.2012.10.004>

Klumpp, F., 2016. Comparison of pumped hydro, hydrogen storage and compressed air energy storage for integrating high shares of renewable energies—Potential, cost-comparison and ranking. *Journal of Energy Storage*. 8, 119-128. <http://dx.doi.org/10.1016/j.est.2016.09.012>

Knight, U.G. *Power Systems in Emergencies - From Contingency Planning to Crisis Management* John Wiley & Sons 2001 ISBN 978-0-471-49016-6 section 7.5 The 'Black Start' Situation.

Knoke, S., 2002. EPRI energy storage handbook: Compressed Air Energy Storage (CAES) Chapter. Energy International, Inc, December 2002.

Laille, J., Molinard, J., & Wents, A. (1988). Inert gas injection as part of the cushion of the Underground storage of Saint-Clair-Sur-Epte, France. *SPE Gas Technology Symposium*. doi:10.2118/17740-ms

Lassin A., M. Dymitrowska, M. Azaroual, (2011) Hydrogen solubility in pore water of partially saturated argillites: Application to Callovo-Oxfordian clayrock in the context of a nuclear waste geological disposal. *Physics and Chemistry of the Earth* 36, 1721–1728

Li, L., Liang, W., Lian, H., Yang, J., Dusseault, M., 2018. Compressed Air energy storage: characteristics, basic principles and geological considerations. *Advances in Geo-Energy Research*, 2, 2, 135-147. <http://dx.doi.org/10.26804/ager.2018.02.03>

Lingen, P.L., 1974. Description of Groningen gas wells performance suitable for medium and long range planning. SPE 4816, presented at the 1974 SPE European Spring Meeting, Amsterdam, April.

Liu, S. (2017). How cells grow. *Bioprocess Engineering*, 545-592. doi:10.1016/b978-0-12-821012-3.00013-0

Machel, H. (2001). Bacterial and thermochemical sulfate reduction in diagenetic settings — old and new insights. *Sedimentary Geology*, 140(1-2), 143-175. doi:10.1016/s0037-0738(00)00176-7

Madani Sani, F., Huizinga, S., Esaklul, K.A., Nestic, S., 2019. Review of the API RP 14E erosional velocity equation: origin, applications, misuses and limitations. *Wear* 426-427, 620-636 pp.

Misra, B., Foh, S., Shikari, Y., Berry, R., & Labaune, F. (1988). The use of inert base gas in Underground natural gas storage. *SPE Gas Technology Symposium*. doi:10.2118/17741-ms

Modak, J. M. (2002). Haber process for ammonia synthesis. *Resonance*, 7(9), 69-77. doi:10.1007/bf02836187

Nakhamkin M, Andersson L, Swensen E, Howard J. AEC 110 MW CAES plant: status of project. *ASME J Eng Gas Turbines Power* 1992;114:695–700.

Nederlandse Gasunie, 2012. Gewijzigd opslagplan Zuidwending (Application for gas storage at the Zuidwending salt dome). Accessible via [link](#).

Nieland, J.D. 2008. Salt cavern thermodynamics – Comparison between hydrogen, natural gas, and air storage. In *Proceedings of the SMRI (Solution Mining Research Institute) Fall 2008 Conference*, 13 - 14 October 2008, Galveston, Texas, USA.

Noordelijke Innovation Board, 2018. *The Green Hydrogen Economy in the Northern Netherlands*.

Oldenburg, C. M. (2003). Carbon dioxide as cushion gas for natural gas storage. *Energy & Fuels*, 17(1), 240-246. doi:10.1021/ef020162b

Oldenburg, C. M., & Pan, L. (2013). Utilization of CO<sub>2</sub> as cushion gas for porous media compressed air energy storage. *Greenhouse Gases: Science and Technology*, 3(2), 124-135. doi:10.1002/ghg.1332

Panfilov, M. (2010). Underground storage of hydrogen: In situ self-organisation and methane generation. *Transport in Porous Media*, 85(3), 841-865. doi:10.1007/s11242-010-9595-7

Parkhurst D.L., Appelo C.A.J., 1999. *User's Guide to PHREEQC (Version 2) – A Computer Program for Speciation, Batch Reaction, One-Dimensional Transport, and Inverse Geochemical Calculations*. Report 99-4259. US Geological Survey Water-Resources Investigations.

A. Pérez, E. Pérez, S. Dupraz, J. Bolcich, “[Patagonia Wind - Hydrogen Project: Underground Storage and Methanation](#)”, 21st World Hydrogen Energy Conference, 2016.

Pollak R. *History of first U.S. Compressed Air Energy Storage (CAES) plant (110MW 26h): volume 2: Construction*. Palo Alto; 1994.

Pruess, K. *ECO2N : A TOUGH2 Fluid Property Module for Mixtures of Water, NaCl, and CO<sub>2</sub>*; Lawrence Berkeley National Laboratory: Berkeley, CA, USA, 2005.

Radgen P., 2008. 30 years compressed air energy storage plant Huntorf – experiences and outlook. In: *3rd international renewable energy storage conference*. Berlin, p. 18.

Reitenbach, V.; Ganzer, L.; Albrecht, D.; Hagemann, B. Influence of added hydrogen on underground gas storage: A review of key issues. *Environ. Earth Sci.* 2015, 73, 6927–6937.

Remmelts, G., 2011. Mogelijke alternatieven voor ondergrondse opslag van gas in de zoutkoepel Pieterburen. TNO rapport, TNO-060-UT-2011-00725.

Succar, S., Williams, R.H., 2011. Compressed Air Energy Storage: Theory, Resources, And Applications For Wind Power. Princeton Environmental Institute, Princeton University, Energy systems analysis group. ‘

Thüns, N., Krooss, B.M., Zhang, Q., and Stanjek, H., 2019. The effect of H<sub>2</sub> pressure on the reduction kinetics of hematite at low temperatures. *Int. journal of hydrogen energy* 44, p. 27615-27625.

Truche L., Berger G., Destigneville C., Guillaume D., Giffaut E., 2010. Kinetics of pyrite to pyrrhotite reduction by hydrogen in calcite buffered solutions between 90 and 180 °C: implications for nuclear waste disposal. *Geochim Cosmochim Acta* 74, 10:2894–2914.

Truche L., Jodin-Caumon M., Lerouge C., Berger G., Mosser-Ruck R., Giffaut E., Michau N., (2013) Sulphide mineral reactions in clay-rich rock induced by high hydrogen pressure. Application to disturbed or natural settings up to 250 °C and 30 bar. *Chemical Geology* 351, 217–228.

Tuschy I, Althaus R, Gerdes R, Keller-Sornig P. Entwicklung der Gasturbinen in der Luftspeicher-Technologie. *VGB PowerTech* 2004;4:84–7.

["Underground Sun.Storage. Publizierbarer Endbericht"](#), Sun.Storage, 2017.

S.F. van Gessel, J.N. Breunese, J. Juez Larré, T.D. Huijskes, G. Remmelts, "Ondergrondse Opslag in Nederland - Technische Verkenning", 2018.

Van Hout, M., Koutstaal, P., Ozdemir, O., and Seebregts, A. (2014). Quantifying flexibility markets, ECN, [ECN-E--14-039](#).

Vogel, J.V., 1968. Inflow performance relationships for solution-gas drive wells. *Journal of Petroleum Technology*, Society of Petroleum Engineers (SPE): 83-92.

J. Wallbrecht, H. Brauner, E. Wicquart, P. Grigelova, G. Martinus, L. Goryl, F. Metzger, "2006-2009 Triennium Work Report October 2009", Study Group 2.1: UGS Database, 24th World Gas Conference, Buenos Aires, Argentina, 5-9. October, 2009.

Wang T, Yang C, Ma H, Daemen JJK, Wu H. Safety evaluation of gas storage caverns located close to a tectonic fault. *J Nat Gas Sci Eng* 2015; v23, p281-293. <https://doi.org/10.1016/j.jngse.2015.02.005>.

Wang, J.; Lu, K.; Ma, L.; Wang, J.; Dooner, M.; Miao, S.; Li, J.; Wang, D. Overview of Compressed Air Energy Storage and Technology Development. *Energies* 2017, 10, 991.

Xu T., Sonnenthal E., Spycher N., Zheng L., (2014) TOUGHREACT V3.0-OMP Reference manual: A parallel simulation program for non-isothermal multiphase geochemical reactive transport. LBNL765 Draft.

Xu, T.; Sonnenthal, E.; Spycher, N.; Pruess, K. TOUGHREACT—A simulation program for non-isothermal multiphase reactive geochemical transport in variably saturated geologic media: Applications to geothermal injectivity and CO<sub>2</sub> geological sequestration. *Computat. Geosci.* 2006, 32, 145–165.

Yekta A.E., Pichavant M., Audigane P., (2018) Evaluation of geochemical reactivity of hydrogen in sandstone: Application to geological storage. *Applied Geochemistry* 95, 182–194.

Yildiz, T. (2006). Assessment of Total Skin Factor in Perforated Wells. Society of Petroleum Engineers. doi:10.2118/82249-PA

Zander-Schiebenhöfer, D. 2010. High Frequency Cycling of Gas Storage Caverns: Phase I: Development of Appropriate Lab Tests & Design Criteria. SMRI (Solution Mining Research Institute) Research Report RR2010-01.

## Appendix A: Techno-economic parameters

### D-CAES and AA-CAES – Asset-specific variables

| Asset-specific variables          |   |           |             |
|-----------------------------------|---|-----------|-------------|
| CAES                              |   |           |             |
| Technical variables               |   |           |             |
| Discharge power capacity of asset |   | 320       | MW          |
| Storage capacity of asset         |   | 3840      | MWh         |
| Lifetime                          |   | 50        | years       |
| Fuel consumption Natural Gas      |   | 1,20      | MWh/MWh     |
| CO2 emission                      |   | 0,210     | ton kg/MWh  |
| E/P ratio                         |   | 12        |             |
| Discharge efficiency 2030         |   | 58%       |             |
| (Dis)charging time                |   | 12        | hours       |
| Economic variables                |   |           |             |
| Investment costs                  | € | 1.100.000 | EUR/MW      |
| Constant O&M costs                |   | 2,5%      | CAPEX/year  |
| Variable O&M costs                |   | 2,00      | EUR/MWh     |
| TSO grid connection costs         | € | 37.000    | EUR/MW/year |

| AA-CAES                           |   |         |             |
|-----------------------------------|---|---------|-------------|
| Technical variables               |   |         |             |
| Discharge power capacity of asset |   | 140     | MW          |
| Storage capacity of asset         |   | 1082    | MWh         |
| Lifetime                          |   | 40      | years       |
| Heat storage                      |   | 0,78    |             |
| Heat supply                       |   | 1,09    |             |
| E/P ratio                         |   | 8       |             |
| Discharge efficiency 2030         |   | 0,70    |             |
| Economic variables                |   |         |             |
| Investment costs                  |   | 1500000 | EUR/MW      |
| Constant O&M costs                |   | 2,5%    | EUR/MW      |
| Variable O&M costs                |   | 2,00    | EUR/MWh     |
| TSO grid connection costs         | € | 37.000  | EUR/MW/year |

| Technological parameter            | Unit    | CAES | AA-CAES |
|------------------------------------|---------|------|---------|
| Charge time                        | h       | 8    | 10.5    |
| Charge power                       | MW      | 250  | 103     |
| Charge efficiency                  | %       | 100  | 100     |
| Charge rate                        | MW/h    | 250  | 103     |
| Energy stored                      | MWh     | 2000 | 1081.5  |
| Discharge efficiency               | %       | 58   | 70      |
| Discharge Power                    | MW      | 320  | 140     |
| Discharge rate                     | MW/h    | 320  | 140     |
| Self-discharge                     | MWh/h   | 0    | 0       |
| Natural gas fuel consumption (LHV) | MWh/MWh | 1.13 |         |
| CO2 Emission                       | kg/MWh  | 210  |         |
| Heat storage                       | MWh/MWh |      | 0.78    |
| Heat supply                        | MWh/MWh |      | 1.09    |

| Economic parameter | Unit           | CAES       | AA-CAES    |
|--------------------|----------------|------------|------------|
| Investment costs   | EUR/MW         | €1,100,000 | €1,500,000 |
| Constant O&M costs | % CAPEX EUR/MW | 2.5        | 2.5        |
| Variable O&M costs | EUR/MWh        | €2         | €2         |
| Variable TSO costs | EUR/MW/year    | €37,000    | €37,000    |

## UHS – Asset-specific variables

| Asset-specific variables                              |             |                 |  |
|---|-------------|-----------------|--|
| Flexible hydrogen production                          |             |                 |  |
| Technical variables                                   |             |                 |  |
| P2G PEM Production capacity                           | 1500        | MW_e            |  |
| P2G PEM Production capacity stand-by                  | 34          | MW_e            |  |
| P2G PEM supply capacity stand-by                      | 20,4        | MW_H2           |  |
| P2G PEM Efficiency                                    | 60%         |                 |  |
| P2G PEM Operating hours                               | 5901        | hours/year      |  |
| P2G PEM Stand-by hours                                | 2859        | hours/year      |  |
| P2G PEM lifetime                                      | 30          | year            |  |
| P2G PEM Stack lifetime hours                          | 50000       | hours           |  |
| P2G PEM Stacks lifetime years                         | 8           | year            |  |
| UGS cavern Storage capacity (power equivalent H2 LHV) | 163150      | MWh_H2_LHV      |  |
| UGS cavern Storage capacity volume normalm3           | 54500000    | Nm3             |  |
| UGS cavern Storage capacity volume tons               | 4895        | ton             |  |
| UGS cavern max charge power                           | 900         | MW_H2_LHV       |  |
| UGS cavern Charge efficiency                          | 60%         |                 |  |
| UGS cavern max charge rate                            | 900         | MW_H2_LHV       |  |
| UGS cavern max charge flow                            | 27          | ton/h           |  |
| UGS cavern max discharge rate                         | 606         | MW_H2_LHV       |  |
| UGS cavern max discharge flow                         | 18          | ton/h           |  |
| UGS cavern Discharge efficiency                       | 99%         |                 |  |
| UGS cavern Discharge rate                             | 600         | MW_H2_LHV       |  |
| Ratio working gas volume/cushion gas volume           | 1,50        | -               |  |
| Required cushion gas volume normalm3                  | 36.333.333  | Nm3             |  |
| Required cushion gas volume ton                       | 1958        | ton             |  |
| Required cushion gas volume MWh                       | 65260       | MWh_H2_LHV      |  |
| Economic variables                                    |             |                 |  |
| Investment costs P2G PEM                              | € 1.000.000 | EUR/MW          |  |
| Investment costs stack replacement                    | € 184.000   | EUR/MW          |  |
| Investment costs Balance of plant                     | € 500.000   | EUR/MW          |  |
| Investment costs Compressor                           | € 4.200.000 | EUR/ton/h       |  |
| Investment costs UGS cavern                           | € 4.800     | EUR/ton         |  |
| Investment costs Expander gas treatment               | € 2.520.000 | EUR/ton         |  |
| Electricity consumption P2G PEM                       | € -         |                 |  |
| Electricity consumption Balance of plant              | € -         |                 |  |
| Electricity consumption Compressor (+drying)          | € 1,10      | MWh_e/ton       |  |
| Electricity consumption Compressor (+drying)          | € 0,033     | MWh_e/MW_H2_LHV |  |
| Electricity consumption UGS cavern                    | € -         | MWh_e/ton       |  |
| Electricity consumption Expander gas treatment        | € 0,10      | MWh_e/ton       |  |
| Constant O&M costs P2G PEM                            | 2,5%        | CAPEX/year      |  |
| Constant O&M costs Balance of plant                   | 1,0%        | CAPEX/year      |  |
| Constant O&M costs Compressor                         | 7,0%        | CAPEX/year      |  |
| Constant O&M costs UGS cavern                         | 4,5%        | CAPEX/year      |  |
| Constant O&M costs Expander gas treatment             | 4,0%        | CAPEX/year      |  |
| TSO grid connection costs                             | € 37.000    | EUR/MW/year     |  |

## Continuous hydrogen production

### Technical variables

|                               |       |            |
|-------------------------------|-------|------------|
| P2G PEM Production capacity   | 1000  | MW_e       |
| P2G PEM Efficiency            | 60%   |            |
| P2G PEM Operating hours       | 8760  | hours/year |
| P2G PEM lifetime              | 30    | year       |
| P2G PEM Stack lifetime hours  | 50000 | hours      |
| P2G PEM Stacks lifetime years | 6     | year       |

|                              |     |           |
|------------------------------|-----|-----------|
| Reference PEM Discharge rate | 600 | MW_H2_LHV |
|------------------------------|-----|-----------|

### Economic variables

|                                    |         |        |
|------------------------------------|---------|--------|
| Investment costs P2G PEM           | 1000000 | EUR/MW |
| Investment costs stack replacement | 184000  | EUR/MW |
| Investment costs Balance of plant  | 500000  | EUR/MW |

|  |   |   |
|--|---|---|
| Electricity consumption P2G PEM          | 0 | 0 |
| Electricity consumption Balance of plant | 0 |   |

|                                     |      |            |
|-------------------------------------|------|------------|
| Constant O&M costs P2G PEM          | 2,5% | CAPEX/year |
| Constant O&M costs Balance of plant | 1%   |            |

|                           |          |             |
|---------------------------|----------|-------------|
| TSO grid connection costs | € 37.000 | EUR/MW/year |
|---------------------------|----------|-------------|

## Appendix B: Detailed sensitivity analysis description

| Sensitivity scenarios |   | Varied parameter(s)      |  |  |  | Base case 2030 |             | Extreme 2030 |             | Base case 2050 |             | Extreme 2050 |             |
|-----------------------|---|--------------------------|--|--|--|----------------|-------------|--------------|-------------|----------------|-------------|--------------|-------------|
| S1                    | Maximum natural gas-fired power plant [GW]  | +3.2 GW operational      |  |  |  | 11.9           | 15.1        | 0            | 0           | 0              | 0           | 0            | 0           |
| S2                    | Installed capacity solar (PV) [GW]          | 200% Solar <2050         |  |  |  | 25.1           | 50.2        | 106          | 106         | 106            | 106         | 106          | 106         |
|                       | Installed capacity offshore wind farms [GW] | 200% OWF >2050           |  |  |  | 13.4           | 13.4        | 51.5         | 103         | 51.5           | 103         | 103          | 103         |
| S3                    | Natural gas price [EUR/MWh]                 | 200% NG price            |  |  |  | 27.36          | 54.72       | 48.24        | 48.24       | 24.12          | 48.24       | 48.24        | 48.24       |
|                       | CO2 price [EUR/ton]                         | 200% CO2 price           |  |  |  | 45.34          | 90.68       | 320          | 320         | 160            | 320         | 320          | 320         |
| S4                    | Electrolyzer power of P2G asset [MW/h]      | 200% production capacity |  |  |  | 1500           | 3000        | 3000         | 3000        | 1500           | 3000        | 3000         | 3000        |
|                       | Cavern charge rate of UGS asset [MW/h]      | 200% charge capacity     |  |  |  | 1500           | 3000        | 3000         | 3000        | 1500           | 3000        | 3000         | 3000        |
|                       | Electrolyzer efficiency [%]                 | +10% efficiency          |  |  |  | 60%            | 70%         | 70%          | 70%         | 60%            | 70%         | 70%          | 70%         |
|                       | Electrolyzer investment costs [EUR/MW]      | -20% investment cost     |  |  |  | 1M             | 0.8M        | 0.8M         | 0.8M        | 1M             | 0.8M        | 0.8M         | 0.8M        |
| S5                    | TSO costs flex [EUR/MW]                     | 50% TSO costs            |  |  |  | 39k            | 18.5k       | 18.5k        | 18.5k       | 39k            | 18.5k       | 18.5k        | 18.5k       |
|                       | Hydrogen price [EUR/kg (EUR/MWh)]           | 50% H2 price             |  |  |  | 1              | 0.5 (18.22) | 1            | 0.5 (16.11) | 1              | 0.5 (16.11) | 1            | 0.5 (16.11) |
| S6                    | Hydrogen price [EUR/kg (EUR/MWh)]           | 500% H2 price            |  |  |  | 1              | 5 (182.16)  | 1            | 5 (161.1)   | 1              | 5 (161.1)   | 1            | 5 (161.1)   |

## Appendix C: Business case details 2025, 2030, 2050

In this Appendix the cash flows for D-CAES, AA-CAES, continuous hydrogen production and flexible hydrogen production and storage are presented. The remaining years from 2025-2060 are covered as follows:

- 2025 is the year in which all investments take place
- No cash flows in 2026-2029. In practice, these years will be used for engineering and construction
- 2030 is the first year of operation
- 2031-2049 are identical to 2030 (except for investments in stack replacement for the hydrogen electrolyser, they occur each 6 years for continuous production and once in 8 years for flexible hydrogen production)
- From 2050, operation is based on a different EYE simulation compared to 2030.
- 2061-2060 are identical to 2050 (except stack replacement for hydrogen)

|                  |                                 | NPV |                     | 2025     |          |                     | 2030     |                    |          | 2050               |          |  |
|------------------|---------------------------------|-----|---------------------|----------|----------|---------------------|----------|--------------------|----------|--------------------|----------|--|
|                  |                                 |     |                     | EUR      | EUR/year | EUR                 | EUR/year | EUR                | EUR/year | EUR                | EUR/year |  |
| <b>Revenue</b>   | <b>Total</b>                    | €   | <b>84,682,181</b>   | EUR/year | €        | -                   | €        | <b>5,832,000</b>   | €        | <b>3,833,952</b>   |          |  |
|                  | Wholesale market sales          | EUR | 84,682,181          | EUR/year | €        | -                   | €        | 5,832,000          | €        | 3,833,952          |          |  |
| <b>OPEX</b>      | <b>Total</b>                    | €   | <b>309,064,755</b>  | EUR/year | €        | -                   | €        | <b>24,246,416</b>  | €        | <b>23,479,910</b>  |          |  |
|                  | Electricity consumption costs   | EUR | 4,647,158           | EUR/year | €        | -                   | €        | 372,900            | €        | -                  |          |  |
|                  | Variable TSO costs              | EUR | 184,618,876         | EUR/year | €        | -                   | €        | 11,840,000         | €        | 11,840,000         |          |  |
|                  | Constant O&M costs              | EUR | 137,216,732         | EUR/year | €        | -                   | €        | 8,800,000          | €        | 8,800,000          |          |  |
|                  | Variable O&M costs              | EUR | 2,101,376           | EUR/year | €        | -                   | €        | 139,520            | €        | 115,840            |          |  |
|                  | Fuel consumption                | EUR | 37,598,284          | EUR/year | €        | -                   | €        | 2,464,063          | €        | 2,201,053          |          |  |
|                  | CO2 emission                    | EUR | 9,487,714           | EUR/year | €        | -                   | €        | 629,933            | €        | 523,018            |          |  |
| <b>CAPEX</b>     | <b>Total</b>                    | €   | <b>352,000,000</b>  |          | €        | <b>352,000,000</b>  | €        | -                  | €        | -                  |          |  |
|                  | Investment costs CAES           | EUR | 352,000,000         | EUR/year | €        | 352,000,000         | €        | -                  | €        | -                  |          |  |
| <b>Cash Flow</b> | <b>Total</b>                    | €   | <b>591,396,515-</b> |          | €        | <b>352,000,000-</b> | €        | <b>18,414,416-</b> | €        | <b>19,645,958-</b> |          |  |
|                  | Cash Flow Cumulatief            |     |                     |          | €        | 352,000,000-        | €        | 370,414,416-       | €        | 739,934,269-       |          |  |
|                  | Discounted cumulative cash flow |     |                     |          | €        | 352,000,000-        | €        | 366,428,176-       | €        | 546,598,824-       |          |  |

|                  |                                  | NPV      |                     | 2025     |          |                     | 2030     |                   |          | 2050              |          |  |
|------------------|----------------------------------|----------|---------------------|----------|----------|---------------------|----------|-------------------|----------|-------------------|----------|--|
|                  |                                  |          |                     | EUR      | EUR/year | EUR                 | EUR/year | EUR               | EUR/year | EUR               | EUR/year |  |
| <b>Revenue</b>   | <b>Total</b>                     | €        | <b>84,906,227</b>   | EUR/year | €        | -                   | €        | <b>6,053,866</b>  | €        | <b>3,022,320</b>  |          |  |
|                  | Wholesale market sales           | EUR/year | 84,906,227          | EUR/year | €        | -                   | €        | 6,053,866         | €        | 3,022,320         |          |  |
| <b>OPEX</b>      | <b>Total</b>                     | €        | <b>160,465,487</b>  | EUR/year | €        | -                   | €        | <b>12,953,956</b> | €        | <b>10,736,560</b> |          |  |
|                  | Electricity consumption costs    | EUR      | 29,942,757          | EUR/year | €        | -                   | €        | 2,348,956         | €        | 213,880           |          |  |
|                  | Electricity transportation costs | EUR      | 80,770,758          | EUR/year | €        | -                   | €        | 5,180,000         | €        | 5,180,000         |          |  |
|                  | Constant O&M costs               | EUR      | 81,862,255          | EUR/year | €        | -                   | €        | 5,250,000         | €        | 5,250,000         |          |  |
|                  | Variable O&M costs               | EUR      | 2,471,031           | EUR/year | €        | -                   | €        | 175,000           | €        | 92,680            |          |  |
|                  | Fuel consumption                 | EUR      | -                   | EUR/year | €        | -                   | €        | -                 | €        | -                 |          |  |
|                  | CO2 emission                     | EUR      | -                   | EUR/year | €        | -                   | €        | -                 | €        | -                 |          |  |
| <b>CAPEX</b>     | <b>Total</b>                     | €        | <b>210,000,000</b>  |          | €        | <b>210,000,000</b>  | €        | -                 | €        | -                 |          |  |
|                  | Investment costs CAES            | EUR      | 210,000,000         | EUR/year | €        | 210,000,000         | €        | -                 | €        | -                 |          |  |
| <b>Cash Flow</b> | <b>Total</b>                     | €        | <b>300,612,924-</b> |          | €        | <b>210,000,000-</b> | €        | <b>6,900,090-</b> | €        | <b>7,714,240-</b> |          |  |
|                  | Cash Flow Cumulatief             |          |                     |          | €        | 210,000,000-        | €        | 216,900,090-      | €        | 355,716,044-      |          |  |
|                  | Discounted cumulative cash flow  |          |                     |          | €        | 210,000,000-        | €        | 215,406,401-      | €        | 283,022,531-      |          |  |

## Continuous H2 production 1000 MW

|                                |  |                | NPV                     | 2025                    | 2030                  | 2050                  |
|--------------------------------|--|----------------|-------------------------|-------------------------|-----------------------|-----------------------|
| <b>PEM reference operation</b> |  |                |                         |                         |                       |                       |
|                                | PEM H2 production hours                        | MW_H2/year     |                         | €                       | 8.759                 | 8759                  |
|                                | PEM H2 supplied                                | MW_H2/year     |                         | €                       | 5.255.400             | 5255400               |
| <b>Revenue</b>                 | <b>Total</b>                                   |                | <b>€ 2.399.174.538</b>  | <b>€ -</b>              | <b>€ 191.467.663</b>  | <b>€ 169.328.988</b>  |
|                                | Wholesale H2 market sales                      | EU/year        | € 2.916.211.646         | €                       | 191.467.663           | € 169.328.988         |
| <b>OPEX</b>                    | <b>Total</b>                                   |                | <b>€ 7.390.092.078</b>  | <b>€ -</b>              | <b>€ 585.125.000</b>  | <b>€ 530.881.500</b>  |
|                                | Electricity consumption costs PEM              | EU/year        | € 7.706.473.600         | €                       | 505.625.000           | € 448.881.500         |
|                                | Electricity consumption costs Balance of plant | EU/year        | € -                     | €                       | -                     | € -                   |
|                                | Constant O&M costs PEM                         | EU/year        | € 584.730.394           | €                       | 37.500.000            | € 37.500.000          |
|                                | Constant O&M costs Balance of plant            | EU/year        | € 114.565.126           | €                       | 5.000.000             | € 7.500.000           |
|                                | Variable TSO costs PEM                         | EU/year        | € 576.933.989           | €                       | 37.000.000            | € 37.000.000          |
| <b>CAPEX</b>                   | <b>Total</b>                                   |                | <b>€ 1.842.115.447</b>  | <b>€ 1.500.000.000</b>  | <b>€ -</b>            | <b>€ -</b>            |
|                                | Investment costs P2G PEM                       |                | € 1.000.000.000         | € 1.000.000.000         | € -                   | € -                   |
|                                | Investment costs stack replacement             | 1x per 8 years | € 796.623.707           | €                       | -                     | € -                   |
|                                | Investment costs Balance of plant              |                | € 500.000.000           | € 500.000.000           | €                     | €                     |
| <b>Cash Flow</b>               | <b>Total</b>                                   |                | <b>€ 6.833.032.987-</b> | <b>€ 1.500.000.000-</b> | <b>€ 393.657.337-</b> | <b>€ 361.552.512-</b> |
|                                | Cash Flow Cumulatief                           |                |                         | € 1.500.000.000-        | € 1.893.657.337-      | € 10.334.199.254-     |
|                                | Discounted cumulative cash flow                |                |                         | € 1.500.000.000-        | € 1.808.440.824-      | € 5.926.640.458-      |

## Flexible H2 production 1500 MW + storage

|                          |  |                | NPV                     | 2025                    | 2030                  | 2050                  |
|--------------------------|--|----------------|-------------------------|-------------------------|-----------------------|-----------------------|
| <b>P2G+UGS operation</b> |  |                |                         |                         |                       |                       |
|                          | PEM H2 production hours                        | MW_H2/year     |                         | €                       | 5.901                 | € 5.897               |
|                          | PEM H2 constant supplied                       | MW_H2/year     |                         | €                       | 3.598.320             | € 3.596.001           |
|                          | Storage total H2 charged                       | MW_H2/year     |                         | €                       | 1.681.786             | € 1.680.646           |
|                          | Storage total H2 discharged                    | MW_H2/year     |                         | €                       | 1.657.080             | € 1.659.399           |
|                          | Total H2 supplied                              | MW_H2/year     |                         | €                       | 5.255.400             | € 5.255.400           |
|                          | End-of-year H2 stored                          | MW_H2          |                         | €                       | 7.558                 | € 4.074               |
| <b>Revenue</b>           | <b>Total</b>                                   |                | <b>€ 336.317.843</b>    | <b>€ -</b>              | <b>€ 191.743.009</b>  | <b>€ 169.460.262</b>  |
|                          | Wholesale H2 market sales                      | EU/year        | € 335.936.535           | €                       | 191.467.664           | € 169.328.983         |
|                          | End-of-year H2 gas sale                        | EU/year        | € 381.307               | €                       | 275.345               | € 131.279             |
|                          | Sale cushion H2 gas                            | EU/year        | € -                     | €                       | -                     | € -                   |
| <b>OPEX</b>              | <b>Total</b>                                   |                | <b>€ 1.047.005.411</b>  | <b>€ -</b>              | <b>€ 598.302.172</b>  | <b>€ 526.106.185</b>  |
|                          | Electricity consumption costs P2G              | EU/year        | € 850.342.725           | €                       | 492.298.509           | € 420.589.421         |
|                          | Electricity consumption costs Balance of plant | EU/year        | € -                     | €                       | -                     | € -                   |
|                          | Electricity consumption costs Compressor       | EU/year        | € 5.260.664             | €                       | 3.046.930             | € 2.600.605           |
|                          | Electricity consumption costs UGS cavern       | EU/year        | € -                     | €                       | -                     | € -                   |
|                          | Electricity consumption costs Expander gas tre | EU/year        | € 478.242               | €                       | 276.994               | € 236.419             |
|                          | Constant O&M costs P2G                         | EU/year        | € 69.727.891            | €                       | 37.500.000            | € 37.500.000          |
|                          | Constant O&M costs Balance of plant            | EU/year        | € 13.945.578            | €                       | 7.500.000             | € 7.500.000           |
|                          | Constant O&M costs Compressor                  | EU/year        | € 2.108.782             | €                       | 1.134.113             | € 1.134.113           |
|                          | Constant O&M costs UGS cavern                  | EU/year        | € 1.092.215             | €                       | 587.399               | € 587.399             |
|                          | Constant O&M costs Expander gas treatment      | EU/year        | € 852.033               | €                       | 458.228               | € 458.228             |
|                          | Variable TSO costs P2G                         | EU/year        | € 103.197.279           | €                       | 55.500.000            | € 55.500.000          |
| <b>CAPEX</b>             | <b>Total</b>                                   |                | <b>€ 2.435.107.644</b>  | <b>€ 2.435.107.644</b>  | <b>€ -</b>            | <b>€ -</b>            |
|                          | Investment costs P2G PEM                       |                | € 1.500.000.000         | € 1.500.000.000         | € -                   | € -                   |
|                          | Investment costs Fuel cell stack replacement   | 1x per 8 years | € 750.000.000           | € 750.000.000           | € -                   | € -                   |
|                          | Investment costs Balance of plant              |                | € 113.411.341           | € 113.411.341           | € -                   | € -                   |
|                          | Investment costs Compressor                    |                | € 23.495.950            | € 23.495.950            | € -                   | € -                   |
|                          | Investment costs UGS cavern                    |                | € 45.822.764            | € 45.822.764            | € -                   | € -                   |
|                          | Investment costs Expander gas treatment        |                | € 2.377.589             | € 2.377.589             | € -                   | € -                   |
| <b>Cash Flow</b>         | <b>Total</b>                                   |                | <b>€ 3.145.795.212-</b> | <b>€ 2.435.107.644-</b> | <b>€ 406.559.163-</b> | <b>€ 356.645.923-</b> |
|                          | Cash Flow Cumulatief                           |                |                         | € 2.435.107.644-        | € 2.841.666.807-      | € 11.474.936.831-     |
|                          | Discounted cumulative cash flow                |                |                         | € 2.435.107.644-        | € 2.753.657.386-      | € 6.954.188.550-      |